MODIFICATION AND REPLICATION OF INTRICATE 3D STRUCTURES WITH THIN FILMS COMPRISED OF COMPLEX OXIDES

A Dissertation
Presented to
The Academic Faculty

By

Philip Davis Brooke

In Partial Fulfillment
Of the Requirements for the Degree
Doctor of Philosophy in Materials Science and Engineering

Georgia Institute of Technology

December 2015

MODIFICATION AND REPLICATION OF INTRICATE 3D STRUCTURES WITH THIN FILMS COMPRISED OF COMPLEX OXIDES

Approved by:

Dr. Kenneth H. Sandhage, Advisor
School of Materials Science and Engineering
Georgia Institute of Technology

Dr. Carson Meredith
School of Chemical & Biomolecular Engineering
Georgia Institute of Technology

Dr. Meilin Liu
School of Materials Science and Engineering
Georgia Institute of Technology

Dr. Joseph Perry
School of Chemistry & Biochemistry
Georgia Institute of Technology

Dr. Nazanin Bassiri-Gharb
School of Materials Science and Engineering
Georgia Institute of Technology

Date Approved: November 2, 2015

ACKNOWLEDGEMENTS

I would like to thank my advisor, Dr. Sandhage for all of the guidance and support he has given to me while here at Georgia Tech. Dr. Sandhage always encouraged me to analyze a problem scientifically and stressed the need to perform and represent scientific data in an ethical manner. I would also like to thank my committee members, Dr. Liu, Dr. Perry, Dr. Bassiri-Gharb, and Dr. Meredith for all of their advice and for their time spent reading and evaluating my work. I would like to thank my undergraduate advisor, Dr. Paul Eason, whose advice and enthusiasm about materials science inspired me to pursue my PhD.

I have had the opportunity to work in a distinguished lab with excellent lab mates. Dr. Yunshu Zhang, Dr. Yunnan Fang, and Dr. Ye Cai have been wonderful research scientists who have been enormously helpful in teaching me how to conduct high quality research. To my fellow graduate students, Ben deGlee, Nikolay Semenikhin, Melony Ochieng, Taylor Mclachlan Shapero, Haiyang Zou, Jeremy Yoo, Yihong Li, Dr. Brandon Goodwin, Dr. Craig Cameron, Dr. Stan Davis, Dr. Ari Gordin, Dr. John Vernon, and Dr. Dan Berrigan: thank you for innumerable conversations, both technical and nontechnical that have helped me broaden my understanding of materials science and the world.

I have been fortunate to have been able to collaborate with hard-working individuals that expanded the scope of my research to areas that I could not have done on my own. Thank you Gordon Waller, Donglee Shin, Greg Cohoon, Christine Alvarez, Dr. Robert Norwood, Dr. Dimitri Deheyn, and Dr. Vincent Chen for your hard work and your patience when I was slow to return

samples. I would especially like to thank Don Woodyard and Brian Markowicz who fabricated the crucial glass components used in the robotic coating systems. Without their skill and expertise much of this work would not have been possible.

The staff and administration in the School of Materials Science at Georgia Tech have always been willing to go above and beyond in assisting me with any questions I have had. In particular, I would like to thank Susan Bowman and Mechelle Kitchings for their guidance and advice for navigating financial, academic, and logistical questions and problems.

I have been very fortunate to have many people who have supported and encouraged me to work hard and to strive for greatness. My parents, Al and Katherine Brooke, instilled in me at a young age, a drive to understand reality and to pursue truth. To Alban, Priscilla, Sarah, and Thomas, you are the best siblings anyone could ask for. I would never have been able to accomplish this goal without the love and support of my beautiful and intelligent fiancée, Cecilia Rosand. She has been infinitely patient with me during this endeavor and has always supported me through difficulties and celebrated with me in my successes.

TABLE OF CONTENTS

LIST OF TABLES

LIST OF FIGURES

LIST OF SYMBOLS AND ABBREVIATIONS

3D	Three Dimensional
ACS	Average Crystallite Size
AFM	Atomic Force Microscopy
BF	Bright Field
DI	Deionized
EDS	Energy Dispersive X-ray Spectroscopy
FIB	Focused Ion Beam
GUI	Graphical User Interface
hr	Hour(s)
HRTEM	High Resolution Transmission Electron Microscopy
IPA	Isopropyl Alcohol
ICP-MS	Inductively Coupled Plasma Mass Spectrometry
λ	Wavelength (nm)
LbL	Layer-by-Layer
µm	Micrometer
nm	Nanometer
P. sesostris	*Parides Sesostris*
PWM	Pulse Width Modulated
QCM-D	Quartz Crystal Microbalance with Dissipation
RT	Room Temperature
SE	Secondary Electron
SEM	Scanning Electron Microscopy
SSG	Surface Sol Gel
TEM	Transmission Electron Microscopy
TG	Thermogravimetric
UV	Ultra Violet
VDW	van der Waals
WL	White Light
XPS	X-ray Photoelectron Spectroscopy
XRD	X-ray Diffraction

SUMMARY

This dissertation explores methods for the creation and chemical modification of micro- and nano- featured morphologies with intricate, three dimensional (3D) structures for tunable functionality. Nature provides highly evolved structures with optical properties (butterflies) and adhesive properties (pollen) that can be utilized in conjunction with engineering materials to tailor and enhance these functional properties. This research is focused on understanding how to apply thin conformal inorganic coatings to intricate 3D biological templates and how to convert such bio-organic coated templates into inorganic replicas, as a method to generate intricate, hierarchical (macro-to-micro-to-nanoscale) structures with tailorable optical and/or adhesive properties.

The use of complex oxides provides new opportunities for replica functionality, but introduces new complications in controlling the phase purity. Five research areas will be presented in this thesis document: First, robotic coating systems were designed and fabricated to facilitate the surface sol-gel (SSG) coating process used in this research. These robotic coating systems were developed to deposit reproducible layer-by-layer (LbL) coatings and were used to conduct over 6000 SSG deposition cycles, with over 3000 hours of manual labor saved.

Second, freestanding photoluminescent samarium-doped titania replicas of *P. sesostris* green dorsal wing scales were synthesized via LbL SSG deposition and subsequent morphology-preserving thermal treatments to create replicas

that maintained the structural color from the native photonic crystal while adding a tailorable optical response via the photoluminescent replication material.

Third, freestanding ferroelectric (barium titanate) replicas of sunflower pollen were produced via LbL SSG deposition and controlled atmosphere thermal treatments, to allow for tailorable electrostatic adhesion.

Fourth, the deposition behavior of the SSG coating process using a quartz crystal microbalance (QCM) were investigated for Ti(IV) isopropoxide, Ba(II) isopropoxide, and a mixture of 20%at Sn(IV) isopropoxide and 80%at Ti(IV) isopropoxide. For Ti(IV) isopropoxide, the kinetic mechanism (rate limiting step) of reaction was evaluated and the regimes of liquid phase diffusion control and chemical reaction control were identified. A precursory analysis of the chemical reaction of the adsorption of Ti(IV) isopropoxide onto amorphous SiO_2 indicated that a 1^{st} order reaction with respect to the adsorbate best described the adsorption process. This work is expected help guide future research on SSG thin film coatings and replication.

Finally, a synthetic silica inverse opal structure was coated via the SSG method to demonstrate the use of such conformal coatings on inorganic templates. A high index coating material of 20% at Sn(IV) isopropoxide and 80%at Ti(IV) isopropoxide was used and the as-coated and fired spectra were analyzed. It was determined that the deposition of 20%at Sn(IV) isopropoxide and 80%at Ti(IV) isopropoxide via SSG occurred via submonolayer-by-submonolayer deposition.

CHAPTER 1: Summary and Motivation

1.1 Summary and Motivation

Naturally occurring structures that couple multiple modes of functionality demonstrate the ability to combine structural and chemical functionality. Thus the structure of bird feathers may reflect blue light while the pigment of the feathers adsorbs everything but yellow so that the perceived color is green.[1] The ability to combine structural and chemical functionality is critical to achieving the properties necessary for many applications including optics, batteries, and anti-counterfeiting. The use of biological structures (such as diatoms, [2] butterflies[3, 4], beetles[4], and pollen particles[5]) as templates offers unique opportunities because nature has demonstrated mass production of precise three-dimensional (3D) structures with features on both the nanometer and micrometer scale. Biological templates often utilize structure-enabled properties (e.g., unique optical[6], and adhesive[7] properties), which can be prohibitively expensive to mimic synthetically. However, the natural chemical composition of such structures have only limited engineering applications due to structural, thermal, and/or chemical instability. Through conformal coating of the biological templates (e.g. butterfly scales and pollen), and subjecting coated templates to morphology-preserving chemical reactions, the intricate structure may be maintained while tailoring the chemical composition to enhance functionality. The optical properties may be enhanced by selection of a coating material with fluorescent properties, and electrostatic adhesion can be enhanced by the selection of ferroelectric materials.[8]

The primary focus of this research has thus been to develop coating and processing methods to replicate synthetic and bioorganic templates in functional materials so that adhesion and coloration may be tuned.

1.2 Introduction

1.2.1 Bioorganic Templates

Prior work has demonstrated the bioorganic structures (e.g. diatoms,[2] butterflies,[3, 4] beetles,[4] and pollen particles[5]) can be utilized as templates for coating and chemical conversion to maintain structural properties while adding new functional materials properties(e.g. optical, chemical, and magnetic). These biogenic replicas have potential applications such as anti-counterfeiting,[9] catalysis,[10] and chemical filtration.[2] Recently, pollen particles have been used as a template for coating and conversion into magnetic materials for the purpose coupling magnetic and van der Waals forces.[11] However, little work has been done to show multimodal coloration in biological replicas of the structural color from a photonic crystal and the photoluminescence of the replica material or the interaction and coupling of electrostatic and van der Walls forces.[12] Additionally little work has investigated directly coating complex multifunctional oxides onto biological structures.[13] Prior work has relied on complicated microwave hydrothermal post processing to add fluorescent properties to oxide replicas.[9]

The *Parades sesostris* butterfly green dorsal wing scales provide desirable templates due to the structural color of their polycrystalline photonic structure [14, 15] and the chitin material that composes the structure of the butterfly which

has an abundance of hydroxyl groups.[14, 15] Pollen is a desirable template due to the variety of pollen particle shapes, with each pollen species possessing a unique structure, shape, and size.[16] Both pollen and the *P. sesostris* are inexpensive and readily available, in a wide variety of morphologies, and naturally designed to be functional (the *P. sesostris* to be colorful and pollen to be dispersible and adhesive). Pollen grains are made of dicarboxylic acids that form the outer exine structure.[17] Both the chitin of the *P. sesostris* and the acids of the pollen have an abundance of hydroxyl/carboxyl groups that are necessary for a conformal coating to be deposited via LbL SSG processing without the need of a preprocessing amplification of the surface functional groups. Pollen shapes can vary widely and generally can be divided into two groups. Pollen with smooth exines tend to be wind-borne pollinators, as pollen from plants that utilize insects for pollination have higher aspect echini (spines).[18]

1.2.2 Surface Sol-Gel Processing

The layer-by-layer (LbL) surface sol-gel (SSG) coating technique is a method used to apply sub-nanometer metal oxide coatings onto a hydroxyl- or carboxyl- rich surface.[19] The LbL process is facilitated by surface limited reactions allowing for thin conformal coatings on intricate 3D structures. The process starts with a clean substrate with exposed hydroxyl or carboxyl groups. This functionalized surface is incubated with an alkoxide precursor to allow for chemisorption of the precursor onto the surface via reaction with the functional groups. The substrate being coated is thoroughly rinsed with anhydrous IPA to

remove any excess, non-chemisorbed precursors. The surface is then hydroxylated by incubating in water which, after incubation, is rinsed away with more anhydrous IPA. To avoid mud cracking, each deposition cycle is concluded by drying the sample.[20] The SSG process can then be repeated in an LbL fashion until the desired coating thickness and composition are obtained. It is important for achieving conformal and repeatable coatings with a wide range of thicknesses that this process be repeated reliably across thousands of individual coatings. To maintain this level of precision, the writer developed a robotic coating system to apply the coatings with incubations times accurate to a fraction of a second.

A range of different chemistries can be applied with SSG to create tunable-thickness, conformal coatings onto intricate 3D templates. Coatings with compositions of TiO_2, SnO_2, $Sn_xTi_{1-x}O_2$, $BaTiO_3$ and Fe_3O_4 have been directly deposited onto butterfly and diatom templates.[2, 3, 21, 22]. Doping TiO_2 with SnO_2 has been shown to induce the crystallization of rutile titania at low temperature (450 ^{o}C) due to the low temperature crystallization of cassiterite (SnO_2) which provides nucleation sites.[22] To date, SSG has been utilized as a coating method to form binary compound and doped-binary compound replicas from various templates, but with limited work being done to directly synthesize complex oxide compounds such as BT or BST. No work has yet investigated using both doped solutions and alternating single precursor exposure to directly apply complex multifunctional oxide coatings such as $Ba_xSr_{1-x}TiO_3$ and Er-doped or Sm-doped $Ba_xSr_{1-x}TiO_3$.

1.2.3 Functionality

1.2.3.1 Coloration

1.2.3.1.1 Structural Color

Structural color can arise from constructive and destructive interference in reflected light off of a periodic structure. A commonly known photonic crystal is the inverse opal structure, which is a relatively simple structure when compared to the gyroid structure.[15] The gyroid structure like other PCs has an angular dependence to its spectral reflectance.[14] To minimize this variability, the *P. sesostris* has a ridge structure that suppresses iridescence. For the purposes of consistent measurements, it is necessary to always orient the *P. sesostris* wing scale normal to the optical axis. Figure 1 shows the intricate internal structure of the *P. sesostris* green dorsal wing scales.

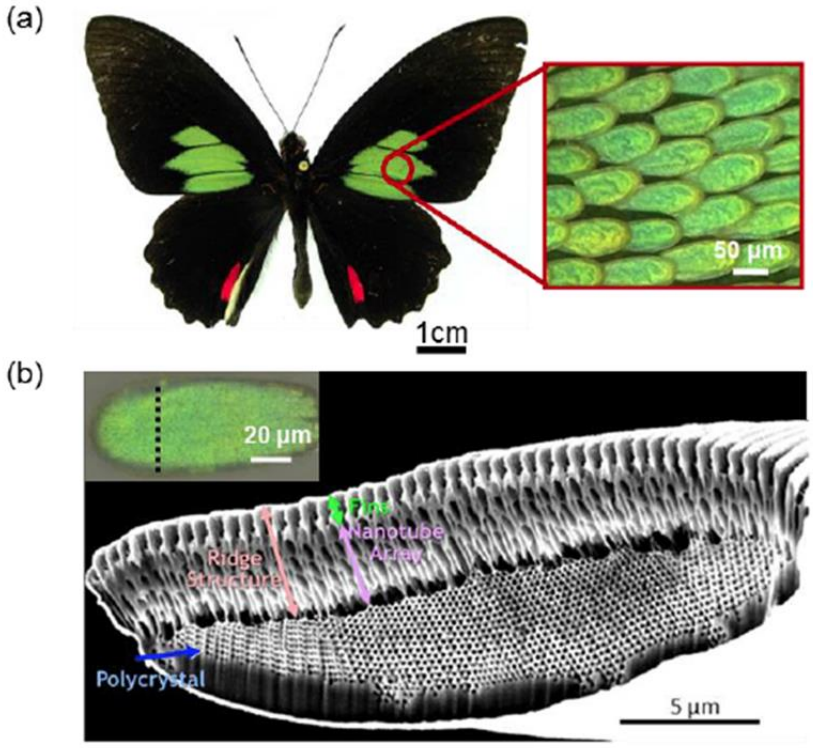

Figure 1: (a) The male butterfly, Parides sesostris © Smithsonian Institution National Museum of Natural History (Inset) Bright field optical image of the green scales attached to the forewing, forming the green patches. (b) Focused Ion Beam (FIB) cross-section of a single, green scale showing the three structural features known in the literature: polycrystal and a ridge structure composed of a nanotube array and a periodic fin structure. (Inset) single green scale showing the direction of the cross-sectional cut (dotted line).[12]

1.2.3.1.2 Photoluminescence

Photoluminescence (PL) is the effect when high energy photons strike a material and cause an electron to become excited from its current state, when the electron drops back to its original energy state, though intermediate states, it releases a photon of lower energy. The released lower energy photons are the PL that is emitted from the material. There is a special case of PL where an electron is excited more than once before it undergoes radiative decay. This is called

upconversion and has the ability to release a photon that has more energy than one of the photons that excited it.

1.2.3.2 Adhesion

1.2.3.2.1 Van der Waals Forces

The adhesion forces between native pollen and various surfaces have previously been investigated by Meredith, et al.[7] The van der Waals (VDW) adhesive force was studied between Ragweed (*A. artemisiifolia*) and planar surfaces, such as polystyrene and polyamide.[7] Understanding how VDW force effects pollen adhesion is important in separating the effect of increased adhesion due to the introduction of new electrostatic adhesion and the increased VDW adhesion from having a replica made of material with a higher Hamaker constant. The adhesive force between a pollen particle and a flat substrate can be measured by attaching a pollen or pollen replica to an atomic force microscope (AFM) cantilever tip and measuring the adhesion to flat substrates. Previous work by Lin, et al.[23] has reported that the measured VDW force can be accurately modeled by using the radius of a spine in the Hamaker model. The VDW force of a single hemisphere near an infinitely large flat plate can be approximated using Equation (1).

$$F_{VDW} = \frac{A_{132}R}{6D^2} \quad \textbf{(1)}$$

In the equation above, R is the radius of the tip of a pollen contact, D is the cut off separation distance, taken to be 0.165 nm and A_{132} is the non-retarded

Hamaker constant for the material.[24, 25] The non-retarded Hamaker describes the interaction between the pollen hemispherical material, the planar material, and the medium in between the two surfaces. The non-retarded Hamaker constant is approximated for this system by combining the contributions from each material, calculated using Equation (2).[11, 24]

$$A_{132} \approx \frac{3}{4} kT \left(\frac{\varepsilon_1 - \varepsilon_3}{\varepsilon_1 + \varepsilon_3}\right)\left(\frac{\varepsilon_2 - \varepsilon_3}{\varepsilon_2 + \varepsilon_3}\right) + \frac{3h\nu_e}{8\sqrt{2}} \frac{(n_1^2 - n_3^2)(n_2^2 - n_3^2)}{(n_1^2 - n_3^2)^{1/2}(n_2^2 - n_3^2)^{1/2}\{(n_1^2 - n_3^2)^{1/2} + (n_2^2 - n_3^2)^{1/2}\}} \quad \textbf{(2)}$$

In this equation, h is Planck's constant, k is Boltzmann's constant, T is the temperature, ν_e is the media absorption frequency, ε_1, ε_2 and ε_3 are the dielectric constants, n_1, n_2 and n_3 are the refractive indices of the surface, medium, and particle. For an uncoated native sunflower pollen and a silicon wafer with a medium of air, the Hamaker constant has been calculated to be 0.83×10^{-19} J.[23] For barium titanate and strontium titanate particles adhering to silica in air, the Hamaker constants are 1.76-1.93 x 10^{-19} J and 1.48 x 10^{-19} J respectively.[26] Through understanding of the materials involved in the adhesion system (particle, planar substrate, and medium) the non-retarded Hamaker constant can be calculated. From analysis of the pollen particle or replica using scanning electron microscopy(SEM), the radius of curvature of the contacting surface can be measured and then the adhesive force from VDW adhesion can be calculated over the distance in which VDW adhesion has an effect (<0.165 nm). These theoretical calculations can be used to verify the validity of direct measurements

and later account for part of the adhesive force when electrostatics becomes a factor in adhesion.

The experimental method for measuring the VDW force on a pollen particle involves the use of an atomic force microscope (AFM). To measure the adhesion force, a pollen particle or replica is first attached to a cantilever tip with a known spring constant. The deflection of the cantilever is measured after the pollen particle contacts the surface and is then pulled back. Such deflection is used to directly calculate the adhesion of the particle by multiplying the maximum deflection on removal by the spring constant of the cantilever tip. A typical plot showing the interaction of a single pollen tip as it is brought near a surface, adheres, and is removed from the surface can be seen in Figure 2.

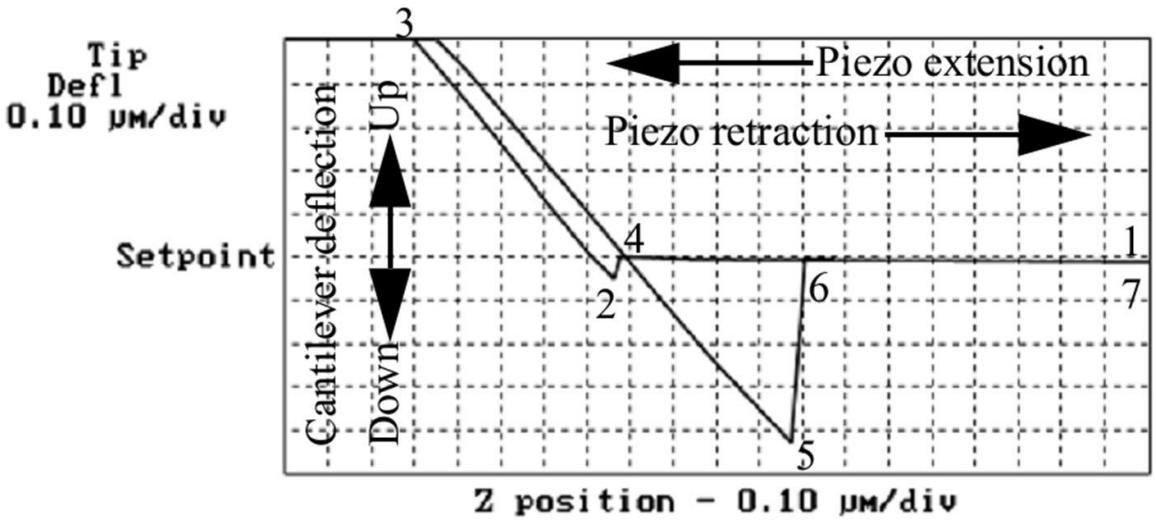

Figure 2: Diagram of characteristic force curve for a sample with adhesive force measured on an AFM. Courtesy of Dr. Goodwin

In the above figure, the cantilever with pollen attached is moved down towards the surface (position 1). At position 2 the particle has come close enough to the surface to jump and become adhered to the surface. At position

3, the cantilever is pressing the pollen particle to the surface and is deflecting upwards. As the cantilever is then pulled back from the surface, the deflection becomes zero at position 4. Position 5 is the point of maximum downward deflection and is what is used to calculate the adhesive force. At position 6, the particle has released from the surface and the cantilever is displaying no deflection, and at position 7 the particle has returned to its original position 1. The force measured by using the deflection between position 5 and position 6 can be used to verify the validity of the calculations performed using Equations 1 and 2.

1.2.3.2.2 Electrostatic Adhesion

Electrostatic adhesion is commonly simplified to only be defined by the interaction of charged particles at a distance (see Equation (3)).[27]

$$F = -\alpha \frac{Q^2}{16\pi\varepsilon_0 R^2} \quad \textbf{(3)}$$

This is an easily understood approximation where Q is the charge on the surface of the particle, R is the distance of the particle to the conducting surface, ε_0 is the permittivity of free space and a is a correction factor for the polarization of the dielectric particle (a is commonly assumed to be unity, but this approximation does not yield accurate results when compared to experimentation when using particles with high dielectric constants).[28] Electrostatic adhesion is a complicated and in some ways a poorly understood field.[29] A large portion of the research in this field comes from charged toner

adhesion research from printer companies which are commonly focused on particles with dielectric constants less than 5.[28, 30-33] The force on a dielectric particle near a substrate has been evaluated for many different conditions.[27, 30, 34-36] For all conditions, the following equation is used to evaluate the electrostatic force (see Equation (4)).

$$F_{Electrostatic} = -\alpha \frac{Q^2}{16\pi\varepsilon_0 R^2} + \beta QE - \gamma\pi\varepsilon_0 R^2 E^2 \quad \textbf{(4)}$$

In this equation, the first term on the right side of the equation represents the electrostatic image force due to the charge on the particle and its attraction to its image in the substrate. The second term is the Coulombic force generated from the interaction of the charge on the particle and the external electric field. The third term is the attraction of the polarization of the dielectric particle in the external field to its mirror image in the substrate. Q is the charge on the particle, ε_0 is the vacuum permittivity, R is the radius of the particle, E is the externally applied field, and α, β, and γ are dimensionless coefficients that depend on the dielectric constant of the particle material, the geometry of the particle and electrodes, etc. Multiple methods for determining the constants have been demonstrated by Feng et al.[37] and by Hartman et al.[36] These methods demonstrate both how to calculate the coefficients via numerical methods and also via testing under controlled conditions (i.e. E = 0 or Q = 0) to simplify the equation to solve for the coefficients individually.

Davis et al. has analytically analyzed the electrostatic adhesion force of a dielectric particle near a conducting flat plate.[38] In that work, two scenarios

were analyzed, the first was for a dielectric particle in an electric field near a grounded plate and the second was for a charged sphere near a grounded plate. In both scenarios, as the dielectric constant of the sphere increased, the electrostatic adhesion force increased.

1.2.4 Functional Materials

1.2.4.1 Lanthanide Doped Titania

Titanium dioxide (TiO_2) is a commonly-used host material for lanthanides (Erbium, Samarium, Europium, Neodymium) [39] for achieving photoluminescence (PL), due to its large band gap (3.2 eV).[40] Titania can be doped with trivalent Erbium (Er^{3+}) to produce a greenish PL[40] or it can be doped with trivalent samarium (Sm^{3+}) to produce a reddish PL color when excited with UV light (~350 nm).[41] In both cases, the material retains an overall whitish color when not excited by high energy photons. Both Erbium and Samarium are reported to dope via substitution defects at the Ti^{4+} sites.[39]

The optimal amount of samarium in titania to produce PL is approximately 1%.[41] Trivalent samarium doped into a titania matrix produces a reddish PL due to the excitation of the electrons from the valence band of titania to the conduction band and subsequent transfer of energy to the samarium atoms and excitation of electrons to the $^4G_{5/2}$ energy level, upon which radiative relaxation occurs and produces PL. The four main bands of PL from Sm^{3+} are due to the relaxation of electrons from the $^4G_{5/2}$ energy level to the $^6H_{5/2}$, $^6H_{7/2}$, $^6H_{9/2}$ and $^6H_{11/2}$ energy levels which produce 580 nm (yellow), 613 nm (orange), 666 nm (red), and 730 nm(red) light (see Figure 3).[41]

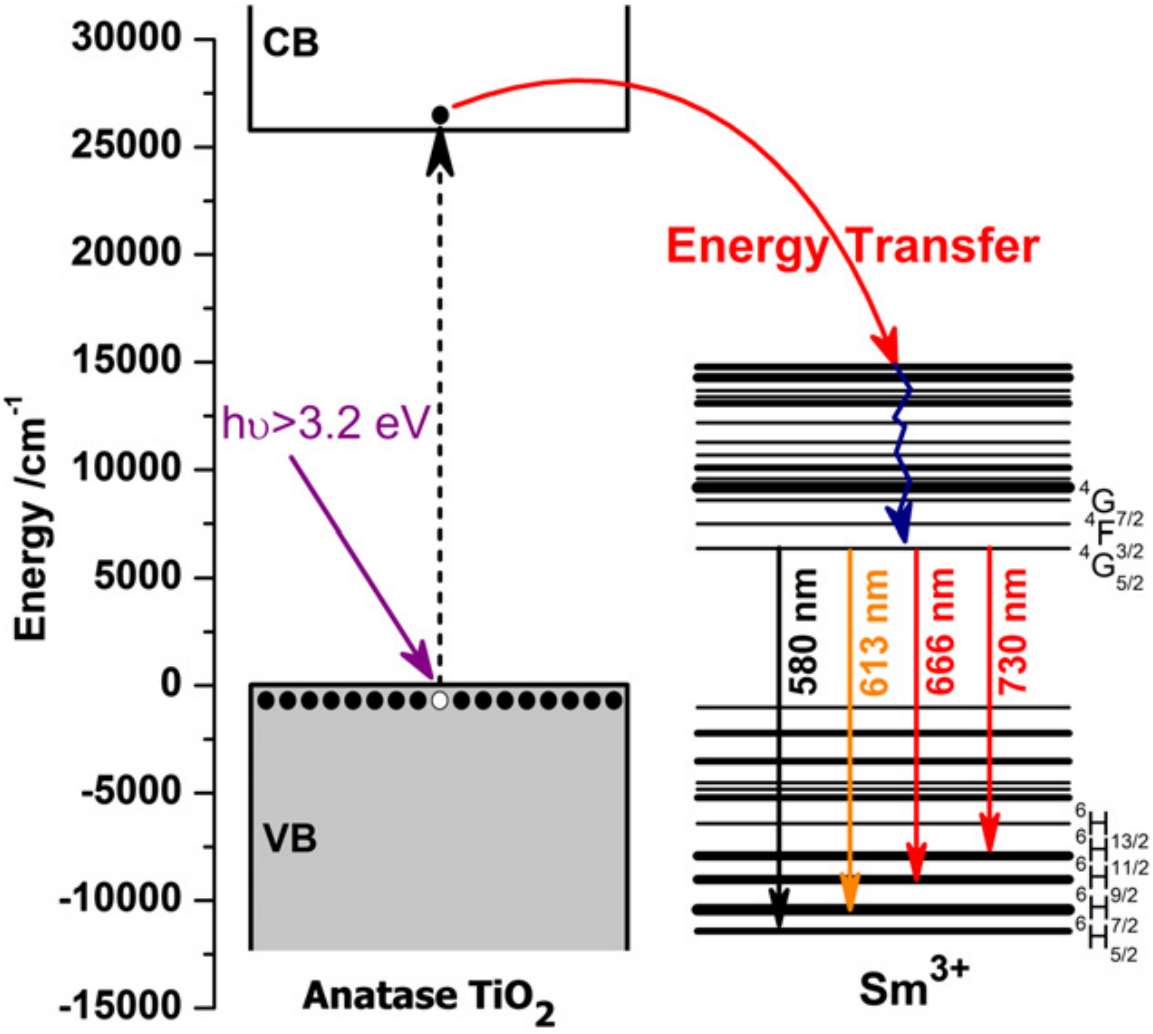

Figure 3: Energy transfer mechanism in anatase Titania doped with trivalent samarium for producing reddish light.

Trivalent Erbium doped into titania can be excited by high energy light (UV), but it also has the less common mode of PL known as upconversion. Upconversion involves the repeated excitation of an electron with a lower energy photon than that ejected upon PL. Patra et al. found that doping 0.25% at erbium in titania produced the strongest PL.[42] In Er^{3+} doped titania, PL

induced by upconversion occurs when 970 nm light excites electrons from the $^4I_{15/2}$ to the $^4I_{11/2}$ which is then excited to the $^4F_{7/2}$. Non-radiative decay from the $^4F_{7/2}$ to the $^4S_{3/2}$ is followed by radiative decay to produce green (500 nm) PL (see Figure 4). [42]

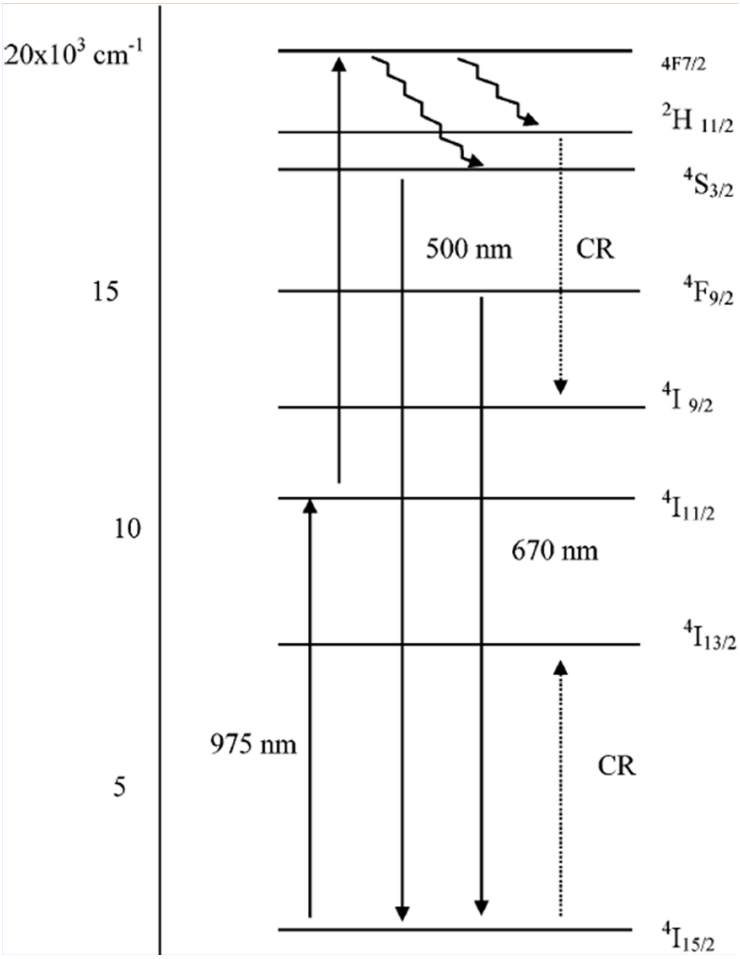

Figure 4: Upconversion in Erbium doped titania involves the repeated excitation of electrons before PL occurs in the visible spectrum.

1.2.4.2 Barium Titanate

Barium Titanate ($BaTiO_3$, BT) is a ferroelectric ceramic with an ABO_3 perovskite crystal structure. At 120°C, BT undergoes a phase transformation from

FCC into a tetragonal crystal which is ferroelectric.[43] This cubic to tetragonal phase transformation distorts the TiO_6 octahedra causing a spontaneous polarization which is the source of the relatively high dielectric constant of BT. When the BT is below the Curie temperature the c dimension is elongated and the Ti^{4+} is displaced along the axis. The average polarization in polycrystalline BT caused by the lattice distortion is typically zero unless an external electric field, magnetic field, or mechanical stress is applied. By transforming BT by cooling from the cubic to the tetragonal polymorph in the presence of an applied electromagnetic field, it is possible to align the net polarization of the grains to create a net directionally-oriented polarization that can allow for strong electrostatic attraction.

BT also has wide band gap (3.2 eV)[44] and can serve as a host lattice for lanthanide elements to create photoluminescence materials.[45] Dopants can be hosted on only A sites, only B sites or can occupy both sites. When the ionic radius of the dopant is less than 0.87 Å, the dopant will only occupy B sites (ex. lutetium R=0.861).[45] If the ionic radius is greater than 0.94 Å, such as Samarium(R=0.958), it will only occupy the A sites.[45] Many dopants, like Er fall between these bounds and can occupy either site and are referred to as amphoteric dopants.[45] BT's PL intensity is two orders of magnitude more intense than TiO_2 (with the same level of dopant, 0.25%at).[42] When doped with erbium atoms and excited with 975 nm light, BT can undergo a two photon upconversion process and emit light at 550 nm and 670 nm.[42] [46] This upconversion process can allow for a unique optical signature for the pollen replica in addition to the van der Waals and electrostatic adhesion.

1.2.4.3 Barium Strontium Titanate

Barium Strontium Titanate ($Ba_xSr_{1-x}TiO_3$, BST) like BT can be a ferroelectric ceramic with an ABO_3 perovskite crystal structure. BST is a solid solution of Strontium Titanate and Barium Titanate with lattice parameters between that of ST and BT.[47], [48] Vegard's law can be used to estimate the lattice parameters of BST over the range of possible compositions (see Equation 5).[49], [50]

$$a_{BST} = x_{BT}a_{BT} + (1 - x_{ST})a_{ST} \quad \textbf{(5)}$$

Here, a_{BST}, a_{BT}, a_{ST}, represent a lattice parameter for BST, BT, and ST, respectively. x_{BT}, and x_{ST} are the atomic fraction of BT and ST in the solid solution. XRD has been used to show that over the complete range of ST to BT only a single phase is present.[47] Additionally, the lattice parameter $\sqrt[3]{a^2c}$ and the composition showed a very close relationship to Vegard's law.[47]

Also because the Curie temperature of ST is near 35 Kelvin[51], [52] that of BT is around 393 Kelvin. Hence, by controlling the ratio of barium to strontium, it is possible to tune the Curie point.[53] [54] Furthermore, the dielectric constant of a ferroelectric material is dependent on temperature. When a material is near its Curie temperature, there is maximum strain on the lattice and, because of this, the dielectric constant is greatly increased.[54]

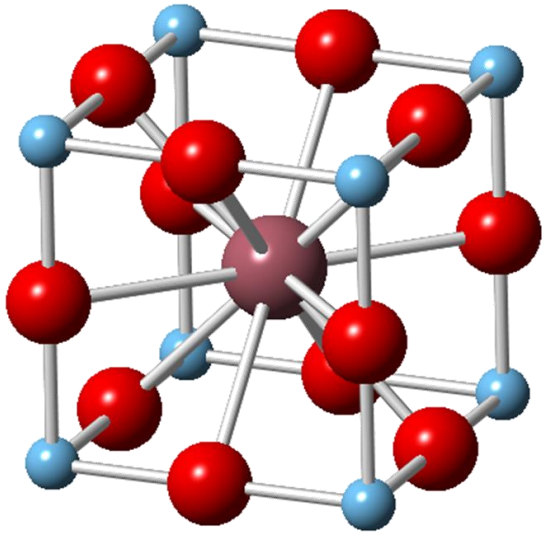

Figure 5: Perovskite structure of BST where Ti^{4+} ions are at the corners of the lattice, O^{2-} ions at the octahedral centers, and with alternating individual unit cells having Sr^{2+} or Ba^{2+} ions in the body center location.

Depending on the application environment, it would be necessary to tune the composition to position the Curie temperature such that the dielectric constant would be high under thermal conditions where adhesion is preferred and to be lower when adhesion would not be required. In the case of requiring greatest adhesion at room temperature, a concentration of ~35% strontium in the A site is preferable. [54]

Like BT, BST also exhibits a large band gap (3.25 eV)[55] and is capable of being doped with a lanthanide to produce photoluminescence through upconversion. [56, 57]

1.3 Equilibrium Adsorption & Kinetic Rate Limiting Steps

Adsorption of material onto a surface is commonly represented by isothermal adsorption graphs.[58-66] Adsorption isotherms were studied in this research to better understand the SSG coating process. Isotherm models have

been created to model different situations with different material interactions. Adsorption isotherms define the influence of the concentration of a precursor in solution on the equilibrium on a surface. For example, with the Langmuir isotherm, each surface site is assumed to accommodate one molecule, all adsorption sites are assumed to have equal affinity for the adsorbing species, and the adsorption of a given molecule is assumed to be independent from neighboring sites.[67] The Langmuir model assumes no interaction between molecules. An alternative is the Freundlich model which considers the presence of surface sites with different enthalpies of adsorption.[68] The filling of these sites results in an exponential decay in the adsorption enthalpy of remaining adsorption sites. Unlike the Langmuir model, the Freundlich model has been shown to be accurate at high concentrations, but to fail to adhere to Henry's law for low concentrations where Γ_i should be linearly related to C_i.[62, 66] To produce a more accurate model, Redlich and Peterson developed a hybrid isotherm which is characteristic of Langmuir at low concentrations and of Freundlich at high concentrations.[58, 62, 69, 70] As mentioned, the Langmuir model is the simplest model and it assumes that the adsorption of a given molecule is independent of the occupation of neighboring adsorption sites. For a given precursor, this assumption may not be valid at sufficiently high levels of adsorption. With high levels of adsorption, the influence of lateral interactions (electrostatic or steric) may have a significant influence on the adsorption equilibrium. To account for these interactions, Fowler and Guggenheim have modified the Langmuir isotherm.[71] In such a case, the value of ω is negative or positive for repulsive or attractive interactions, respectively, with the magnitude

of ω revealing the strength of the interaction between adsorbates. These two possible deviations from the Langmuir model were accounted for and the data was compared to the models. For non-negligible heterogeneity in the binding affinity of surface sites the Freundlich model was used, for non-negligible interactions between adsorbates the Fowler and Guggenheim model was used. Other models have been produced to provide more accurate isotherms for different systems, but they were not used in this research.

The process of adsorption from a liquid solution may be rate limited by mass transport of a reactant species toward, or product species from, the solid/liquid interface and/or by a chemical reaction at the solid/liquid interface.

For liquid-phase diffusion control (i.e., for rapid chemical reactions at the solid/liquid interface), the change of adsorption with time, $d(\Gamma_i^t)/dt$ (expressed as the change in adsorbed mass per area per time), may be described by a Noyes-Whitney-Nernst-type equation[72] [73]:

$$\frac{d(\Gamma_i^t)}{dt} = \frac{D_i(C_b - C_s)}{\delta_i} \quad \textbf{(6)}$$

Here, Γ_i^t is the adsorption of species i in time t; D_i is the diffusion coefficient of this species through a concentration boundary layer in the liquid; C_s and C_b refer to the concentration of this species in the liquid at the solid/liquid interface and in the bulk solution, respectively; and δ_i is the concentration boundary layer thickness for species i. For chemical reaction control (i.e., for rapid mass transport through the liquid), several cases may be considered.

1.4 References

[1] D. L. Fox, *Animal biochromes and structural colours: physical, chemical, distributional & physiological features of coloured bodies in the animal world*: Univ of California Press, 1976.

[2] G. Wang, Y. Fang, P. Kim, A. Hayek, M. R. Weatherspoon, J. W. Perry*, et al.*, "Layer-By-Layer Dendritic Growth of Hyperbranched Thin Films for Surface Sol-Gel Syntheses of Conformal, Functional, Nanocrystalline Oxide Coatings on Complex 3D (Bio)silica Templates," *Advanced Functional Materials,* vol. 19, pp. 2768-2776, Sep 9 2009.

[3] M. R. Weatherspoon, Y. Cai, M. Crne, M. Srinivasarao, and K. H. Sandhage, "3D rutile titania-based structures with Morpho butterfly wing scale morphologies," *Angewandte Chemie-International Edition,* vol. 47, pp. 7921-7923, 2008 2008.

[4] M. Srinivasarao, "Nano-optics in the biological world: Beetles, butterflies, birds, and moths," *Chemical Reviews,* vol. 99, pp. 1935-1961, Jul 1999.

[5] F. Cao and D.-X. Li, "Morphology-controlled synthesis of SiO2 hollow microspheres using pollen grain as a biotemplate," *Biomedical Materials,* vol. 4, Apr 2009.

[6] W. Peng, S. Zhu, W. Wang, W. Zhang, J. Gu, X. Hu*, et al.*, "3D Network Magnetophotonic Crystals Fabricated on Morpho Butterfly Wing Templates," *Advanced Functional Materials,* vol. 22, pp. 2072-2080, 2012.

[7] B. J. R. Thio, J. H. Lee, and J. C. Meredith, "Characterization of Ragweed Pollen Adhesion to Polyamides and Polystyrene Using Atomic Force Microscopy," *Environmental Science & Technology,* vol. 43, pp. 4308-4313, Jun 2009.

[8] G. H. Haertling, "Ferroelectric ceramics: History and technology," *Journal of the American Ceramic Society,* vol. 82, pp. 797-818, Apr 1999.

[9] J. P. Vernon, N. Hobbs, Y. Cai, A. Lethbridge, P. Vukusic, D. D. Deheyn*, et al.*, "3D photoluminescent lanthanide-doped barium titanate structures synthesized by coating and shape-preserving reaction of complex-shaped bioorganic templates," *Journal of Materials Chemistry,* vol. 22, pp. 10435-10437, 2012 2012.

[10] Z. Bao, M.-K. Song, S. C. Davis, Y. Cai, M. Liu, and K. H. Sandhage, "High surface area, micro/mesoporous carbon particles with selectable 3-D biogenic morphologies for tailored catalysis, filtration, or adsorption," *Energy Environ. Sci.,* vol. 4, pp. 3980-3984, 2011.

[11] W. B. Goodwin, I. J. Gomez, Y. N. Fang, J. C. Meredith, and K. H. Sandhage, "Conversion of Pollen Particles into Three-Dimensional Ceramic

Replicas Tailored for Multimodal Adhesion," *Chemistry of Materials,* vol. 25, pp. 4529-4536, Nov 2013.

[12] C. Cameron, "NATURAL AND ARTIFICIAL FLUORESCENCE ON 3-DIMENSIONAL BIOORGANIC NANOSTRUCTURES," Ph.D. Dissertation, Materials Science and Engineering, Georgia Institute of Technology, Georgia Institute of Technology, 2014.

[13] J. Vernon, "Morphology-preserving chemical conversion of bioorganic and inorganic templates," Ph.D. Dissertation, Materials Science and Engineering, Gerorgia Institute of Technology, Gerorgia Institute of Technology, 2012.

[14] C. Pouya and P. Vukusic, "Electromagnetic characterization of millimetre-scale replicas of the gyroid photonic crystal found in the butterfly Parides sesostris," *Interface Focus,* vol. 2, pp. 645-650, Oct 2012.

[15] K. Michielsen and D. Stavenga, "Gyroid cuticular structures in butterfly wing scales: biological photonic crystals," *Journal of The Royal Society Interface,* vol. 5, pp. 85-94, 2008.

[16] S. Rosenfeldt and B. G. Galati, "Pollen morphology of Oxalis species from Buenos Aires province (Argentina)," *Biocell,* vol. 31, pp. 13-21, 2007.

[17] E. Dominguez, J. A. Mercado, M. A. Quesada, and A. Heredia, "Pollen sporopollenin: degradation and structural elucidation," *Sexual Plant Reproduction,* vol. 12, pp. 171-178, Sep 1999.

[18] N. Tanaka, K. Uehara, and J. Murata, "Correlation between pollen morphology and pollination mechanisms in the Hydrocharitaceae," *Journal of Plant Research,* vol. 117, pp. 265-276, 2004/08/01 2004.

[19] I. Ichinose, H. Senzu, and T. Kunitake, "A surface sol-gel process of TiO2 and other metal oxide films with molecular precision," *Chemistry of Materials,* vol. 9, pp. 1296-&, Jun 1997.

[20] M. Weatherspoon, "CONFORMAL SOL-GEL COATINGS ON THREE-DIMENSIONAL NANOSTRUCTURED TEMPLATES," Ph.D. Dissertation, Materials Science & Engineering, Georgia Institute of Technology, 2008.

[21] J. P. Vernon, Y. Fang, Y. Cai, and K. H. Sandhage, "Morphology-Preserving Conversion of a 3D Bioorganic Template into a Nanocrystalline Multicomponent Oxide Compound," *Angewandte Chemie,* vol. 122, pp. 7931-7934, 2010.

[22] M. R. Weatherspoon, M. B. Dickerson, G. Wang, Y. Cai, S. Shian, S. C. Jones*, et al.*, "Thin, conformal, and continuous SnO2 coatings on three-dimensional biosilica templates through hydroxy-group amplification and

layer-by-layer alkoxide deposition," *Angewandte Chemie-International Edition,* vol. 46, pp. 5724-5727, 2007 2007.

[23] H. Lin, I. Gomez, and J. C. Meredith, "Pollenkitt Wetting Mechanism Enables Species-Specific Tunable Pollen Adhesion," *Langmuir,* vol. 29, pp. 3012-3023, Mar 5 2013.

[24] J. N. Israelachvili, *Intermolecular and surface forces: revised third edition*: Academic press, 2011.

[25] H. Hamaker, "The London—van der Waals attraction between spherical particles," *physica,* vol. 4, pp. 1058-1072, 1937.

[26] L. Bergström, "Hamaker constants of inorganic materials," *Advances in Colloid and Interface Science,* vol. 70, pp. 125-169, 1997.

[27] D. A. Hays, "Toner adhesion," *The Journal of Adhesion,* vol. 51, pp. 41-48, 1995.

[28] B. A. Kemp and J. G. Whitney, "Electrostatic adhesion of multiple non-uniformly charged dielectric particles," *Journal of Applied Physics,* vol. 113, p. 6, Jan 2013.

[29] L. Schein, "Recent progress and continuing puzzles in electrostatics," *Science,* vol. 316, pp. 1572-1573, 2007.

[30] J. Q. Feng and D. A. Hays, "A finite-element analysis of the electrostatic force on a uniformly charged dielectric sphere resting on a dielectric-coated electrode in a detaching electric field," *Ieee Transactions on Industry Applications,* vol. 34, pp. 84-91, Jan-Feb 1998.

[31] J. Q. Feng and D. A. Hays, "Relative importance of electrostatic forces on powder particles," *Powder Technology,* vol. 135, pp. 65-75, Oct 2003.

[32] H. Mizes, M. Ott, E. Eklund, and D. Hays, "Small particle adhesion: measurement and control," *Colloids and Surfaces a-Physicochemical and Engineering Aspects,* vol. 165, pp. 11-23, May 2000.

[33] B. Techaumnat, M. Kadonaga, and T. Takuma, "Analysis of Electrostatic Adhesion and Detachment of a Nonuniformly Charged Particle on a Conducting Plane," *Ieee Transactions on Dielectrics and Electrical Insulation,* vol. 16, pp. 704-710, Jun 2009.

[34] J. Q. Feng and D. A. Hays, "Theory of electric field detachment of charged toner particles in electrophotography," *Journal of Imaging Science and Technology,* vol. 44, pp. 19-25, 2000.

[35] D. Hays, "ELECTRIC-FIELD DETACHMENT OF TONER," *Photographic Science and Engineering,* vol. 22, pp. 232-235, 1978.

[36] G. C. Hartmann, L. M. Marks, and C. C. Yang, "PHYSICAL MODELS FOR PHOTOACTIVE PIGMENT ELECTROPHOTOGRAPHY," *Journal of Applied Physics,* vol. 47, pp. 5409-5420, 1976 1976.

[37] J. Q. Feng and D. A. Hays, "Electric field detachment of a uniformly charged dielectric sphere on a dielectric coated electrode," in *Industry Applications Conference, 1996. Thirty-First IAS Annual Meeting, IAS'96., Conference Record of the 1996 IEEE*, 1996, pp. 1883-1890.

[38] M. H. Davis, "ELECTROSTATIC FIELD AND FORCE ON A DIELECTRIC SPHERE NEAR A CONDUCTING PLANE - A NOTE ON APPLICATION OF ELECTROSTATIC THEORY TO WATER DROPLETS," *American Journal of Physics,* vol. 37, pp. 26-&, 1969.

[39] X. Chen and W. Luo, "Optical Spectroscopy of Rare Earth Ion-Doped TiO2 Nanophosphors," *Journal of Nanoscience and Nanotechnology,* vol. 10, pp. 1482-1494, Mar 2010.

[40] W. Q. Luo, C. Y. Fu, R. F. Li, Y. S. Liu, H. M. Zhu, and X. Y. Chen, "Er3+-Doped Anatase TiO2 Nanocrystals: Crystal-Field Levels, Excited-State Dynamics, Upconversion, and Defect Luminescence," *Small,* vol. 7, pp. 3046-3056, Nov 2011.

[41] Y. C. Cao, Z. Y. Zhao, J. Yi, C. S. Ma, D. C. Zhou, R. F. Wang*, et al.*, "Luminescence properties of Sm3+-doped TiO2 nanoparticles: Synthesis, characterization, and mechanism," *Journal of Alloys and Compounds,* vol. 554, pp. 12-20, Mar 2013.

[42] A. Patra, C. S. Friend, R. Kapoor, and P. N. Prasad, "Fluorescence Upconversion Properties of Er3+-Doped TiO2 and BaTiO3 Nanocrystallites," *Chemistry of Materials,* vol. 15, pp. 3650-3655, 2003/09/01 2003.

[43] L. Delaey, "Phase Transformations In Materials," in *Wiley-vch Verlag Gmbh*, G. Kostorz, Ed., ed Weinheim Germany, 2001.

[44] J. Li and M. Kuwabara, "Preparation and luminescent properties of Eu-doped BaTiO< sub> 3</sub> thin films by sol–gel process," *Science and Technology of Advanced Materials,* vol. 4, pp. 143-148, 2003.

[45] Y. Tsur, T. Dunbar, and C. Randall, "Crystal and Defect Chemistry of Rare Earth Cations in BaTiO3," *Journal of Electroceramics,* vol. 7, pp. 25-34, 2001/10/01 2001.

[46] P. Ghosh, S. Sadhu, T. Sen, and A. Patra, "Upconversion emission of BaTiO3: Er nanocrystals," *Bulletin of Materials Science,* vol. 31, pp. 461-465, 2008/06/01 2008.

[47] J. A. Basmajian and R. C. DeVries, "Phase Equilibria in the System BaTiO3–SrTiO3," *Journal of the American Ceramic Society,* vol. 40, pp. 373-376, 1957.

[48] D. Barb, E. Bărbulescu, and A. Bărbulescu, "Diffuse Phase Transitions and Ferroelectric-Paraelectric Diagram for the BaTiO3-SrTiO3 System," *physica status solidi (a),* vol. 74, pp. 79-83, 1982.

[49] L. Vegard, "Die Konstitution der Mischkristalle und die Raumfüllung der Atome," *Zeitschrift für Physik,* vol. 5, pp. 17-26, 1921/01/01 1921.

[50] A. R. Denton and N. W. Ashcroft, "Vegard's law," *Physical Review A,* vol. 43, pp. 3161-3164, 03/01/ 1991.

[51] H. Weaver, "Dielectric properties of single crystals of SrTiO< sub> 3</sub> at low temperatures," *Journal of Physics and Chemistry of Solids,* vol. 11, pp. 274-277, 1959.

[52] R. A. Cowley, "Lattice Dynamics and Phase Transitions of Strontium Titanate," *Physical Review,* vol. 134, pp. A981-A997, 05/18/ 1964.

[53] H. V. Alexandru, C. Berbecaru, A. Ioachim, L. Nedelcu, and A. Dutu, "BST solid solutions, temperature evolution of the ferroelectric transitions," *Applied Surface Science,* vol. 253, pp. 354-357, Oct 2006.

[54] C. L. Fu, C. R. Yang, H. W. Chen, Y. X. Wang, and L. Y. Hu, "Microstructure and dielectric properties of BaSr1-xTiO3 ceramics," *Materials Science and Engineering B-Solid State Materials for Advanced Technology,* vol. 119, pp. 185-188, May 2005.

[55] K. van Benthem, C. Elsässer, and R. H. French, "Bulk electronic structure of SrTiO3: Experiment and theory," *Journal of Applied Physics,* vol. 90, pp. 6156-6164, 2001.

[56] S. Y. Kuo, C. S. Chen, T. Y. Tseng, S. C. Chang, and W. F. Hsieh, "Dependence of luminescence efficiency on dopant concentration and sintering temperature in the erbium-doped Ba0.7Sr0.3TiO3 thin films," *Journal of Applied Physics,* vol. 92, pp. 1868-1872, Aug 15 2002.

[57] S. Y. Kuo and W. F. Hsieh, "Structural and optical properties of erbium-doped Ba0.7Sr0.3TiO3 thin films," *Journal of Vacuum Science & Technology A,* vol. 23, pp. 768-772, Jul-Aug 2005.

[58] O. Redlich and D. L. Peterson, "A useful adsorption isotherm," *Journal of Physical Chemistry,* vol. 63, pp. 1024-1024, 1959.

[59] J. Lawrence and R. Parsons, "Adsorption isotherms in mixed solvent systems," *The Journal of Physical Chemistry,* vol. 73, pp. 3577-3581, 1969.

[60] H. Dhar, B. Conway, and K. Joshi, "On the form of adsorption isotherms for substitutional adsorption of molecules of different sizes," *Electrochimica Acta,* vol. 18, pp. 789-798, 1973.

[61] P. Nikitas, "Generalized Flory–Huggins isotherms for adsorption from solution," *Journal of the Chemical Society, Faraday Transactions 1: Physical Chemistry in Condensed Phases,* vol. 80, pp. 3315-3329, 1984.

[62] Y. Ho, J. Porter, and G. McKay, "Equilibrium isotherm studies for the sorption of divalent metal ions onto peat: copper, nickel and lead single component systems," *Water, Air, and Soil Pollution,* vol. 141, pp. 1-33, 2002.

[63] K. G. Bhattacharyya and S. S. Gupta, "Adsorption of Fe (III) from water by natural and acid activated clays: studies on equilibrium isotherm, kinetics and thermodynamics of interactions," *Adsorption,* vol. 12, pp. 185-204, 2006.

[64] O. Hamdaoui and E. Naffrechoux, "Modeling of adsorption isotherms of phenol and chlorophenols onto granular activated carbon: Part I. Two-parameter models and equations allowing determination of thermodynamic parameters," *Journal of Hazardous Materials,* vol. 147, pp. 381-394, 2007.

[65] Y. Aoki, M. Hashizume, S. Onoue, and T. Kunitake, "Determination of Surface Area and Porosity of Small, Nanometer-Thick Films by Quartz Crystal Microbalance Measurement of Gas Adsorption," *Journal of Physical Chemistry B,* vol. 112, pp. 14578-14582, Nov 2008.

[66] K. Foo and B. Hameed, "Insights into the modeling of adsorption isotherm systems," *Chemical Engineering Journal,* vol. 156, pp. 2-10, 2010.

[67] I. Langmuir, "the constitution and fundamental properties of solids and liquids. part i. solids," *Journal of the American Chemical Society,* vol. 38, pp. 2221-2295, 1916.

[68] H. Freundlich, "Over the adsorption in solution," *J. Phys. Chem,* vol. 57, p. e470, 1906.

[69] F. Haghseresht and G. Lu, "Adsorption characteristics of phenolic compounds onto coal-reject-derived adsorbents," *Energy & Fuels,* vol. 12, pp. 1100-1107, 1998.

[70] L. Jossens, J. Prausnitz, W. Fritz, E. Schlünder, and A. Myers, "Thermodynamics of multi-solute adsorption from dilute aqueous solutions," *Chemical Engineering Science,* vol. 33, pp. 1097-1106, 1978.

[71] S. R. H. FOWLER and E. A. Guggenheim, *Statistical Thermodynamics, Etc.(Second Impression with Corrections.)*: University Press, 1949.

[72] A. A. Noyes and W. R. Whitney, "The rate of solution of solid substances in their own solutions," *Journal of the American Chemical Society,* vol. 19, pp. 930-934, 1897.

[73] W. Nernst, "Theory of reaction velocity in heterogenous systems," *Zeit. physikal. Chem,* vol. 47, pp. 52-55, 1904.

CHAPTER 2: Automated Coating Systems for Deposition of Layer-by-Layer Coatings onto Various Substrates

2.1 Summary

To aid in the deposition of LbL SSG Coatings, robotic coating systems were created. These systems were designed and built in-house specifically for SSG coatings, but have been used for non-SSG deposition as well as SSG. In this chapter, the design and validation of the robotic systems is explained. These systems have been used to deposit alkoxides onto a variety of substrates including *P. sesostris* butterfly wing scales, *M. Menelaus wing* scales, sunflower pollen, carbon fiber paper, QCM quartz crystals, silica inverse opals, silica slides, and silicon wafers. These coating systems have been designed to be robust, easy to use and capable of running continuously for multiple days without stopping.

Four automated coating systems have been built to facilitate this research. Two of the systems are designed to coated substrates of various size and shape and are operated with only a computer. The other two systems control low volume, multiport, solenoid valves and are used for flow selection in conjunction with a QCM. The coating systems have removed human variability between coatings and have been used in all of the areas of research in this dissertation. These coating systems have opened up an area of research that previously was prohibitively time consuming to explore. Coatings of up to 300 cycles have been deposited using these automated systems. Depositing this many coatings by hand would have required approximately 100 hours of continuous work.

2.2 Introduction

Surface sol-gel is a slow and repetitive procedure that requires a clean environment and close attention to detail to produce clean, reliable thin-film coatings. The solutions used in SSG are highly reactive with water and react if left in contact with air (the precise amount of water vapor has not been evaluated in this research). Previous research has involved dipping individual wing segments into small containers of precursor, rinse and DI water and repeating this for the number of layers required.[1-5] This method had significant potential for human error because it required a user to process the samples repeatedly in a precise timeframe and involved having solutions repeatedly exposed to lab air. Other computer controlled coating systems have been proposed for the deposition of LbL coatings.[6, 7] The first of these systems could only deposit coatings on powder substrates and required the user to program complex commands to control the system.[6] Additionally, this first system did not have any degree of feedback to the user to indicate if the system finished coating or if it had had failed. The second system was a dipping system which required the sample to be repeatedly dipped into a solutions to deposit the coating.[7] This repeated mechanical manipulation makes coating fragile substrates either difficult or impossible and makes coating powder impossible without major modifications. Because neither of these systems were deemed appropriate for coating both powders and fragile substrates a new system was devised with a control system robust enough to be safe and user friendly.

2.3 Safety

All of the robotic systems were created to precisely control fluid that can be highly flammable. To mitigate the risk of fire, the parts of the robotic systems that came in contact with fluid were always separated from the electronics. Each robotic system was designed with non-flammable materials where possible. When operating with flammable solvents, the robotic systems were located in a fume-hood or under an elephant trunk to remove potential smoke from the area. In addition, all of the robotic systems were designed with a manual power kill switch so that in the event of a malfunction the system could be turned off immediately. In addition to the manual kill-switch, each robotic system can be turned off remotely if a malfunction occurs. To allow the user to monitor the health of the robotic systems during coating, optical cameras were placed at strategic locations and connected to the same computer that controls the robotic system itself. In this way, the operator out of the lab could monitor the coating progress without entering the lab. With the addition of a VPN (Cisco AnyConnect, Cisco Systems Inc., CA, USA) the operator can monitor, modify, and stop the coating process remotely from a different lab or even when not on Georgia Tech's campus. Due to bandwidth limitations, the use of the VPN off campus was limited to making sure the system had not malfunctioned.

2.4 Hardware Design

Multiple coating systems were created to aid in this research. The initial two robots were created to deposit LbL SSG coatings onto wafer-type substrates. The robots go by the designation Robot 1 and 2 respectively and Design 1. The

second two robots were created to control the flow of precursors to the QCM reaction chambers. The robots go by the designation Robot 1 and 2 respectively and Design 2. In this way the robots are designated R1-D1, R2-D1, R1-D2, and R2-D2. All four robotic systems are represented in Figure 6.

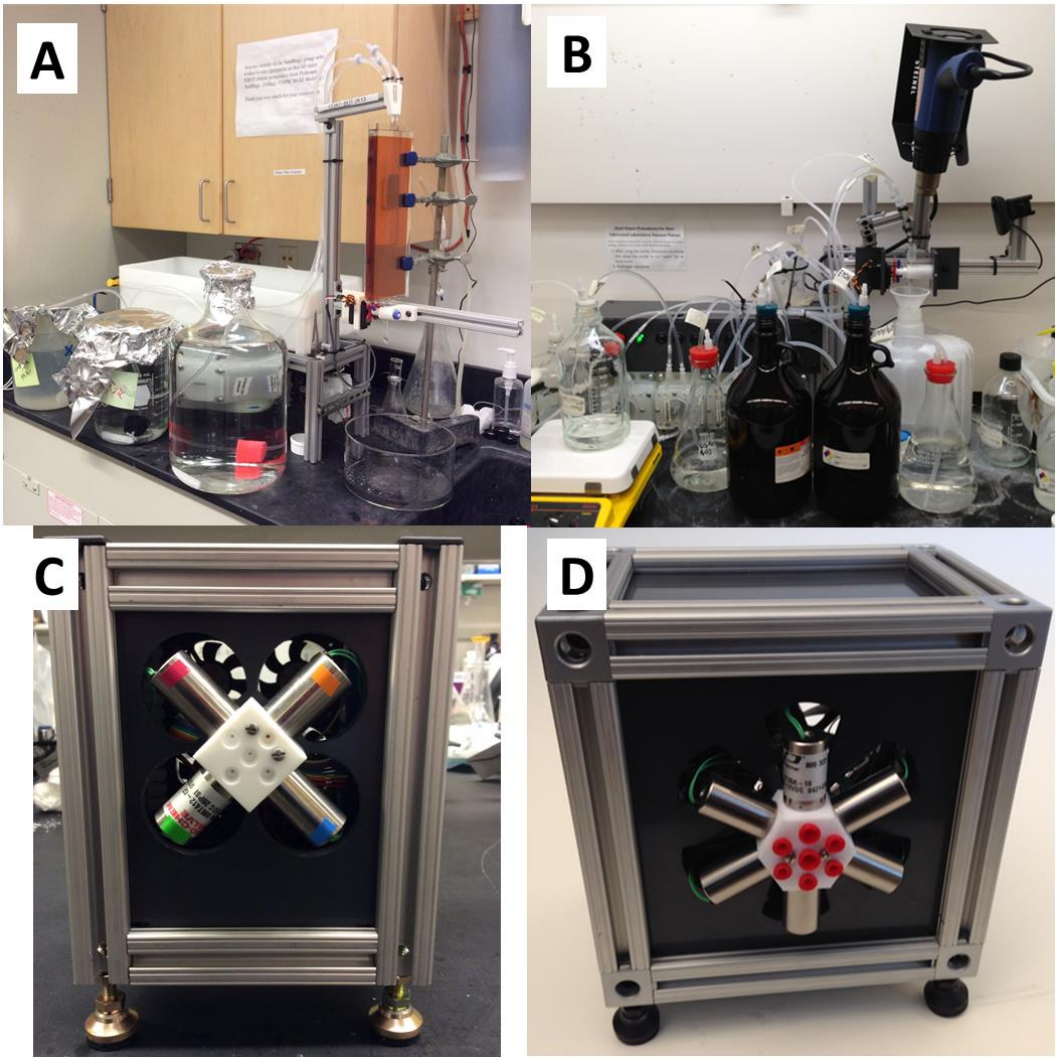

Figure 6: All four coating systems displayed: A) R1-D1 coating a non-SSG LbL water based coating onto a full A4 sheet of Kapton. B) R2-D1 set up for coating a solid substrate with SSG. C) R1-D2 after completion of construction. D) R2-D2 after completion of construction.

The structural support of robots is made using 1" aluminum T-slotted framing (McMasterCarr, GA, USA), pumps and valves are mounted on ABS plastic. For

the D2 systems, used with the QCM, the electronics are mounted inside the sealed box and fans are mounted on the back to force cool air over the solenoid valves.

For both the D1 and the D2 systems, the precursor solutions are not open to the air, but instead are constantly back filled with nitrogen gas (Refrigerated Liquid, AirGas, PA, USA). Due to the lack of water vapor in the N_2 gas, the precursors do not react with the air inside the bottles before being deposited in the reaction chamber. This is very important, because it avoids depositing agglomerations of precursor onto the template which would result in a non-uniform coating, but it also reduces the concentration of the precursor which affects the reaction rate.

2.4.1 Automated Coating System

For the two D1 systems, the pumps are low flow peristaltic pumps (McMasterCarr, GA, USA) that allow for precise control of the quantity of fluid dispensed. To avoid back flow though the tubes, to keep them primed, each tube is capped with a check valve and then a PTFE tube to direct the flow of precursor. The PTFE tubes also allow for the precursors to be directed in a controlled manner into the reaction chamber, as can be seen in Figure 7.

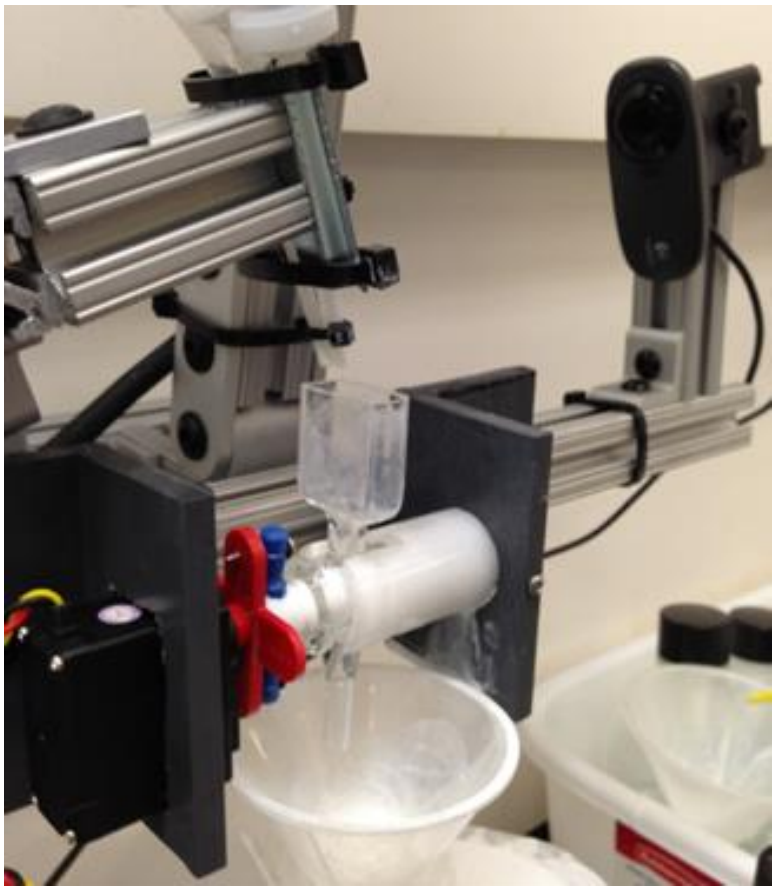

Figure 7: Example of reaction chamber in R2-D1 being secured in place via the #2 PTFE stopcock housing. Above the reaction chamber the precursor tubes can be seen. Also in view is (left) the servo motor and (right) the camera used to monitor the volume of solution in the reaction chamber.

The parts shown in Figure 7 were custom parts machined by hand and by using a Flash Cut CNC with simple designs in SOLIDWORKS. These were one-time parts that would be difficult to duplicate if damaged. To create a more sustainable system, 3D CAD models were created of the complex parts and the parts were 3D-printed in ABS plastic.

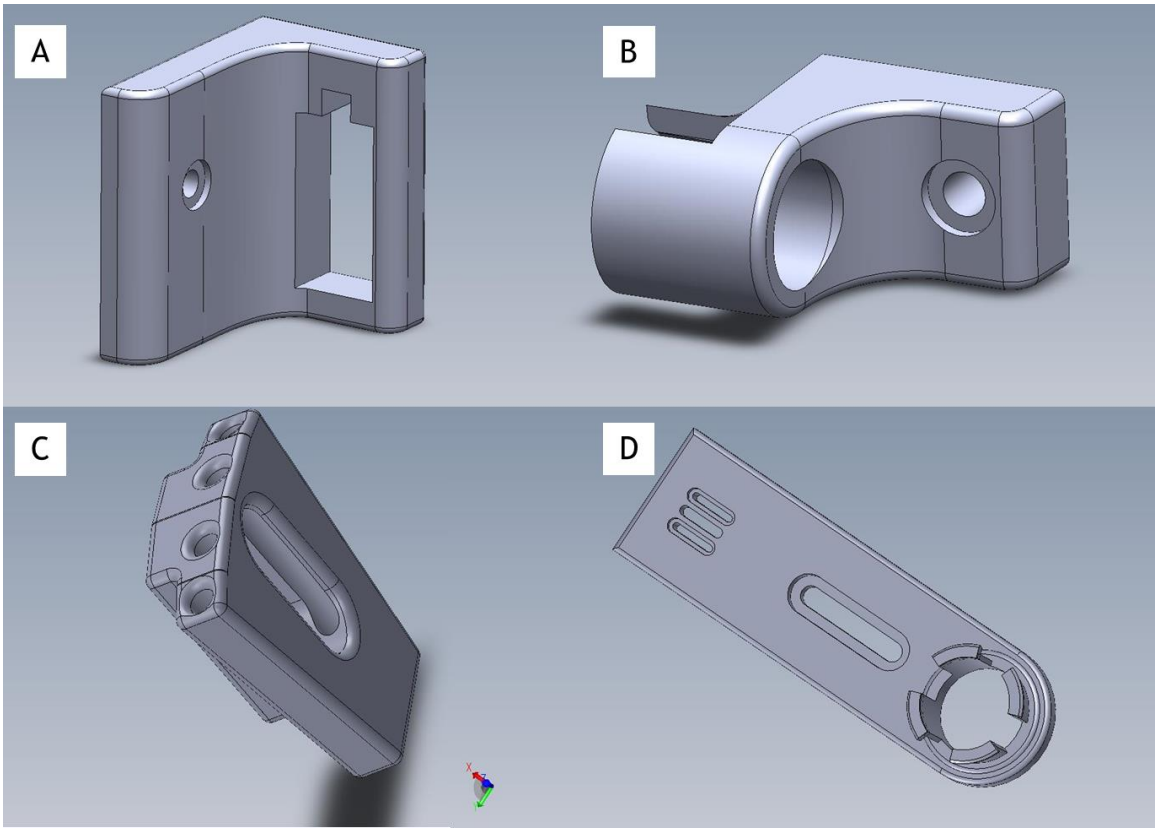

Figure 8: 3D SOLIDWORKS models of complex parts for coating systems that were 3D printed. A) t-slot to Servo holder, B) t-slot to stopcock holder, C) t-slot to PTFE tube holder which acts to direct the flow into the small reaction chambers, D) Bearing holder for spinner used for mixing solutions during coating of powder-type substrates.

The 3D printed parts (Figure 8) were created to replace the parts shown in Figure 9. With the 3D models of these parts, new pieces were made for the second coating system when it was constructed without having to build new parts by hand.

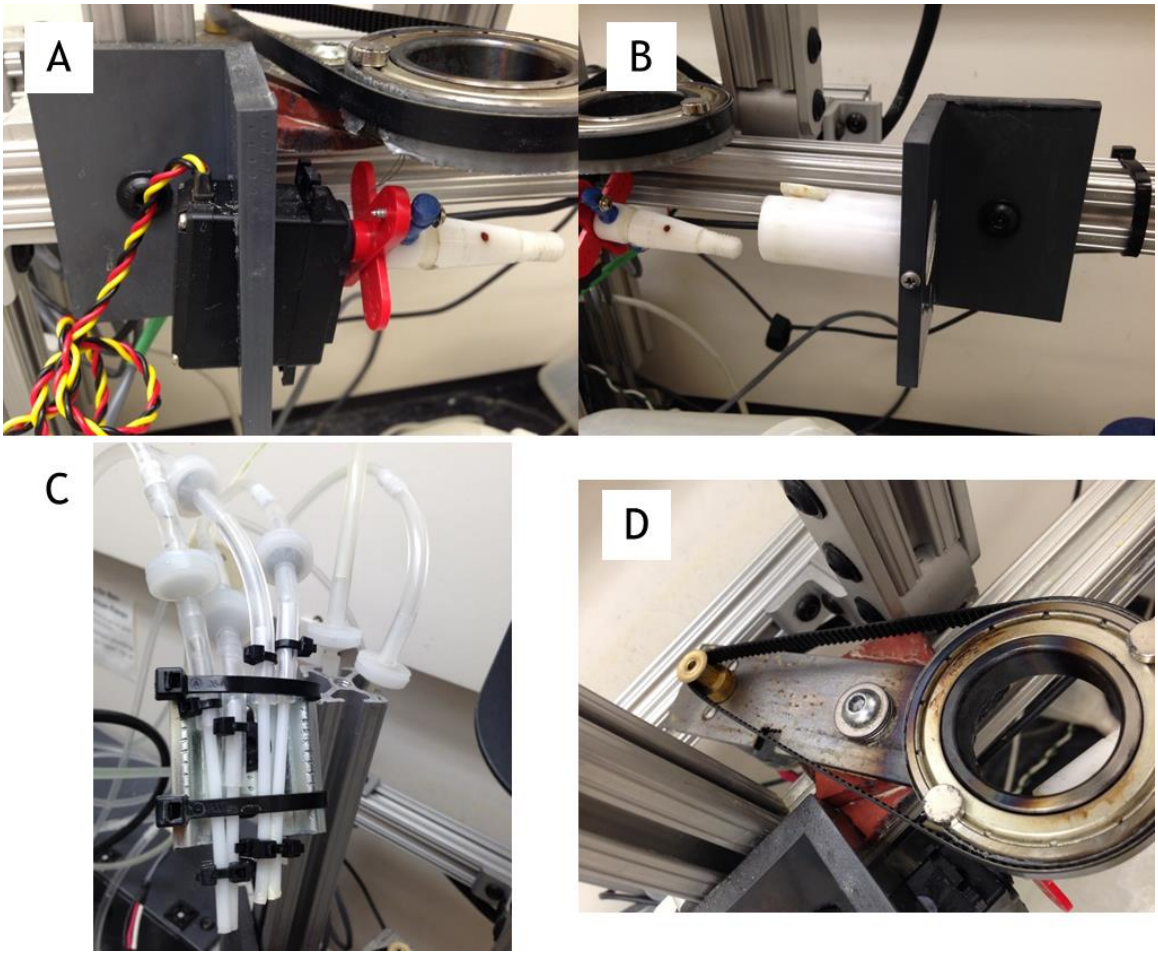

Figure 9: Original handmade complex parts for coating systems. A) t-slot to Servo holder, B) t-slot to stopcock holder, C) t-slot to PTFE tube holder which acts to direct the flow into the small reaction chambers, D) Bearing holder for spinner used for mixing solutions during coating of powder-type substrates.

The development 1 coating systems were designed to replace the need for hand dipping each wafer-like substrate.

2.4.2 Automated QCM-D Control System

The two D2 systems were designed and built after the D1 systems and had to benefit of the knowledge gained in construction of the D1 systems. The D2 systems have arrays of relays inside that control the overall power as well as the individual solenoid valves and the cooling fans. Both systems are controlled with

Arduino Uno R3 micro controllers (Arduino, Ivrea, Italy). The cooling fans operate off of a higher voltage than the solenoid valves and require an external power supply to be plugged into the Arduino. The solenoid valves (Flow Selection Valves, Western Analytical Products, CA, USA) heat up by design. This is not a problem if the valves are open for only a small amount of time, but when operated with the QCM for 30 minutes of more, the valves can become hot. If the valves become hot, the temperature of the fluid could be affected which changes the reaction conditions.

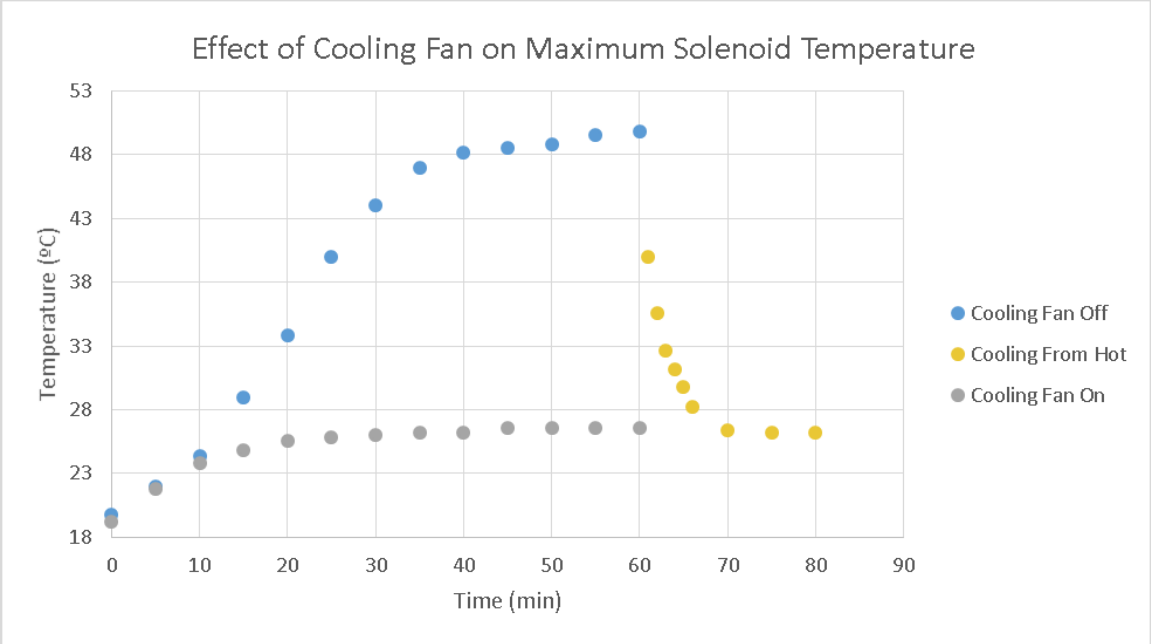

Figure 10: The Maximum temperature of a solenoid valve on the R2-D2 system while energized under various conditions. A) Blue dots represent the temperature with the fans off. B) The yellow dots represent the temperature when the fans are turned on at the solenoid valve cools. C) The green dots represent the temperature with the cooling fans on.

For this reason, the solenoid valves are actively cooled be forcing air through vents cut out around the solenoid valves. This has proved to sufficiently cool the valves during continuous use.

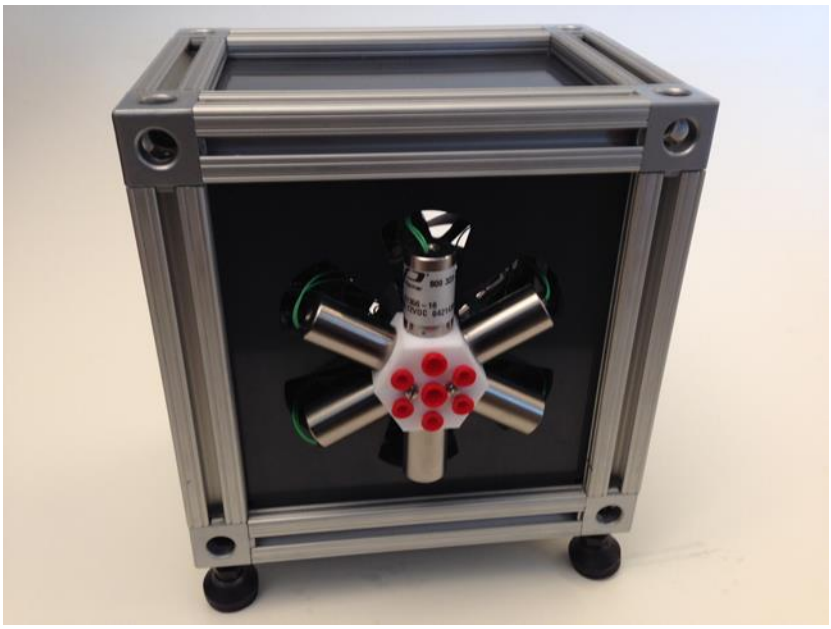

Figure 11: Image of the front of R2-D2 showing the six solenoid valves and the air vents behind each valve. All of the electronic is housed inside and the cooling fan is located on the back.

The cutouts on the panels of the D2 systems were made using CAD models created in SOLIDWORKS, with CAM created using CAMWorks, and a 3D Flash Cut CNC.

2.5 Software Design

The coating robots have been designed to be controlled by a computer using a LabVIEW based program. This LabVIEW based program was written specifically for the purpose of controlling the robotic coating systems. This control program has evolved as the robotic systems have been upgraded and as the new systems have been built, but only the final version of the program will be discussed.

The GUI is designed to allow the user to quickly select the system being used and to input the type and number of coatings to be applied. On the left side of the Front Panel is a cluster of seven arrays which make up the Step Parameters.

This is a step-by-step procedure that the program followed during the coating process. Each row is made up of an indicator, a number designating the row, a ref num designation the type of action, a # sign used with the GoTo action, a repeat numeric, an incubation time in minutes, and a pump time in seconds. In a central column is the feedback for timing. This allows the user to see the Current Time, Predicted Finish, Time Predicted, Time Elapsed, Time Remaining and Step Time Left. These times are all outputs and do not affect the operation of the physical system, but instead are present to inform the user of the progress being made. Below the times are four buttons, labeled Start, Pause, Skip Step and Restart. The action of Start is immediate, but the action of the others occur only after the current step has completed. To the right of the times are five more indicators to inform the user of the current location of the coating process. Layer Time gives to total time to progress though the Step Parameters once. Section # Counter is coupled to the GoTo action and indicates the current iteration number. Step Number indicates which step is currently executing. Step # Counter is coupled with the X in the Step Parameters and controls the number of times a step repeats. Current Step is the Ref Num value of the current step, this is the same as Step Number.

On the top of the Front Panel is the Error Communications. These errors do not stop the program from progressing, but instead are designed to remind the user of best practices. There are also error clusters in the code that automatically shut down the program if there is a failure and they display when the program finished execution. Below the error string are three large numerics that show the number of Starting Layers, Layers to Added, and Layers Added. The Starting

Layers number does not affect the program, but is there for the user to keep track of the number of layers on the sample if the program needs to be stopped. The Layers to Added number is coupled with the Finish Layer action in the Step Order in the Step Parameters. The Layers Added function is the number of complete iterations of the step parameters.

Below Layers to Add, is a dropdown box for the System. When the program is executed, a dialog box will appear prompting the user to select a system to use. The user should select the system, select the VISA resource and click USE. The VISA resource is the communication port with which the system is connect to the computer. Below is the Drying Type where the user can select either vacuum (for powder-type samples) or Heat Gun (for wafer-type samples). Drain Time defines the amount of time for each step that the stopcock is open. Mixer is a Boolean control which is used with powder-type samples. Power controls the power to the system, and the two Boolean indicators below show if the system is plugged in and powered. On the very bottom in the Stop button and directly above it are manual control switches to turn on and off individual parts of the systems.

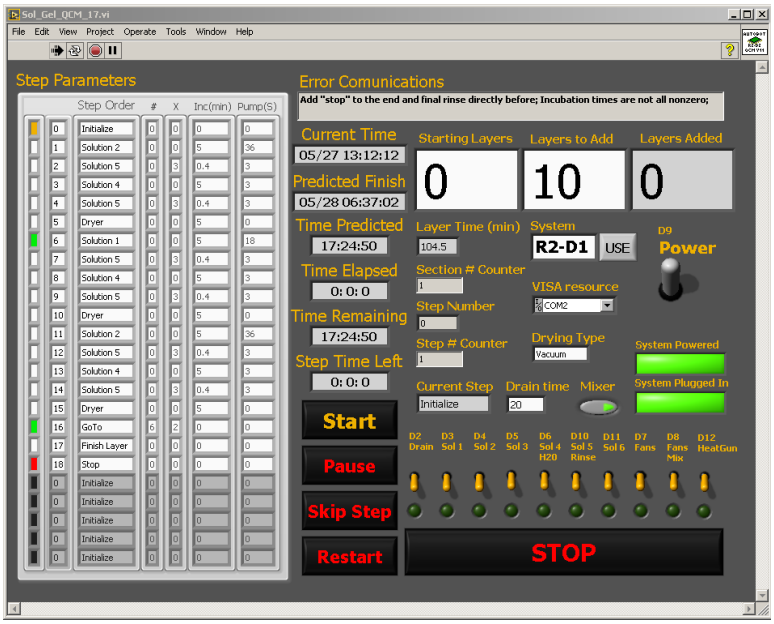

Figure 12: Graphical User Interface for controlling the robotic coating systems. The interface is set up in the figure above for coating 50 cycles onto a powder-type sample with mixing and drying via vacuum. Below the times are four buttons, labeled [Start], [Pause], [Skip Step] and [Restart]. The action of [Start] is immediate, but the action of the bottom three is after the current step has completed.

The core of the program displays the current step in the coating process and what should be happening and correspondingly turns on the various pumps and valves. The program sends commands via USB to an Arduino microcontroller (MEGA 2560 R3, Arduino, Ivrea, Italy) which in turn controls individual components. LabVIEW provides a program that can be flashed onto the Arduino board to allow LabVIEW to directly control the board outputs without having to program in the Arduino specific language[8]. The program has been designed to also work with the older coating robot developed by Mike Weatherspoon[6].

Table 1: Digital in/outs (DIO) and Analog Ins (AI) for the microcontrolers for the various robotic systems. The left two columns show the numeric value of the control in the program. The right six columns represent the physical pins that are connected to which action.

System Name:		R1-D0	R2-D0	R1-D1	R2-D1	R1-D2	R2-D2
Board:		Ni-Daq	Ni-Daq	Uno	MEGA	Uno	Uno
#	Action						
DIO							
0		Mixer	Not Analyzed				
1		Vacuum					
2	Drain	Sol 1		Power	Power		Power
3	Sol 1	Rinse/5		Water/4	Water/4	Sol 1	
4	Sol 2	Water/4				Sol 2	Fans/Cooler
5	Sol 3	Sol 2		Rinse/5	Rinse/5	Sol 3	Sol 6
6	Sol 4	Sol 3		Sol 3	Sol 3	Sol 4	Sol 5
7	Fans			Drier	Drier	Fans	Sol 4
8	Mix			Mixer	Mixer	Fans(TBR)	Sol 3
9	NA			Sol 2	Sol 2	Power	Sol 2
10	Sol 5			Sol 1	Sol 1		Sol 1
11	Sol 6			CS	CS		
12	Heat gun						
AI							
0					Drier		
1					Rinse		
2				Power?	Power?		
3					Water		
4					Sol 2		
5					Sol 1		
6					CS		
7					Mixer		

The program is based on a State Machine architecture which allows for individual states to be defined and allows for each state to be executed in a specified order. In this program the order is defined by primarily by the Step Order, but there are exceptions to the Order. When the X value for a step is above 1 then it will repeat that step X times. When the GoTo function is present, the next step is defined by the number in the # variable X times. If the Skip Step

button is clicked, the state machine will skip the next state. If the Restart button is clicked, the state machine will go back to the initialize step (always 0) and the user will need to click Start to restart the program.

2.6 Experimental Procedures

2.6.1 Coating of Wafer-Type Templates

For coating of wafer-type templates, the primary concerns are contamination, efficiency of solution volume, and mechanical destruction of the template. Contamination arises in many forms, from a failure to rinse the substrate of solutions, dripping from precursor hoses, reaction of alkoxides with the air, and contamination in the precursor solutions. Standard procedures of cleaning were used to produce precursor solutions with no contamination. To limit the reaction of the alkoxides with the water vapor in the air, the precursor solutions were constantly backfilled with dry nitrogen. Solutions back filled with air show degradation after approximately a week. Once solutions show any haze or precipitation they are considered degraded and not fit for use in the SSG coating process. Solutions backfilled with dry nitrogen have maintained a clear appearance and as expected coating qualities for up to three months.

Specifically for wafer-type templates, to maximize the efficiency of solution usage, rectangle reaction chambers were fabricated in the chemistry glass shop. Designs were fabricated by Don Woodyard and Brian Markowicz. The rectangular glass was purchased from Technical Glass Products and varied in size from (T X W X H) 10 mm X 15 mm X 25 mm to 20 mm X 100 mm X 280 mm. Directly below the reaction chamber is a #2 PTFE stopcock, and below that is a

hose barb fitting with a "drip-tip". Figure 13 shows an example rectangle crucible.

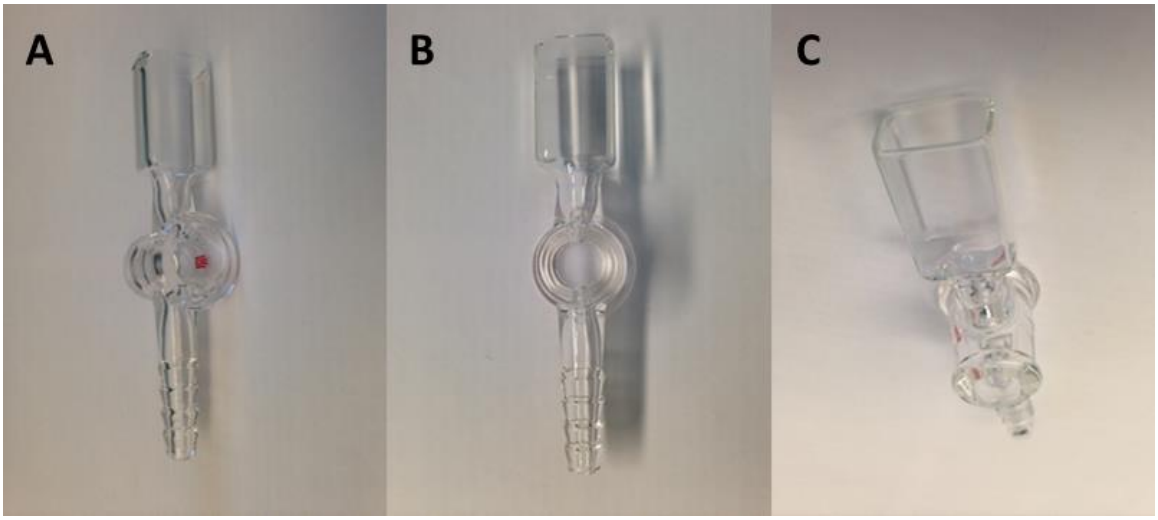

Figure 13: Optical images of a 10 mm X 15 mm crossection glass reaction crucible. Image is A side view, B is a forward view, and C is a corner view of the same crucible.

The rectangular design of the crucible is preferable to the simpler cylindrical design because it saves fluid. In the scenario where a rectangular substrate, like a butterfly wing segment needs to be coated, the volume of reaction chamber is given by Equation (7).

$$V_r = H * W * T \quad \textbf{(7)}$$

Here, H, W, and T are the height, width and thickness of the rectangular crucible and V_r is the volume of the chamber. For a cylindrical crucible, the volume is given by Equation (8).

$$V_C = \frac{\pi H D^2}{4} \quad \textbf{(8)}$$

Here, D is the diameter, H is the height and V_c is the volume of the cylinder. For a flat substrate, the sample needs to be placed vertically to assure proper rinsing which dictates that the height is the same for both crucibles. Because the thickness of the samples used in this research is <1 mm it was assumed to be zero in these calculations. This means that the defining factor is the width of the sample. Because the widest part of the cylinder is its diameter the necessary width of a rectangle and the necessary diameter of a cylinder are the same. To find the ratio of fluid required to coat the same substrate with a rectangular rather than cylindrical crucible Equation (7) is divided be Equation (8) to give.

$$R_V = \frac{V_R}{V_C} = \frac{4T}{\pi W} \quad \textbf{(9)}$$

Equation (9) shows that the ratio of solution used is proportional to the thickness and the width of the rectangle chamber (or diameter of the cylinder). On a commonly used crucible that is 30 mm by 10 mm, the use of the rectangular crucible uses only 42.44 percent of the solution that a cylindrical crucible would have used. This can be seen graphically in Figure 14.

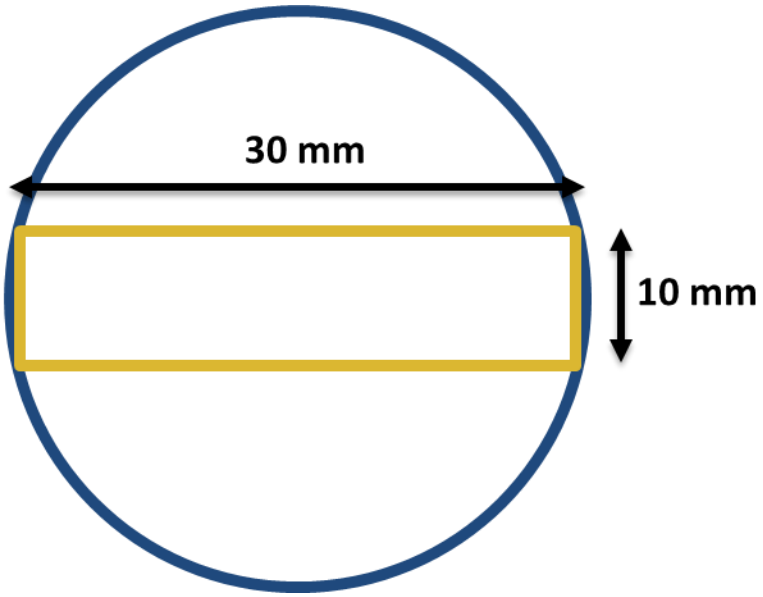

Figure 14: A schematic showing the relative cross sections necessary to coat a 30 mm wide sample. This illustrates the need for rectangular crucibles.

For samples sensitive to physical motion, like butterfly wing segments, the sample was clipped onto the glass wall with a copper alligator clip (McMasterCarr, GA, USA). For robust samples being coated without other samples present, the sample could be simply placed in the crucible with no physical attachment.

2.6.2 Coating of Powder-Type Templates

Powder-type substrates offer some increased complications for coating, but with the proper design can be more efficient with solution that a wafer-type substrate coating. Powders cannot be coated in the same types of chambers as wafer-type substrates because the powder would flow out of the chamber upon draining. The powder-type substrates need to be filtered out of the coating solution. This was achieved by using a custom made Buchner funnel (#89000-428, VWR International, PA, USA) with a #2 PTFE stopcock and hose barb in the same fashion as the rectangle reaction chambers. The hose barb was connected to a

4L filter flask(#89090-736, VWR International, PA, USA) for waste containment attached to a 500 mL filter flask(#89090-760, VWR International, PA, USA) in an ice bath as a solvent trap with vacuum achieved via a diaphragm pump (#4176K11, McMaster, GA, USA).

The powders in this research are generally around 30 um in diameter. To avoid having the particles slip through the pores, the frits originally used were "Fine" (10 – 20 um pore diameter). These frits would work properly for the first 30 – 40 cycles, but as the SSG coated the silica frit the pore size would decrease and lead to clogging and failure to drain. To fix this problem, Buchner funnels with larger pores were used. "Coarse" fritted Buchner funnels (#89000-428, VWR International, PA, USA), proved to be fine enough to not allow particles to escape, but also did not clog within 200 coatings.

To coat all particles evenly, Dr. Goodwin showed that it is necessary to mix the powder-type substrate in the precursor solutions.[9] Figure 15 shows the uneven coating that can occur when the sample is not stirred.

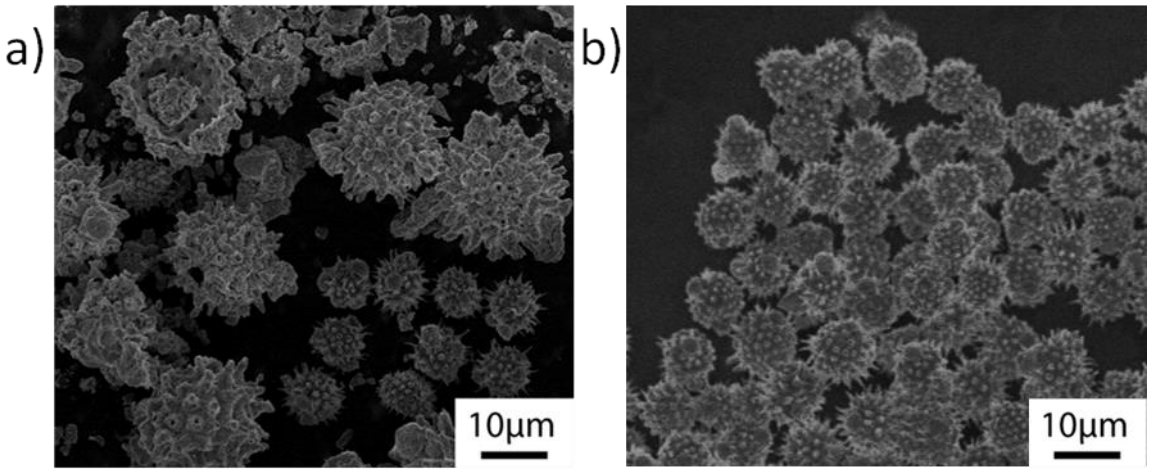

Figure 15: SE micrographs of sunflower pollen coated with 30 Fe-O SSG cycles (a) without a stir bar and (b) with a stir bar followed combustion at 600°C for 4 h in air Courtesy of Dr. Goodwin.

To achieve thorough mixing, a PTFE stir bar was used on the inside of the Buchner funnel and a custom made stirring apparatus was fabricated out of a DC motor, a steel bar and a steel ball bearing with magnets mounted on the outer ring. This design allows for the inert stir bar to be influenced eternally.

2.6.3 Firing Conditions

Inorganic replicas were created by firing coated samples in inert crucibles (MgO or Al_2O_3) in a tube furnace (Lindberg Blue M, Thermo Fisher Scientific Inc., MA, USA) at generally 450 °C to 600 °C and held at temperature for generally 4 to 6 hr in air to allow for combustion of the organic and crystallization of the coating material. The furnace was then cooled at 120°C/hr to below 100°C before removal of the sample from the furnace.

Different methods were used to preserve the structure of the bioorganic templates. For butterflies, individual coated scales were scraped off of coated butterfly wing sections with a scalpel (36325A63, McMaster-Carr, PA, USA) with a #15 blade. Because the samples have structural color, the quartz slide could be visually inspected to assure an even distribution of scales. Samples were clipped (Staples® Small Satin Silver Metal Binder, MA, USA) between two polished (2.54 x 2.54 x 0.159 cm) fused quartz plates (Technical Glass Products, OH, USA) and then heated in an MgO crucible.

For powder substrates being fired solely for EDS, XRD, and ICP-MS analysis, fusing of individual particles is not problematic; thus they could be fired directly in an MgO crucible. However, when the individual particles needed to be identified, MgO wafers (MTI Corp, Ca, USA) were used as substrates and powders

were dispersed on the surface. Coated powders were dispersed in IPA and subsequently pipetted onto MgO wafers and allowed to dry. Each wafer was inspected using an optical microscope to insure even dispersal of the particles (A-Zoom2, Micromanipulator Inc., CA, USA). The wafer could then be placed in an MgO crucible and fired.

2.6.4 Replica Characterization

Standard SEM, EDS, XRD and optical were utilized to characterize the structure retention and purity of coating. The microstructures of uncoated substrates, SSG-coated substrates, and all inorganic replicas of substrates were imaged with a field-emission scanning electron microscope (1530 FESEM, Carl Zeiss, NY USA). The chemical composition was evaluated with an energy dispersive X-ray spectrometer (EDS) (INCA 7426, Oxford Instruments, UK) which was used in combination with the above SEM.

For samples sputtered with gold, a Quorum Q150T ES (Energy Beam Sciences, INC., CT, USA) sputter coater was utilized to sputter gold for 60 seconds at 20 mA. Cross-sections of samples were created by milling via focused ion beam (FIB) milling (Nova Nanolab 200 FIB/SEM, FEI, OR, USA).

Phase identification of replicas was evaluated using X-ray diffraction (XRD) analysis. XRD was conducted using an X'Pert Pro Alpha-1 diffractometer (PANalytical B.V., ALMELO, Netherlands) with monochromatic Cu Ka1 (1.540598 Å) radiation from a 1.8 kW (45 kV, 40 mA) X-ray tube filtered via a symmetrical Johannson monochromator and detected by an X'Celerator detector. The source was limited by a 1° fixed anti-scatter slit, a ½° programmable divergence

slit, and a 15 mm mask. The diffracted x-rays were subject to a 0.04 radian soller slit and a 5.5 mm anti-scatter slit before the X'Celerator detector. Diffraction specimens were placed on B doped p-type Si zero background plate (MTI Corp, CA, USA). The sample support was rotated at 8 sec per revolution. The phases of replica materials were identified using the HighScore Plus (PANalytical, Almelo, the Netherlands). Scherrer's formula, Equation (10), was used to calculate the average crystallite size for powdered samples.[10]

$$t = \frac{k\lambda}{B\cos\theta} \quad \textbf{(10)}$$

Here, t = crystallite size, k = 0.89, λ= 1.54 Å ($Cu_{K\alpha 1}$), θ = peak position, and B = full width at half maximum (FWHM).

2.7 Results and Discussion

To demonstrate that the coating systems perform as designed and at or above the standards set by manual control, all three scenarios were analyzed. To test the coating of powder-type substrates, sunflower pollen were coated with Ti-O and then replicated. To test the coating of wafer like substrates, a *P. sesostris* was coated with Ti-O and then replicated. To test the precursor control using the QCM setup, Ti-O was deposited onto SiO_2 coated QCM resonators.

2.7.1 Powder-Type Substrate Verification

Clean sunflower pollens were coated with SSG and fired to demonstrate the shape preserving nature of the SSG technique and coating system. For

demonstration, the pollens were coated with 50 cycles of Ti-O via the SSG coating method using Ti(IV) isopropoxide. The Particles were analyzed with SEM, EDS and XRD to confirm morphology preservation, elemental deposition, and crystallographic phase.

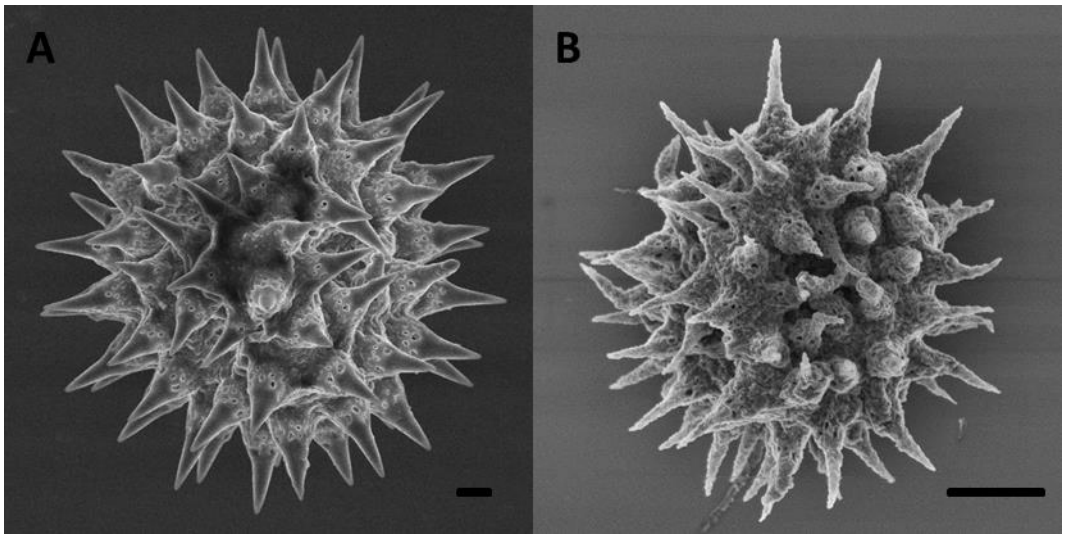

Figure 16: SEM micrographs of A) SF pollen coated with 50X SSG Ti-O and B) replica of the same pollen particle after firing at 600 °C after 4 hours. Courtesy of Ben deGlee

The SEM micrographs in Figure 16 show that the overall structure of the sunflower pollen was replicated by the SSG coating deposited by the automated coating system.

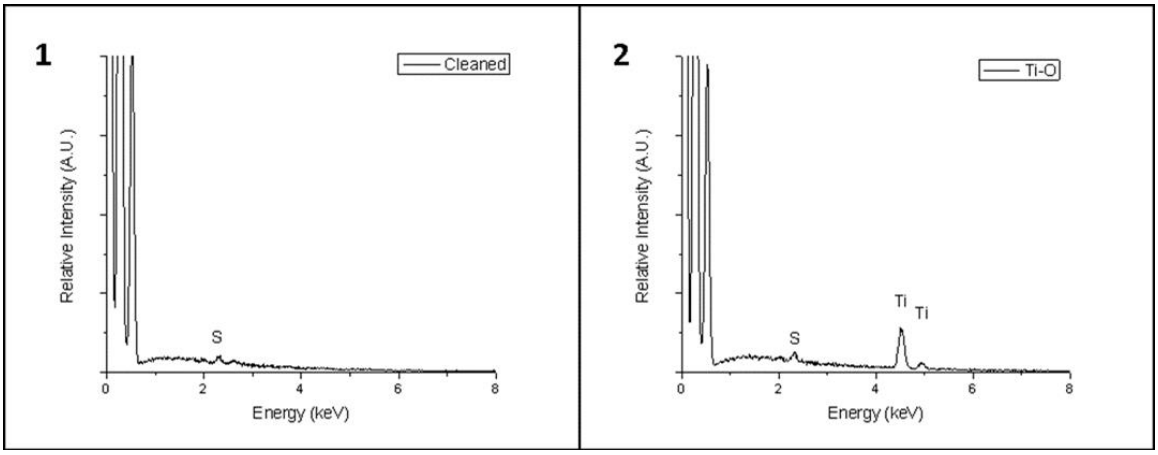

Figure 17: EDS spectra of 1) cleaned SF pollen particles and 2) SF pollen replicas of Ti-O.

The EDS spectra show that the replica material does bear titanium, but also has some sulfur that was native to the pollen.

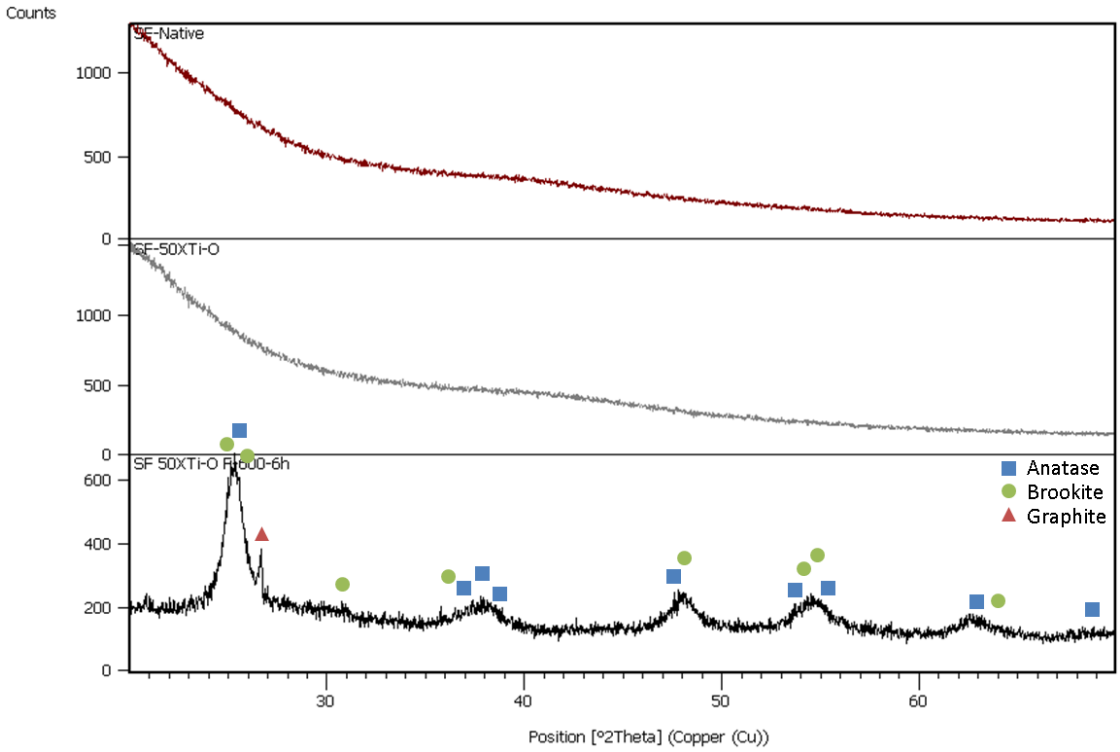

Figure 18: XRD powder diffraction scans of Top: Native sunflower pollen, Middle: Sunflower pollen coated with 50 cycles of Ti-O and Bottom: replica pollens that were coated with 50X Ti-O SSG with the automated coating system and fired at 600 °C for 4 hr. Sample shows only Ti-O polymorphs present in the replica consisting of Anatase and Brookite. The Graphite peak is from XRD sample container preparation contamination.

Analysis of the XRD powder diffraction scan shows that only titanium oxide polymorphs are present in the replica. This confirms that the titania coating took the form of the pollen and replaced its chemical construction.

2.7.2 Wafer-Type Substrate Verification

To verify the validity of the robotic coating system for coating wafer type substrates, an intricate 3D structure was selected to be replicated. The wafer-type substrate selected was the *P. sesostris* butterfly dorsal wing scales. With this demonstration, the dorsal wing scales were coated with Ti-O for 100 SSG cycles via Ti(IV) isopropoxide as the titanium precursor. The as-coated *P. sesostris* butterfly dorsal wing scales were fired at 450 °C for 4 hr to burn away the native chitin and crystallize the Ti-O coating. The butterfly wing scale replicas were analyzed with SEM, EDS and XRD to confirm morphology preservation, elemental deposition, and crystallographic phase.

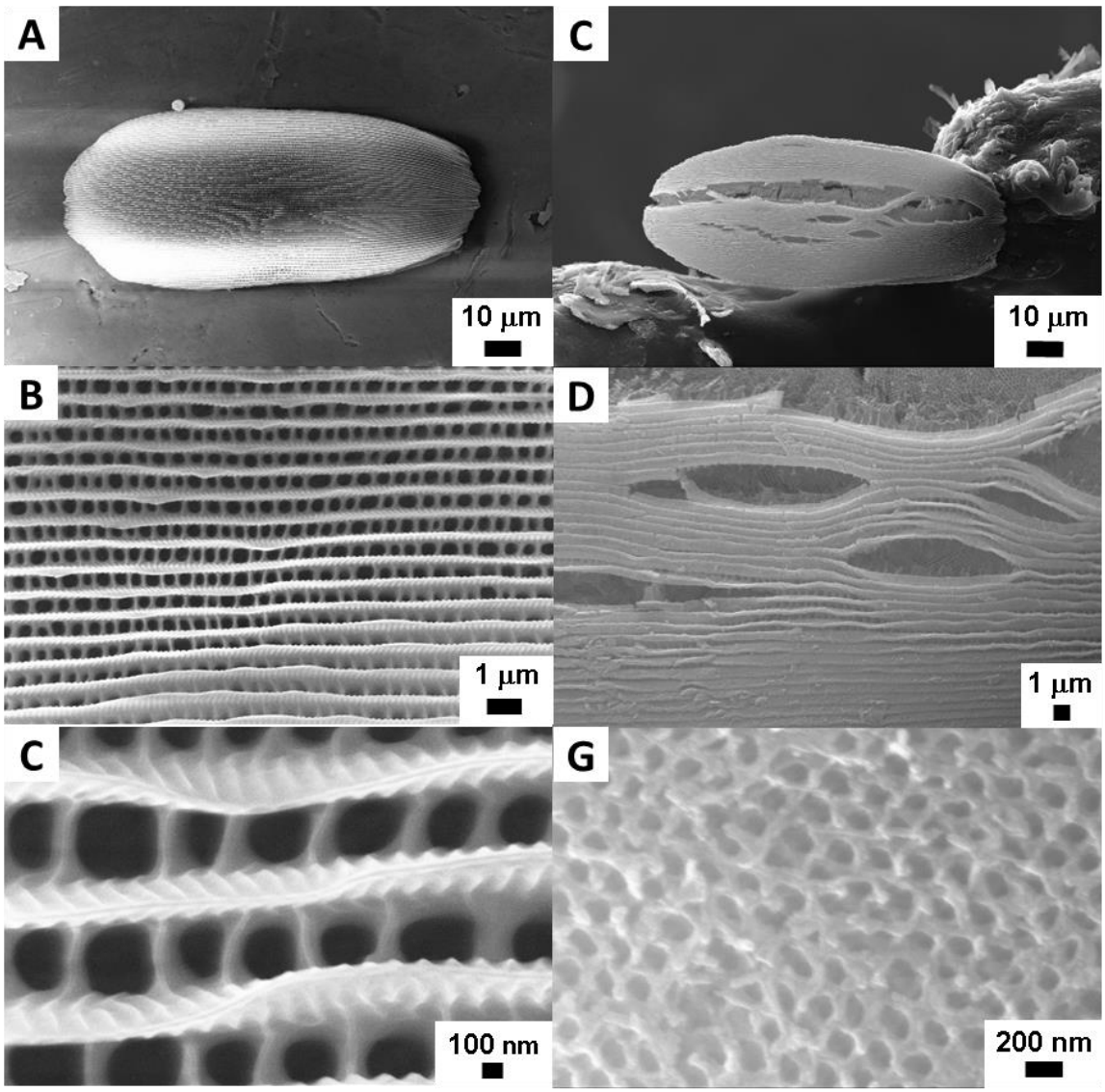

Figure 19: SEM micrographs of A, B, C: a native uncoated *P. sesostris* butterfly dorsal wing scale sputtered with gold and D, E, F: replica of a *P. sesostris* dorsal wing scale coated with 100X SSG Ti-O after firing at 450 °C after 4 hours.

The SEM micrographs in Figure 19 show the replication of the *P. sesostris* wing scale. Due to splitting of the ridge structure, the replica displays the replicated, now titania, gyroid structure.

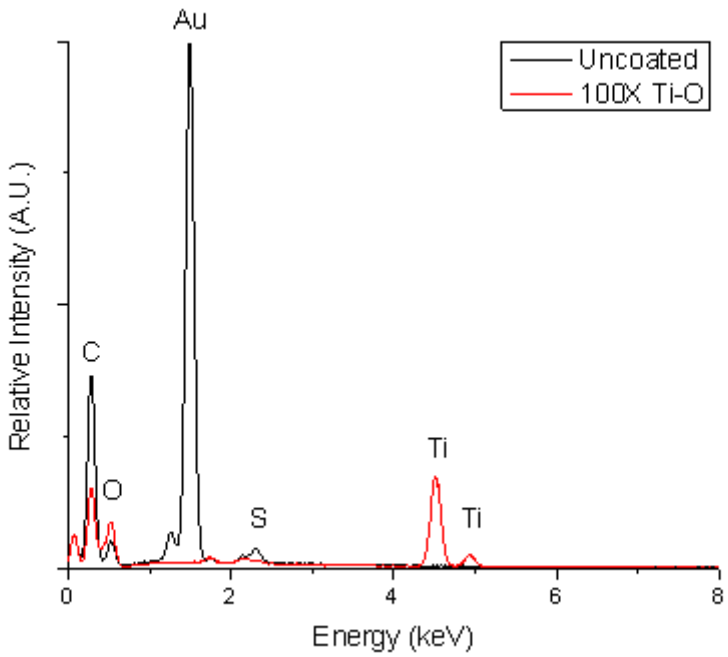

Figure 20: EDS spectra of (Black line) an uncoated *P. sesostris* wing scale with gold coating for imaging on SEM and (Red line) titania replica on a *P. sesostris* wing scale after 100 cycles of SSG.

EDS analysis shows that the titanium oxide is the primary constituent in the replica material. The native sample was coated in gold to increase avoid charging of the surface.

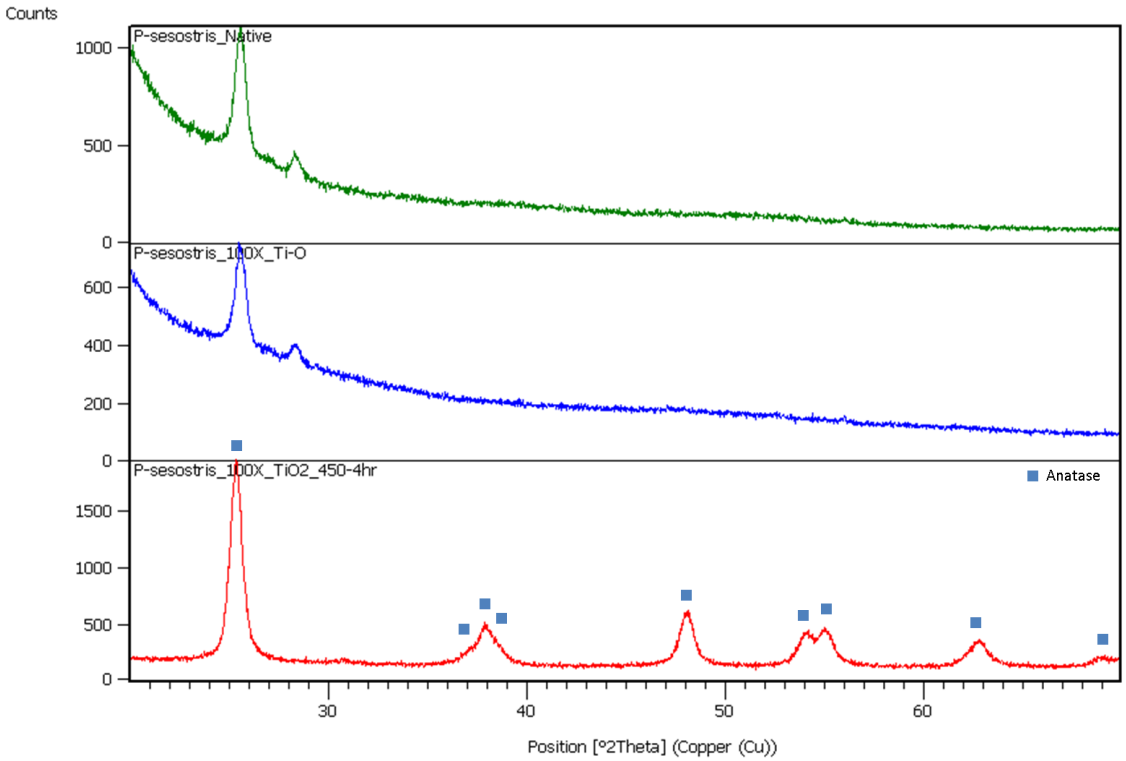

Figure 21: XRD spectra of Top: an uncoated *P. sesostris* butterfly wing scales, Middle: *P. sesostris* wing scales coated with 100 cycles of SSG Ti-O and Bottom: Titania *P.sesostris* wing scale replicas after firing at 450 °C for 4 hr.

The XRD spectra show the presence of only titanium oxide polymorphs in the replica which indicates that the replica composition was replaced by the Ti-O without contamination.

2.7.3 QCM-D Control Validation

The QCM-D control system was validated in a different manner than that of the coating systems. Limited data exists on LbL deposition of alkoxides. Ichinose et al. have investigated the deposition of some SSG precursors although their testing method is not in-situ and is admittedly prone to time-dependent degradation. [2, 3] Ichinose et al. use an ex-situ SSG coating method of a QCM crystal.[2, 3] The QCM crystal used in that research is a 9 MHz crystal where the

crystal used in this research is a 5 MHz resonator. For a dense film, this relationship is described by the Sauerbrey equation.[11]

$$\Delta F = -\frac{2f_0^2}{A\sqrt{\rho_q G_q}}\Delta m \quad \textbf{(11)}$$

Above, ΔF is the change in frequency of the QCM crystal, f_0 is the resonance frequency of the QCM crystal, Δm is the change in mass on the QCM, A is the area of the sensor, ρ_q is the density of quartz (2.648 g/cm^3) and G_q is the shear modulus of the QCM (29.47 GPa). Based on information provided by Ichinose et al. and by use of the Sauerbrey equation, the evaluation of their results, represented as a frequency change, and the results found in this research can be compared.

Table 2: Comparison of QCM resonators used in this research and the research of Ichinose et. Al.

	Ichinose et al.	**This Research**
$f_O(MHz)$	9	5
$\frac{\Delta m}{\Delta F \cdot A}\ (mg/m^2 \cdot Hz)$	-0.0275	-0.1767

Ichinose et al. report a per cycle frequency change for deposition of 100mM Ti(IV) butoxide as 61 Hz ± 37 Hz deposited at 18 °C.[2] In this research, a similar chemical, Ti(IV) isopropoxide, was used in the same concentration and temperature.

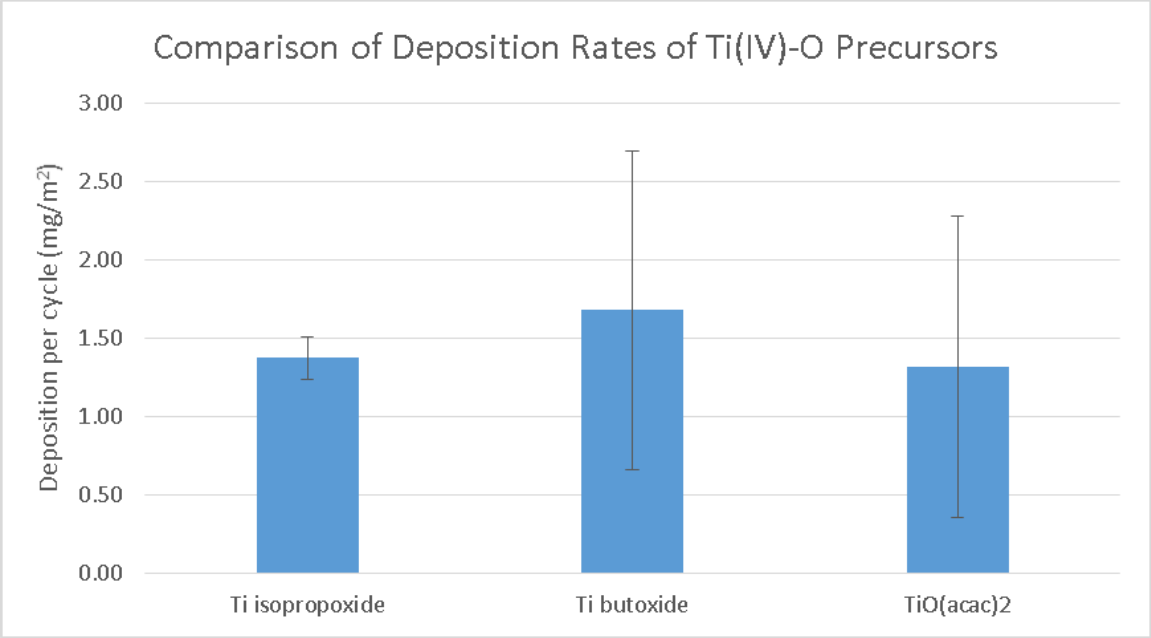

Figure 22: Bar graph showing comparison of deposition rate of Ti(IV) butoxide and Ti (IV) oxyacetylacetonate as reported by Ichinose et al. and the deposition rate of Ti(IV) isopropoxide as found in this work.[2]

The results of the deposition of Ti(IV) isopropoxide show that the QCM deposited a statistically similar amount of Ti-O per-cycle as to published research.[2] It is notable that the variability of the amount deposited was significantly less than published research, likely due to the precision of the robotically controlled deposition.

2.8 Concluding Remarks

The coating systems were designed and built individually and have been used for coating a variety of materials and chemistries including Ti-O, Sn-O, Er-O, Sm-O, Fe-O, Ba-O, Sr-O, W-O, Zr-O and mixtures of these oxides. They have been used to create multifunctional butterfly wing scales and to create high dielectric pollen particles. The D2 systems have been used to control the flow to the QCM for time periods of over 48 hours continuously. The R2-D1 system

has run for 150 hr straight and has deposited over 6000 SSG layers. All of the systems combined have operated for over 3000 hours saving approximately a year and half of labor. The systems have been involved in many projects and have been key to over seven publications currently being prepared. All three parts of the coating systems (powder-type and wafer-type substrates and QCM deposition) have been validated to accurately and repeatedly deposit LbL SSG coatings without contamination.

2.9 References

[1] J. Vernon, "Morphology-preserving chemical conversion of bioorganic and inorganic templates," Ph.D. Dissertation, Materials Science and Engineering, Gerorgia Institute of Technology, Gerorgia Institute of Technology, 2012.

[2] I. Ichinose, H. Senzu, and T. Kunitake, "Stepwise adsorption of metal alkoxides on hydrolyzed surfaces: A surface sol-gel process," *Chemistry Letters,* pp. 831-832, 1996 1996.

[3] I. Ichinose, H. Senzu, and T. Kunitake, "A surface sol-gel process of TiO2 and other metal oxide films with molecular precision," *Chemistry of Materials,* vol. 9, pp. 1296-&, Jun 1997.

[4] I. Ichinose, T. Kawakami, and T. Kunitake, "Alternate molecular layers of metal oxides and hydroxyl polymers prepared by the surface sol-gel process," *Advanced Materials,* vol. 10, pp. 535-539, May 1998.

[5] I. Ichinose and T. Kunitake, "Wrapping and inclusion of organic molecules with ultrathin, amorphous metal oxide films," *Chemical Record,* vol. 2, pp. 339-351, 2002.

[6] M. Weatherspoon, "CONFORMAL SOL-GEL COATINGS ON THREE-DIMENSIONAL NANOSTRUCTURED TEMPLATES," Ph.D. Dissertation, Materials Science & Engineering, Georgia Institute of Technology, 2008.

[7] W.-S. Jang and J. C. Grunlan, "Robotic dipping system for layer-by-layer assembly of multifunctional thin films," *Review of Scientific Instruments,* vol. 76, p. 103904, 2005.

[8] N. Instruments. (2015). *LabVIEW Interface for Arduino Firmware*. Available: http://digital.ni.com/public.nsf/allkb/8C07747189606D148625789C005C2DD6?OpenDocument

[9] W. B. Goodwin, "Controlled Modulation of Short- and Long-range Microscale Biogenic Replicas," Ph.D. Dissertation, Materials Science & Engineering, Georgia Institute of Technology, Georgia Institute of Technology, 2014.

[10] B. D. Cullity and S. R. Stock, *Elements of X-ray Diffraction* vol. 3: Prentice hall Upper Saddle River, NJ, 2001.

[11] G. Sauerbrey, *The use of quartz crystal oscillators for weighing thin layers and for microweighing applications*, 1991.

CHAPTER 3: Conversion of *P. sesostris* into Three-Dimensional Ceramic Replicas with Tailorable and Predictable Multimodal Coloration

3.1 Summary

In this chapter, SSG LbL deposition was used to apply Ti-O and Ti-Sm-O bearing coatings onto the *Parides sesostris* butterfly dorsal wing scales to understand i) how the inclusion of Sm–O in the coating affected the reflected color of the scales, ii) how the replicated structure was affected by the addition of Sm-O and the potential for photoluminescence, and iii) to see if multimodal colored replica wing scales could be created. The inclusion of the Sm-O into the coating process had limited effect of the reflected color of the as-coated *P. sesostris* wing scales. The limited red-shift that was seen is likely due to the increased deposition rate of the samarium (III) isopropoxide, but could also have been due to a slight increase in the refractive index of the coating. The replica samples that were created with Sm in the coating showed intense photoluminescence when stimulated with UV light. The addition of Sm limited the crystallization of the Ti-O matrix causing samples of pure Ti-O to have excessive grain growth under the firing conditions that produced maximum photoluminescence in the Sm doped samples.

To demonstrate dynamic multimodal coloration of a biological replica through color mixing of structural color and photoluminescence, samarium doped titania replicas of *P. sesostris* were imaged under UV, white light (WL) and a combination of UV and WL. The results showed that the replica changed color

from red (UV illumination only) to purple (UV and WL illumination) to blue (WL illumination only).

3.2 Introduction

Prior work has demonstrated the bioorganic structures (e.g. diatoms,[1] butterflies,[2, 3] beetles,[3] and pollen particles[4]) can be utilized as templates for coating and chemical conversion to maintain structural properties while adding new functional materials properties(e.g. optical, chemical, and magnetic). These biogenic replicas have applications such as anti-counterfeiting,[5] catalysis,[6] and chemical filtration.[1] Recently, pollen particles have been used as a template for coating and conversion into magnetic materials for the purpose coupling magnetic and van der Waals forces.[7] Recent work has also demonstrated that butterfly wing scales can be modified to change their static reflected color.[8] However, little work has been done to show multimodal coloration in biological replicas of the structural color from a photonic crystal and the photoluminescence of the replica material or the interaction and coupling of electrostatic and van der Walls forces.[9] Additionally little work has investigated directly coating complex multifunctional oxides onto biological structures.[8] Prior work has relied on complicated microwave hydrothermal post processing to add fluorescent properties to oxide replicas.[5]

The *Parades sesostris* butterfly green dorsal wing scales provide desirable templates due to the structural color of their polycrystalline photonic structure [10, 11] and the chitin material that composes the structure of the butterfly which

has an abundance of surface hydroxyl groups.[10, 11] The *P. sesostris* are inexpensive, readily available, and naturally designed to be optically active. The chitin of the *P. sesostris* has an abundance of hydroxyl groups that are necessary for a conformal coating to be deposited via LbL SSG processing without the need of a preprocessing amplification of the surface functional groups.

3.3 Experimental Procedures

P. sesostris butterflies were purchased deceased and dehydrated (Bugmaniac, Makassar, Indonesia) and were chemically transformed into TiO_2:Sm replicas by first: application of a thin Ti-Sm-O bearing coating through a LbL SSG process with use of an automated coating system, followed by: combustion of the chitinous template and crystallization of the Ti-Sm-O coating into a photoluminescent replica. These replicas both retained their structural color and had the added functionality of being photoluminescent.

3.3.1 Bioorganic Template

The *Parides sesostris* butterfly green scale is a desirable template because it has a highly intricate structure that can be used as validation for a conformal coating process (if the coating process can succeed on the micro to nanometer sized features of the *P. sesostris* green scale then it will likely be capable of coating less intricate structures as well). The chemical structure of chitin is made up of long chains of N-acetylglucosamine[12] which on each unit have two hydroxyl groups making it highly reactive to the SSG process without any need for preprocessing to functionalize the surface. The green dorsal wing scales of

the *P. sesostris* are also desirable due their availability, low cost, and reproducible intricate structure. The dorsal wings also have the advantage of supporting the green scales to allow for easy securing of the wing segments without any need to filter the scales after each step.

3.3.2 Hydrolysis of Mixed Alkoxide

Precipitation via hydrolysis of Ti – Sm – O bearing powders was performed using 10 mL of DI water added to 40 mL of 99.25%at Titanium isopropoxide and 0.75%at Samarium isopropoxide (25 mM total concentration) with DI water in a centrifuge tube (VWR International, PA, USA). The solution of precursor and water was thoroughly mixed using a Vortex Genie 2 (Scientific Industries Inc, Bohemia, NY, USA) for 5 minutes and then was spun down with a centrifuge for 5 minutes at 5000 RPM (5408R centrifuge with #A-4-44 rotor, Eppendorf, Hamburg, Germany). After centrifugation, the supernatant, now clear, was poured off and the precipitate was dried at in air at 80^{o}C for 30 min.

3.3.3 SSG Coating of *P. sesostris* Process

Ti-Sm-O bearing coatings were deposited using the SSG method using a D1 robotic coating system explained in CHAPTER 2 on page 27. Coatings were applied to clean dry wing segments clipped to the wall of a glass reaction chamber. Each SSG deposition layer carried out by: i) immersing the wing segment in 25 mM mixed alkoxide precursor of 99.25% at Titanium isopropoxide and 0.75%at Samarium isopropoxide (Alfa Aesar, Ward Hill, MA, USA) in anhydrous isopropanol (99.8+% purity, Acros Organics, Geel, Belgium) for 5 min to

allow for chemisorption of Sm-Ti-O bearing layer, ii) rinsing three times with isopropanol (99.5+% purity, BDH, PA, USA) to remove any physisorbed precursor, iii) immersion in 60%v DI water in isopropanol for 5 min, to allow for hydrolysis of alkoxide layer, iv) rinsing 3 times with isopropanol and v) drying with warm air from a heat gun for 5 minutes.

This process (alkoxide incubation, isopropanol rinse, DI incubation, isopropanol rinse, drying) was repeated for 25, 50, 75, 100, 125, 150, and 175 cycles to apply a Sm-Ti-O bearing coating. The process is represented in Figure 23.

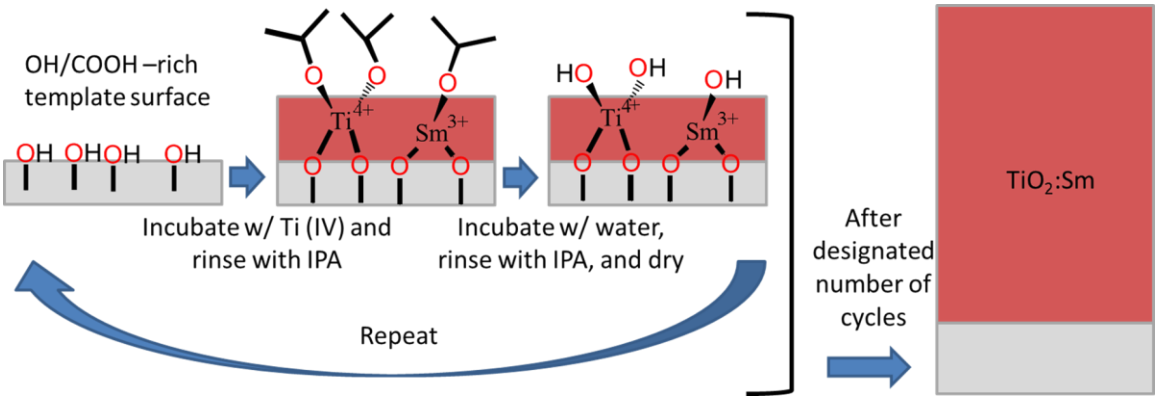

Figure 23: A schematic representation of the SSG process for deposition of a mixed precursor solution of titanium(IV) isopropoxide and samarium (III) isopropoxide.

3.3.4 Organic Removal and Conversion to Oxide Replica

Inorganic scales were created by scraping individual coated scales off of coated butterfly wing sections with a scalpel (36325A63, McMaster Carr, PA, USA) with a #15 blade. Samples were clipped (Staples® Small Satin Silver Metal Binder, MA, USA) between two polished (2.54 x 2.54 x 0.159 cm) fused quartz plates (Technical Glass Products, OH, USA) and then heated in an MgO crucible

in a tube furnace (Lindberg Blue M, Thermo Fisher Scientific Inc., MA, USA) at 120°C/hr to 600°C and held at temperature for 6 hr in air to allow for combustion of the chitin and crystallization of the titania doped with samarium. The furnace was then cooled at 120°C/hr to below 100°C before removal of the sample from the furnace.

3.3.5 Morphology, Phase and Chemical Analyses

Standard SEM, EDS, XRD and optical were utilized to characterize the structure retention and purity of coating. The microstructure of uncoated substrates, SSG-coated substrates, and all inorganic replicas of substrates were imaged with a field-emission scanning electron microscope (1530 FESEM, Carl Zeiss, NY USA). The chemical composition was evaluated with an energy dispersive X-ray spectrometer (EDS) (INCA 7426, Oxford Instruments, UK) which was used in combination with the above SEM.

For samples sputtered with gold, a Quorum Q150T ES (Energy Beam Sciences, INC., CT, USA) sputter coater was utilized to sputter gold for 60 seconds at 20 mA. Cross-sections of samples were created by milling via focused ion beam (FIB) milling (Nova Nanolab 200 FIB/SEM, FEI, OR, USA).

Phase identification of replicas was evaluated using X-ray diffraction (XRD) analysis. XRD was conducted using an X'Pert Pro Alpha-1 diffractometer (PANalytical B.V., ALMELO, Netherlands) with monochromatic Cu Ka1 (1.540598 Å) radiation from a 1.8 kW (45 kV, 40 mA) X-ray tube filtered via a symmetrical Johannson monochromator and detected by an X'Celerator detector. The source was limited by a 1° fixed anti-scatter slit, a ½° programmable divergence

slit, and a 15 mm mask. The diffracted x-rays were subject to a 0.04 radian soller slit and a 5.5 mm anti-scatter slit before the X'Celerator detector. Diffraction specimens were placed on B doped p-type Si zero background plate (MTI Corp, CA, USA). The sample support was rotated at 8 sec per revolution.

3.3.6 Control of UV Illumination

Imperative to the color mixing experiments is the ability to control the intensity of the UV and WL illumination. The WL can be reliably modulated with the use on a 0.3 Neutral Density Filter (Thorlabs, Inc., NJ, USA). The UV light could not be modulated in such a way based on the geometry and the need for NDFs that have good range in the UV. To control the intensity of the UV light (BLS-LCS-0365-02-22, Mightex System, Pleasanton, CA, USA) an Arduino microcontroller (Uno R3, Arduino, Ivrea, Italy) was connected to a computer and the LED control box (SLC-MA02-U, Mightex System, Pleasanton, CA, USA). The Arduino was controlled using a program written in the LabVIEW language.

The LabVIEW program was designed to control a PWM DIO output of an Arduino Uno board. The program was designed with an input to define any integer from 0 to 100, but also with three presets to allow for quick adjustments in the intensity during testing, see Figure 24.

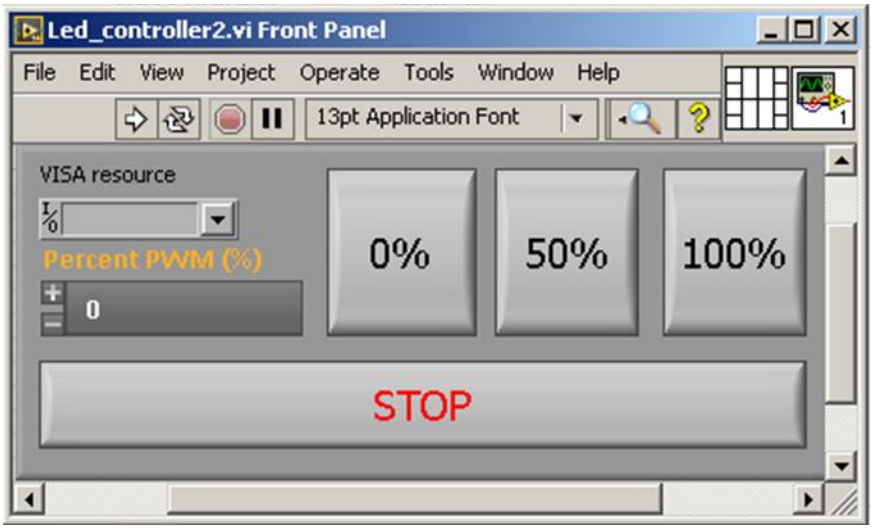

Figure 24: Front Panel of LED controller program. This program allows the user to control the PWM output of an Arduino board from 0 to 100%.

The LED control box receives the PWM 5V signal from the Arduino and delivers the same intensity of UV light. To confirm that this system was working, the PWM output was varied from 0 to 100% with the UV light illuminating a precipitate photoluminescent particle of TiO_2:Sm. The photoluminescence was measured using the procedure described below. The intensity of the PL was measured at the main peak for TiO_2:Sm which is at 613 nm.

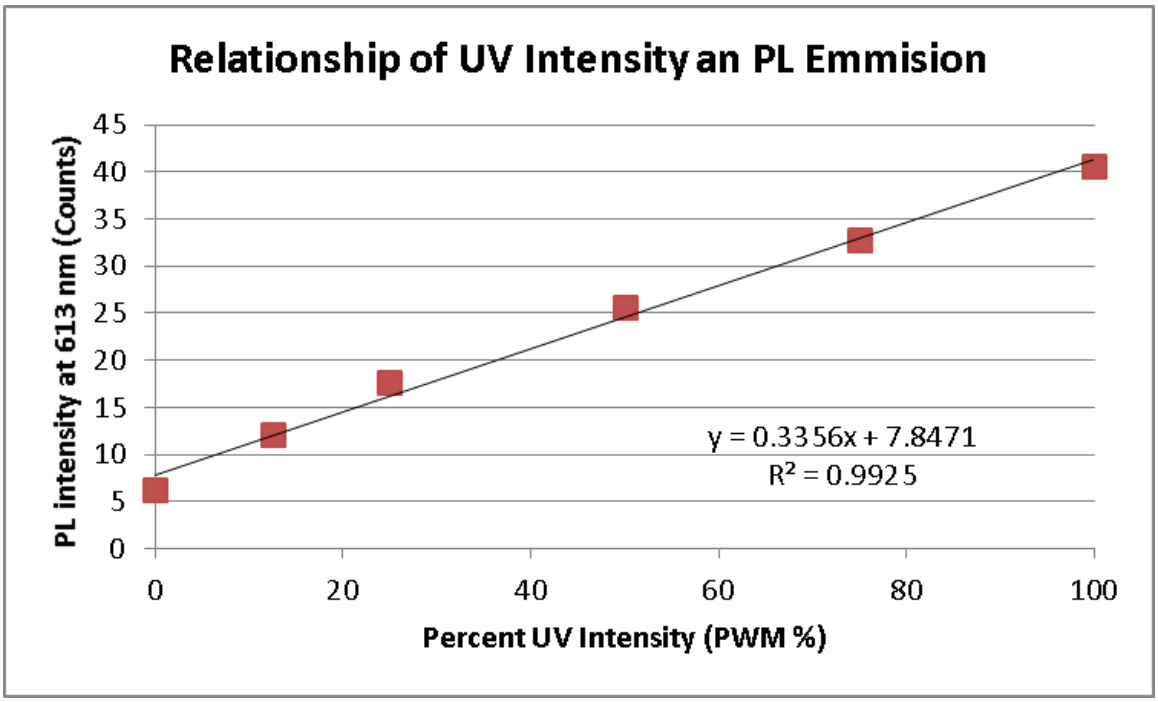

Figure 25: PL intensity of TiO_2:Sm particle with varying intensity of UV light to confirm the linearity of the emmision with PWM %.

Figure 25 shows that there is a linear trend between the PL intensity of the TiO_2:Sm and the UV illumination from the LED light source. This allows for the intensity of the emission to be set from the computer program.

3.3.7 Fluorescence Analyses

Fluorescence measurements were performed using an Olympus BX60 (Olympus America, Inc., PA, USA) upright microscope. Spectral measurements were acquired with a SEE 1000 microscope spectrometer (SEE Science, MA, USA) attached to the microscope camera port with software from Craic Technologies (Version 4.3.1, Craic Technologies, CA, USA). Spectra were acquired with an Olympus MPlan FL N 50X objective (0.80 numerical aperture) using a 6 µm x 6 µm spot size. For this experiment, a fluorescent filter cube (Chroma Technologies, VT, USA) was used with an excitation filter to transmit 325 – 375 nm (full width at half

maximum), a dichroic mirror with half-maximum wavelength at 415 nm and the emission long pass filter enabling transmission above 425 nm (half-maximum wavelength).

3.3.8 Optical Analyses

Optical measurements were acquired using an Olympus BX60 (Olympus America, Inc., PA, USA) upright microscope. Images were gathered with a Nikon D300 (Nikon USA, NY, USA) attached to the camera port. Spectral measurements were acquired with a SEE 1000 microscope spectrometer (SEE Science, MA, USA) attached to the microscope camera port with software from Craic Technologies (Version 4.3.1, Craic Technologies, CA, USA). Images and spectra were acquired with an Olympus MPlan FL N 50X objective (0.80 numerical aperture) using a 6 μm x 6 μm spot size. For bright field (BF) white light (WL) illumination, a halogen lamp (Olympus America, Inc., PA, USA) was used. A diffuse reflectance standard (WS-1-SL, Ocean Optics, FL, USA) was used as the WL standard.

Large area optical and FIB-milled single scale optical measurements were acquired using a Keyence Digital Optical Microscope (VHX 600, Osaka, Japan). For large area images the VH-Z20R objective was used and has a range from 20X to 200X. For single scale images, the VH-Z250 which has a range from 250X to 2500X. The working distance of this microscope can be digitally controlled so that composite images can be created for structures that span the focal plane. To capture images of individual scales it was necessary to use the composite image capabilities of the microscope. Generally images could be captured in 10 stacked images. The white balance for each image was set by imaging a

diffuse reflectance standard (WS-1-SL, Ocean Optics, FL, USA) in bright field imaging mode with the intensity of the halogen lamp set based on the intensity required for the sample. With the WL intensity set, it remained constant for all other images.

For images of large wing sections, the wing section was sandwiched between to glass slides (16004-418, VWR, PA, USA) because the entire wing segments tend to curl after coating. Sandwiching between slides held the wings segments flat during imaging.

3.3.9 Multimodal Coloration Analyses

The structurally reflected color of the template replica needs to be significantly different from that of the selected photoluminescent emission. If the colors are not significantly different, then there is no possibility of detecting color mixing. To be able to demonstrate dynamic coloration without interfering with the reflection spectrum due to scattering of the excitation light, a PL material needs to be selected that requires excitation in the ultraviolet or infrared regions of the electromagnetic spectrum. The PL emission spectrum of the material can be determined through fluorescence microscopy.

To perform the key color mixing experiment, the structurally-colored, PL biological structure were evaluated using a fluorescence microscope with a custom light source and filter cube. The light source was a standard halogen white light with a UV source coupled along the same light path using a beam combiner. The UV light source was filtered with a 400 nm short pass (SP) filter to remove any light in the visible light spectrum that would alter the color of the

reflected light through scattering off of the sample. The white light was unfiltered, but still passed though the beam combiner and filter cube. To assure that the light path does not significantly affect the reflection spectra of the sample, it was also tested under bright light illumination. Figure 26 shows the optical setup for interrogating the sample along the same light path with UV and WL.

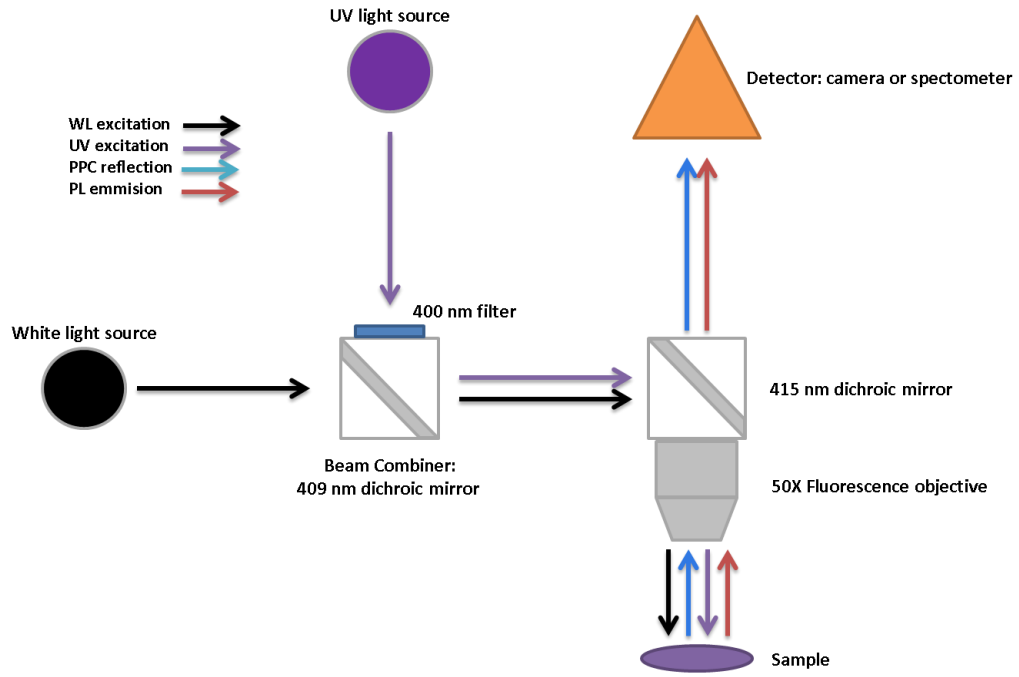

Figure 26: The light path in a fluorescence microscope during evaluation of multimodal color mixing (reflection + PL) by a PL replica of a structurally colored biological structure.

For gathering the optical spectra for the three possible illumination conditions (WL only, UV only, UV + WL), the two conditions using WL was gathered in reflectance mode whereas the UV only illumination was gathered in fluorescence mode. The reason for this is based on the way each is calculated by the spectrometer, see Equation (12) and Equation (13).

$$S_{Fluorescence} = S_{Sample} - S_{Dark} \quad \textbf{(12)}$$

$$S_{Reflectance} = \frac{S_{Sample} - S_{Dark}}{S_{Reference} - S_{Dark}} \quad \textbf{(13)}$$

In these equations, S_{Dark} is the spectrum gathered when the light path is closed to the spectrometer, $S_{Reference}$ is the spectrum of a white standard under WL illumination and S_{Sample} is the spectra gathered from the sample under the respective conditions of the test. Equation (12) describes the calculation for gathering a fluorescence spectrum ($S_{Fluorescence}$) where the dark scan spectrum (S_{Dark}) is subtracted from the sample spectrum (S_{Sample}). In Equation (13), the reflection spectrum ($S_{Reflectance}$) is calculated by dividing the difference in the sample spectrum and dark spectrum by the difference in the reference spectrum ($S_{Reference}$) and dark spectrum. The fluorescence spectrum is reported in counts whereas reflectance is reported in percent relative to the reference scan, so the two spectral intensities cannot be compared, but the relative intensities can be compared. When the white light illumination is changed, the reference scan is no longer valid and thus Equation (13) cannot be used under conditions where the WL source is off. To test if Equation (13) can be used when the UV and white light are both illuminating the sample, a test sample with no PL was evaluated under WL and then UV + WL conditions. Because of the filtering of the UV light source and the dichroic mirror, there was no difference in the two spectra.

3.4 Results & Discussion

3.4.1 TGA Analyses and Selection of Coating Technique

The LbL coating methods investigated for this research were atomic layer deposition (ALD) and SSG. A temperature of 250˚C was selected for use in the ALD, because it is a suggested deposition temperature of TiO_2 and Er_2O_3 from the ALD manufacturer (Ultratech). Sm_2O_3 has been reported as requiring 300˚C for deposition.[13]

Based on TG analysis of the *P. sesostris* butterfly, shown in Figure 27, when the sample was heated at 1˚C/min to 250˚C, there was between 13% and 23% weight lost at 250˚C, depending on the atmosphere, which increased to 24% and 35% after 1 hour at temperature.

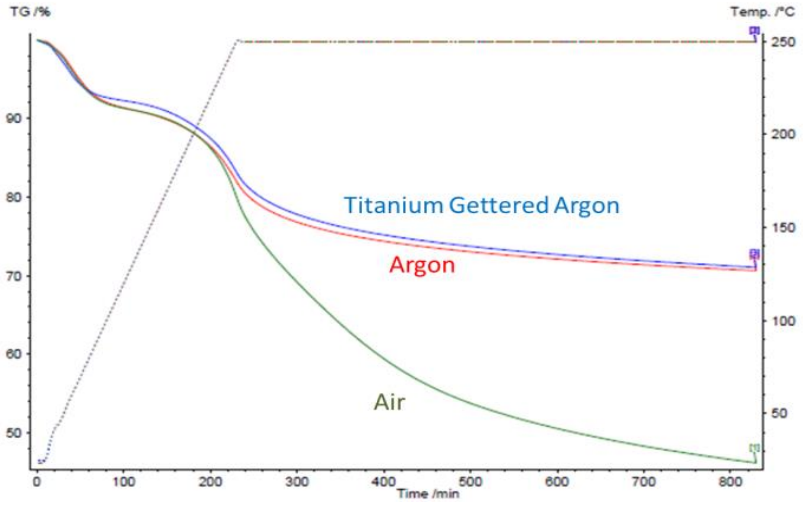

Figure 27: TGA plot of percent weight vs. time in minutes for combustion/pyrolysis of *P. sesostris* dorsal wing scales in Air, Argon and Titanium gettered Argon.

Samples fired at 250˚C in an inert atmosphere after one hour showed visible charring of the chitin. This severely limited the usefulness of ALD. Although it is

possible to reduce the titanium deposition temperature, the lanthanide deposition has not been shown at lower temperatures. Additionally, the current available ALD setup is limited by the precursors available and the inability of mixing such precursors. The mixing of precursors is required to obtain the very low doping required of lanthanides in TiO_2 which are less than 1% for erbium and samarium. [14, 15] The solutions cannot be mixed because the precursors all have different partial pressures, and so the lanthanide precursors need to be heated to a much higher temperature than the titanium precursor (Ultratech). While the materials could be deposited by a full layer of lanthanide followed by many TiO_2 layers, this would not be preferred due to the heterogeneity of the dispersion of the lanthanide in the TiO_2 matrix. The high local concentration of lanthanide in the absence of prolonged thermal treatment for interdiffusion would quench the PL. This makes ALD an unattractive approach.

Surface sol-gel offers solutions to most of the problems with ALD. The deposition temperature is not a problem, because SSG can be conducted at room temperature. SSG also is easier with regard to precursor handling because the precursors are liquid in standard glass bottles instead of in sealed steel cylinders. SSG also allows for easy mixing of the precursor alkoxide solutions. Because the solutions are well mixed, and if the precursor deposition rates are known, the deposit should then be uniformly mixed as well. The composition still needs to be verified with ICP-MS.

A drawback to SSG is that the process as currently conducted is slower than ALD. One SSG coating cycle currently takes approximately 20 minutes opposed to that of ALD which takes less than a minute. Previous researchers

have used a manual dipping method, which required the researcher to personally coat each sample by hand. This was time consuming, considering that some samples required as many as 200 layers which involved over 66 hours of constant labor. Hence, an automated coating system was developed which is described in CHAPTER 2 on page 27. This system greatly reduced the human time required for coating and has been shown to be robust enough to work continuously for up to 70 hours (the longest time examined to date).

3.4.2 Dopant Quantity Effect on Photoluminescence

Determination of the appropriate dopant quantity was achieved through an initial literature review which suggested less than 1% mol of samarium with respect to titanium atoms.[15-17] Precipitation of solutions of mixed precursors of compositions of 0.25%, 0.5%, 0.75% and 1% were obtained and the resulting precipitates were fired at 600 ˚C for 4 hr and intensities were measured. The precipitate from the 0.75% solution produced the greatest emission. More of the 0.75% precipitate was fired at 500 ˚C for 4 hr, 500 ˚C for 6 hr, 600 ˚C for 6 hr and 800 ˚C for 2 hr all were tested with 365 nm illumination and the sample that was fired for 6 hr at 600 ˚C had the greatest emission intensity.

3.4.3 Firing Conditions Effect on Photoluminescence

Initial analysis was performed on the effect of firing conditions on the photoluminescence of titanium oxide doped with samarium. This analysis was carried out to inform the optimal conditions for creating intense photoluminescence in TiO_2:Sm replicas of *P. sesostris* dorsal wing scales. Previous

research by Vernon et al. has investigated SSG coatings of tin-doped titania for creating high index replicas. In this research they used firing conditions of 450°C for 4 hr.[8] These firing conditions have proved to replicate the photonic crystal of the *P. sesostris* although these conditions may not produce significant PL from the samarium-doped titania. Cao et al. have found that powders of TiO_2:Sm produce the greatest PL intensity when fired at 650 °C for 3 hr.[15] To find optimal conditions for retention of the photonic crystal and for intense PL a range of firing conditions were performed on precipitated TiO_2:Sm.

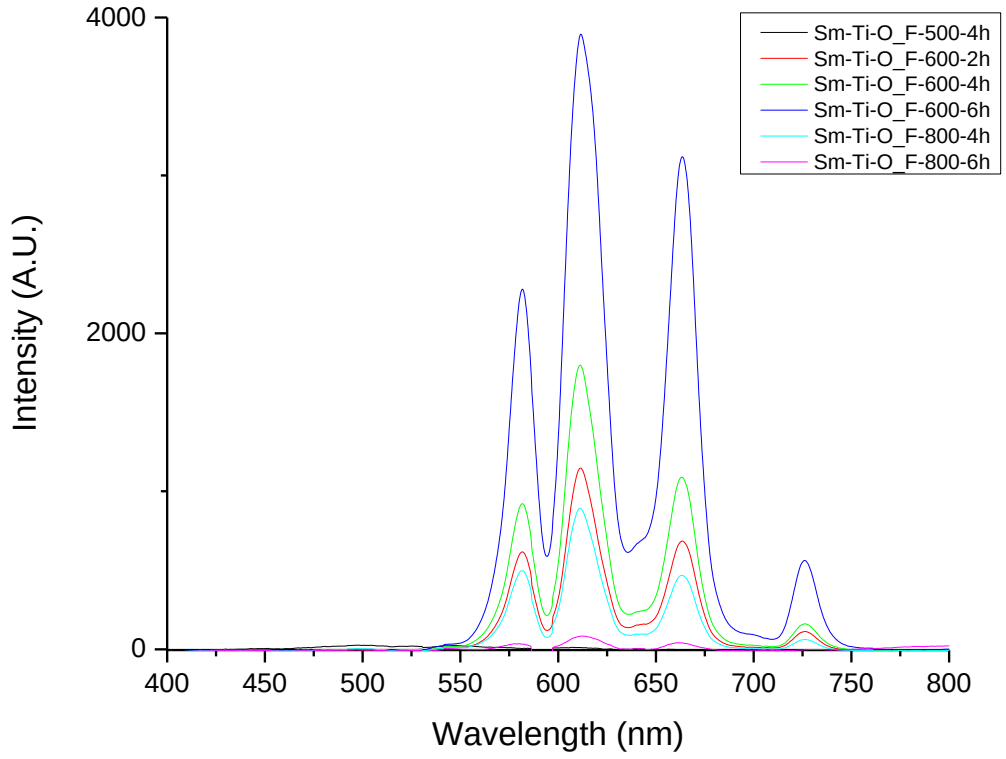

Figure 28: Photoluminescence spectra of precipitates of Ti-Sm-O with various firing conditions showing the change in intensity of the PL.

Figure 28 shows that the PL of the TiO_2:Sm increased as the time and temperature were increased until reaching a maximum at 600 °C for 6 hr. For temperatures greater than 600 °C the PL was greatly decreased.

3.4.4 Shape Preservation and Coating Quality

The PL material selected was titania doped with samarium. Prior work by J. Vernon, and subsequent verification experiments, showed that the reflection spectra of 100 layer TiO_2 fired *P. sesostris* green scale replicas exhibited a predominant peak associated with a blue color. This was appropriate evidence to investigate the reflection spectra of Sm: TiO_2, which, if consistent with the TiO_2 replication spectra would color mix well with the reddish emission of the PL Sm: TiO_2. Figure 29, shows the reflection spectra of *P. sesostris* green scale replica after 175 layers of Sm: TiO_2 with a peak reflection in the blue-green at 512 nm ±3 nm which worked well for color mixing with the reddish PL of Sm: TiO_2.

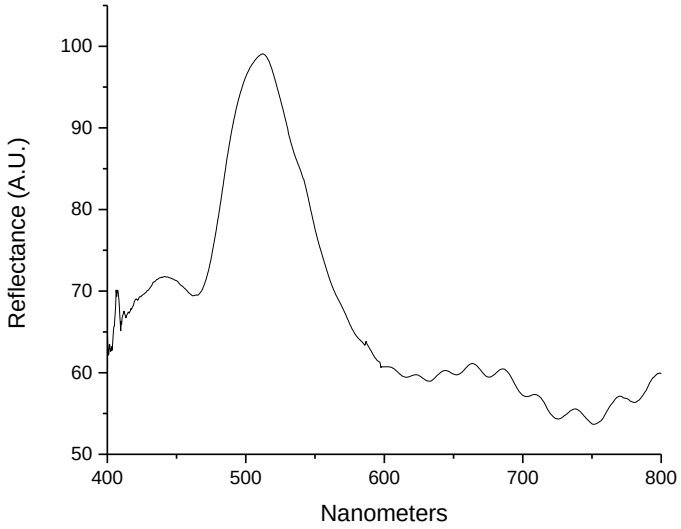

Figure 29: Reflection spectra of 175X TiO_2:Sm layer coated P. sesostris replica illuminated with white light only showing reflectance from the replicated gyroid structure.

Free standing replicas of *P. sesostris* butterfly dorsal wing green scales have been fabricated using a LbL SSG approach in which 0.75%mol Sm was doped directly via solution mixing into a titanium oxide matrix. In this fabrication method, the Sm is deposited at the same time as the Ti is being deposited leading to a well dispersed dopant in the host TiO_2 matrix. This is important in the creation of PL replicas, due to the concentration quenching that occurs when lanthanide atoms are too near each other. This can either be due to too high of a concentration upon deposition or it can be due to a local density of Sm atoms. To achieve PL replicas, the coated *P. sesostris* dorsal wing green scales were fired in air to 600 ˚C for 6 hours with a ramp rate of 2 ˚C/min. The firing treatment allowed for full combustion of the native *P. sesostris* chitin while crystallizing the Ti-Sm-O amorphous matrix.

To verify the color being reflected was indeed coming from the structure, some TiO_2:Sm coated *P. sesostris* replicas were mounted on tungsten needle

(Model 7A probe, Micromanipulator Company, NV, USA) and were then FIB milled to remove the ridge structure of the *P. sesostris* replica to expose the gyroid structure underneath. Figure 30 shows an example of a 150X TiO_2:Sm coated *P. sesostris* replica after FIB milling showing the retention of the gyroid structure.

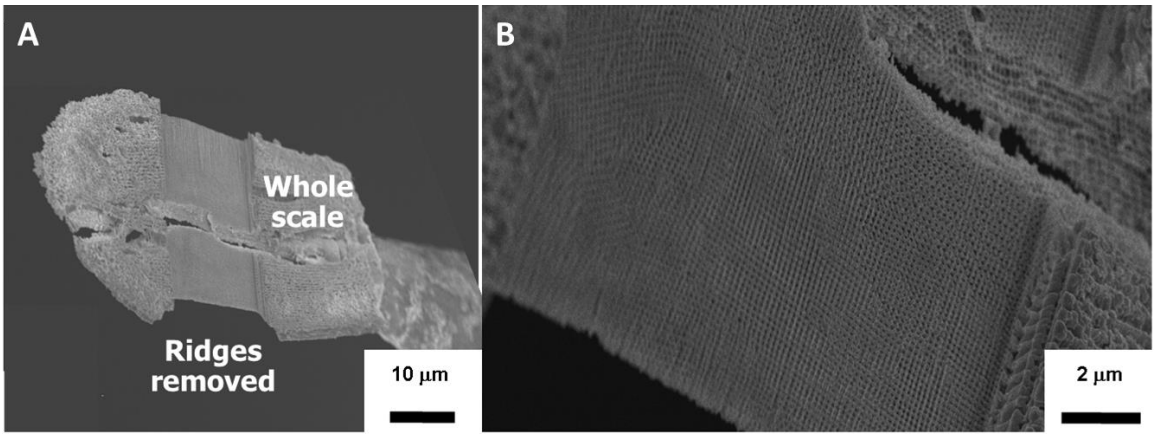

Figure 30: SEM micrograph of FIB milled 150X TiO_2:Sm layer coated P. sesostris replica. A) View of full butterfly ling scale and B) zoomed in region of FIB milled region displaying the replicated gyroid structure.

3.4.5 Effect of SSG Precursor Concentration on As-Coated Color Change

For different applications of SSG, different concentrations of precursors have been used. Because different precursors have different reaction rates with water this is not surprising, but previous research has found concentrations for deposition that are adequate although not necessarily ideal.[7, 8] Previous research by John Vernon for coating the *P. sesostris* dorsal wing scales used a deposition concentration of 25 mM. This concentration was used for coating of butterflies in this research with Sm-Ti-O bearing coatings with similar results. To evaluate if the concentration could be reduced and still produce the same

results, the concentration of the coating solution was reduced to 12.5 mM and *P. sesostris* butterflies were coated in the same fashion as before.

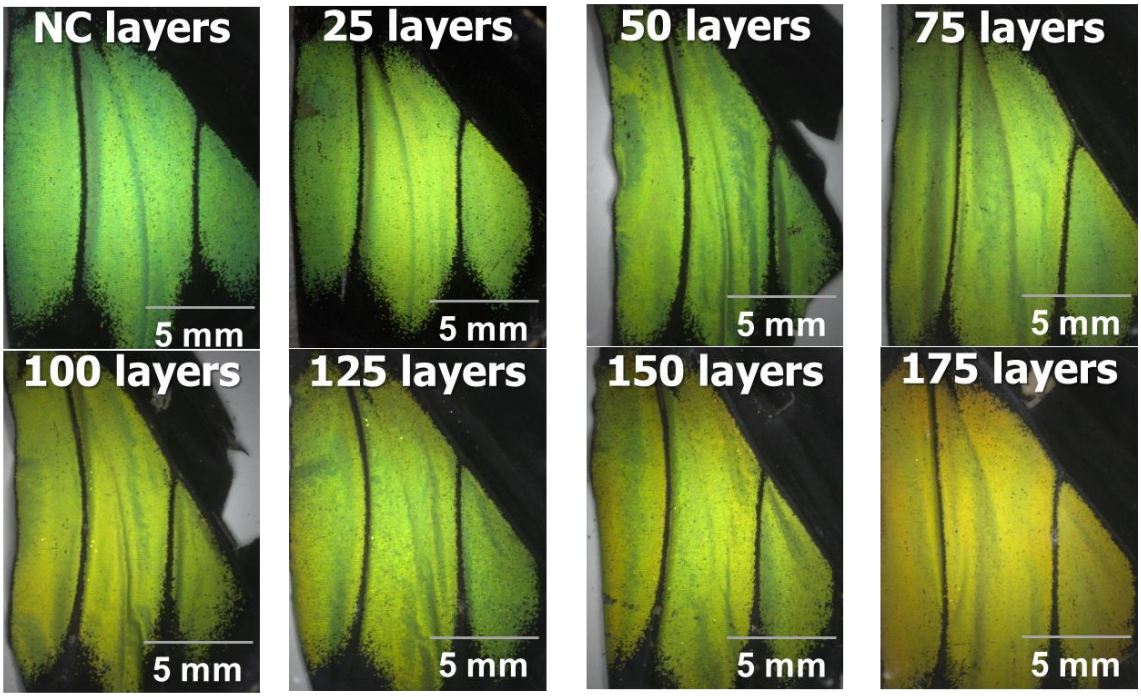

Figure 31: Optical Images of Surface sol-gel 12.5 mM Ti-O-coated P. sesostris green dorsal scales in increments of 25 layers from no coating to 175 layers.

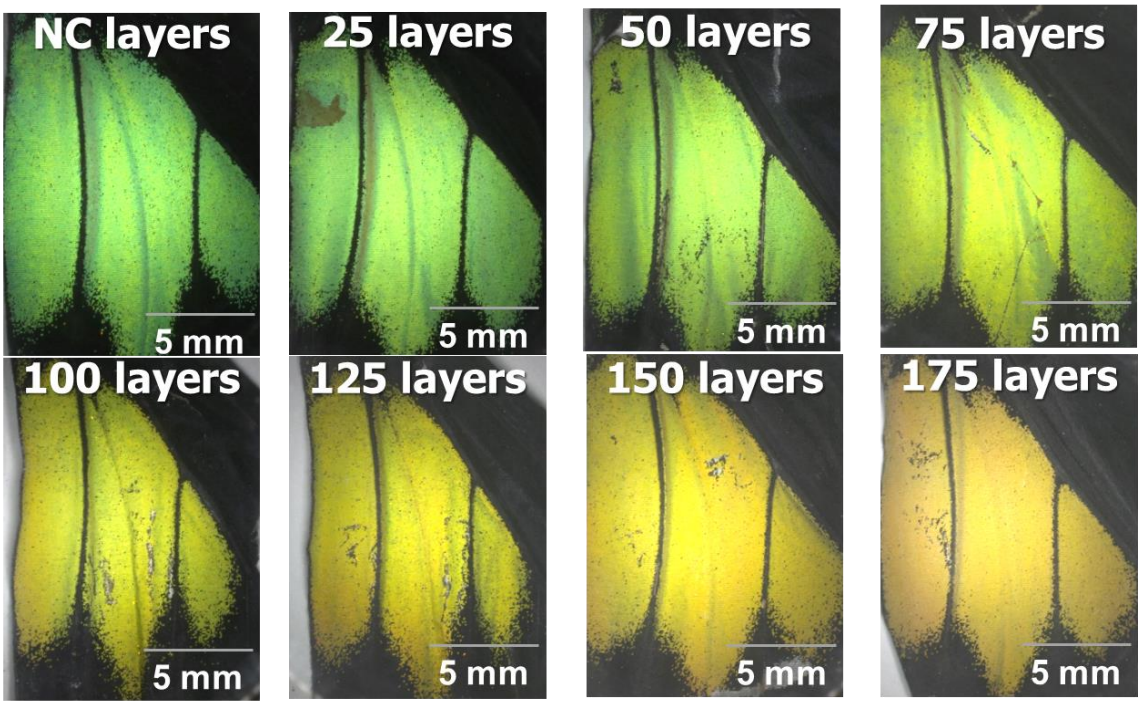

Figure 32: Optical Images of Surface sol-gel 25 mM Ti-O-coated P. sesostris green dorsal scales in increments of 25 layers from no coating to 175 layers.

Figures Figure 31 and Figure 32 show the relative change of the *P. sesostris* dorsal wing sections reflected color with deposition of SSG with 12.5 mM and 25 mM solutions, respectively. Figure 32 shows a significant increase in the red shift of the reflected color as compared to Figure 31. This suggests that there is significantly less Ti-O being deposited per layer when the solution concentration is 12.5 mM as compared to 25 mM. To be consistent with previous research on coating the *P. sesostris* with SSG, all coatings used 25 mM solutions for testing.

3.4.6 Static Reflection Measurements

The *P. sesostris* dorsal wing green scales have been replicated using a few as 25 layers of Sm: TiO_2 and as many as 175 layers. Although the precise coating

thickness has not been measured, from analog pure titania deposition each layer of Sm-Ti-O may be approximately 1 Å.

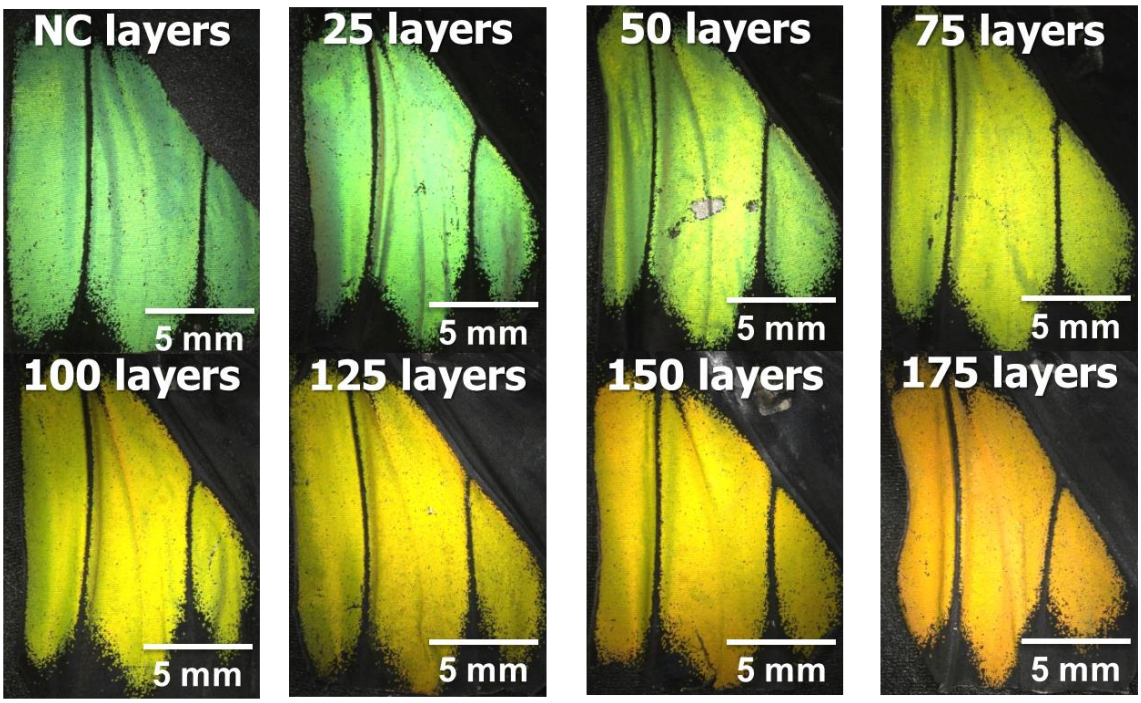

Figure 33: The static tuning of the peak reflection of the as coated P. sesostris through additional layers of Sm-Ti-O

Each additional layer of Sm-Ti-O that is applied to the poly photonic crystal (PPC) increases the filling fraction of the structure and shifts the peak reflected wavelength into the red. During the first 25 layers this effect is almost inappreciable but as more layers are added the effect is clearly apparent. Figure 34 shows the static tuning of reflected color by increasing the filling fraction of the native *P. sesostris* butterfly dorsal wing green scales through increased number of layers.

The peak reflected color of the replica TiO_2:Sm is likewise shifted to the red as more layers are applied to the native structure. Replicas with less than 50

layers have limited structural color and are dominated by scattered light. Near 75 layers, the peak reflected light in the replica is vaguely blue and as more layers are added the color gradually shifts into the blue-green. The effect of coating thickness on reflection spectra can be seen in Figure 34. As the number of coatings increased, the peak reflected wavelength shifted nearly 100 nm.

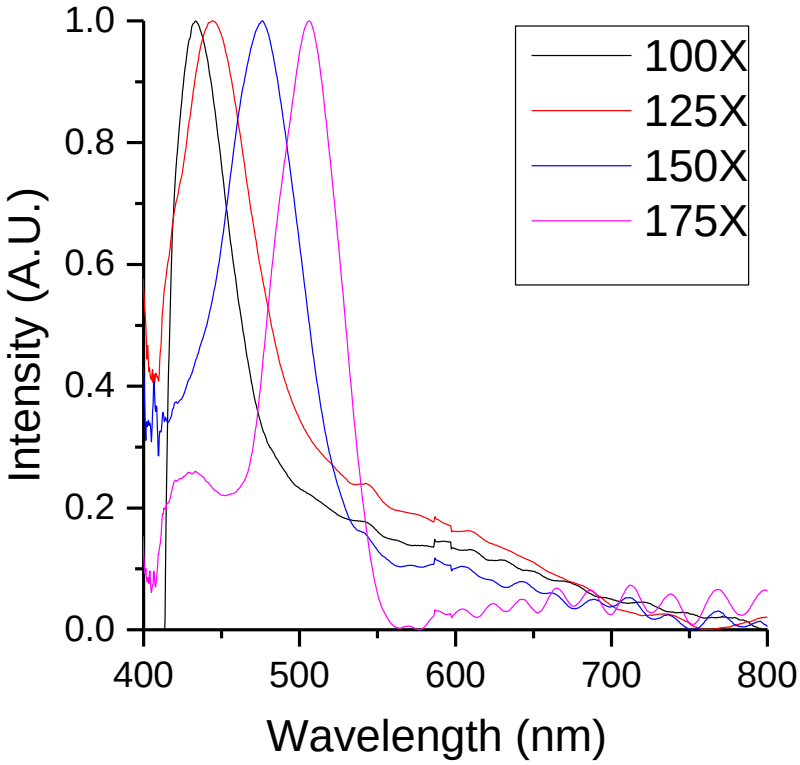

Figure 34: Peak reflection spectra of Sm: TiO_2 *P. sesostris* replicas with 100, 125, 150 and 175 layers showing a progressive increase in the static reflection peak with increase in layer number.

Individual *P. sesostris* replica scales were mounted on needles and were subsequently etched with a focused ion beam (FIB) to expose the PPC and then imaged using an SEM.

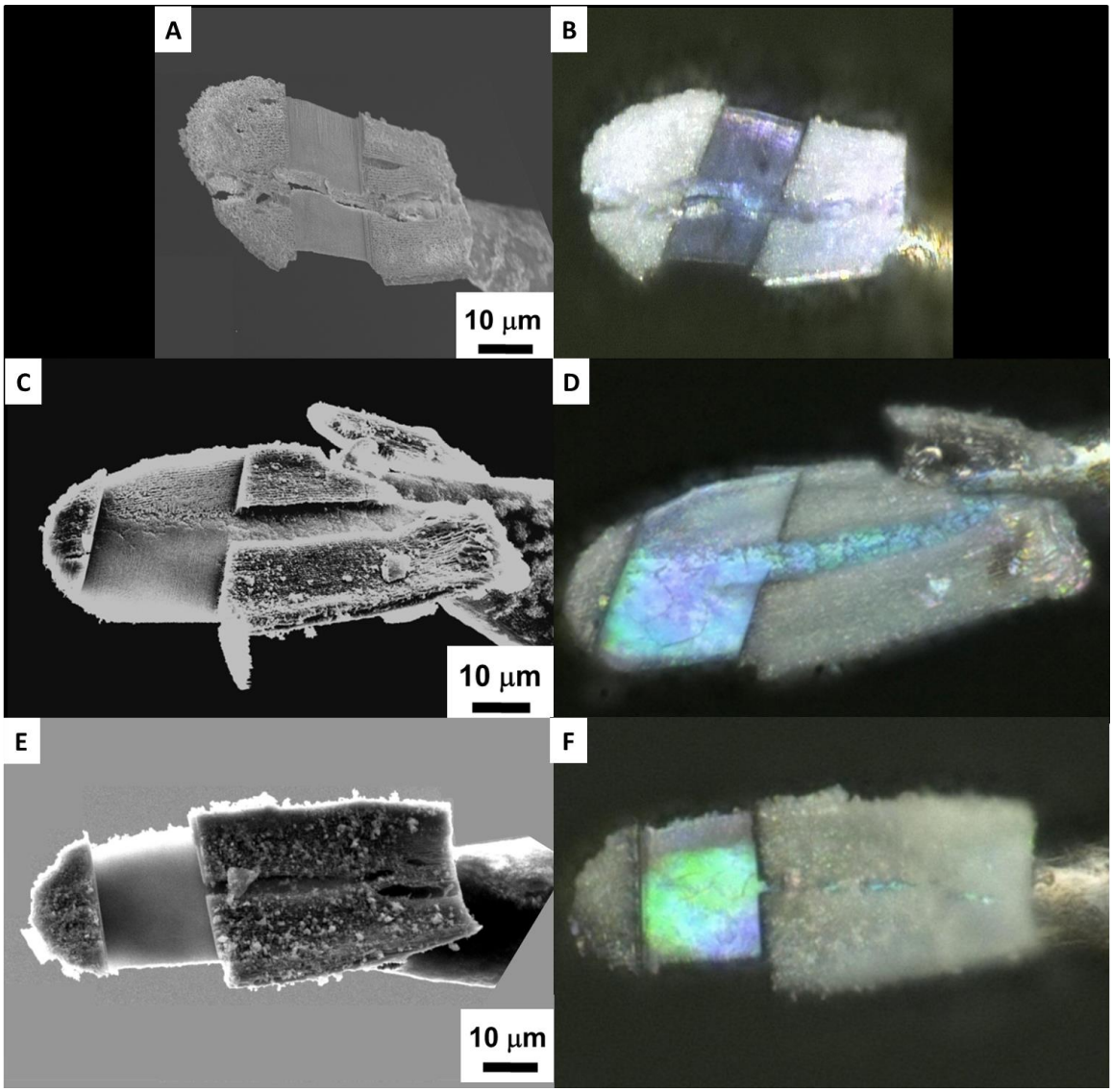

Figure 35: SEM micrographs and optical images of *P. sesostris* wing scale replicas with A/B) 100 cycles, C/D) 125 cycles, and E/F)150 cycles of a 25 mM mixture of 0.75%at Sm(III) isopropoxide and 99.25%at Ti(IV) isopropoxide. In all images, the ridge structure has been etched away using a FIB.

Figure 35 shows the incremental color change in individual *P. sesostris* wing scale replicas.

3.4.7 Multimodal Coloration Measurements

Unaffected by the static structural coloration of the *P. sesostris* replica is the photoluminescent response of the Sm: TiO_2 replica material. From 25 layers to

175 layers of Sm: TiO_2, all replicas exhibited the same characteristic luminescence when stimulated with 365 nm light (see Figure 36). This corresponded to the PL emission spectrum of Sm^{3+} in titania reported previously [15].

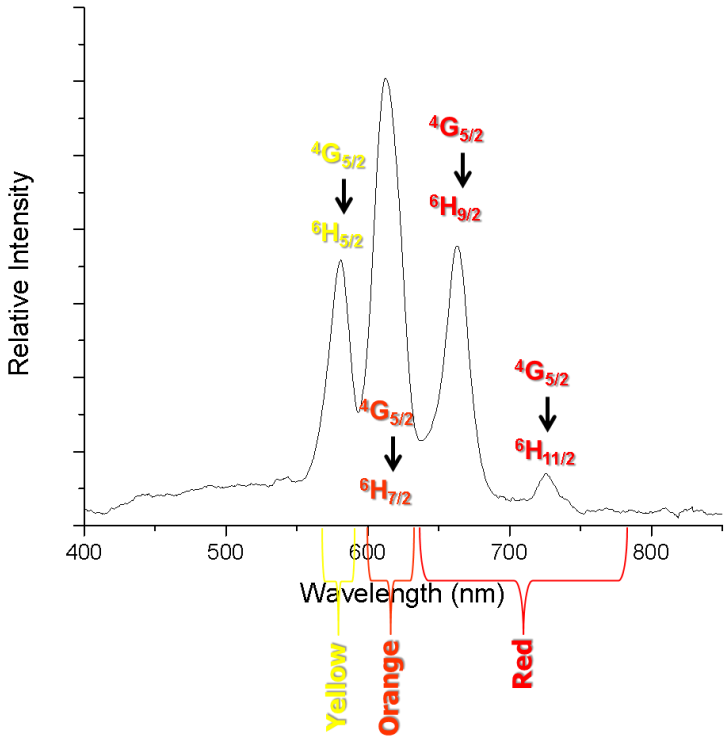

Figure 36: PL detected from a 75 layer TiO_2:Sm *P. Sesostris* replica scale when excited under 365nm light. The spectra shows characteristic emission lines for Sm-doped titania.

Both the PL of the replica material, Sm: TiO_2, and the structural color from the replicated PPC have been shown independently through white light and UV illumination, respectively. The spectra of the two color sources do not overlap which suggests that there is the possibility for color mixing. To maintain the proper reference spectra and to keep the WL and UV illuminations constant though the various tests, the tests were performed in the order: WL only, UV +WL, UV only.

When the level of WL had been selected, the white standard was imaged as the reference, this was followed by closing the shutter and collecting a dark scan. The sample to be evaluated was then located and the spectra was gathered in reflectance mode. Next, the UV light source was added to the illumination and the spectra was gathered again in the reflectance mode. Then the WL source was turned off and the PL spectra was gathered in fluorescence mode. Figure 37, below shows the three methods of illumination, the three spectra gathered, the three corresponding optical images of the full scale and three optical images of the area from which the spectra was gathered.

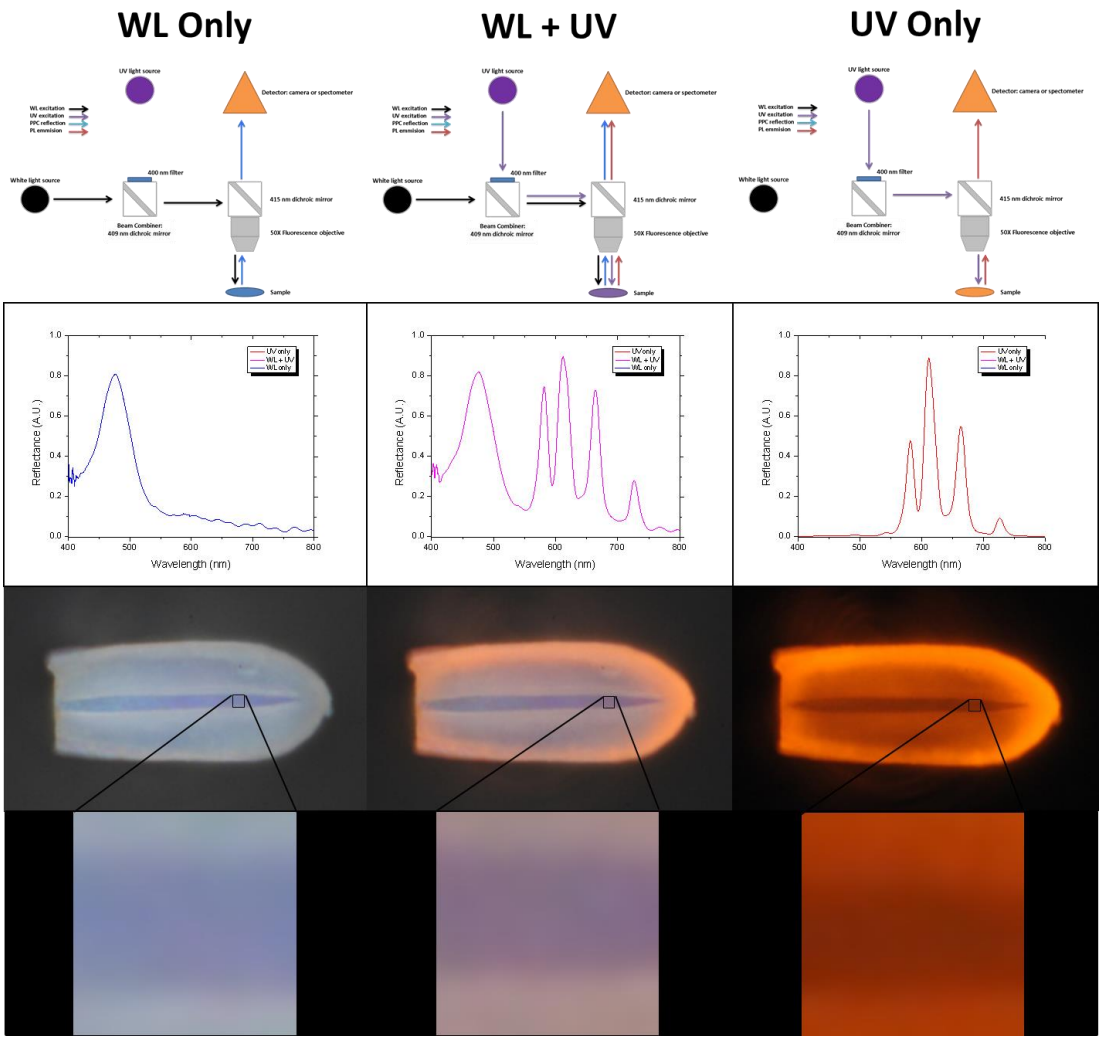

Figure 37: Demonstration of multimodal coloration in a Sm: TiO_2 *P. sesostris* replica with 150 SSG layers. The three types of illumination are displayed from left to right: WL only, WL + UV, and UV only. Top to bottom are: the method of illumination, the gathered spectra, and the optical image for each method of illumination with overlaid on the optical images is a 6 µm X 6 µm square representing the location the spectral data was gathered and the last row is the optical image of the location the spectra was gathered. The spectral data was gathered from the exact same location with only change in the illumination method.

To demonstrate that the optical reflectance of the structural color is not affected by the UV illumination, spectra gathered from all three modes is presented in Figure 38. This shows no change in the reflection spectra in the blue region due to the PPC when the UV illumination is added to the WL illumination.

The graph shows the characteristic PL spectra of samarium doped in titania in the color mixed spectra as well as in the UV only spectra.

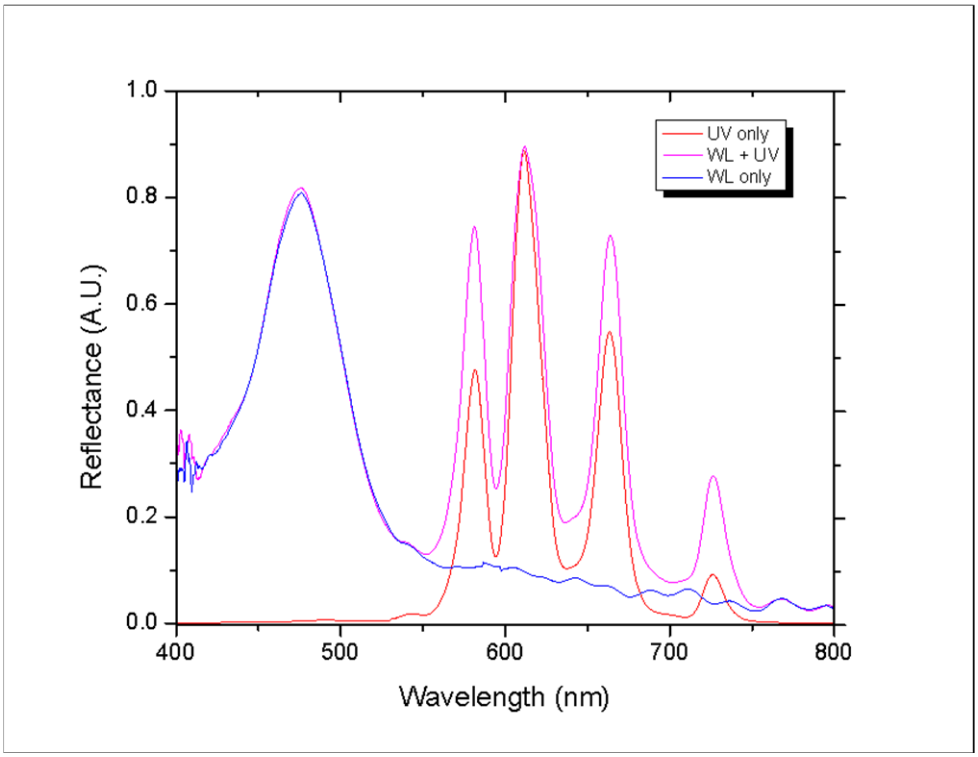

Figure 38: Individual spectra gathered from three illumination conditions (WL, UV+WL, UV) on a Sm: TiO_2 P. sesostris replica with 150 SSG layers.

3.5 Concluding Remarks

An intricate 3D biological structure was replicated with a conformal LbL SSG coated method and subsequent thermal treatment. It was demonstrated that the static reflection color can be tuned by controlling the number of deposition layers of the SSG coating. This work has shown that it is possible to fabricate freestanding inorganic photoluminescent replicas of biological structures that exhibit multimodal coloration. These structures have been shown to have both structural color which was retained during the replication process

along with PL coloration due to the replication material, Sm: TiO_2. Future work could investigate using multiple PL materials to produce optically active structures that could produce the entire visible spectrum.

3.6 References

[1] G. Wang, Y. Fang, P. Kim, A. Hayek, M. R. Weatherspoon, J. W. Perry*, et al.*, "Layer-By-Layer Dendritic Growth of Hyperbranched Thin Films for Surface Sol-Gel Syntheses of Conformal, Functional, Nanocrystalline Oxide Coatings on Complex 3D (Bio)silica Templates," *Advanced Functional Materials,* vol. 19, pp. 2768-2776, Sep 9 2009.

[2] M. R. Weatherspoon, Y. Cai, M. Crne, M. Srinivasarao, and K. H. Sandhage, "3D rutile titania-based structures with Morpho butterfly wing scale morphologies," *Angewandte Chemie-International Edition,* vol. 47, pp. 7921-7923, 2008 2008.

[3] M. Srinivasarao, "Nano-optics in the biological world: Beetles, butterflies, birds, and moths," *Chemical Reviews,* vol. 99, pp. 1935-1961, Jul 1999.

[4] F. Cao and D.-X. Li, "Morphology-controlled synthesis of SiO2 hollow microspheres using pollen grain as a biotemplate," *Biomedical Materials,* vol. 4, Apr 2009.

[5] J. P. Vernon, N. Hobbs, Y. Cai, A. Lethbridge, P. Vukusic, D. D. Deheyn*, et al.*, "3D photoluminescent lanthanide-doped barium titanate structures synthesized by coating and shape-preserving reaction of complex-shaped bioorganic templates," *Journal of Materials Chemistry,* vol. 22, pp. 10435-10437, 2012 2012.

[6] Z. Bao, M.-K. Song, S. C. Davis, Y. Cai, M. Liu, and K. H. Sandhage, "High surface area, micro/mesoporous carbon particles with selectable 3-D biogenic morphologies for tailored catalysis, filtration, or adsorption," *Energy Environ. Sci.,* vol. 4, pp. 3980-3984, 2011.

[7] W. B. Goodwin, I. J. Gomez, Y. N. Fang, J. C. Meredith, and K. H. Sandhage, "Conversion of Pollen Particles into Three-Dimensional Ceramic Replicas Tailored for Multimodal Adhesion," *Chemistry of Materials,* vol. 25, pp. 4529-4536, Nov 2013.

[8] J. Vernon, "Morphology-preserving chemical conversion of bioorganic and inorganic templates," Ph.D. Dissertation, Materials Science and Engineering, Gerorgia Institute of Technology, Gerorgia Institute of Technology, 2012.

[9] C. Cameron, "NATURAL AND ARTIFICIAL FLUORESCENCE ON 3-DIMENSIONAL BIOORGANIC NANOSTRUCTURES," Ph.D. Dissertation, Materials Science and Engineering, Georgia Institute of Technology, Georgia Institute of Technology, 2014.

[10] C. Pouya and P. Vukusic, "Electromagnetic characterization of millimetre-scale replicas of the gyroid photonic crystal found in the butterfly Parides sesostris," *Interface Focus,* vol. 2, pp. 645-650, Oct 2012.

[11] K. Michielsen and D. Stavenga, "Gyroid cuticular structures in butterfly wing scales: biological photonic crystals," *Journal of The Royal Society Interface,* vol. 5, pp. 85-94, 2008.

[12] P. Karrer and A. Hofmann, "Polysaccharide XXXIX. Über den enzymatischen Abbau von Chitin und Chitosan I," *Helvetica Chimica Acta,* vol. 12, pp. 616-637, 1929.

[13] J. Päiväsaari, M. Putkonen, and L. Niinistö, "A comparative study on lanthanide oxide thin films grown by atomic layer deposition," *Thin Solid Films,* vol. 472, pp. 275-281, 2005.

[14] A. Bahtat, M. Bouazaoui, M. Bahtat, and J. Mugnier, "FLUORESCENCE OF ER3+ IONS IN TIO2 PLANAR WAVE-GUIDES PREPARED BY A SOL-GEL PROCESS," *Optics Communications,* vol. 111, pp. 55-60, Sep 1994.

[15] Y. C. Cao, Z. Y. Zhao, J. Yi, C. S. Ma, D. C. Zhou, R. F. Wang*, et al.*, "Luminescence properties of Sm3+-doped TiO2 nanoparticles: Synthesis, characterization, and mechanism," *Journal of Alloys and Compounds,* vol. 554, pp. 12-20, Mar 2013.

[16] A. Bahtat, M. C. M. deLucas, B. Jacquier, B. Varrel, M. Bouazaoui, and J. Mugnier, "IR luminescence decays and radiative lifetime of the I-4(13/2) level in Er3+ doped sol-gel TiO2 planar waveguides," *Optical Materials,* vol. 7, pp. 173-179, May 1997.

[17] V. Reedo, S. Lange, V. Kiisk, A. Lukner, T. Tätte, and I. Sildos, "Influence of ambient gas on the photoluminescence of sol-gel derived TiO2: Sm3+ films," in *Optical Materials and Applications*, 2005, pp. 59460F-59460F-6.

CHAPTER 4: Synthesis of TiO_2 and $BaTiO_3$ Based Pollen Replicas

4.1 Summary

Intricate three dimensional (3D) complex $BaTiO_3$ & $Ba_{1-x}Sr_xTiO_3$, replicas of pollen particles have been synthesized with controlled deposition chemistry through the use of surface sol-gel (SSG) coating and subsequent thermal treatment.

Tunable multimodal adhesion through coupling of structural VDW adhesion and electrostatic adhesion in a pollen replica was shown. A template, coating processes, and post-coating processing conditions were determined to create particles with a high dielectric constant made of nearly phase pure $BaTiO_3$. The 3D structure of the SF template was shown to be reproduced in a consistent manner. Prior work by Dr. Goodwin has shown that various species of pollen can be readily reproduced and that Sunflower pollen in particular is a useful structure to replicate for purposes of adhesion.[1] Sunflower pollen has high aspect echini that allow for simplified VDWs force modeling due to the limited surface contact area.

Replicating pollen has two major differences to that of replicating butterfly wing segments. The first is the structural material. Butterflies are made of chitin and pollen is made of sporopollenin. Both sporopollenin and chitin have an abundance of surface functional groups, with carboxyls on sporopollenin and hydroxyls on chitin that can be utilized for coating. The second major difference important for replication is the size of the pollen particles. SF pollen particles are

approximately 30 micron in diameter which requires filtration to allow for separation from the coating solutions.

The materials and processing conditions used in the replication of the pollen particles were selected to produce high dielectric constant replicas. SEM was used to determine the as-coated and post firing condition of the particle. EDS and ICP-MS were used to determine the presence of components and composition of the coating. XRD was used to characterize the phases of the coatings and Scherer analysis was used to characterize the grain size of the coatings.

4.2 Introduction

Adhesive microparticles play an important role in a variety of developing and mature technologies, including drug delivery, catalysis, water purification, anti-fouling coatings, semiconductor processing, paints, printing, and xerography.[2-9] Models have been proposed to understand the adhesion of spherical particles onto planar surfaces [10-15], and microparticles with non-spherical textured shapes are desired for a number of such technologies. Scalable production of microparticles with controllable surface features in a variety of 3D morphologies and tunable chemical properties remains a challenge.

Pollen particles vary greatly in their size and shape and have a variety of surface morphologies.[16-21] Pollen partiles are also produced in large and reproducible quantities naturally.[22-29] Recently, adhesion measured via AFM has shown that for 3D replicas of pollen made of ferromagnetic hematite (a-

Fe_2O_3)[30] or ferrimagnetic magnetite (Fe_3O_4) show significantly increased magnetic adhesion.[31]

This research is focused on tailoring the attractive forces of intricate 3D particle through replication with a high dielectric material. One method of demonstrating electrostatic adhesion is to apply a voltage between the particle and the surface that it is attracted to. Native sunflower pollen have been converted into intricate 3D replicas via a SSG LbL coating process.[32, 33] Adhesion of replica sunflower pollen was measured via use of an AFM cantilever. An increase in the attraction was observed for the BT replicas when a voltage was applied between the replica and the nickel substrate. By controlling the replica material, the electrostatic adhesion was tailored. Other authors have demonstrated methods to chemically modify pollen [34-41] and other biological structures [42-51] for additional functionality.

Barium titanate is of particular interest due to its use in the electro-ceramic industry for its ferroelectric properties. BT exhibits a cubic to tetragonal phase transition when its perovskite crystal structure is cooled below its Curie temperature (~120°C).[52, 53] Above the Curie temperature the BT has a cubic structure and is paraelectric, but below ~120 °C BT becomes tetragonal and has a permanent dipole which causes it to be ferroelectric. BT is commonly used in many applications including: ceramic capacitors, [54-57] PTC thermistors,[58-61] and piezoelectric transducers.[62, 63] Because of this wide range of applications, extensive research has been conducted to produce a verity of forms of BT(powders,[64, 65] thin films,[66, 67] nanoribbons,[68] nanorods,[69] nanospheres,[70, 71] nanotubes,[72] and nanowires [73, 74]). Limited research

has investigated the replication of intricate 3D structures with ferroelectric materials. Previous research has used a MWHT treatment to convert TiO_2 butterflies into BT while retaining the general morphology of the butterfly on the macro scale.[75, 76]

Prior work has utilized the single precursor coating method to create TiO_2 replicas followed by conversion into BT.[77] In this work, a more direct method of producing BT replicas of organic structures was used that avoids the structure degrading volume contraction and expansion involved with crystalizing a replica into TiO_2 and then hydrothermally converting it into BT.[77] The second method involved alternating exposure to the individual precursors, Barium and Titanium isopropoxide, to directly synthesize BT replicas after combustion of the pollen template and reaction of the BaO and TiO_2 layers. When using the method by Vernon et al., there is a volume increase during the conversion from TiO_2 to BT of approximately 89%.[77] When directly synthesizing BT for layers of BaO and TiO_2 there is no longer an increase in volume, but instead a smaller decrease in volume of ~15% (The volume changes were calculated using the molar densities from PDF cards (96-101-1363) for BaO, (00-021-1272) for Anatase, and (00-005-0626) for tetragonal BT). Minimizing the volume change helped preserve the structure being replicated. This method was used to synthesize phase pure strontium titanate (ST), by alternating exposure to strontium isopropoxide and titanium isopropoxide precursors. Preliminary research into creating phase-pure BT replicas of pollen particles has been performed by Dr. Goodwin, [78] but the replicas in this research were not made of tetragonal BT and additionally had extensive sulfur contamination.

Barium Strontium Titanate ($Ba_xSr_{1-x}TiO_3$, BST) like BT can be a ferroelectric ceramic with an ABO_3 perovskite crystal structure. BST is a solid solution of Strontium Titanate and Barium Titanate with lattice parameters between that of ST and BT.[79, 80] Vegard's law can be used to estimate the lattice parameters of BST over the range of possible compositions (see Equation (14)).[81, 82]

$$a_{BST} = x_{BT}a_{BT} + (1 - x_{ST})a_{ST} \quad \textbf{(14)}$$

Here, a_{BST}, a_{BT}, a_{ST}, represent a lattice parameter for BST, BT, and ST, respectively. x_{BT}, and x_{ST} are the atomic fraction of BT and ST in the solid solution. XRD has been used to show that over the complete range of ST to BT only a single phase is present.[79] Additionally, the lattice parameter $\sqrt[3]{a^2c}$ and the composition showed a very close relationship to Vegard's law.[79]

Also, because the Curie temperature of ST is near 35 Kelvin[83, 84] that of BT is around 393 Kelvin. Therefore, by controlling the ratio of barium to strontium, it is possible to tune the Curie point.[85, 86] Furthermore, the dielectric constant of a ferroelectric material is dependent on temperature. When a material is near its Curie temperature, there is maximum strain on the lattice and, because of this, the dielectric constant is greatly increased.[86] A potentially useful ratio of Ba:Sr is near 60:40. At this ratio, the Curie temperature is ~6.3 °C.[87] The increase in dielectric constant should be beneficial to electro static adhesion.[88] Because the Curie temperature of BST can be tuned, BST can be used in applications in which BT is not sufficient such as switches,[89] tunable phase shifters,[90-93]

capacitors for tunable radio frequency and microwave devices,[94, 95] and dynamic random access memory.[96, 97]

4.3 Experimental Procedures

4.3.1 Template

Pollen is a desirable type of template to use due to its biological replicability, availability, abundance and low cost. Although less intricate than the structure presented in the *P. sesostris* dorsal wing scales, pollen templates offer a wide range of features at both the micro- and nanometer range. Pollen templates were selected based on the general size, shape, and consistency of the features. The outer shell of pollen particles (the exine) is composed of sporopollenin, a polymer consisting of carboxylic acids cross-linked with aliphatic chains (HOOC-(CH2)n-COOH).[98] Similar to the effect of the abundant hydroxyl groups on chitin, the presence of abundant carboxyl groups allows for a direct reaction with isopropoxide precursors used in the SSG coating process. The templates of pollen used in this research were selected for their echini aspect ratio to allow for comparison to previous research on magnetic replication of the same species. The templates selected, were Sunflower (*H. annuus*) pollen particles.

4.3.2 Cleaning of Pollen Particles

Defatted pollen particles obtained from Greer Laboratories, (Lenoir, NC USA) were cleaned by soaking in 1 M hydrochloric acid (VWR, Suwanee, GA USA) for 1 h to remove residual inorganic material, followed by rinsing three times

with de-ionized water. The pollen particles were the soaked in anhydrous IPA for 1 hr and dried by vacuum aspiration at room temperature for 15 min.

4.3.3 SSG Coating of Pollen Particles

Ti-Ba-O bearing coatings were deposited using the SSG method using a D1 robotic coating system explained in CHAPTER 2 on page 27. Coatings were applied to clean dry pollen in a special modified Medium or Coarse Buchner funnel (VWR, PA, USA) attached to a stopcock. The reaction chamber was connected to a waste container and solvent trap and then to a vacuum pump. Inside of the reaction chamber with the pollen was a stir bar to mix the pollen and the precursors thoroughly during coating. On the outside of the reaction chamber was a bearing driven by a DC motor with a magnet attached. When the DC motor was turned on, the solution would be mixed. The mixer was used for each step of the deposition process when solution was in the reaction chamber.

Each SSG deposition layer carried out by immersing pollen in 25 mM Ti (IV) isopropoxide (Alfa Aesar, Ward Hill, MA, USA) in anhydrous isopropanol (99.8+% purity, Acros Organics, Geel, Belgium) for 5 min at allow for chemisorption of Ti-O bearing layer for deposition of purely Ti-O coatings.

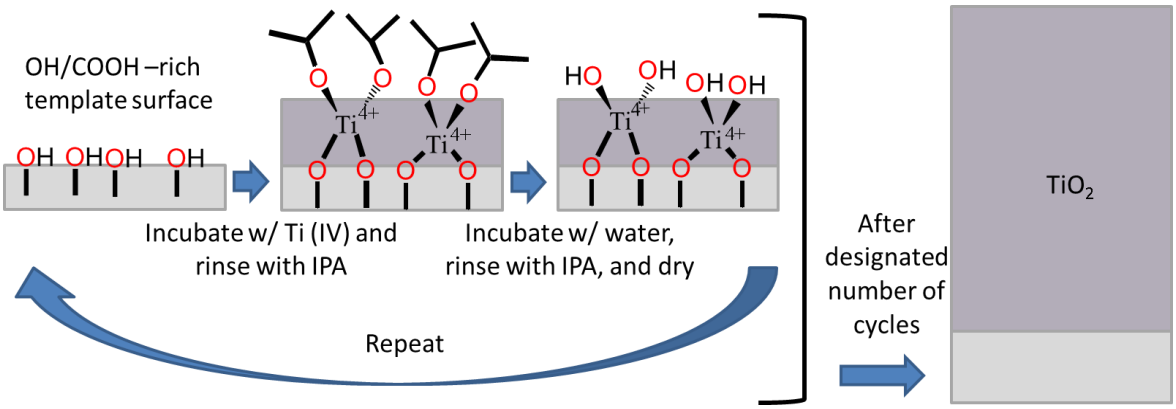

Figure 39: Schematic showing SSG deposition of Ti (IV) isopropoxide in individual layers.

For deposition of Ba-Ti-O bearing coatings, i) immersing pollen in alternating layers of 12.5 mM Ba (II) isopropoxide in anhydrous isopropanol (99.8+% purity, Acros Organics, Geel, Belgium) or 12.5 mM Ti (IV) isopropoxide (Alfa Aesar, Ward Hill, MA, USA) in anhydrous isopropanol (99.8+% purity, Acros Organics, Geel, Belgium) for 5 min at allow for chemisorption of Ba-O or Ti-O. The ratio of Ba-O layers to Ti-O layers was varied. ii) The pollen were rinsed three times with isopropanol (99.5+% purity, BDH, PA, USA) to remove any physisorbed precursor, iii)immersed in 60%v DI water in isopropanol for 5 min, to allow for hydrolysis of alkoxide layer, iv) rinsed 3 times with isopropanol and v) and dried with RT air by vacuum filtration for 5 minutes. This process (alkoxide incubation, isopropanol rinse, DI incubation, isopropanol rinse, drying) was repeated for up to 50 cycles to apply Ba-Ti-O bearing coatings.

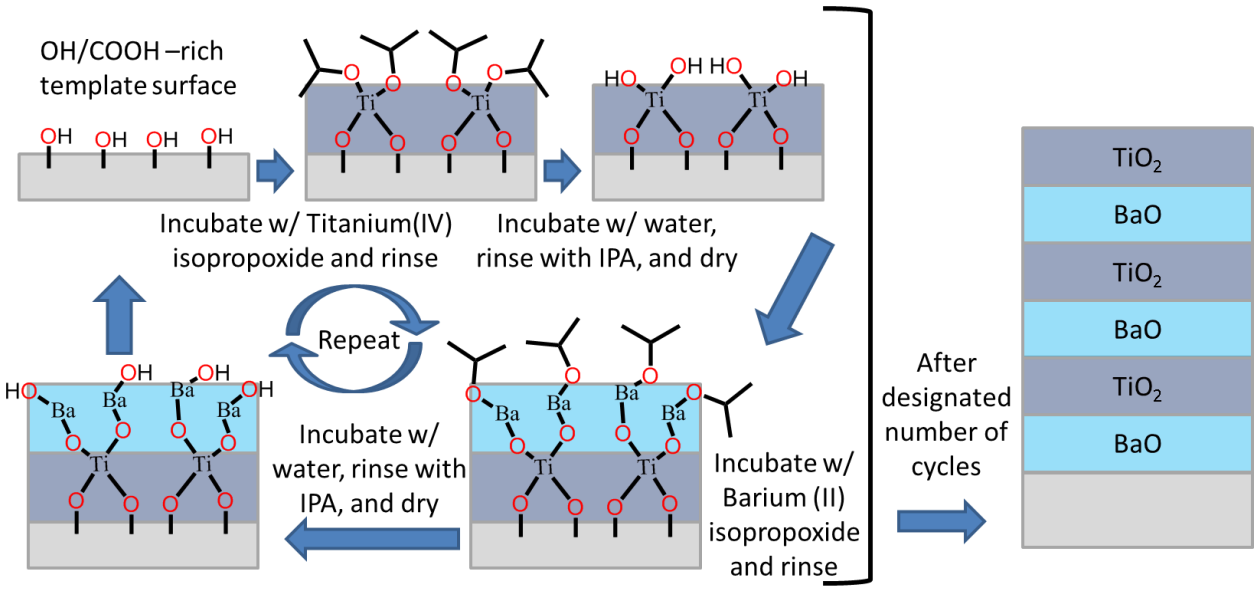

Figure 40: Schematic showing SSG deposition of Ba(II) isopropoxide and Ti (IV) isopropoxide in alternating layers. The ratio of Ba-O to Ti-O layers could be varied to control the ratio of barium to titanium in the coating.

For deposition of strontium, barium, and titanium oxides, the Ba (II) isopropoxide was mixed with the Sr (II) isopropoxide and alternatingly deposited with the titanium.

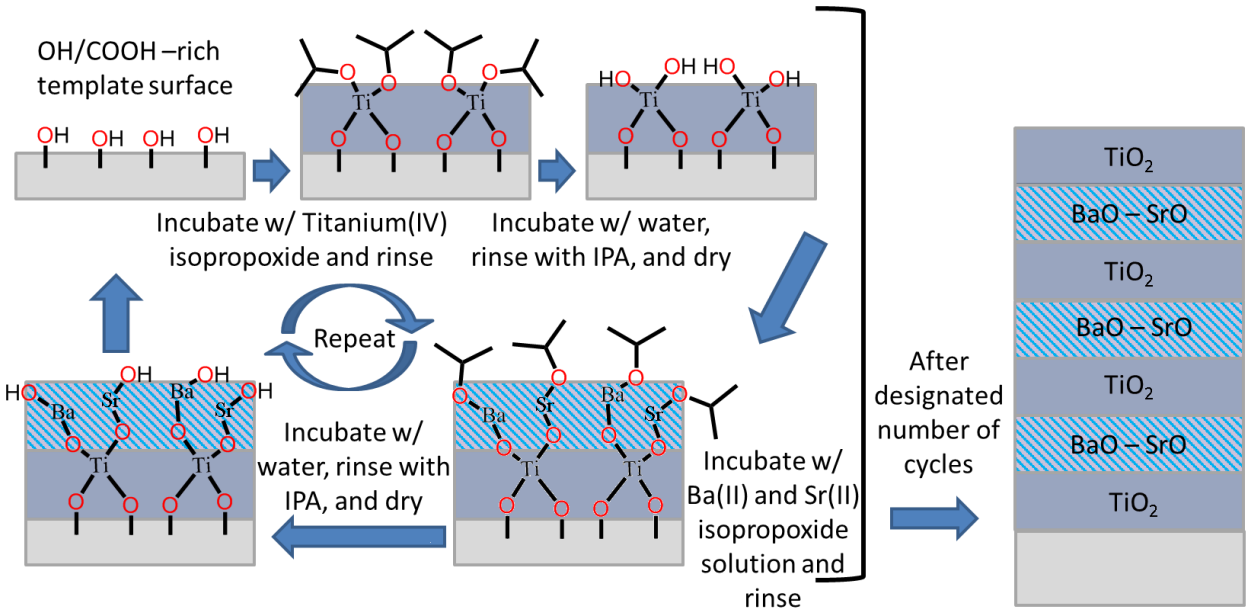

Figure 41: Barium and Strontium isopropoxide are mixed together in a common solution in method 4 to create a solution with the desired Ba:Sr alkoxide ration to yield the desired ratio in the final coating. Ba/Sr-iso and Ti-iso layers are alternated to attain the appropriate ratio of site A atoms to site B atoms.

4.3.4 Organic Removal and Conversion to Oxide Replica

Inorganic replicas were created by firing coated samples in inert crucibles (MgO or Al_2O_3) in a tube furnace (Lindberg Blue M, Thermo Fisher Scientific Inc., MA, USA) at generally 450 °C to 600 °C and held at temperature for generally 4 to 6 hr in air to allow for combustion of the organic and crystallization of the coating material. The furnace was then cooled at 120°C/hr to below 100°C before removal of the sample from the furnace.

Coated pollen being fired solely for EDS, XRD, and ICP-MS analysis, fusing of individual particles is not problematic thus they could be fired directly in an MgO crucible. Alternatively, when the individual particles needed to be identified, MgO wafers (MTI Corp, CA, USA) or onto nickel foil (25.4 µm thick, McMaster-Carr, Cleveland, OH, USA) were used as substrates and powders were

dispersed on the surface. Coated powders were dispersed in IPA and then pipetted onto MgO wafers and allowed to dry. Each wafer was inspected using an optical microscope to insure even dispersal of the particles (A-Zoom2, Micromanipulator inc., CA, USA). The wafer could then be placed in an MgO crucible and fired.

4.3.5 Morphology Analyses

The morphologies of the uncoated pollen particles, SSG-coated pollens, coated and fired pollens, titania replicas, and barium titanate replicas were characterized with SEM, EDS, and XRD. The microstructure of uncoated pollens, SSG-coated pollens, and all inorganic replicas were imaged with a field-emission scanning electron microscope (1530 FESEM, Carl Zeiss, NY USA). The chemical composition was evaluated with an energy dispersive X-ray spectrometer (EDS) (INCA 7426, Oxford Instruments, UK) which was used in combination with the above SEM.

For samples sputtered with gold, a Quorum Q150T ES (Energy Beam Sciences, INC., CT, USA) sputter coater was utilized to sputter gold for 60 seconds at 20 mA. Cross-sections of samples were created by milling via focused ion beam (FIB) milling (Nova Nanolab 200 FIB/SEM, FEI, OR, USA).

Phase identification of replicas was evaluated using X-ray diffraction (XRD) analysis. XRD was conducted using an X'Pert Pro Alpha-1 diffractometer (PANalytical B.V., ALMELO, Netherlands) with monochromatic Cu Ka1 (1.540598 Å) radiation from a 1.8 kW (45 kV, 40 mA) X-ray tube filtered via a symmetrical Johannson monochromator and detected by an X'Celerator detector. The

source was limited by a 1° fixed anti-scatter slit, a ½° programmable divergence slit, and a 15 mm mask. The diffracted x-rays were subject to a 0.04 radian soller slit and a 5.5 mm anti-scatter slit before the X'Celerator detector. Diffraction specimens were placed on B doped p-type Si zero background plate (MTI Corp, CA, USA). The sample support was rotated at 8 sec per revolution.

4.4 Results and Discussion

4.4.1 Pollen Shape Preservation

The as-coated SF pollen particles were fired in air to 500 °C at a ramp rate of 0.5 °C/min with no hold, the ramp rate was then increased to 3 °C/ min and the furnace was heated to 1000 °C and held for 2 hours. The slow ramp in temperature to 500 °C was used to allow for combustion of the organic pollen template.

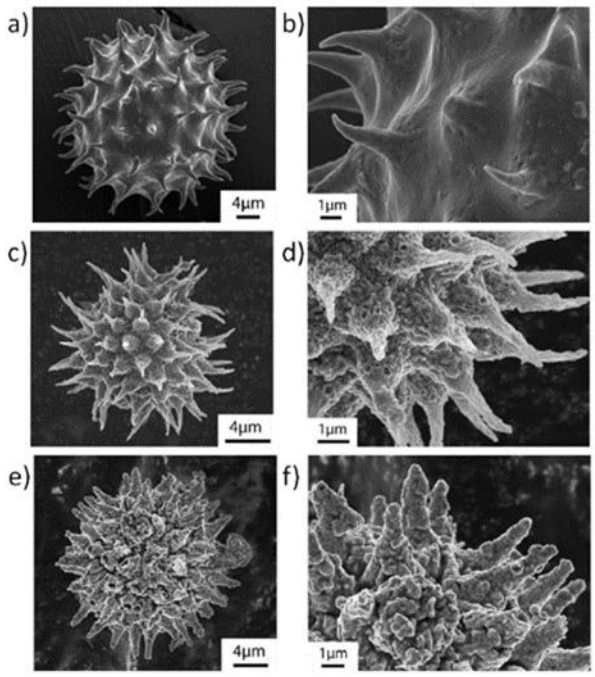

Figure 42: Secondary electron (SE) images of a,b) the native Sunflower pollen particles, c,d) a Ti-O SSG pollen particle after organic combustion and conversion into TiO_2 and, e,f) non-phase-pure BT replicas synthesized with an alternating SSG layer approach after firing to 1000 °C for 2 hr. Images courtesy of Dr. Goodwin.

After combustion was completed, the replica was heated to allow for reaction of the Ba-O and Ti-O into polycrystalline BT. The diameter average of the native SF pollen was 28 ± 5 μm. The BT replicas showed a 35% reduction in size with inorganic replica diameters of 18 ± 5 μm. The pure TiO_2 replicas showed a greater reduction in size shrinking approximately 56% from the initial size and having diameters of 12 ± 4 μm. The greater reduction in size of the TiO_2 is suspected to be due to the increased deposition of Ba-O compared to Ti-O per layer. The high aspect spines and general shape were maintained even with the high temperature treatments (Figure 42).

4.4.2 Control of Barium to Titanium & Barium to Strontium Ratios in SSG Coatings

For purposes of maximizing the potential dielectric constant of a replica material and thus the potential electrostatic adhesion, the deposition of barium to titanium oxides must be equivalent to produce phase pure $BaTiO_3$. If the stoichiometry is off, secondary phases form. The binary phase diagram of BaO and TiO_2 shows that barium titanate is a line compound at 50% titania and thus the ratio of BaO to TiO_2 needs to be 1-1.[99, 100]

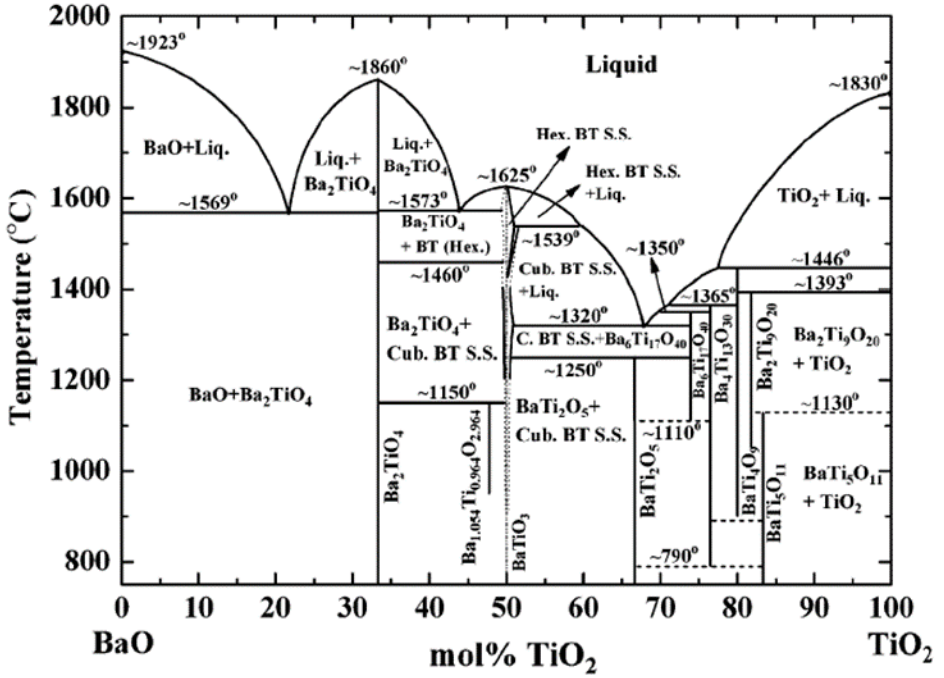

Figure 43: The binary phase diagram of BaO-TiO_2. The desired phase, $BaTiO_3$ is represented as a line compound at 50% TiO_2.[100]

The binary phase diagram above shows that if there is an excess of TiO_2 then a solid solution of BT and $BaTi_2O_5$ would form, but if there is an excess of BaO, Ba_2TiO_4 could form as a secondary phase. Because of this, it is greatly preferably to have equal amounts of BaO and TiO_2. To control the ratio of BaO to TiO_2 in the coating, the number of ratio of layers was varied. If both precursors

deposited the same amount of material per cycle, the required ratio would be 1:1, but this has not been shown to be true. Previous investigation looked into a 1:1 coating procedure, but found there was too much barium in the coating.[78] The as-coated barium to titanium ratio was investigated by coating 50 total layers of material onto sunflower pollen in an alternating fashion. The ratios used were 1 Ba : 1 Ti, 1 Ba : 2 Ti, 2 Ba : 3 Ti, 3 Ba : 4 Ti. In this investigation the following precursors were used: 25 mM Ti(IV) isopropoxide (Alfa Aesar, Ward Hill, MA USA) and 12.5 mM Ba(II)isopropoxide (Alfa Aesar, Ward Hill, MA USA). To quantify the as coated ratio of barium to titanium, EDS (INCA Model 7426, Oxford Instruments, Bucks, UK) was used after being calibrated with a piece of titanium foil (McMaster-Carr, Cleveland, OH, USA). Result of the four coating ratios can be seen in Figure 44.

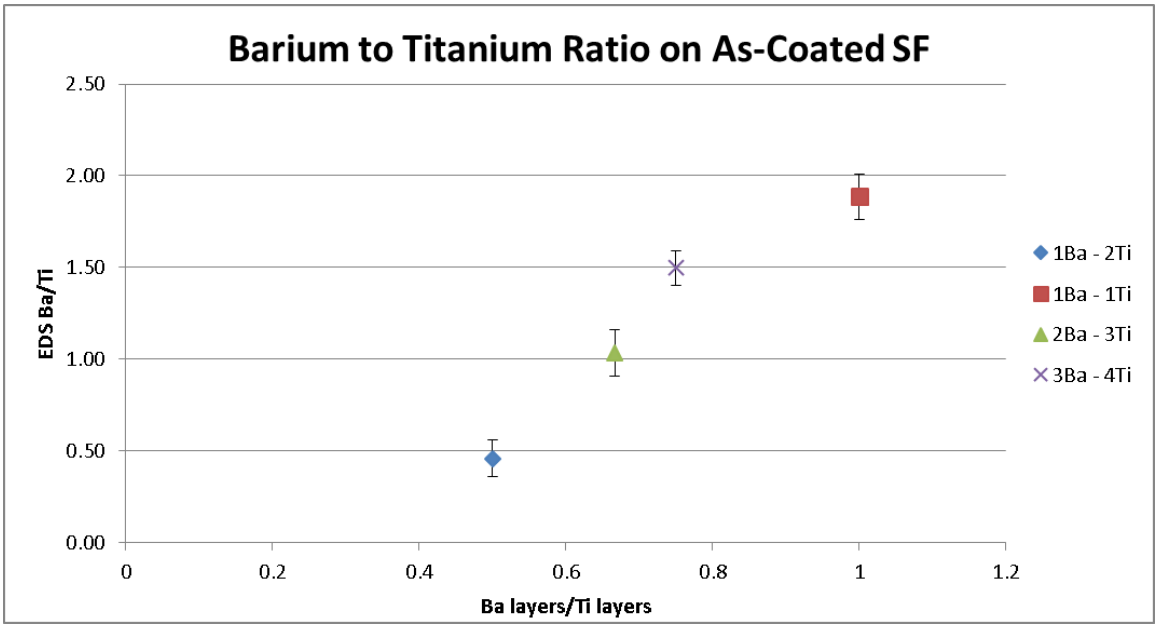

Figure 44: Graph of Barium to Titanium ratio from EDS vs Barium to Titanium ratio of layers deposited via SSG. EDS data was gathered from a minimum of three samples and the error bars represent one standard deviation.

This data suggest that when a ratio of 2 barium layers to 3 titanium layers is deposited, the ratio of material deposited should be nearly 1:1. Thus for producing phase pure BT, a ratio of 2:3 barium to titanium was used.

The samples with the variable amounts of barium and titanium were then fired to 1000 °C for 2 hr to crystallize the coating and remove the pollen template. EDS analysis of the replica pollen shows that the amount of barium in the coating is proportional to the amount of sulfur retained in the replica shell, see Figure 45.

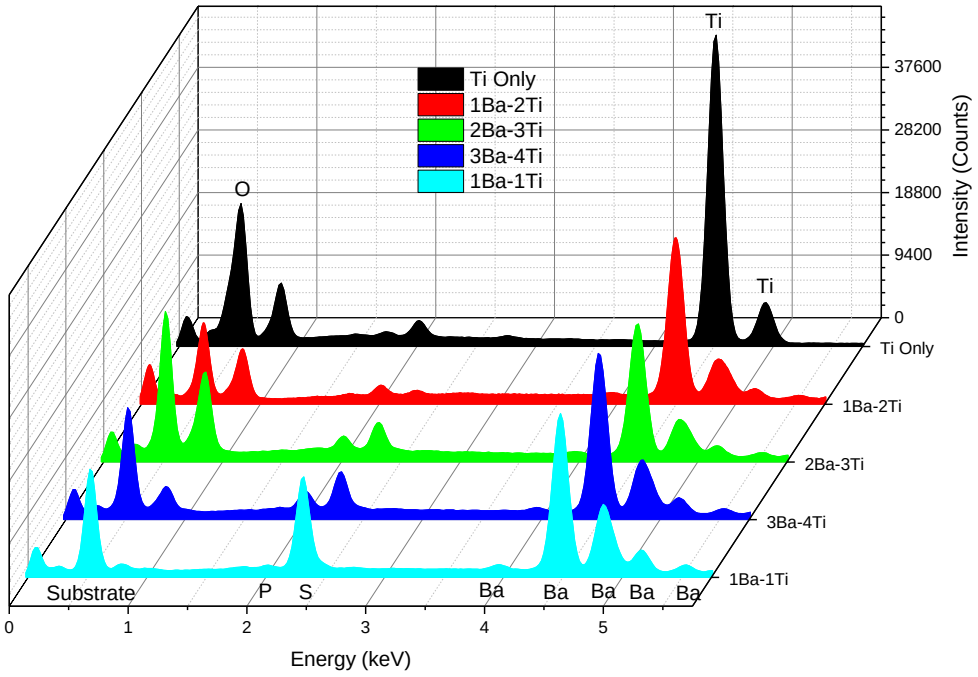

Figure 45: Defatted pollen, 1M HCl; 50 total SSG cycles w/Ba(II), Ti(IV) isopropoxide, Ba:Ti ratio = 1:2; 2:3; 3:4; 1:1; 1 °C/min to 500 °C, 3 °C/min to 1000 °C, 2 hr; in stagnant air) Ti only: 1oC/min 800 °C, 2 hr stagnant air

This data suggests that the sulfur is being retained in the replica shell and is possibly inhibiting the growth of BT by leaching away the barium to form $BaSO_4$. If

the amount of sulfur in the replica was minimal then the coating could be designed to have excess barium to bond with the sulfur and still have enough to form BT.

Controlling the barium to strontium in the SSG coating was determined in a separate manner. Barium titanate and strontium titanate have complete solid solubility and as such it does not have a phase related necessity to have a precise ratio in the coating, see Figure 46.

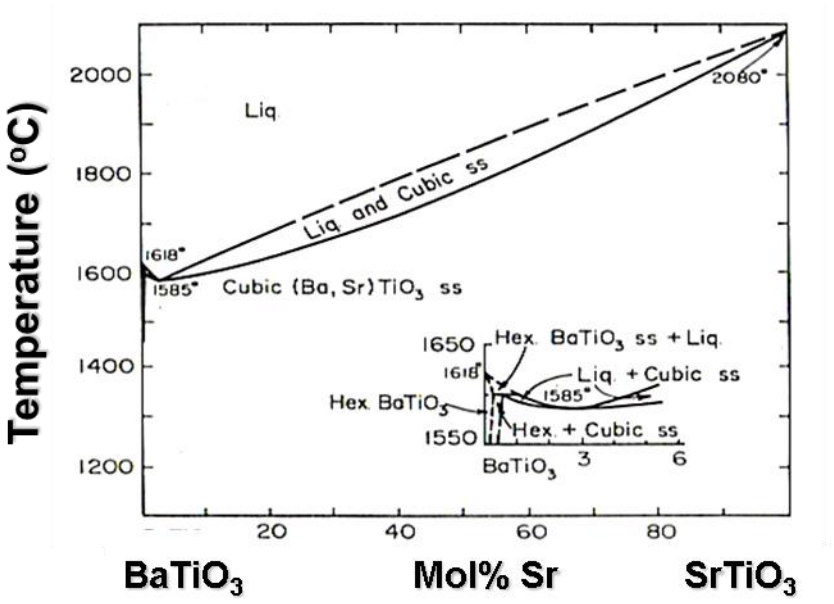

Figure 46: $BaTiO_3$ and $SrTiO_3$ exhibit complete mutual solid solubility.[79]

The ratio in the coating is important for controlling the curie temperature of the BST and thus the point at which the structure undergoes a phase change from cubic to tetragonal. When a material is near its Curie temperature, there is maximum strain on the lattice and, because of this, the dielectric constant is greatly increased.[86]

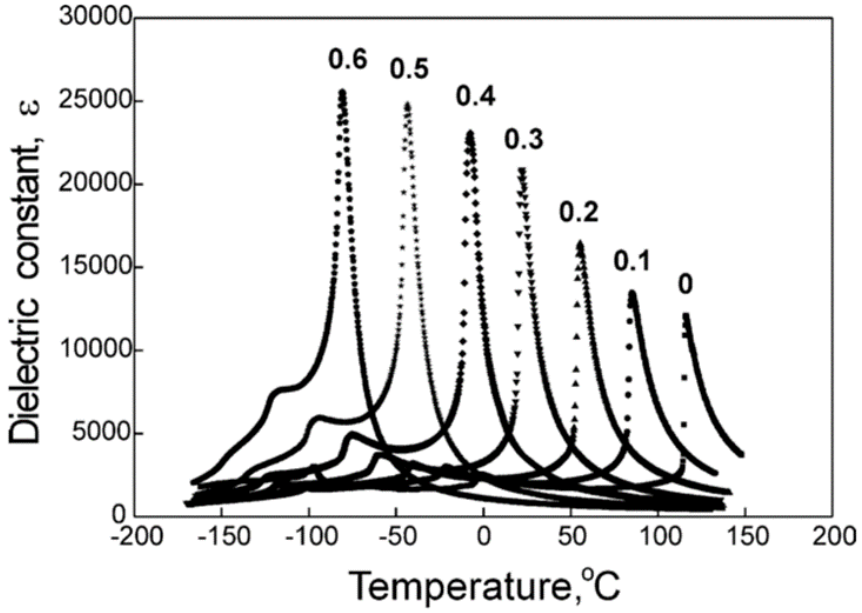

Figure 47: A plot of the dielectric constant of various compositions of $Ba_{1-x}Sr_xTiO_3$ sintered at 1450 °C for 1 hr.[101] The dielectric constant increases as the temperature nears the curie temperature.

To produce replica particles that are ferroelectric, the ratio of barium to strontium needs to be such that the Curie point is just above that of the operating conditions. When the sample temperature is above the Curie temperature BST is paraelectric. The barium to strontium ratio was evaluated by performing inductively coupled plasma mass spectroscopy (ICP-MS) analysis on samples with varying amounts of barium and strontium. The samples were coated with two precursors, the first was 25 mM Ti(IV) isopropoxide (Alfa Aesar, Ward Hill, MA USA) and second was a mixture of Ba(II)isopropoxide (Alfa Aesar, Ward Hill, MA USA) and Sr(II)isopropoxide (Alfa Aesar, Ward Hill, MA USA) to produce an overall concentration of 12.5 mM. All of the samples were coated with a 3:2 ratio of barium/strontium layers to titanium layers. The only variable that was changed was the relative amounts of barium and strontium precursors in the coating solution. The results, Figure 48, suggest that strontium precursor is

slightly less reactive than that of the barium precursor and thus a less than unity deposition rate was observed.

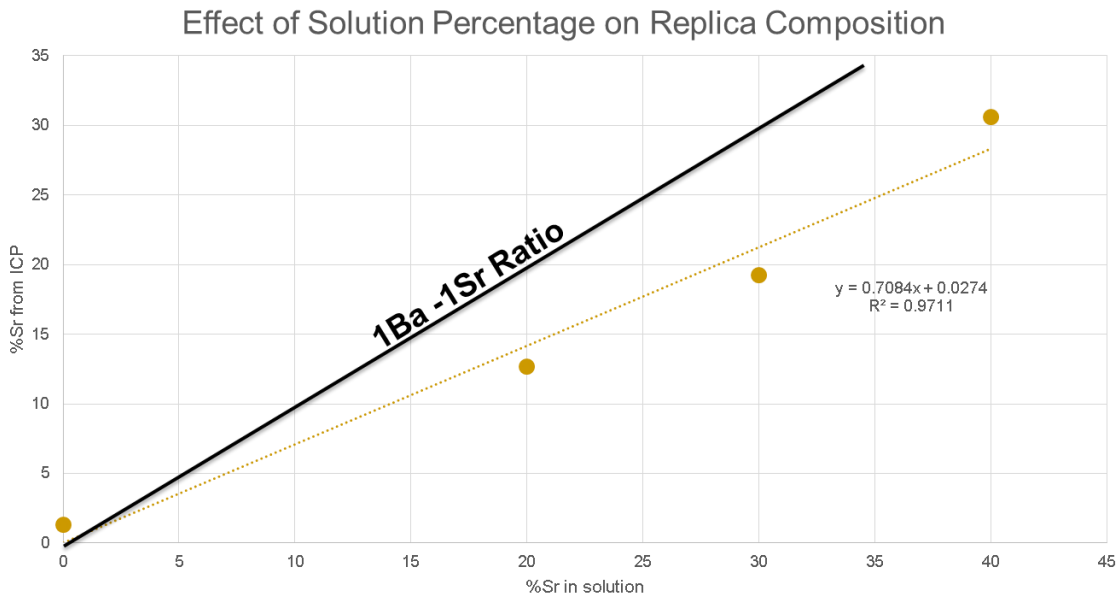

Figure 48: ICP results of Barium to Strontium ratio obtained by coating defatted SF pollen with 50 layers of Sr, Ba and Ti isopropoxide. The A-B ratio was held at 2-3 and only the ratio of Sr-Ba was changed in solution.

By using the data from this analysis, the amounts of barium, strontium and titanium could be predicted in the replica particle to produce replicas with specific compositions.

4.4.3 Removal of Sulfur During Replication

Preliminary to the synthesis of BST replicas of pollen particles, BT replicas of Sunflower (SF) pollen via a LbL SSG process were created using an alternating layer deposition method. The previous section has already discussed how the ratio of BaO and TiO_2 was controlled and why it is important for forming phase pure BT. Initially, the as-coated SF pollen particles were fired in air to 500 °C at a

ramp rate of 0.5 °C/min with no hold, the ramp rate was then increased to 3 °C/ min and the furnace was heated to 1000 °C and held for 2 hours. This process produced shape replicating pollen particles, but there were contaminate phases present.

Sulfur was detected by EDS in the replica coating and $BaSO_4$ was confirmed as an impurity phase by the XRD analysis in Figure 49. To create a replica with a high, reproducible, and known dielectric constant, it is highly preferable that the replica be phase pure, only containing BT without any contamination phases like $BaSO_4$. $BaSO_4$ has a low dielectric constant of ~9 [102] and also consumes some of the barium from the BT, which can cause the formation of a titanium-rich phase to further contaminate the replica.

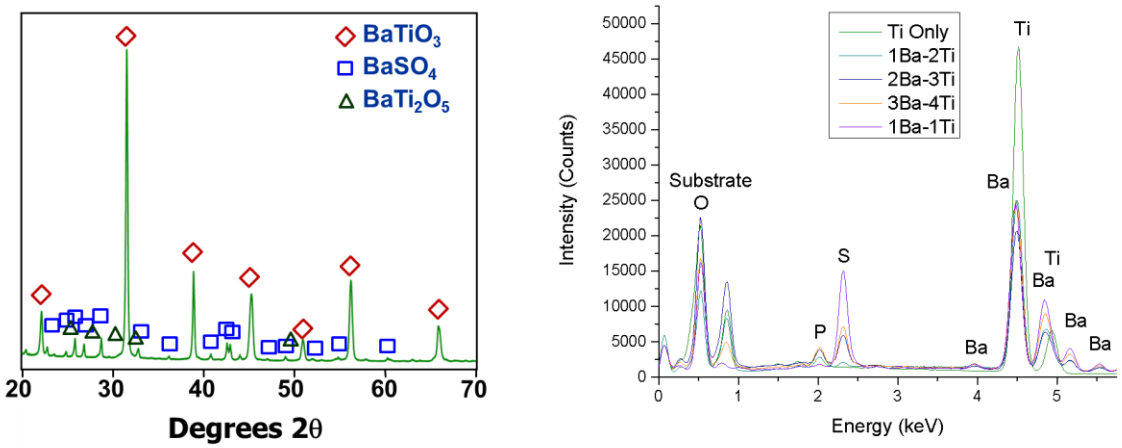

Figure 49: Left) XRD pattern for the BT replicas synthesized with alternating layers of Ti/Ba SSG. Courtesy of Dr. Goodwin. Right) EDS of various replica compositions from pure Ti-O to increasing amounts of Ba-O up to equal amounts of Ba to Ti layers.

Barite ($BaSO_4$) forms readily under commonly used firing conditions. Barium reacts with sulfur in the presence of oxygen to form barite which is not easily removed. Solubility of Barite in hot water was found to be around 10^{-5}

M.[103] Barite can be successfully dissolved (1 M solubility) using a mixture of NH_2OH-HCl in 1 M HNO_3 when boiled for 20 min.[104] Unfortunately, BT is also soluble in warm HNO_3-HCl.[105] Hence, if the Barite was dissolved the BT would also be dissolved. The sulfur is present in the native pollen structure as indicated by the EDS analysis in Figure 50.

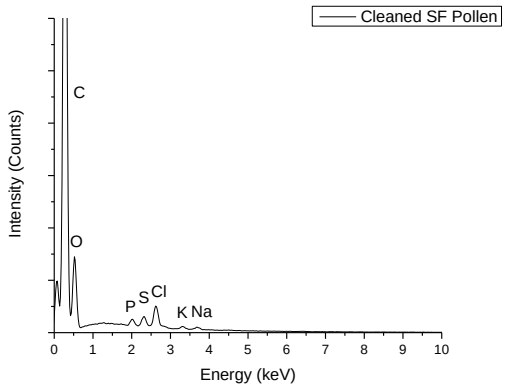

Figure 50: EDS of cleaned sunflower pollen with no SSG coatings shows the presence of sulfur.

Although the barite cannot easily be selectively dissolved, it can be removed via decomposition at high temperature into SO_3 gas and BaO. The BaO can then react with TiO_2 to form BT. The reaction is shown in Equation (15):

$$BaSO4 = BaO + SO_3(g) \quad \textbf{(15)}$$

For this reaction to able to occur, the standard Gibbs free energy change of the reaction needs to be negative (see Figure 51).[106, 107]

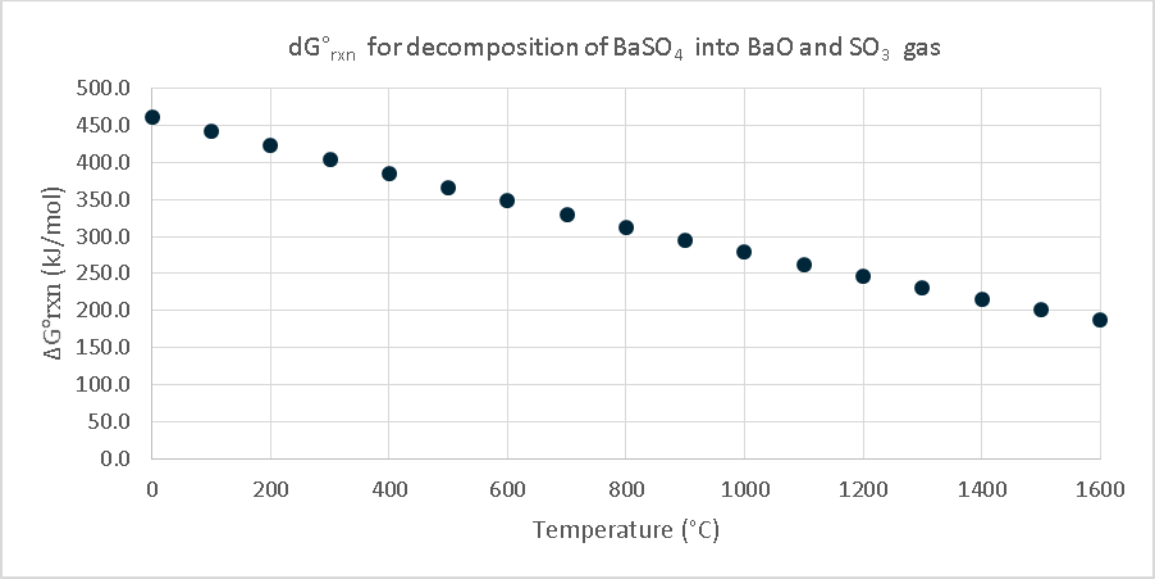

Figure 51: The standard Gibbs free energy change for the reaction of $BaSO_4$ into BaO and SO_3 gas.

Equation 9 gives the relation of the activities of the reaction products and reactants and the Gibbs free energy.

$$\Delta G^{o}_{RXN} = -RT\ ln \frac{aBaO * aSO_3}{aBaSO_4} \quad \textbf{(16)}$$

If the activities of the solids are assumed to pure, stoichiometric oxides & pure stoichiometric oxide reference state, they become unity. If the SO_3 gas is assumed to be an ideal gas and the activity of an ideal gas is the partial pressure divided by the reference pressure (1 atm) then Equation 9 becomes Equation 10.

$$\Delta G_f = -RT\ ln\ pSO_3 \quad \textbf{(17)}$$

Therefore, with the temperature dependence of the standard Gibbs free energy change, the equilibrium partial pressure of SO_3 gas can be determined. When the partial pressure of the SO_3 gas is lower than that of the equilibrium pressure, the reaction was thermodynamically favorable.

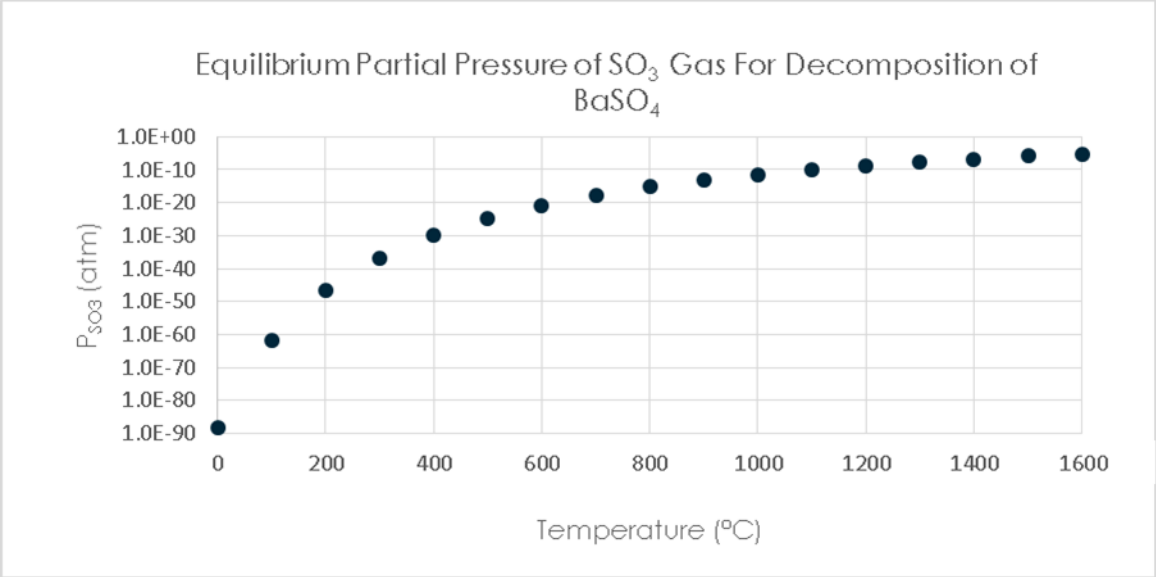

Figure 52: The equilibrium partial pressure of SO_3 in the decomposition of $BaSO_4$ from 0 °C to 1600 °C.

By flowing air over the sample while it was fired at 1200 °C the sulfur was removed from the samples. EDS shows that when identical samples were fired in stagnant air the sulfur was retained, but when it was fired in flowing air the sulfur was removed.

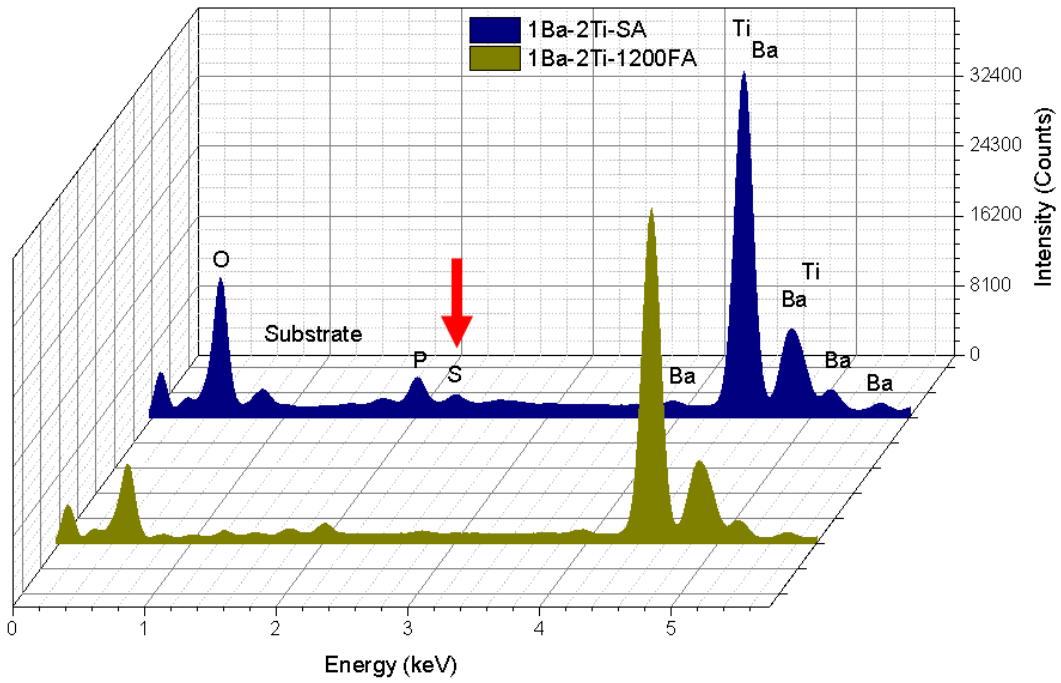

Figure 53: EDS of fired pollen replicas in stagnant air at 1000 °C and in flowing air at 1200 °C for 2 hr shows no sulfur in the sample with flowing air.

The problem with this method for sulfur removal is that it involved a high temperature firing process and the coated pollen does not retain its shape at 1200°C (see Figure 54).

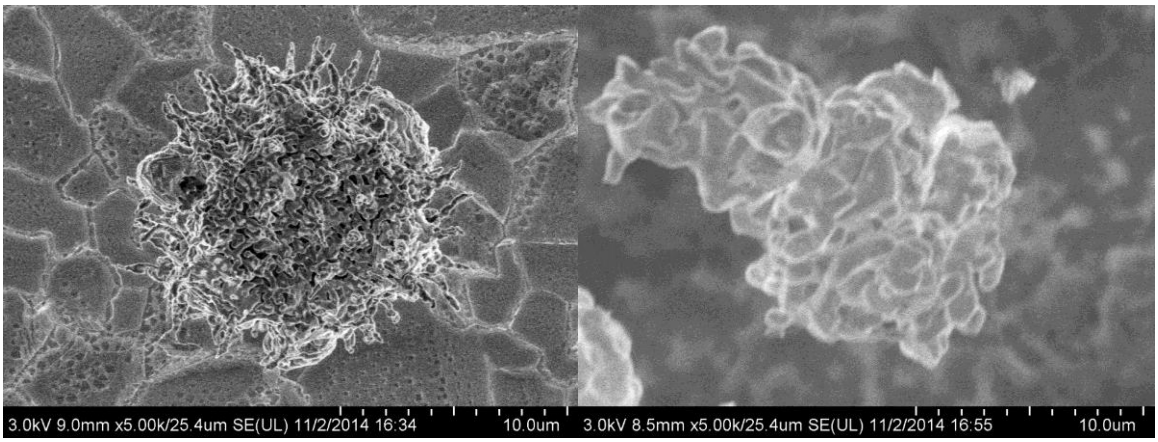

Figure 54: 30 layer 3Ti-2Ba SSG coated SF pollen replicas fired (left) at 1000 °C in stagnant air and (right) in flowing air at 1200 °C. The sample fired at 1200 °C in flowing air did not retain its shape, but was sulfur free.

Because the sample does not retain its shape at the temperature required to remove the sulfur, a new method was developed. In a closed atmosphere, if the partial pressure of SO_3 could be brought below that of the equilibrium partial pressure for the SO_3 gas at the sample then the sulfur could be removed from the sample. The new method utilizes the fact that the equilibrium partial pressure of SO_3 decreases exponentially as the temperature is reduced, see Figure 52. The sample was placed at one end of a closed ampule with an abundance of BaO_2 at the other end (Figure 55).

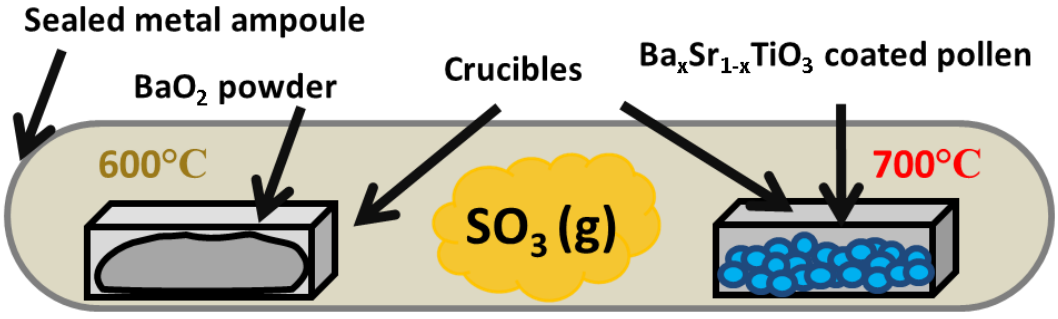

Figure 55: Schematic of the controlled atmosphere reactor design used to remove Sulphur from the barium titanate. On the left was BaO_2 used to getter the SO_3(g) from the atmosphere at a lower temperature than the BT on the right side at a higher temperature.

The sample was in one zone of a multi zone furnace set to 700 °C, the BaO_2 was positioned in a different zone set to 600 °C. Because there was an abundance of BaO_2, and it was set at a lower temperature, the partial pressure of SO_3(g) in the atmosphere would be that of the equilibrium partial pressure at 600 °C and would remove the SO_3 from the sample that has a higher equilibrium partial pressure.

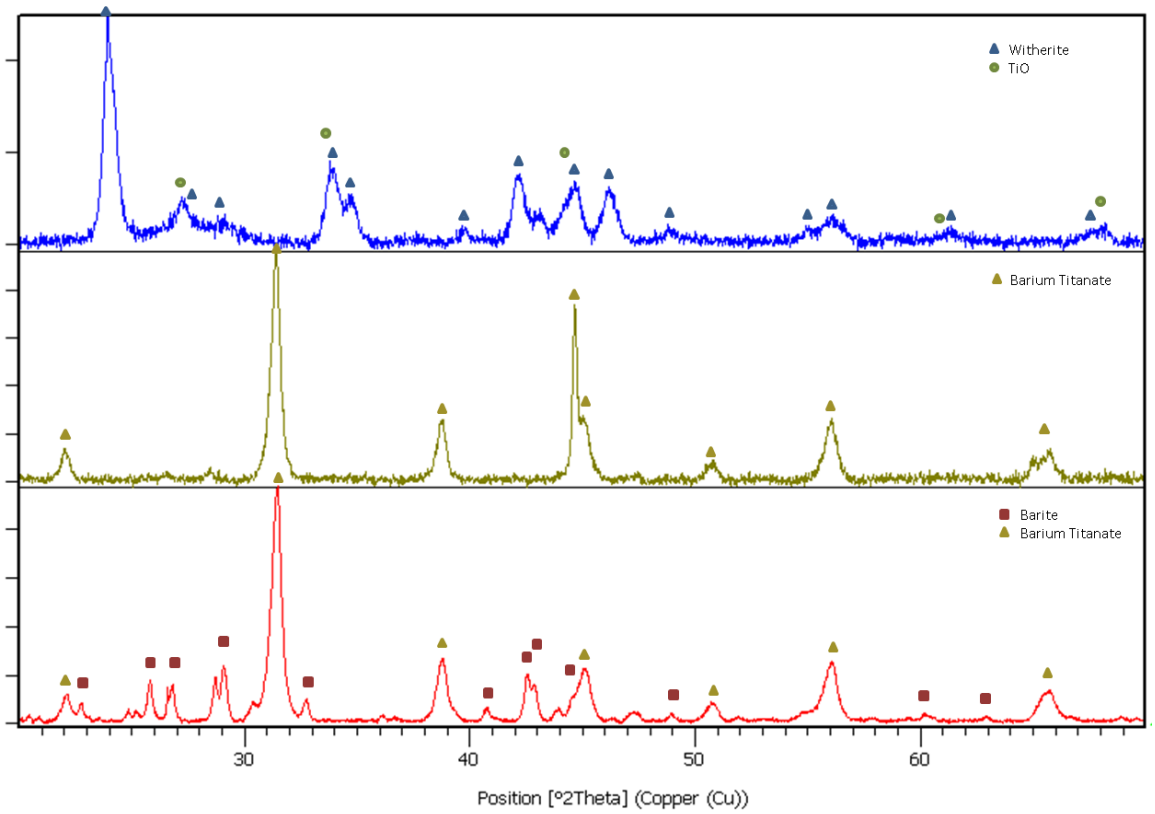

Figure 56: XRD patterns of 30 layer 3Ti-2Ba SSG coated SF pollen replicas fired at 700 °C in sealed ampule with (top) no SO_3 getter on other side at 700 °C, (center) with BaO_2 on other side at 600 °C, (bottom) with ampule open to air .

The data (Figure 56) on this work suggests that firing with a controlled atmosphere with BaO_2 at a lower temperature than the sample can yield phase pure BT. The presence of Witherite suggests a low pO_2 which could assist in

inhibiting the formation of Barite. The presence of Barite in the open ampule confirms that the heating conditions alone are not the cause of the pure BT. Although BaS was occasionally found in the replicas, it could be removed via washing with DIW.

4.4.4 Creation of Tetragonal BT Sunflower Replicas

The initial conditions used to remove the sulfur were adequate to form sulfur-free phase-pure barium titanate, but the resulting phase was not tetragonal BT. This cubic BT was due to the small grain size of the replica shell. When BT has a very small grain size, the Curie temperature is shifted to a lower temperature and thus pure BT can be cubic at room temperature.[108, 109]

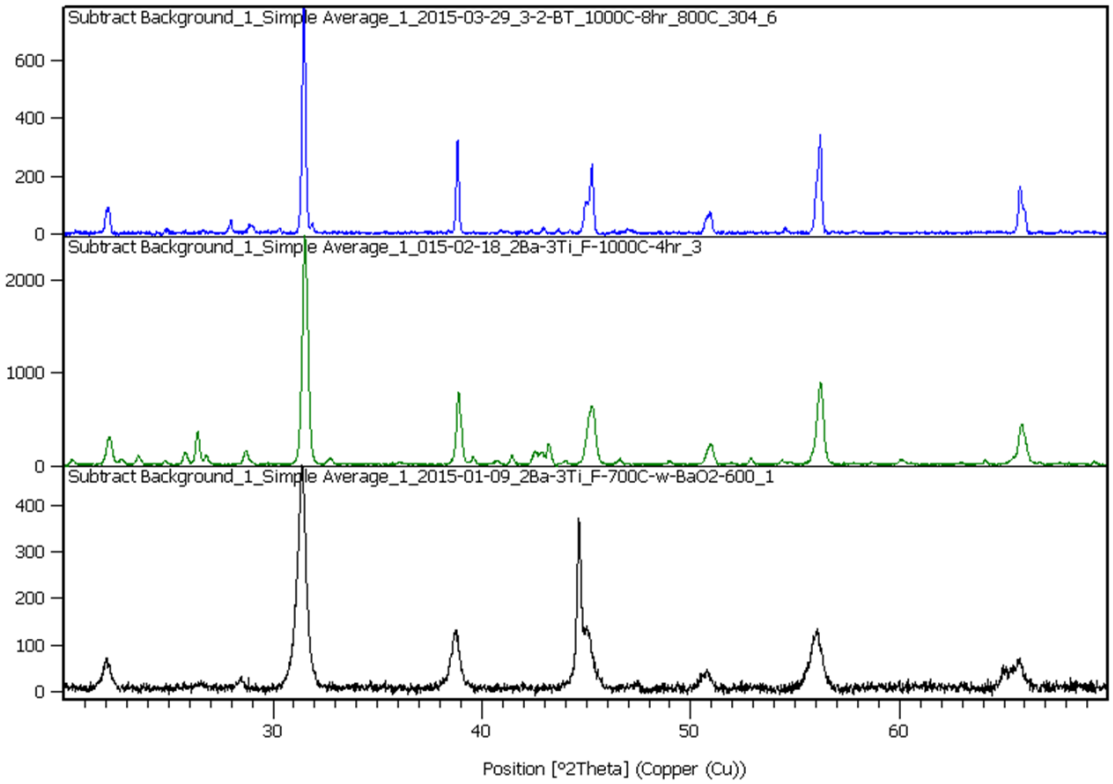

Figure 57: XRD patterns of 50 layer 3Ti-2Ba SSG coated SF pollen replicas fired at 1000 °C in sealed ampule with BaO_2 on other side at 800 °C for top: 8 hours and middle: 4 hours. The bottom sample was fired 800 °C in sealed ampule with BaO_2 on other side at 600 °C for 4 hours. The sample fired for 8 hours has larger grains and is tetragonal.

Figure 57 shows that the when the 50 layer 3Ti-2Ba SSG coated SF pollen replicas were fired for 4 hr at 1000 °C as opposed to 800 °C the peaks became sharper, but the sample was not tetragonal. When the sample was fired for 8 hr at1000 °C the XRD shows that the phase is tetragonal BT. This is significant because the grains must be grown large enough to be tetragonal at room temperature without destroying the sample morphology.

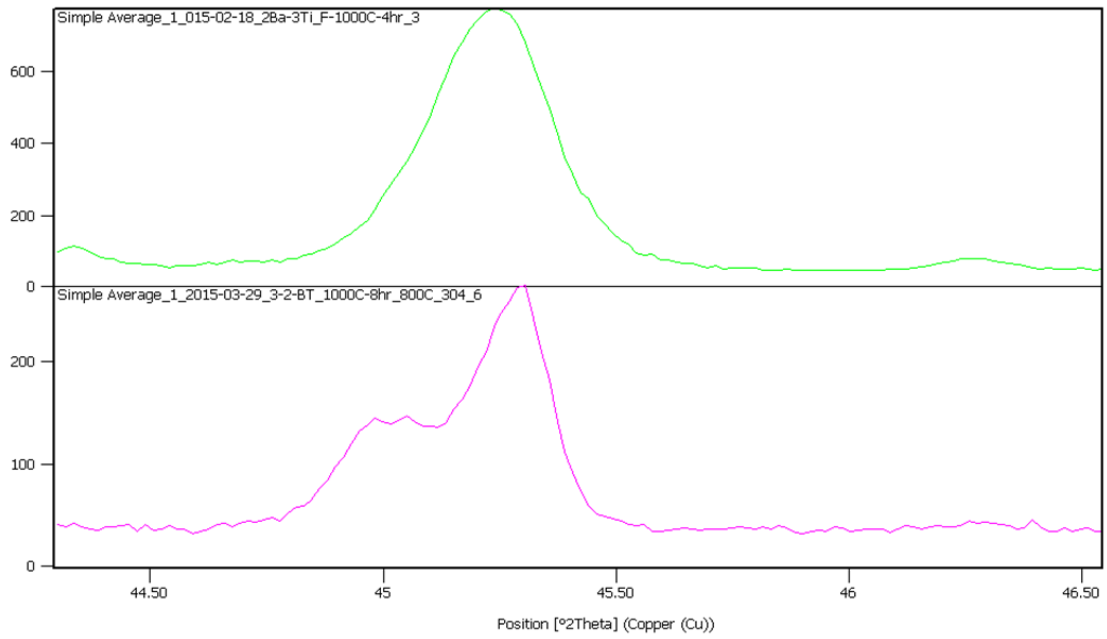

Figure 58: Zoomed in view of the (002) peak of the cubic BT (Top) and of the (002) and (020) peaks in the tetragonal BT (Bottom). The tetragonal sample was fired for 8 hours as opposed to on 4 hours for the cubic sample, both at 1000 °C.

Scherrer analysis of the (110) peak of the barium titanate in each sample showed how the grains grew as expected with higher temperatures and longer dwell time.

Table 3: Effect of firing conditions on crystallite size based on Scherrer analysis of BT (110) peak.

Firing Conditions	Crystallite size (Å)
800 °C – 4 hr	151 ± 10
1000 °C – 4 hr	302 ± 10
1000 °C – 8 hr	560 ± 10

4.4.5 Long Range Electrostatic Attraction

Scherrer analysis of the BT (110) diffraction peak from Figure 49 yielded an average crystallite size of 28 ± 1 nm. Measurements of adhesion of TiO_2 and BT inorganic replicas of SF pollen particles on various substrates (mica, Si, PVA, PVAc, PS, and Au-Si) have shown a stronger VDW adhesion in the BT replicas

compared to the TiO_2 replicas. When the replicas are tested on a freshly cleaved mica substrate, with a charged surface, the BT replica has an increase in electrostatic adhesion of approximately 50 nN whereas the TiO_2 replica has an increase of only ~10 nN.

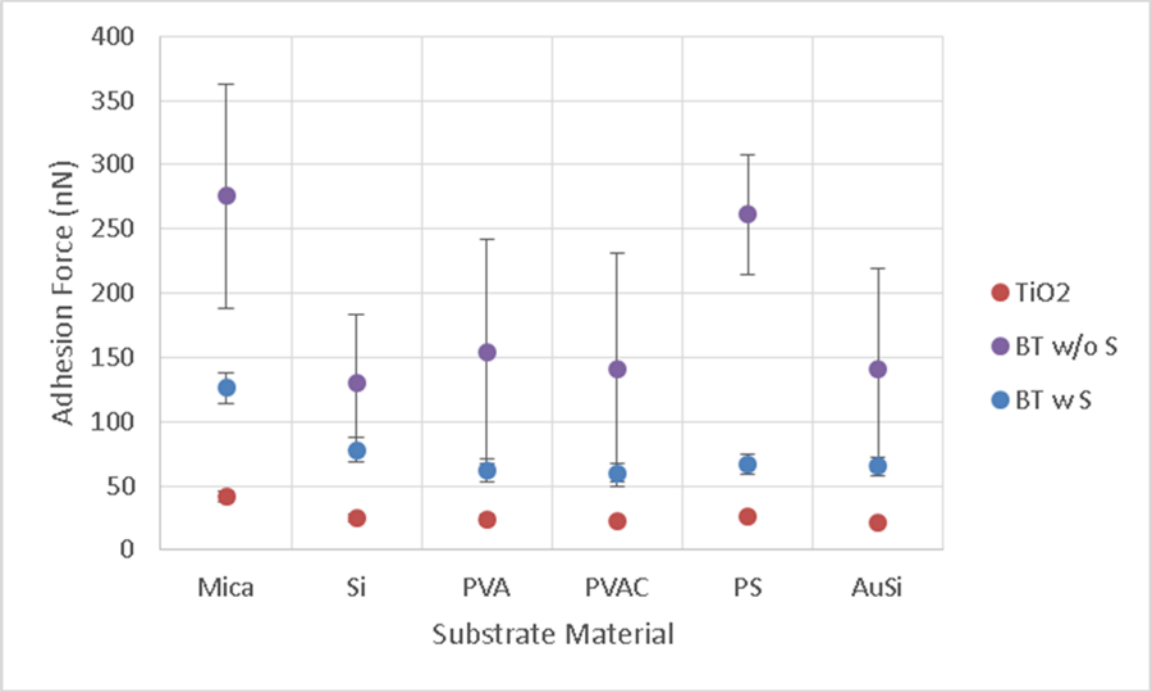

Figure 59: AFM adhesion values for TiO_2, BT with barite contamination, and BT without barite contamination (fired for 8 hr) replicas on different substrates. Courtesy of Donglee Shin.

Long range adhesion measurements have been made with pollen replicas made of titania, cubic BT, and Sulphur free tetragonal BT. The data is represented below in Figure 60.

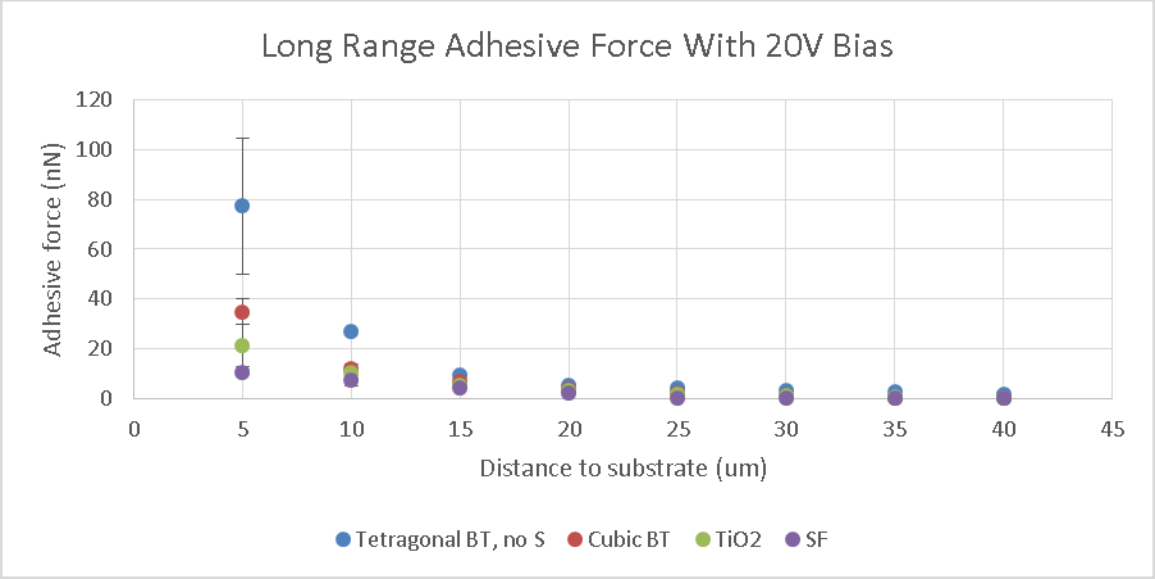

Figure 60: AFM long range adhesion forces for Native Sunflower pollen, TiO_2 replicas, cubic BT replicas, and tetragonal Sulphur free BT replicas under 20V bias. The Sulphur free samples show statistically significate increase in long rang adhesion compared to all other samples. All error bars represent one standard deviation. Courtesy of Donglee Shin.

The long range adhesive force of the tetragonal Sulphur free pollen replicas is statistically greater than all other samples. The significant increase in the force in comparison to the cubic BT is likely due to the increase in dielectric constant.

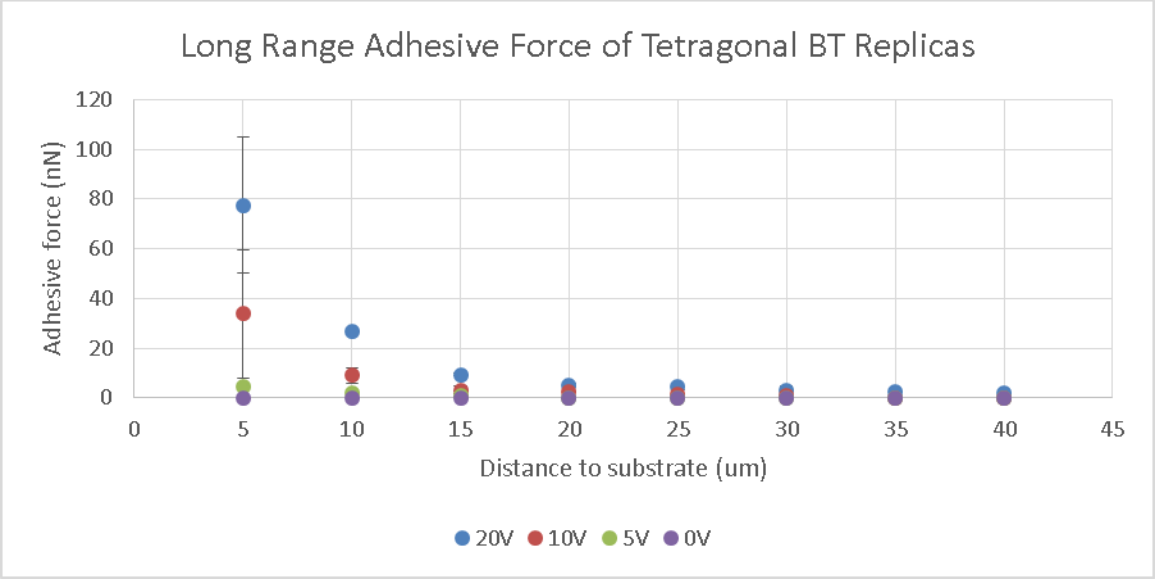

Figure 61: AFM long range adhesion forces for tetragonal Sulphur free BT replicas under 0V to 20V bias. Although there is a large amount of error in the nearest measurement, the samples show statistically significate increase in long rang adhesion upon increase in applied voltage. All error bars represent one standard deviation. Courtesy of Donglee Shin.

Initial data has also been recorded for non-phase-pure BT and $Ba_{0.7}Sr_{0.3}TiO_3$ for long range adhesion with applied voltages of 0, 10 and 20V. The data shows an increased adhesive force in the BST when compared to the BT, see Figure 62.

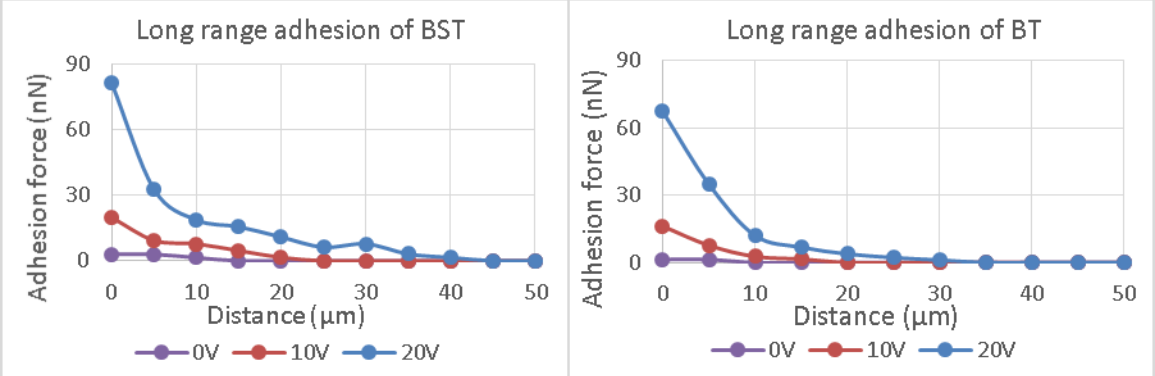

Figure 62: Long range adhesion data measured against Ni substrate with voltage applied for $Ba_{0.7}Sr_{0.3}TiO_3$ and (right) BT. Courtesy of Donglee Shin.

Preliminary XRD results of non-phase-pure BST show a shift in the (110) diffraction peak demonstrating mixing of the barium and the strontium in the A sites. There

are many contamination phases present, by applying the methods described above, for removing barite from BT, most if not all of the contamination phases may go away.

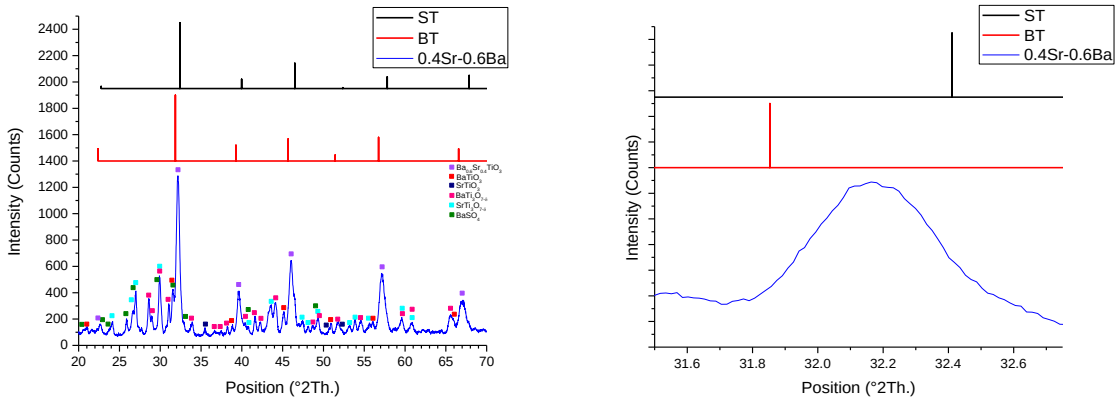

Figure 63: Powder XRD results showing a shift in the (110) peak showing the mixing of BT and ST. Left: Entire XRD plot shows contamination and multiple phases. Right: Peak shift of (110) is due to mixing of Ba and Sr on A sites.

4.4.6 Concluding Remarks

An automated SSG coating process has been developed to apply chemisorbed Ti-O and Ba-O coatings to sunflower pollen via alternating layers of Ti-O and Ba-O via exposure to the alkoxide precursor solution followed by rinsing and water. Subsequent burning of Ba-Ti-O coated specimens yielded BT replicas that retained the 3D pollen shape and sharp spines, which indicated that the surface carboxyl density of the sporopollenin on the pollen exine was sufficient as to allow for the generation of continuous chemisorbed Ba-Ti-O-bearing layers that remained inter-connected upon firing. The Ba-O to Ti-O ratio was investigated and a method of controlling the deposition ratio was devised based on solution concentrations and ratio of SSG cycles.

Sulfur-containing phases were commonly found in $BaTiO_3$ containing replicas. The sulfur-containing phases were either removed of prohibited from forming via thermal treatments in a closed ampule. The SO_3 gas in the sealed ampules was controlled with the use on BaO_2 at a lower temperature than that of the Barium Titanate Replicas to pin the partial pressure below that in the BT. This process was successful in prohibiting the formation of $BaSO_4$ in the replica particles. Although BaS was occasionally found in the replicas, it was removed via washing with DIW. Tetragonal BT pollen replicas that maintained the structure of the pollen were synthesized by firing the coated pollens at 1000 °C for 8 hours.

BST pollen replicas were generating using a SSG process consisting of alternating a Ti-O precursor and precursor solution mixed with Sr and Ba. The ratio of Ba:Sr was varied in solution and the resulting effect on the Ba:Sr ratio was monitored. This allowed for pollen replicas with tunable dielectric constants to be fabricated.

These processes were shown to be capable of producing BT and BST pollen replicas that have long range electrostatic adhesive properties. These replicas also showed increased adhesion when a voltage was applied to them in the proximity of a grounded plate.

4.5 References

[1] W. B. Goodwin, I. J. Gomez, Y. N. Fang, J. C. Meredith, and K. H. Sandhage, "Conversion of Pollen Particles into Three-Dimensional Ceramic Replicas Tailored for Multimodal Adhesion," *Chemistry of Materials,* vol. 25, pp. 4529-4536, Nov 2013.

[2] M. L. Ott and H. A. Mizes, "Atomic force microscopy adhesion measurements of surface-modified toners for xerographic applications," *Colloids and Surfaces A: Physicochemical and Engineering Aspects,* vol. 87, pp. 245-256, 8/16/ 1994.

[3] W. Richard Bowen and T. A. Doneva, "Atomic Force Microscopy Studies of Membranes: Effect of Surface Roughness on Double-Layer Interactions and Particle Adhesion," *Journal of Colloid and Interface Science,* vol. 229, pp. 544-549, 9/15/ 2000.

[4] K. Cooper, A. Gupta, and S. Beaudoin, "Simulation of the Adhesion of Particles to Surfaces," *Journal of Colloid and Interface Science,* vol. 234, pp. 284-292, 2/15/ 2001.

[5] M. A. Meitl, Z. T. Zhu, V. Kumar, K. J. Lee, X. Feng, Y. Y. Huang*, et al.*, "Transfer printing by kinetic control of adhesion to an elastomeric stamp," *Nat. Mater.,* vol. 5, p. 33, 2006.

[6] S. Mitragotri and J. Lahann, "Physical approaches to biomaterial design," *Nat. Mater.,* vol. 8, p. 15, 2009.

[7] Y. Huang, M. Liu, J. Wang, J. Zhou, L. Wang, Y. Song*, et al.*, "Controllable Underwater Oil-Adhesion-Interface Films Assembled from Nonspherical Particles," *Advanced Functional Materials,* vol. 21, pp. 4436-4441, Dec 6 2011.

[8] K. E. Fischer, G. Nagaraj, R. H. Daniels, E. Li, V. E. Cowles, J. L. Miller*, et al.*, "Hierarchical nanoengineered surfaces for enhanced cytoadhesion and drug delivery," *Biomaterials,* vol. 32, p. 3499, 2011.

[9] L. Zhang, J. Shi, Z. Jiang, Y. Jiang, R. Meng, Y. Zhu*, et al.*, "Facile Preparation of Robust Microcapsules by Manipulating Metal-Coordination Interaction between Biomineral Layer and Bioadhesive Layer," *ACS Appl. Mater. Interfaces,* vol. 3, p. 597, 2011.

[10] K. L. Johnson, K. Kendall, and A. D. Roberts, "Surface Energy and the Contact of Elastic Solids," *Proc. R. Soc. London, Ser. A,* vol. 324, p. 301, 1971.

[11] B. V. Derjaguin, V. M. Muller, and Y. P. Toporov, "Effect of contact deformations on the adhesion of particles," *J. Colloid Interface Sci.,* vol. 53, p. 314, 1975.

[12] D. Tabor, *J. Colloid Interface Sci.,* vol. 58, p. 2, 1977.

[13] V. M. Muller, V. S. Yushchenko, and B. V. Derjaguin, *J. Colloid Interface Sci.,* vol. 77, p. 91, 1980.

[14] D. Maugis and H. M. Pollock, "Surface forces, deformation and adherence at metal microcontacts," *Acta Metall.,* vol. 32, p. 1323, 1984.

[15] W. A. Ducker, T. J. Senden, and R. M. Pashley, "Direct measurement of colloidal forces using an atomic force microscope," *Nature,* vol. 353, p. 239, 1991.

[16] G. O. W. Kremp, *Morphologic Encyclopedia of Palynology*, 1968.

[17] J. W. Walker and J. A. Doyle, *Ann. Mo. Bot. Gard.,* vol. 62, p. 664, 1975.

[18] G. Erdtman, *Pollen Morphology and Plant Taxonomy*, 1986.

[19] S. Blackmore and S. H. Barnes, *Pollen and Spores: Patterns of Diversification*, 1991.

[20] A. Ressayre, B. Godelle, C. Raquin, and P. H. Gouyon, "Aperture Pattern Ontogeny in Angiosperms," *J. Exp. Zool.,* vol. 294, p. 122, 2002.

[21] M. Hesse, H. Halbritter, R. Zetter, M. Weber, R. Buchner, A. Frosch-Radivo*, et al.*, *Pollen Terminology: An Illustrated Handbook*, 2009.

[22] E. Horn, *Trans. Kans. Acad. Sci.,* vol. 36, p. 91, 1933.

[23] W. Grater and T. Stemen, "The plant, the pollen and the patient," *Rev. Paleobot. Palynol.,* vol. 4, p. 187, 1967.

[24] L. H. Ziska, D. E. Gebhard, D. A. Frenz, S. Faulkner, B. D. Singer, and J. G. Straka, "Cities as harbingers of climate change: Common ragweed, urbanization, and public health," *J. Allergy Clin. Immunol.,* vol. 111, p. 290, 2003.

[25] P. J. Beggs, "Impacts of climate change on aeroallergens: past and future," *Clin. Exp. Allergy,* vol. 34, p. 1507, 2004.

[26] C. A. Rogers, P. M. Wayne, E. A. Macklin, M. L. Mullenberg, C. J. Wagner, P. R. Epstein*, et al.*, "Interaction of the Onset of Spring and Elevated Atmospheric CO_2 on
Ragweed Pollen Production," *Environ. Health Perspect.,* vol. 114, p. 865, 2006.

[27] B. Fumanal, B. Chauvel, and F. Bretagnolle, "Estimation of pollen and seed production of common ragweed in France," *Ann. Agric. Environ. Med.,* vol. 14, p. 233, 2007.

[28] L. Ziska, K. Knowlton, C. Rogers, D. Dalan, N. Tierney, M. A. Elder, *et al.*, "Recent warming by latitude associated with increased length of ragweed pollen season in central North America," *Proc. Natl. Acad. Sci. U.S.A.,* vol. 108, p. 4248, 2011.

[29] M. D. Bajin, C. Cingi, F. Oghan, and M. K. Gurbuz, "Global warming and allergy in Asia Minor," *Arch. Oto-Rhino-Laryngol.,* vol. 270, p. 27, 2013.

[30] W. Brandon Goodwin, I. J. Gomez, Y. Fang, J. C. Meredith, and K. H. Sandhage, "Conversion of Pollen Particles into Three-Dimensional Ceramic Replicas Tailored for Multimodal Adhesion," *Chemistry of Materials,* vol. 25, pp. 4529-4536, 2013.

[31] H. Lin, I. Gomez, and J. C. Meredith, "Pollenkitt wetting mechanism enables species-specific tunable pollen adhesion," *Langmuir,* vol. 29, pp. 3012-3023, Mar 5 2013.

[32] I. Ichinose, H. Senzu, and T. Kunitake, "Stepwise adsorption of metal alkoxides on hydrolyzed surfaces: A surface sol-gel process," *Chemistry Letters,* pp. 831-832, 1996 1996.

[33] I. Ichinose, H. Senzu, and T. Kunitake, "A surface sol-gel process of TiO2 and other metal oxide films with molecular precision," *Chemistry of Materials,* vol. 9, pp. 1296-&, Jun 1997.

[34] S. R. Hall, H. Bolger, and S. Mann, "Morphosynthesis of complex inorganic forms using pollen grain templates," *ChemComm,* pp. 2784-2785, 2003.

[35] Y. Wang, Z. Liu, B. Han, Z. Sun, J. Du, J. Zhang, *et al.*, "Replication of biological organizations through a supercritical fluid route," *ChemComm,* pp. 2948-2950, Jun 21 2005.

[36] S. R. Hall, V. M. Swinerd, F. N. Newby, A. M. Collins, and S. Mann, "Fabrication of Porous Titania (Brookite) Microparticles with Complex Morphology by Sol-Gel Replication of Pollen Grains," *Chem. Mater.,* vol. 18, pp. 598-600, 2006.

[37] P. Li, C. F. Zeng, L. X. Zhang, and N. P. Xu, *J. Inorg. Mater.,* vol. 23, p. 49, 2008.

[38] F. Cao and D. X. Li, "Morphology-controlled synthesis of SiO_2 hollow microspheres using pollen grain as a biotemplate," *Biomed Mater,* vol. 4, pp. 1-6, Apr 2009.

[39] X. Yang, X. Song, Y. Wei, W. Wei, L. Hou, and X. Fan, "Synthesis of spinous ZrO_2 core–shell microspheres with good hydrogen storage properties by the pollen bio-template route," *Scripta Materialia,* vol. 64, pp. 1075-1078, 2011.

[40] B. J. Thio, K. K. Clark, and A. A. Keller, "Magnetic pollen grains as sorbents for facile removal of organic pollutants in aqueous media," *J Hazard Mater,* vol. 194, pp. 53-61, Oct 30 2011.

[41] Y. Xia, W. Zhang, Z. Xiao, H. Huang, H. Zeng, X. Chen*, et al.*, "Biotemplated fabrication of hierarchically porous NiO/C composite from lotus pollen grains for lithium-ion batteries," *Journal of Materials Chemistry,* vol. 22, pp. 9209-9215, 2012 2012.

[42] M. W. Anderson, S. M. Holmes, N. Hanif, and C. S. Cundy, "Hierarchical Pore Structures through Diatom Zeolitization " *Angew. Chem., Int. Ed.,* vol. 39, p. 2707, 2000.

[43] N. L. Rosi, C. S. Thaxton, and C. A. Mirkin, "Control of nanoparticle assembly by using DNA-modified diatom templates," *Angew. Chem., Int. Ed.,* vol. 43, p. 5500, 2004.

[44] C. S. Gaddis and K. H. Sandhage, "Freestanding Microscale 3-D Polymeric Structures with Biologically-derived Shapes and Nanoscale Features," *J. Mater. Res.,* vol. 19, p. 2541, 2004.

[45] J. Zhao, C. S. Gaddis, Y. Cai, and K. H. Sandhage, "Free-standing Microscale Structures of Zirconia Nanocrystals with Biologically Replicable 3-D Shapes,," *J. Mater. Res.,* vol. 20, p. 282, 2005.

[46] E. K. Payne, N. L. Rosi, C. Xue, and C. A. Mirkin, "Sacrificial biological templates for the formation of nanostructured metallic microshells," *Angew. Chem., Int. Ed.,* vol. 44, p. 5064, 2005.

[47] M. R. Weatherspoon, M. S. Haluska, Y. Cai, J. S. King, C. J. Summers, R. L. Snyder*, et al.*, "Phosphor Microparticles of Controlled 3-D Shape from Phytoplankton," *J. Electrochem. Soc.,* vol. 153, p. H34, 2006.

[48] D. Losic, J. G. Mitchell, R. Lai, and N. H. Voelcker, "Rapid Fabrication of Micro- and Nanoscale Patterns by Replica Molding from Diatom Biosilica," *Adv. Funct. Mater.,* vol. 17, p. 2439, 2007.

[49] U. Kusari, Z. Bao, Y. Cai, G. Ahmad, K. H. Sandhage, and L. G. Sneddon, "Formation of Nanostructured, Nanocrystalline Boron Nitride Microparticles with Diatom-Derived 3-D Shapes," *Chem. Commun.,* vol. 11, p. 1177, 2007.

[50] Z. Bao, E. M. Ernst, S. Yoo, and K. H. Sandhage, "Syntheses of Porous Self-Supporting Metal Nanoparticle Assemblies with 3-D Morphologies Inherited from Biosilica Templates (Diatom Frustules)," *Adv. Mater.,* vol. 21, p. 474, 2009.

[51] Y. Fang, Q. Wu, M. B. Dickerson, Y. Cai, S. Shian, J. D. Berrigan*, et al.*, "Protein-Mediated Layer-by-Layer Syntheses of Freestanding Microscale

Titania Structures with Biologically Assembled 3-D Morphologies," *Chemistry of Materials,* vol. 21, pp. 5704-5710, 2009.

[52] C. J. Johnson, "Some dielectric and electro-optic properties of $BaTiO_3$ single crystals," *Applied Physics Letters,* vol. 7, 1965.

[53] L. Delaey, "Phase Transformations In Materials," in *Wiley-vch Verlag Gmbh*, G. Kostorz, Ed., ed Weinheim Germany, 2001.

[54] T. C. Rutt and J. A. Stynes, "Fabrication of multilayer ceramic capacitors by metal impregnation," *IEEE Transactions on Parts, Hybrids, and Packaging,* vol. 9, 1973.

[55] H. Igarashi, C. Betoh, and K. Okazaki, "Vapor-phase diffusion of metal oxides into barium titanate(IV) ceramics and its application to multilayer boundary layer capacitors," *Advances in Ceramics,* vol. 1, 1981.

[56] R. Wernicke, "Ceramic multilayer capacitors and nonlinear resistors," *Science of Ceramics,* vol. 12, 1984.

[57] H. J. Hagemann, D. Hennings, and R. Wernicke, "Ceramic multilayer capacitors," *Philips Technical Review,* vol. 41, 1984.

[58] P. D. Levett, "Properties and applications of positive temperature coefficients thermistors," *Ceramic Age,* vol. 83, 1967.

[59] J. Daniels, K. H. Haerdtl, and R. Wernicke, "The PTC effect of barium titanate," *Philips Technical Review,* vol. 38, 1979.

[60] M. Kuwabara, "Explanation for the PTCR effect in barium titanate ceramics," *Advances in Ceramics,* vol. 7, 1983.

[61] G. V. Lewis, C. R. A. Catlow, and R. E. W. Casselton, "PTCR effect in barium titanate ($BaTiO_3$)," *Journal of the American Ceramic Society,* vol. 68, 1985.

[62] L. S. Lukic, Z. Preradovic, V. Dimic, D. Stefanovic, and L. Vulicevic, "Prognosis the properties of $BaTiO_3$ ceramics for piezoelectric transducers," presented at the Sintering and Materials, Proceedings of the International Symposium on the Science and Technology of Sintering, Haikou, Peop. Rep. China, 1995.

[63] D. Stefanovic, V. Dimic, M. Radmanovic, D. Mancic, L. Lukic, and L. Vulicevic, "Synthesis of $BaTiO_3$ ceramics for piezoelectric transducers," *Science of Sintering,* vol. 28, 1996.

[64] K. Kiss, J. Magder, M. S. Vukasovich, and L. R. J., "Ferroelectrics of ultrafine particle size. I. Synthesis of titanate powders of ultrafine particle size," *Journal of the American Ceramic Society,* vol. 49, 1966.

[65] K. S. Mazdiyasni, R. T. Dolloff, and J. S. Smith II, "Preparation of high-purity submicron barium titanate powders," *American Ceramic Society,* vol. 52, 1969.

[66] A. E. Feuersanger, A. K. Hagenlocher, and A. L. Solomon, "Preparation and properties of thin barium titanate films," *Journal of the Electrochemical Society,* vol. 111, 1964.

[67] K. M. Hung, C. S. Hsieh, W. D. Yang, and Y. J. Sun, "The preparatory optimal conditions of barium titanate thin film from a hydrothermal method at low temperature," *Journal of Materials Science,* vol. 42, 2007.

[68] J. F. Scott, "Dimensional effects on ferroelectrics. Ultra-thin single crystals, nanotubes, nano-rods, and nano-ribbons," *Ferroelectrics,* vol. 316, 2005.

[69] J. H. Wei, J. Shi, Z. Y. Liu, and J. B. Wang, "Polymer-assisted synthesis of $BaTiO_3$ nanorods," *Journal of Materials Science,* vol. 41, 2006.

[70] X. Zhu, J. Zhu, S. Zhou, Z. Liu, N. Ming, and D. Hesse, "$BaTiO_3$ nanocrystals: hydrothermal synthesis and structural characterization," *Journal of Crystal Growth,* vol. 283, 2005.

[71] S. Yoon, S. Baik, M. G. Kim, N. Shin, and I. Kim, "Synthesis of tetragonal barium titanate nanoparticles via alkoxide-hydroxide sol-precipitation: effect of water addition," *Journal of the American Ceramic Society,* vol. 90, 2007.

[72] Y. Luo, I. Szafraniak, N. D. Zakharov, V. Nagarajan, M. Steinhart, R. B. Wehrspohn*, et al.*, "Nanoshell tubes of ferroelectric lead zirconate titanate and barium titanate," *Applied Physics Letters,* vol. 83, 2003.

[73] J. J. Urban, J. E. Spanier, L. Ouyang, W. S. Yun, and H. Park, "Single-crystalline barium titanate nanowires," *Advanced Materials,* vol. 15, 2003.

[74] U. A. Joshi, S. Yoon, S. Baik, and J. S. Lee, "Surfactant-Free Hydrothermal Synthesis of Highly Tetragonal Barium Titanate Nanowires: A Structural Investigation," *Journal of Physical Chemistry B,* vol. 110, 2006.

[75] J. P. Vernon, Y. Fang, Y. Cai, and K. H. Sandhage, "Morphology-preserving conversion of a 3D bioorganic template into a nanocrystalline multicomponent oxide compound," *Angew Chem Int Ed Engl,* vol. 49, pp. 7765-7768, Oct 11 2010.

[76] J. P. Vernon, N. Hobbs, Y. Cai, A. Lethbridge, P. Vukusic, D. D. Deheyn*, et al.*, "3D photoluminescent lanthanide-doped barium titanate structures synthesized by coating and shape-preserving reaction of complex-shaped bioorganic templates," *Journal of Materials Chemistry,* vol. 22, pp. 10365-10940, 2012.

[77] J. P. Vernon, Y. Fang, Y. Cai, and K. H. Sandhage, "Morphology-Preserving Conversion of a 3D Bioorganic Template into a Nanocrystalline Multicomponent Oxide Compound," *Angewandte Chemie,* vol. 122, pp. 7931-7934, 2010.

[78] W. B. Goodwin, "Controlled Modulation of Short- and Long-range Microscale Biogenic Replicas," Ph.D. Dissertation, Materials Science & Engineering, Georgia Institute of Technology, Georgia Institute of Technology, 2014.

[79] J. A. Basmajian and R. C. DeVries, "Phase Equilibria in the System BaTiO3–SrTiO3," *Journal of the American Ceramic Society,* vol. 40, pp. 373-376, 1957.

[80] D. Barb, E. Bărbulescu, and A. Bărbulescu, "Diffuse Phase Transitions and Ferroelectric-Paraelectric Diagram for the BaTiO3-SrTiO3 System," *physica status solidi (a),* vol. 74, pp. 79-83, 1982.

[81] L. Vegard, "Die Konstitution der Mischkristalle und die Raumfüllung der Atome," *Zeitschrift für Physik,* vol. 5, pp. 17-26, 1921/01/01 1921.

[82] A. R. Denton and N. W. Ashcroft, "Vegard's law," *Physical Review A,* vol. 43, pp. 3161-3164, 03/01/ 1991.

[83] H. Weaver, "Dielectric properties of single crystals of SrTiO< sub> 3</sub> at low temperatures," *Journal of Physics and Chemistry of Solids,* vol. 11, pp. 274-277, 1959.

[84] R. A. Cowley, "Lattice Dynamics and Phase Transitions of Strontium Titanate," *Physical Review,* vol. 134, pp. A981-A997, 05/18/ 1964.

[85] H. V. Alexandru, C. Berbecaru, A. Ioachim, L. Nedelcu, and A. Dutu, "BST solid solutions, temperature evolution of the ferroelectric transitions," *Applied Surface Science,* vol. 253, pp. 354-357, Oct 2006.

[86] C. L. Fu, C. R. Yang, H. W. Chen, Y. X. Wang, and L. Y. Hu, "Microstructure and dielectric properties of BaSr1-xTiO3 ceramics," *Materials Science and Engineering B-Solid State Materials for Advanced Technology,* vol. 119, pp. 185-188, May 2005.

[87] H. Abdelkefi, H. Khemakhem, G. Velu, J. C. Carru, and R. V. d. Muhll, "Dielectric properties and ferroelectric phase transitions in $Ba_xSr_{1-x}TiO_3$ solid solution," *Journal of Alloys and Compounds,* vol. 399, 2005.

[88] L. Zhou, P. M. Vilarinho, and J. L. Baptista, "Dependence of the structural and dielectric properties of $Ba_{1-x}Sr_xTiO_3$ ceramic solid solutions on raw material," *Journal of the European Ceramic Society,* vol. 19, 1999.

[89] G. Subramanyam, F. Ahamed, R. Biggers, and A. Campbell, "Design considerations for a novel coplanar waveguide based ferroelectric varactor shunt switch," *Integrated Ferroelectrics,* vol. 77, 2005.

[90] S. B. Majumder, M. Jain, R. S. Katiyar, F. W. Keuls, and F. A. Miranda, "Sol-gel derived grain oriented barium strontium titanate thin films for phase shifter applications," *Journal of Applied Physics,* vol. 90, 2001.

[91] F. Zimmermann, M. Voigts, C. Weil, R. Jakoby, P. Wang, W. Menesklou, *et al.*, "Investigation ofbarium strontium titanate thick films for tunable phase shifters," *Journal of the European Ceramic Society,* vol. 21, 2001.

[92] H. S. Kim, T. S. Hyun, H. G. Kim, I. D. Kim, T. S. Yun, and J. C. Lee, "Orientation effect on microwave dielectric properties of Si-integrated Ba0.6Sr0.4TiO3 thin films for frequency agile devices," *Applied Physics Letters,* vol. 89, 2006.

[93] X. Wang, W. Lu, J. Liu, F. Liang, and D. Zhou, "Influence of MgO on structure and low-frequency properties of $Ba_{0.6}Sr_{0.4}TiO_3$ ferroelectric ceramics," *Guisuanyan Xuebao,* vol. 32, 2004.

[94] B. Su, J. E. Holmes, C. Meggs, and T. W. Button, "Dielectric and microwave properties of barium strontium titanate (BST) thick films on alumina substrates," *Journal of the European Ceramic Society,* vol. 23, 2003.

[95] P. M. Suherman, T. J. Jackson, Y. Y. Tse, I. P. Jones, R. I. Chakalova, M. J. Lancaster, *et al.*, "Microwave properties of $Ba_{0.5}Sr_{0.5}TiO_3$ thin film coplanar phase shifters," *Journal of Applied Physics,* vol. 99, 2006.

[96] A. Kumar and S. G. Manavalan, "Characterization of barium strontium titanate thin films for tunable microwave and DRAM applications," *Surface and Coatings Technology,* vol. 198, 2005.

[97] Y. H. Xie, Y. Y. Lin, and T. A. Tang, "Characteristics of BST Thin Film Prepared by Novel Chemical Solution Deposition Method for High-Density DRAM " *Application. Integrated Ferroelectrics,* vol. 47, 2002.

[98] S. Rosenfeldt and B. G. Galati, "Pollen morphology of Oxalis species from Buenos Aires province (Argentina)," *Biocell,* vol. 31, pp. 13-21, 2007.

[99] W. O. Statton, "The Phase Diagram of the BaO–TiO2 System," *The Journal of Chemical Physics,* vol. 19, pp. 33-40, 1951.

[100] S. Lee, C. A. Randall, and Z. K. Liu, "Modified phase diagram for the barium oxide-titanium dioxide system for the ferroelectric barium titanate," *Journal of the American Ceramic Society,* vol. 90, pp. 2589-2594, Aug 2007.

[101] J. H. Jeon, "Effect of SrTiO3 concentration and sintering temperature on microstructure and dielectric constant of Ba1-xSrxTiO3," *Journal of the European Ceramic Society,* vol. 24, pp. 1045-1048, 2004 2004.

[102] G. V. Keller, "Rock and mineral properties," *Electromagnetic methods in applied geophysics,* vol. 1, pp. 13-52, 1988.

[103] C. Blount, "Barite solubilities and thermodynamic quantities up to 300/sup 0/C and 1400 bars," *Am. Mineral.;(United States),* vol. 62, 1977.

[104] H. Puchelt and I. J. Setiobudi, "New dissolution technique for rarely soluble sulfate minerals for AAS and ICP investigations," *Fresenius' Zeitschrift für analytische Chemie,* vol. 335, pp. 692-694, 1989.

[105] J. Wang, J. Fang, S. C. Ng, L. M. Gan, C. H. Chew, X. Wang*, et al.*, "Ultrafine barium titanate powders via microemulsion processing routes," *Journal of the American Ceramic Society,* vol. 82, pp. 873-881, 1999.

[106] M. W. Chase, "JANAF thermochemical tables," *JANAF thermochemical tables, by Chase, MW Washington, DC: American Chemical Society; New York: American Institute of Physics for the National Bureau of Standards, c1986.. United States. National Bureau of Standards.,* vol. 1, 1986.

[107] I. Barin, *Thermochemical Data of Pure Substances, Thermochemical Data of Pure Substances*: Wiley-VCH, 1997.

[108] K. Kinoshita and A. Yamaji, "Grain-size effects on dielectric properties in barium titanate ceramics," *Journal of Applied Physics,* vol. 47, pp. 371-373, 1976.

[109] T. M. Shaw, S. Trolier-McKinstry, and P. C. McIntyre, "The properties of ferroelectric films at small dimensions," *Annual Review of Materials Science,* vol. 30, pp. 263-298, 2000.

CHAPTER 5: Evaluation of the Deposition Behavior of Titanium and Barium Alkoxides on Silica

5.1 Summary

In this chapter, the deposition behavior of titanium, and barium isopropoxide precursors on silica substrates has been investigated. The scientific knowledge gained in this study is directly relevant to the SSG coating method used in the previous chapters. The titanium precursor, Ti(IV) isopropoxide, was studied the most thoroughly, with preliminary investigation into the deposition of Ba(II) isopropoxide. Isothermal models were evaluated for titanium and for barium precursors. The layer-by-layer deposition of Ba(II) isopropoxide, and Ti(IV) isopropoxide were evaluated. Additionally for Ti(IV) isopropoxide, the limited kinetic rate of reaction was evaluated at the concentration of 12.5 mM.

5.2 Introduction

The surface sol-gel coating method has been used to deposit a variety of oxides including Sn-O, Ti-O, W-O, Er-O, Sm-O, Ba-O, Fe-O, and Zr-O. It has been shown that the various precursors for these oxides react at different rates[1]. However, no research to date has investigated the specific kinetics of reaction occurring during SSG deposition and how the process rate might be controlled. Control of the reaction kinetics would be useful for making the coating process more efficient, more precise, and less expensive. As an initial investigation into the kinetics of deposition of alkoxides via the SSG LbL method, the deposition of

Ba-isopropoxide and Ti-isopropoxide onto a QCM crystal (with SiO_2 on its surface) has been examined in this work.

Ichinose and Kunitake have examined the LbL, as-deposited mass gain of various alkoxide precursors.[1, 2] Silicon methoxide, Titanium n-butoxide and others were analyzed for their per-layer mass gain, but the coatings were examined ex-situ and the thickness of each additional layer increased as the precursor solution was exposed to air.[1] This was likely due to hydrolysis in solution leading to polymerization of the precursor fluid. In this research, the QCM in-situ measurements allowed for avoidance of such contamination.

5.3 Theory

5.3.1 Evaluation of Equilibrium Adsorption

In order to utilize a particular alkoxide for binding to the surfaces of silica (or any hydroxylated or carboxylated surface), the influences of the conditions of the alkoxide-bearing solution (e.g., concentration, temperature) and the surface chemistry of silica (or any hydroxylated or carboxylated surface) on the equilibrium loading and distribution of alkoxide species on such surfaces need to be understood. Knowledge of the influences of such solution and substrate conditions on the rate of alkoxide binding can also shed light on the kinetic mechanism(s) of such binding, as well as to allow for determination of the time required to achieve an equilibrium alkoxide surface concentration.

In-situ Quartz Crystal Microbalance (QCM) analysis was utilized to investigate the kinetics of alkoxide adsorption on, and desorption from, a hydroxylated surface. The rate-limiting step(s), and associated kinetic rate laws,

for a single alkoxide adsorption and desorption to/from a hydroxylated surface under varied solution conditions have been examined.

The alkoxides selected have all been used to generate conformal coatings on hydroxyl-rich surfaces. Initially, the precursors were tested individually to study the growth of individual precursors in solution. Deeper understanding of the mechanism of alkoxide adsorption onto silica (or other hydroxylated surfaces) could be obtained by evaluating the kinetic mechanism(s) associated with such physisorption.

The equilibrium adsorption of a precursor onto a SiO_2 coated quartz crystal was analyzed for various bulk solution concentrations using QCM analysis. The mass deposited per area, Δm/A, resulting from precursor adsorption from a flowing aqueous solution onto the silica coated quartz crystal was tracked in real time via the associated change in resonance frequency (ΔF) of the vibrating quartz crystal. For a dense film, this relationship is described by the Sauerbrey equation.[3, 4]

$$\Delta F = -\frac{2f_0^2}{A\sqrt{\rho_q G_q}}\Delta m \qquad \textbf{(18)}$$

Here, ΔF is the change in frequency of the QCM crystal, f_0 is the resonance frequency of the QCM crystal, Δm is the change in mass on the QCM, A is the area of the sensor, ρ_q is the density of the quartz (2.648 g/cm^3) and G_q is the shear modulus of the QCM (29.47 GPa). The adsorption onto the silica surface was tracked in real time for a variety of concentrations. The influence of the concentration of a precursor in solution on the equilibrium adsorption was

evaluated by comparison to a number of equilibrium isotherms. For example, with the Langmuir isotherm, each surface site is assumed to accommodate one molecule, all adsorption sites are assumed to have equal affinity for the adsorbing species, and the adsorption of a given molecule is assumed to be independent of the presence of adsorbed species on neighboring sites; that is the Langmuir model assumes no interaction between adsorbed molecules.[5] The Langmuir model assumes no interaction between molecules. Under these conditions, the equilibrium adsorption is given by:

$$\Gamma_i = \frac{K\Gamma_i^{sat} a_i}{(1 + Ka_i)} \quad \textbf{(19)}$$

Here, Γ_i is the equilibrium adsorption, K is the equilibrium rate constant, Γ_i^{sat} is the saturation adsorption, and a_i is the activity of the reactive species. For a sufficiently dilute solution (precursor concentration < 100 mM), it is reasonable to assume that the concentration of the precursor will fall in the Henry's law regime for the bulk solution. In this case, the activity coefficient for the precursor is independent of the precursor concentration. Thus, with the use of a Henrian reference state, the activity coefficient for the precursor is unity and Equation (19) becomes:

$$\Gamma_i = \frac{K\Gamma_i^{sat} C_i}{(1 + KC_i)} \quad \textbf{(20)}$$

Here C_i is the concentration of the reactive species in the precursor solution. Commonly, adsorption onto a surface is defined not by the equilibrium

adsorption, Γ_i, but instead by the ratio of equilibrium adsorption to saturation adsorption, giving Equation (21) for the fractional coverage.

$$\theta_i = \frac{\Gamma_i}{\Gamma_i^{sat}} \quad \textbf{(21)}$$

Rearranging Equation (20) to solve for the inverse of the equilibrium adsorption gives Equation (22).

$$\frac{1}{\Gamma_i} = \frac{1}{\Gamma_i^{sat}} + \left(\frac{1}{K\Gamma_i^{sat}}\right)\left(\frac{1}{C_i}\right) \quad \textbf{(22)}$$

This equation allows for the inverse of the equilibrium adsorption to be plotted against the inverse of the bulk solution concentration and, if the model is correct, the plot will produce a straight line. If a straight line is produced, the saturation adsorption can be determined from the y-axis intercept and the equilibrium constant can then be evaluated from the slope of the line.

If the affinities of adsorption sites on the silica surface for a given precursor differ appreciably, then the Langmuir isotherm is not expected to be correct and the plot based on Equation (22) is not expected to be linear.

An alternative is the Freundlich model, which considers the presence of surface sites with different enthalpies of adsorption.[6] The filling of these sites results in an exponential decay in the adsorption enthalpy of remaining adsorption sites, and is expressed as Equation (23).

$$\Gamma_i = K_f (C_i)^{1/n} \quad \textbf{(23)}$$

Here, n is a measure of the heterogeneity in the enthalpy of adsorption for different surface sites and K_f indicates the adsorption capacity of the surface. Unlike the Langmuir model, the Freundlich model has been shown to be accurate at high concentrations, but fails to adhere to Henry's law for low concentrations, where Γ_i should be linearly related to C_i.[7, 8] This model can be evaluated by rearranging Equation (23) after taking the log of both side of the equation.

$$log\, \Gamma_i = log\, K_f + (1/n) log\, C_i \quad \textbf{(24)}$$

With Freundlich's model in this form, the raw data can be plotted and a linear regression can be used to evaluate the quality of fit of the data.

To produce a more accurate model, Redlich and Peterson developed a hybrid isotherm which is characteristic of Langmuir behavior at low concentrations and of Freundlich behavior at high concentrations.[8-11]

$$\Gamma_i = \frac{K \Gamma_i^{sat} C_i}{\left(1 + {}^{K}/_{K_f}\, \Gamma_i^{sat} (C_i)^{[1-(1/n)]}\right)} \quad \textbf{(25)}$$

Here, K, K_f, and n are from the Langmuir and Freundlich models. These models were evaluated to determine the best fit for the adsorption data for a given precursor.

As mentioned, the Langmuir model is the simplest model and it assumes that the adsorption of a given molecule is independent of the occupation of neighboring adsorption sites. For a given precursor, this assumption may not be valid at sufficiently high levels of adsorption. With high levels of adsorption, the influence of lateral interactions (electrostatic or steric) may have a significant influence on the adsorption equilibrium. To account for these interactions, Fowler and Guggenheim have modified the Langmuir isotherm to produce Equation (26).[12]

$$KC_i = \frac{\theta_i}{(1-\theta_i)} e^{\frac{-2\omega}{kT}\theta_i} \quad \textbf{(26)}$$

Here, k is Boltzmann's constant, K is an equilibrium constant, T is Temperature, and ω is the relative interaction energy between nearest-neighbor adsorbed species on the silica surface. The fit of this model can be evaluated with the same method as before, by linearizing the equation and plotting the data. The Fowler and Guggenheim isotherm becomes Equation (27).

$$ln\frac{C_i(1-\theta_i)}{\theta_i} = -ln\,K - \frac{2\omega}{kT}\theta_i \quad \textbf{(27)}$$

If such adsorbate - adsorbate interactions on the silica surface are significant, then a plot of $\ln[C_i(1-\Theta_i)/(\Theta_i)]$ vs. Θ_i will yield a straight line, from which the intercept and slope may be used to calculate the equilibrium reaction constant, K, and the interaction energy, ω, respectively.[13] In such a case, the value of ω is negative or positive for repulsive or attractive interactions, respectively, with

the magnitude of ω revealing the strength of the interaction between adsorbates.

These two possible deviations from the Langmuir model were accounted for and the data was compared to the models. For non-negligible heterogeneity in the binding affinity of surface sites the Freundlich model was used, whereas for non-negligible interactions between adsorbates, the Fowler and Guggenheim model was used. Other models [14-18] have been produced to provide more accurate isotherms for different systems, but they were not examined in this research.

Future researchers could investigate the applicability of other isothermal models. A variety of other isotherms have been developed and reported in the literature and could lead to greater insight into the adsorption. These include, but are not limited to: the Temkin model[14] (the enthalpy of adsorption decreases linearly with an increase in the fraction of filled sites), the Toth model[15, 16] (the enthalpy of adsorption follows an asymmetrical quasi-Gaussian distribution), Flory-Huggins model[17] (pre-adsorbed solvent molecules are replaced by the adsorbate), and the Halsey model[18] (a Fowler and Guggenheim type isotherm for lateral interactions between 3 or more adsorbates).

5.3.2 Kinetic Mechanism (Rate limiting Step) of Reaction

The process of adsorption from a liquid solution may be rate limited by mass transport of a reactant species toward, or product species from, the solid/liquid interface and/or by a chemical reaction at the solid/liquid interface.

For liquid-phase diffusion control (i.e., for rapid chemical reactions at the solid/liquid interface), the change of adsorption with time, $d(\Gamma_i^t)/dt$ (expressed as the change in adsorbed mass per area per time), may be described by a Noyes-Whitney-Nernst-type equation[19] [20]:

$$\frac{d(\Gamma_i^t)}{dt} = \frac{D_i(C_b - C_s)}{\delta_i} \quad \textbf{(28)}$$

Here Γ_i^t is the adsorption of species i in time t; D_i is the diffusion coefficient of this species through a concentration boundary layer in the liquid; C_s and C_b refer to the concentration of this species in the liquid at the solid/liquid interface and in the bulk solution, respectively; and δ_i is the concentration boundary layer thickness for species i. For laminar flow past a flat plate, the concentration boundary layer thickness may be described by[21]:

$$\delta_i = \frac{4.64(X)^{1/2}(D_i)^{1/3}(v)^{1/6}}{(V)^{1/2}} \quad \textbf{(29)}$$

Here X is the distance from the leading edge of the plate, v is the kinematic viscosity of the liquid, and V is the velocity of the bulk fluid. Hence, the mass-transport-controlled change of adsorption with time is given by:

$$\frac{d(\Gamma_i^t)}{dt} = \frac{0.216\ (D_i)^{2/3}(C_b - C_s)(V)^{1/2}}{(X)^{1/2}(v)^{1/6}} \quad \textbf{(30)}$$

This equation indicates that, for the case of liquid phase diffusion control, the change of adsorption with time should be constant with time (since there is no

time-dependent term on the right side of Equation (30), and should increase with the square root of the velocity of the bulk fluid past the plate, until the equilibrium adsorption, Γ_i^{sat}, is achieved.

Because the QCM flow chamber is very small in the z-direction (chamber height = 0.64 mm), it is possible that the flow will not exhibit a standard flow-past-a-flat-plate boundary layer profile. Equations have been proposed, for microfluidic flow chambers with surface reactions, to define the flux of analytes to the reactive surface.[22] [23] Lok, et al. have developed a Lévêque-type equation (Equation (31)).[22]

$$\frac{\partial c_s}{\partial t} = \frac{1}{\Gamma(4/3)9^3}\left(\frac{\gamma}{Dx}\right)^{\frac{1}{3}} D c_0 \quad \textbf{(31)}$$

Here, c_s refers to the surface concentration of the absorbed analyte, *t* is time, $\Gamma(4/3)$ is the gamma function from the value of 4/3, c_0 is the analyte concentration in the bulk liquid, x is the axial location, D is the diffusion coefficient of the analyte in the liquid and γ is the shear rate of the fluid adjacent to the wall.[24]

$$\gamma = \frac{6Q}{b^2 W} \quad \textbf{(32)}$$

The wall shear rate, through a wide rectangle pipe, is defined by Q, the volumetric flow rate, and the height and width of the pipe, b and W, respectively. Hence, the mass-transport-controlled change of adsorption with time is given by:

$$\frac{\partial c_s}{\partial t} = \frac{1}{\Gamma(4/3)9^3}\left(\frac{6Q}{Dxb^2W}\right)^{\frac{1}{3}} Dc_0 \quad \textbf{(33)}$$

Equation (33) indicates that, for the case of liquid phase diffusion control in a microfluidic flow chamber, the change of adsorption with time should be constant with time and should increase with the cube root of the volumetric flow rate of the bulk fluid past the plate, and should increase linearly with bulk analyte concentration until the equilibrium adsorption is achieved.

For chemical reaction control (i.e., for rapid mass transport through the liquid), several cases may be considered. If the rate of reaction is independent of the concentration of a given species, then the reaction would be considered a zeroth order chemical reaction with respect to the species. The change of adsorption with time may be expressed as:

$$\frac{d(\Gamma_i^t)}{dt} = k_0 \quad \textbf{(34)}$$

Here k_0 is the zeroth-order reaction rate constant for adsorption, and Γ_i^t is the adsorption at a given time, t. Separating adsorption terms and time on different sides of this equation, and integrating (for the case where Γ_i^t= 0 at t = 0) yields:

$$\Gamma_i - \Gamma_i^t = \Gamma_i - k_0 t \quad \textbf{(35)}$$

Here, Γ_i is the equilibrium adsorption. This equation applies only for relatively short adsorption times, well below the time required to reach equilibrium adsorption. If

the adsorption is a zeroth-order reaction, the regression of $\Gamma_i - \Gamma_i^t$ vs. time would result in a linear regression with the slope giving $-k_0$ and the intercept giving the saturation adsorption.

The reaction rate may be dependent on the concentration, and could have either first or second order dependence. For a surface chemical reaction that is of first order with respect to an adsorbing species, the change of adsorption with time may be expressed as[25]:

$$\frac{d(\Gamma_i^t)}{dt} = k_1(\Gamma_i - \Gamma_i^t) \quad \textbf{(36)}$$

Here $k_1$is a first-order reaction rate constant for adsorption, and Γ_i and Γ_i^t are the equilibrium adsorption and the adsorption at a given time, t, respectively. Separating adsorption terms and time on different sides of this equation, and integrating (for the case where Γ_i^t= 0 at t = 0) yields:

$$ln[\Gamma_i - \Gamma_i^t] = ln[\Gamma_i] - k_1 t \quad \textbf{(37)}$$

By considering adsorption as a reversible reaction process, with forward and reverse reaction rates expressed as first order rate laws with respect to the species in solution and the adsorbed species, respectively, the following equation has been derived of similar form[26]:

$$ln\left[1-\frac{X_A}{X_A^E}\right]=-\left[\frac{1+\frac{C_B^o}{C_A^o}}{X_A^E+\frac{C_B^o}{C_A^o}}\right]k_1't \quad \textbf{(38)}$$

Here, $X_A$and X_A^E are the fraction of dissolved species adsorbed onto the surface at time t and at equilibrium, respectively, and C_A^o and C_B^o are initial concentrations of the adsorbate on the sorbent and in the solution, respectively. If a first-order chemical reaction is rate limiting, then plots of $\ln\left[\Gamma_i-\Gamma_i^t\right]$ or $\ln[1-X_A/X_A^E]$ vs. time should yield straight lines, the slopes of which may be used to obtain values of the reaction rate constants, k_1 and k_1'.

The following second-order chemical reaction rate law for describing the adsorption kinetics should also be considered:[27]

$$\frac{d\left(\Gamma_i^t\right)}{dt}=k_2\left(\Gamma_i-\Gamma_i^t\right)^2 \quad \textbf{(39)}$$

Separating adsorption terms and time on different sides of this equation, and integrating (for the case where Γ_i^t = 0 at t = 0) yields:

$$\frac{1}{\Gamma_i-\Gamma_i^t}=\frac{1}{\Gamma_i}+k_2t \quad \textbf{(40)}$$

Hence, for a second-order reaction as the rate-limiting step, a plot of $1/\Gamma_i-\Gamma_i^t$ vs. time should yield a straight line, from which the second-order reaction constant, k_2, may be obtained from the slope.

Initial QCM experiments on the kinetics of adsorption of single alkoxide-bearing solutions have been conducted to evaluate the influence of the flow

rate of the alkoxide-bearing solutions on the adsorption kinetics. If the flow rate has no detectable effect on the adsorption kinetics, and if the rate of adsorption is not constant with time (for a given bulk alkoxide solution concentration), then liquid-phase diffusion as the sole rate-limiting step (as per equations (30) and (33)) can be ruled out, and the fits of different rate laws involving chemical reaction control (of the types shown in equations (34),(36),(38), and (39)) to the QCM kinetic data can be examined. In addition to the time dependence, the influences of the starting alkoxide concentration in solution and the solution temperature on the adsorption kinetics have been evaluated. The purpose of the present discussion is to suggest initial rate laws to be considered for comparison with QCM kinetic data. Pending the results of such fitting with the relatively simple rate laws described above, the fits of other rate laws (e.g., for mixed diffusion and chemical reaction control[28]) may also be considered.

In addition to the limiting kinetic rate of reaction, the amount of material deposited is also of interest. The quantity of alkoxide deposited per individual molecule reaction may depend on the number of isopropoxide ligands available to react with the surface. Tin and Titanium isopropoxides each have four ligands and Barium and Strontium isopropoxides each have two. For Tin and Titanium, the ligands are tetrahedrally coordinated and the two ligands of barium and strontium are linearly coordinated. For alkoxides with four ligands, the reaction to the surface may be a two-step process with one ligand reacting quickly and then the second reaction happening after additional time. When the alkoxide only has two ligands, only one may react and the other may not react. Assuming a flat surface with abundant surface hydroxyls, the ratio of

hydroxyls to precursor molecules reacted may be 2-1 and 1-1, for molecules with four and two ligands, respectively.

The mass of precursor deposited can be verified by calculating the predicted deposited mass and evaluation with QCM. Assuming a constant functional group density across multiple QCM samples, the relative amount of material can be calculated by multiplying the surface density by the added mass per functional group and the area of the QCM crystal. By using the QCM, the shift in frequency can be related to the mass deposited, using Equation (18).

5.4 Experimental Procedures

5.4.1 Creation of Precursor Solutions

Precursor solutions for QCM-D analysis were prepared in a nitrogen atmosphere glove box (Vacuum/Atmospheres Corporation, Las Angeles, CA, USA) with a relative humidity maintained below 1%. Relative humidity was measured with an Omega RH32 sensor (OMEGA Engineering, INC. Stamford, CT, USA) before each solution was prepared. Solutions of Ti(IV) isopropoxide were made from Ti(IV) isopropoxide (Alfa Aesar, Ward Hill, MA, USA) diluted with anhydrous isopropanol (99.8+% purity, Acros Organics, Geel, Belgium). Thermal assaying of the as received Ti(IV) isopropoxide by Dr. Vernon indicated that the concentration reported by the vendor was 1.04% less than what was actually in solution.[29] Solutions for hydration were made with 60%v DIW (Milli-Q ultrapure, EMD Millipore, MA, USA) and 40%v isopropanol (99.8+% purity, Acros Organics, Geel, Belgium). The rinse solution was pure anhydrous isopropanol (99.8+% purity, Acros Organics, Geel, Belgium).

Solutions were mixed with a desktop vortexer (Vortex Genie 2, Scientific Industries, NY, USA) and then heated to 40°C and degassed for 5 min. Solutions were prepared immediately before use, to limit solutions with high concentrations of precipitates.

5.4.2 Quartz Crystal Microbalance with Dissipation Principle

A quartz crystal microbalance with dissipation (QCM-D), E4 system from Biolin Scientific (Västra Frölunda, Sweden), was used to study the layer-by-layer deposition of various alkoxides onto a treated SiO_2 surface. For analysis of the LbL deposition, precursor solutions were pumped from solution bottles through an automated solution switching system and into a flow chamber containing the SiO_2 coated QCM crystal. The flow rate was controlled by a down-stream peristaltic pump (Model: ISM935C, Ismatec, IDEX Corporation, IL, USA). The process of deposition of alkoxides was as follows: SiO_2-coated QCM sensors were allowed to achieve a baseline resonance in anhydrous isopropanol (99.8+% purity, Acros Organics, Geel, Belgium). After a baseline was established, a given alkoxide solution of a given concentration in IPA was introduced to the sensor, followed by a second anhydrous IPA rinse. A solution with 40/60%v ratio of water/IPA was then passed by the sensor followed by rinsing with IPA. Each sensor was exposed to multiple deposition cycles.

The shift in fundamental resonance frequency of the QCM crystal and its harmonics (3^{rd}, 5^{th}, 7^{th}, 9^{th}, and 11^{th}) were monitored and recorded simultaneously. The fundamental frequency and harmonics corresponded to the 5 MHz, 15 MHz, 25 MHz, 35 MHz, 45 MHz, and 55 MHz frequencies, respectively.

Dissipation values for the fundamental and the harmonics were monitored with the resonance frequency shifts. The area and depth of sensitivity were different for each harmonic frequency (see Figure 64).

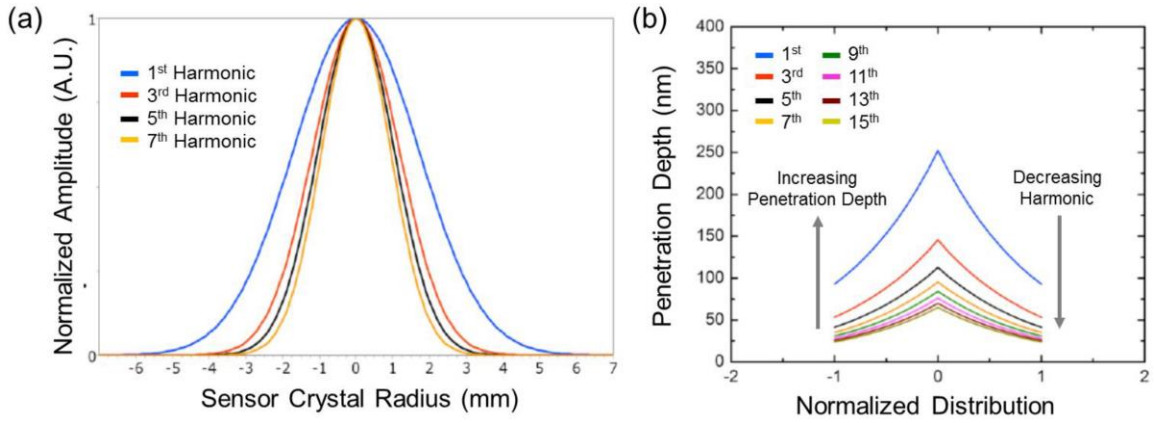

Figure 64: a) Normalized radial amplitude distribution and b) penetration depth for the fundamental frequency (5 MHz) and 3rd (15 MHz), 5th (25 MHz), and 7th (35 MHz) harmonics. Data courtesy of Biolin Scientific (Västra Frölunda, Sweden).

The area sensed by the fundamental frequency was so large, that it was affected by the O-rings securing the sensor in place, whereas the sensitivity for the 13th harmonic was so shallow that, after only a few nm of coating, the signal-to-noise ratio made it statistically irrelevant. The 5th and 7th harmonics (e.i. the 25 MHz and 35 MHz frequencies) were utilized in this research as they are neither extremely shallow nor extremely broad. All evaluations of deposition utilized only the 5th and 7th harmonics.

5.4.3 SiO_2 QCM Sensor Cleaning Protocol

Q-Sense offers many types of flow modules for various purposes (*i.e.*, electrochemistry, ellipsometry, titanium, PTFE, etc.). The polytetrafluoroethylene (PTFE) module was selected for this work to prevent precursor deposition onto

the inside of the flow module. Previous work with the titanium flow module showed internal coating due to the surface hydroxyl groups present on the oxide surface which led to contamination and clogging.

QCM crystals were cleaned before each use to ensure that the starting surfaces were comparable. The SiO_2-coated (~ 50 nm) QCM sensors were purchased from Q-sense (Model QSX 303, Västra Frölunda, Sweden). The cleaning procedure suggested for these sensors by Q-sense proved to be ineffectual and did not produce sensors that could be reused or that gave reproducible results. That initial cleaning procedure was as follows. Sensors were cleaned by a 10 minute UV/Ozone treatment (UV/Ozone ProCleanerTM, Bioforce Nanosciences, CA, USA), followed by a 30 minute soak in 2 wt% sodium dodecyl sulfate (Biotechnology grade, Amresco, OH, USA) solution in 18.2 MΩ·cm water (Milli-Q ultrapure, EMD Millipore, MA, USA)). Sensors were rinsed with DIW (approximately 100 mL each) and dried in compressed nitrogen (Ultra High Purity, AirGas, PA, USA) for 5 minutes. Sensors were then treated with another 10 minute UV/Ozone treatment. [30]

This cleaning procedure did not produce reproducible results and resulted in optically evident markings on the sensor. To achieve reproducibility, a more aggressive cleaning procedure was adopted. The effective cleaning procedure was developed by combining Q-sense's cleaning procedure with the procedure that was used to clean silica inverse opals in Chapter 6 on page 179. The cleaning of the inverse opals had proved to be an effective pretreatment for SSG. Each QCM sensor was cleaned by a 10 minute UV/Ozone treatment (UV/Ozone ProCleanerTM, Bioforce Nanosciences, CA, USA). Each QCM crystal

was then placed in DIW (15 mL) and concentrated NH_4OH (30%, 3 mL, Fisher Scientific), followed by addition of H_2O_2 (30%, 3 mL, Alfa Aesar). The resulting mixture was incubated with stirring in a 75 °C water bath for 10 minutes. The crystals were then rinsed in flowing DIW for 1 minute and dried with nitrogen gas at room temperature for 2 minutes. Finally, the crystals were treated with UV/Ozone a second time for 10 minutes and then immediately used in the QCM. Figure 65, shows two SiO_2 coated QCM crystals and the effect of the two cleaning methods.

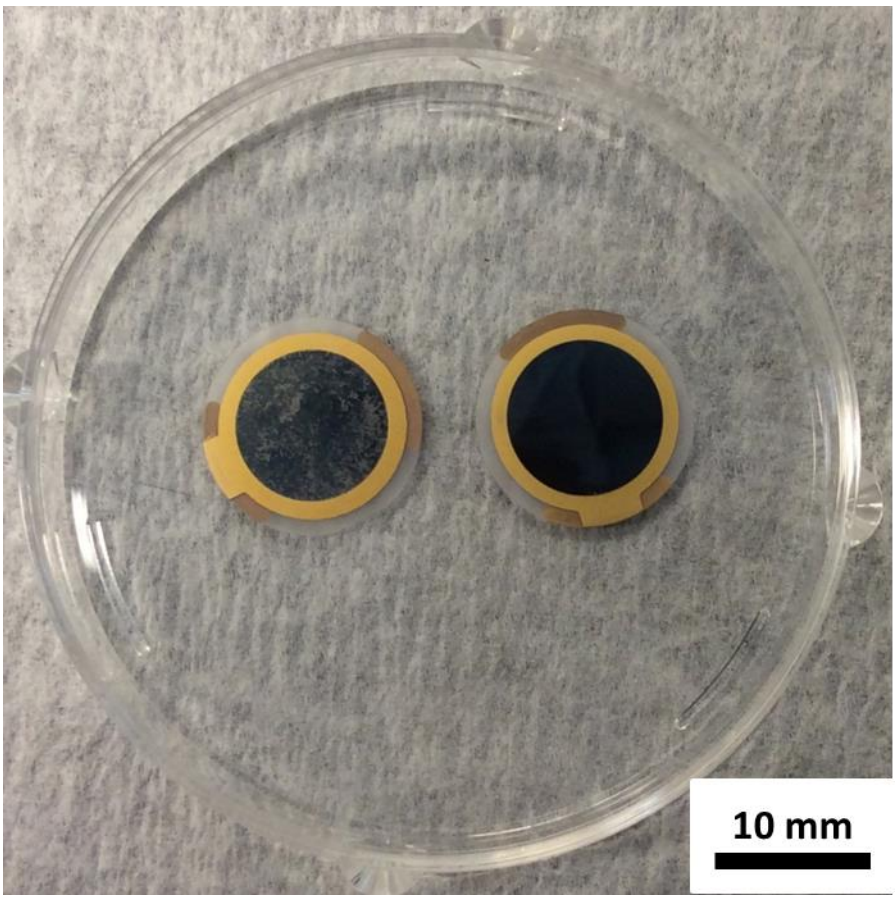

Figure 65: Two SiO_2 coated QCM crystals after coating and subsequent cleaning using left: the Q-sense cleaning protocol and right: using the cleaning method involving 1:1:17 NH_4OH:H_2O_2:H_2O for 10 minutes at 75 °C. The QCM crystal on the right shows a clean surface whereas the crystal on the left shows only partial removal of the coating.

Previous research suggested that this cleaning procedure resulted in samples that were irreparably damaged and were unusable.[31] The research presented here suggests that SiO_2-coated QCM crystals can be cleaned in this manner numerous times (some sensors were cleaned 5 times) without damage to the sensor and yielded reproducible QCM data.

While the PTFE flow modules did not react with the alkoxide precursors, thorough cleaning was still performed to avoid clogging and contamination from other experiments. The cleaning was performed at the end of a run by flowing IPA through the entire system for 30 minutes at 800 µL/min to purge the system. Then, with the use of an adaptor, N_2 was directly injected into the system and allowed to purge and dry the interior for 10 minutes. After drying, the sensors were removed from the module(s) and prepared for cleaning, while sensor(s) that were only used as "cleaning sensors" were used to keep the electronics dry. Next, water was passed into the system, followed immediately by 5 vol% Hellmanex (Hellma Analytics, Müllheim, Germany) in DIW for 30 min. Hellmanex is an alkaline cleaning solution typically used to clean glass and quartz and is effective at removing SSG deposits from the PTFE flow module. The system was then rinsed with DIW for 1 hr, followed by anhydrous IPA for 30 min, with a final N_2 gas purge for 10 min. In cases where the flow channels in the PTFE module were entirely clogged, the flow module was disassembled and the non-electrical parts placed in a 5 vol% Hellmanex solution and sonicated for 30 min (Branson 2510, Bransonic, CT, USA). After sonication, parts were rinsed with DIW and dried with N_2 gas.

5.4.4 QCM-D Analyses

Sensors were first validated for use in air and then in anhydrous IPA (99.8+% purity, Acros Organics, Geel, Belgium) by confirming a stable baseline before commencing with deposition. In this case, a stable baseline was defined by a change in frequency of less than 1/2 Hz over 15 minutes. If a sensor did not reach such a stable baseline after 1 hr, then the sensor would be reseated in the flow module. A mounting error commonly caused time dependent changes in the frequency and was thus corrected before gathering data. Other possible causes of a failure to establish a stable baseline included: temperature fluctuations, a dirty sensor that was either experiencing hydration or wash off, or damage to the sensor (scratches, marks, etc.).[32]

Sensors were first baselined in air and then in IPA to avoid having to dry the module(s) if a sensor needed to be reseated or replaced. Deviations from a stable baseline also occurred if air bubbles were introduced to the surface or nucleated in the flow chamber. Because the solubility of air in IPA decreases with increasing temperature, the chambers were always kept at 18 °C (slightly below lab temperature of 20 °C) using an internal cooling system. [32, 33] The need for keeping the temperature of the solution constant during the duration of an experiment is indicated by the data in Figure 66.

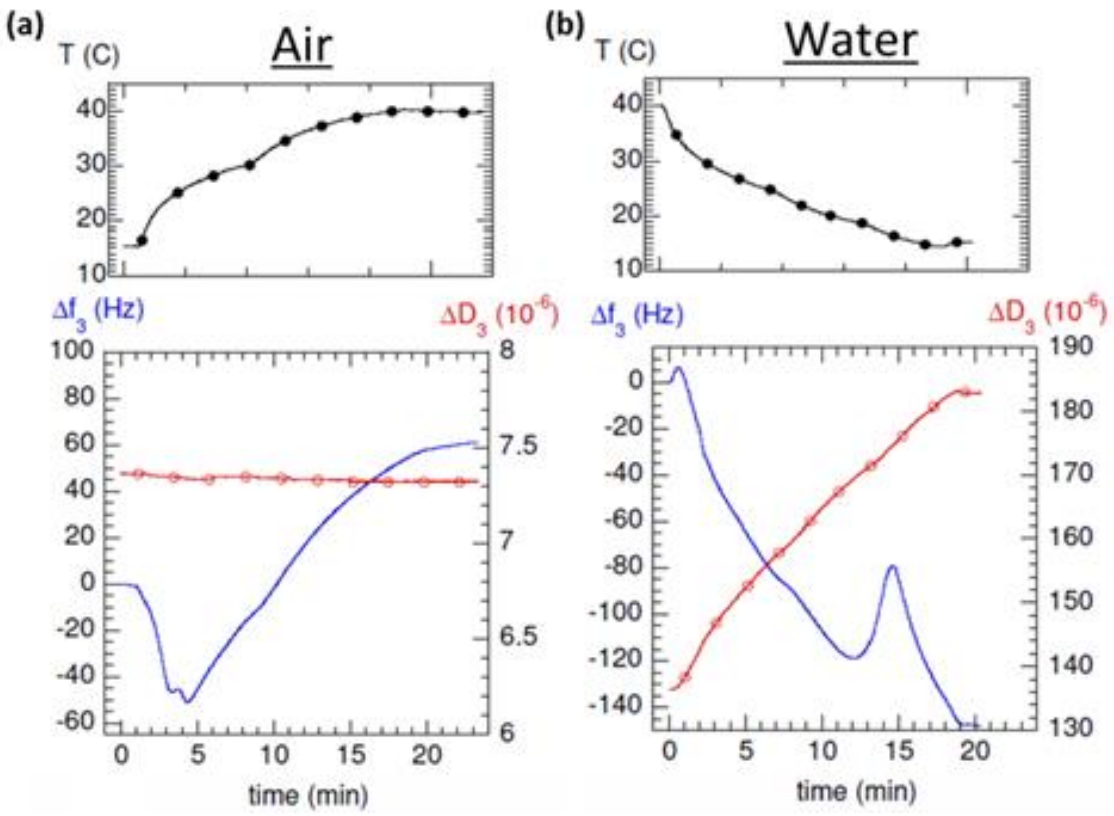

Figure 66: QCM-D data demonstrating the effect of temperature changes on the frequency and dissipation in both a) air and b) water. These plots indicate the need to keep the flow module temperature constant during deposition. Data courtesy of Biolin Scientific (Västra Frölunda, Sweden).

Q-sense advises users to perform all experiments slightly below the temperature of the incoming fluid to avoid any nucleation of air bubbles due to reduced solubility. To reduce the chance of bubble formation, all solutions were degassed for 15 min in a sonicator (Branson 2510, Bransonic, CT, USA) at 35 °C. Deposition was monitored through analysis of the changes in frequency and dissipation with time and the overall changes in these parameters after each rinse cycle.

The large changes in fluid properties (i.e., viscosity and density) between the IPA-based precursors and the 40%vH_2O/60%vIPA hydration solution resulted in splitting of the overtones. Without preforming extensive control experiments, it

was impossible to determine the time dependent reaction that occurred during hydration, and so the hydration kinetics were not investigated in this research.

5.5 Results and Discussion

5.5.1 Determination of Adsorption Isotherms

Adsorption of material onto a surface is commonly represented by isothermal adsorption studies.[7-9, 13, 17, 34-37] Adsorption isotherms were studied in this research to better understand the SSG coating process. Adsorption isotherms were evaluated for two SSG precursors relevant to this research: Ti(IV) isopropoxide, and Ba(II) isopropoxide.

The first alkoxide evaluated was Ti(IV) isopropoxide because it was the most commonly used precursor in this research and offered the most benefit if properly understood. Various concentrations of Ti(IV) isopropoxide were evaluated and each deposition cycle was allowed to run to completion and the difference in adsorption was measured. The real-time adsorption rate was captured. However, for the adsorption isotherm, an important value was the apparent equilibrium adsorption.

A single layer resulting from exposure to a 12.5 mM solution of Ti(IV) isopropoxide shifted the resonance frequency on the QCM crystal approximately 3 Hz upon reaching apparent equilibrium (Figure 67).

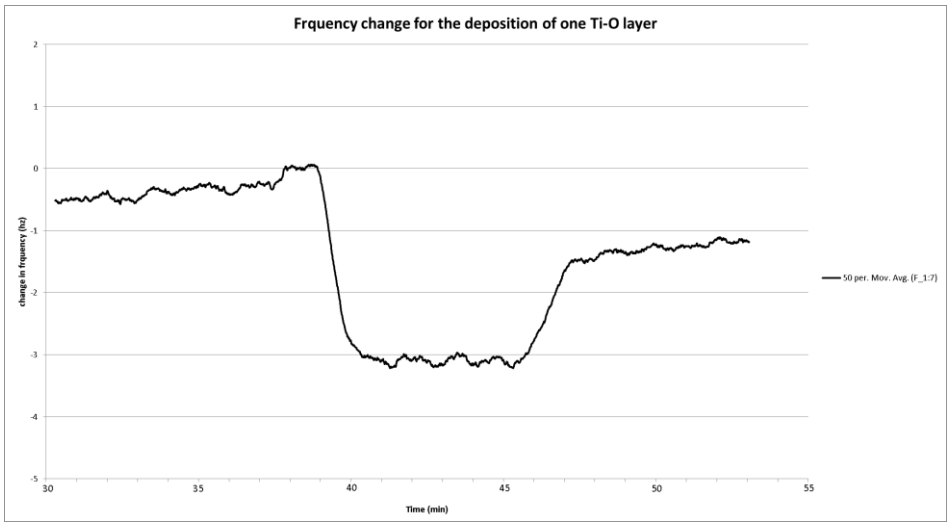

Figure 67: 50 point running average of the frequency change of the QCM during the deposition of one layer from a 12.5 mM solution of Ti(IV) isopropoxide onto an amorphous silica-coated QCM sensor at 18 °C.

This research was focused on the apparent equilibrium adsorption and not on evaluating the portion of the deposit that was chemi- vs physisorbed onto the surface. Figure 68 shows the apparent equilibrium adsorption of Ti(IV) isopropoxide onto amorphous silica at 18 °C for a range of concentrations. An apparent saturation of the surface occurred when the alkoxide concentration in the bulk solution exceeded 50 mM.

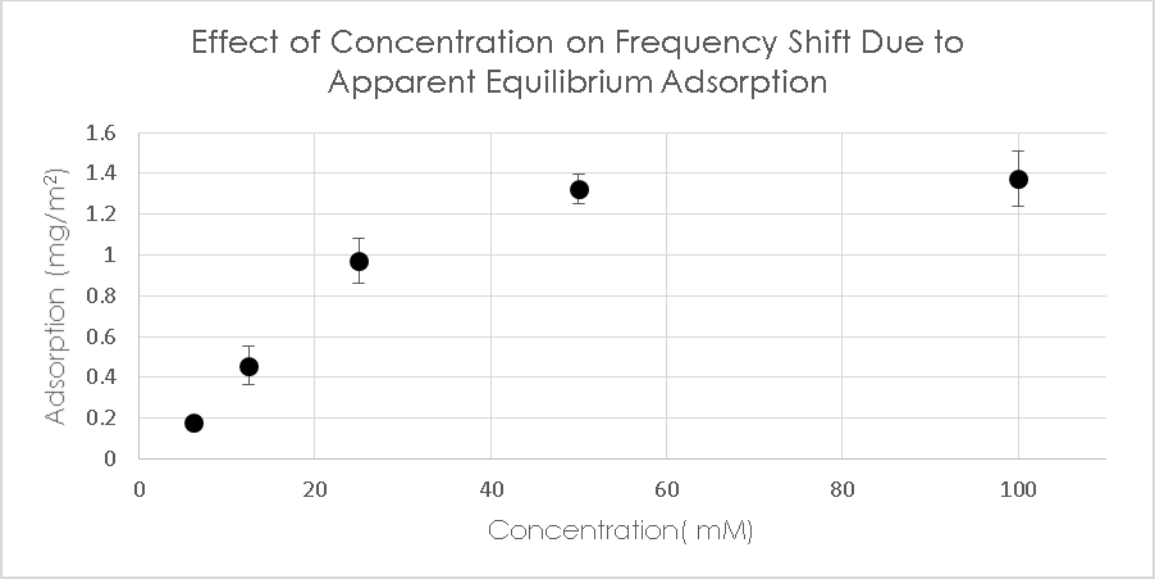

Figure 68: Apparent equilibrium adsorption at 18 °C of Ti(IV) isopropoxide onto amorphous silica at five bulk solution concentrations(6.25 mM, 12.5 mM, 25 mM, 50 mM, 100mM) as measured via QCM-D. Each data point consisted of the average value of a minimum of six adsorption cycles and error bars represented a range of plus or minus one standard deviation.

The data was analyzed and plotted according to the parameters of the various isotherm models. The summary of the isotherm models and their linear forms are represented in Table 4.

Table 4: Isotherm models, their linear forms and the parameters to plot for a linear regression.

Isotherm	Equation	Linear form	Plot
Langmuir	$\Gamma_i = \frac{K\Gamma_i^{sat} C_i}{(1+KC_i)}$	$\frac{1}{\Gamma_i} = \frac{1}{\Gamma_i^{sat}} + \left(\frac{1}{K\Gamma_i^{sat}}\right)\left(\frac{1}{C_i}\right)$	$\frac{1}{\Gamma_i} vs. \frac{1}{C_i}$
Freundlich	$\Gamma_i = K_f (C_i)^{1/n}$	$log\, \Gamma_i = log\, K_f + (1/n) log\, C_i$	$log\, \Gamma_i\, vs. log\, C_i$
Fowler-Guggenheim	$KC_i = \frac{\theta_i}{(1-\theta_i)} e^{\frac{-2\omega}{kT}\theta_i}$	$ln \frac{C_i(1-\theta_i)}{\theta_i} = -ln\, K - \frac{2\omega}{kT}\theta_i$	$ln \frac{C_i(1-\theta_i)}{\theta_i} vs. \theta_i$

Each of the models was plotted with the data using linear regression analysis (Figure 69 though Figure 71). The model that most accurately fit the data was deemed to be the model with the R^2 value closest to unity.

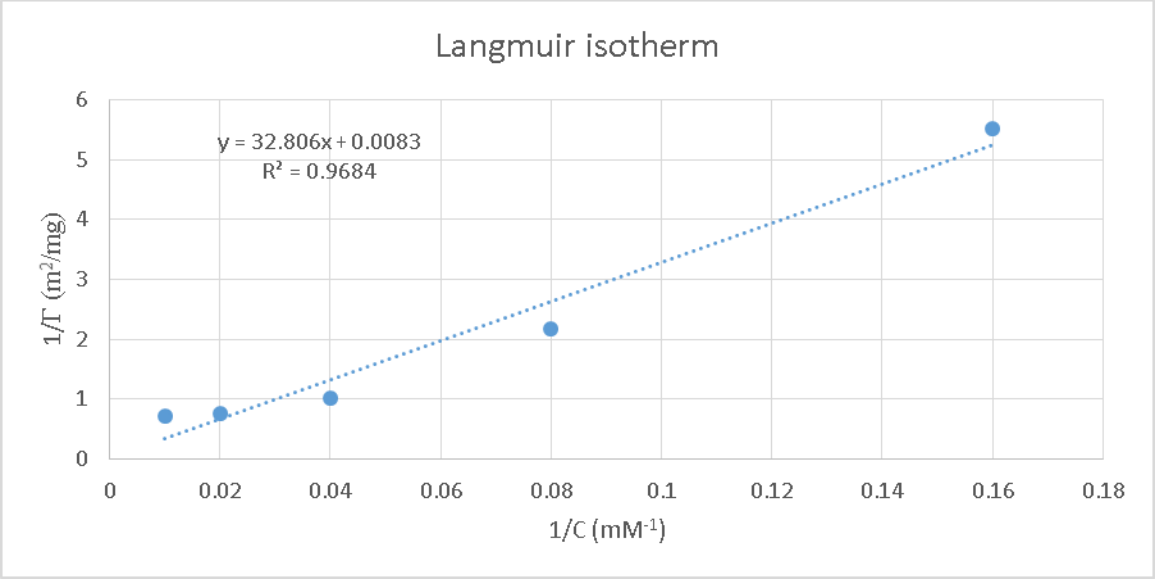

Figure 69: Fit of the apparent equilibrium adsorption of Ti(IV) isopropoxide onto amorphous silica at 18 °C to the Langmuir isotherm model.

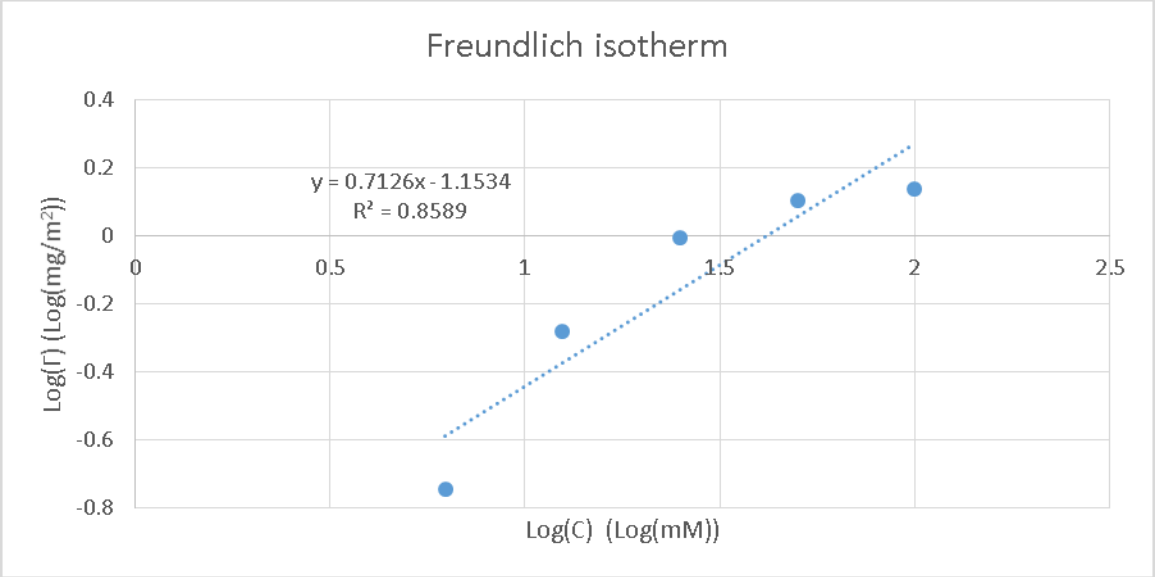

Figure 70: Fit of the apparent equilibrium adsorption of Ti(IV) isopropoxide onto amorphous silica at 18 °C to the Freundlich isotherm model.

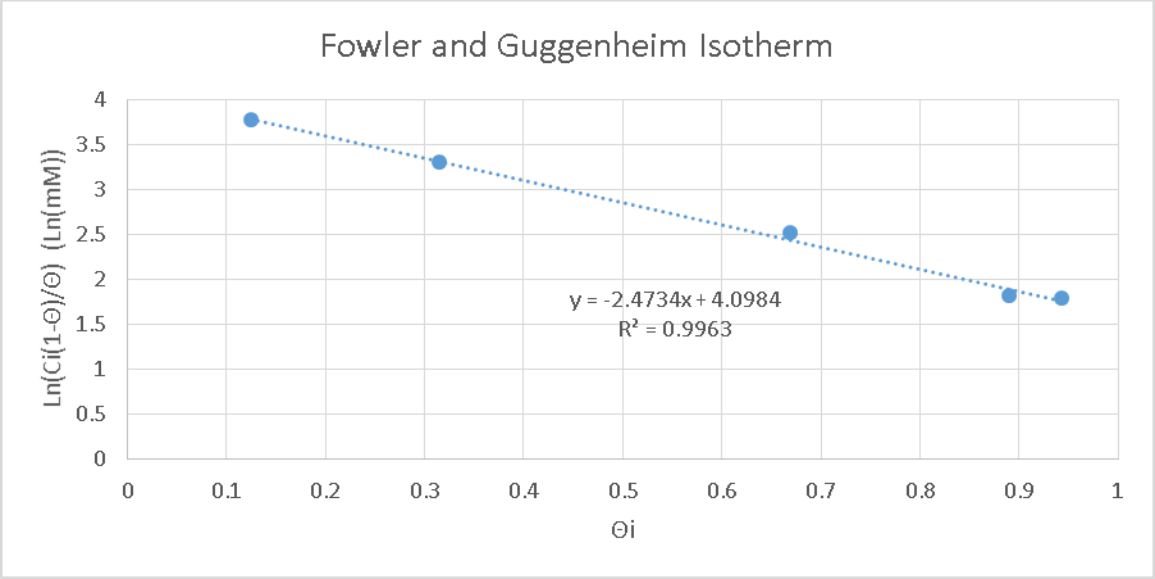

Figure 71: Fit of the apparent equilibrium adsorption of Ti(IV) isopropoxide onto amorphous silica at 18 °C to the Fowler & Guggenheim isotherm model.

The equations from the regressions for each model and the associated R-squared values are tabulated below.

Table 5: Isotherm models, their linear forms, their linear regression, and the quality of fit represented by the R^2 value. The constants produced by the various models are also tabulated.

Variable	Langmuir	Freundlich	Fowler-Guggenheim
Linear Equation	$\frac{1}{\Gamma_i} = \frac{1}{\Gamma_i^{sat}} + \left(\frac{1}{K\Gamma_i^{sat}}\right)\left(\frac{1}{C_i}\right)$	$log\,\Gamma_i = log\,K_f + (1/n) log\,C_i$	$ln\frac{C_i(1-\theta_i)}{\theta_i} = -ln\,K - \frac{2\omega}{kT}\theta_i$
Regression	y = 32.806x + 0.0083	y = 0.7126x – 1.1534	Y = -2.4734X+4.0984
R^2	0.9684	0.8589	0.9963
Γ_i^{sat} (mg/m^2)	121.1	-	1.456
K (mM^{-1})	0.2797	-	-
K_{FG} (mM^{-1})	-	-	0.03569
K_f (mg/m^2)	-	0.398	-
n	-	1.403	-
ω (J)	-	-	3.046 E-21

This data indicates that Ti(IV) isopropoxide adsorbing onto a surface follows most closely to the Fowler-Guggenheim model. The values determined for the

interaction constant, ω, and the equilibrium constant, K, are both within an order of magnitude of values presented in literature.[13] The best fit for each model was determined by linear regression and the equation for that model was then compared to the apparent equilibrium isothermal data, in Figure 72, to visually demonstrate the fit of the Fowler-Guggenheim model.

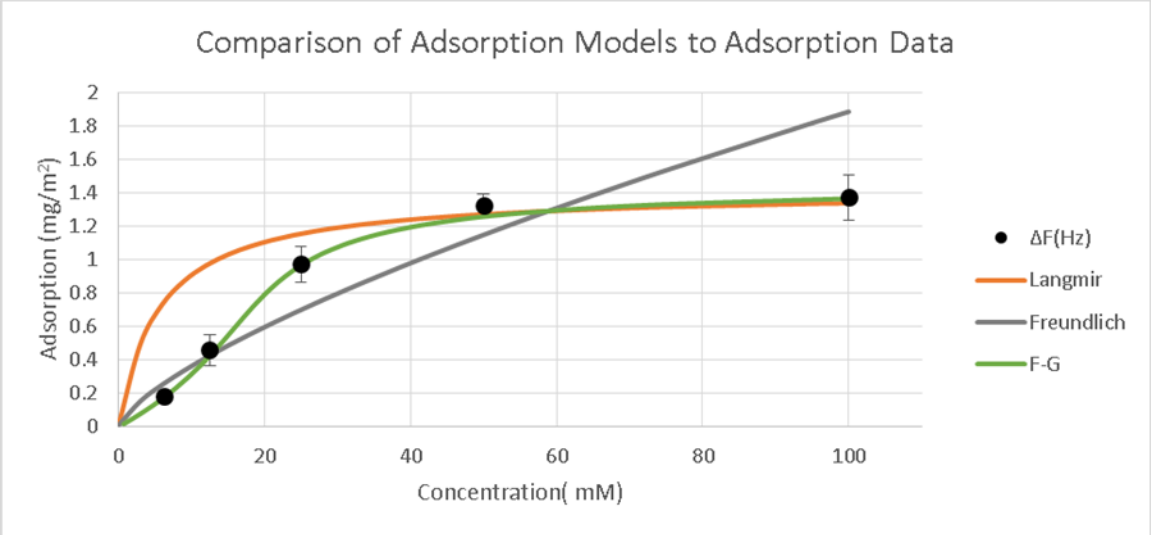

Figure 72: Comparison of Ti(IV) isopropoxide adsorption onto amorphous silica at 18 °C with various isotherm models. The Fowler-Guggenheim model was the best fitting model. The error bars on the data represented a range of plus or minus one standard deviation.

The apparent equilibrium adsorption of barium (II) isopropoxide was also analyzed using the automated QCM system (Figure 73). The reactivity of the Ba(II) isopropoxide precursor to the amorphous silica substrate at 18 °C has been found to be much greater that its titanium counterpart. For this reason, a precursor solution with lower Ba(II) isopropoxide concentration was initially studied.

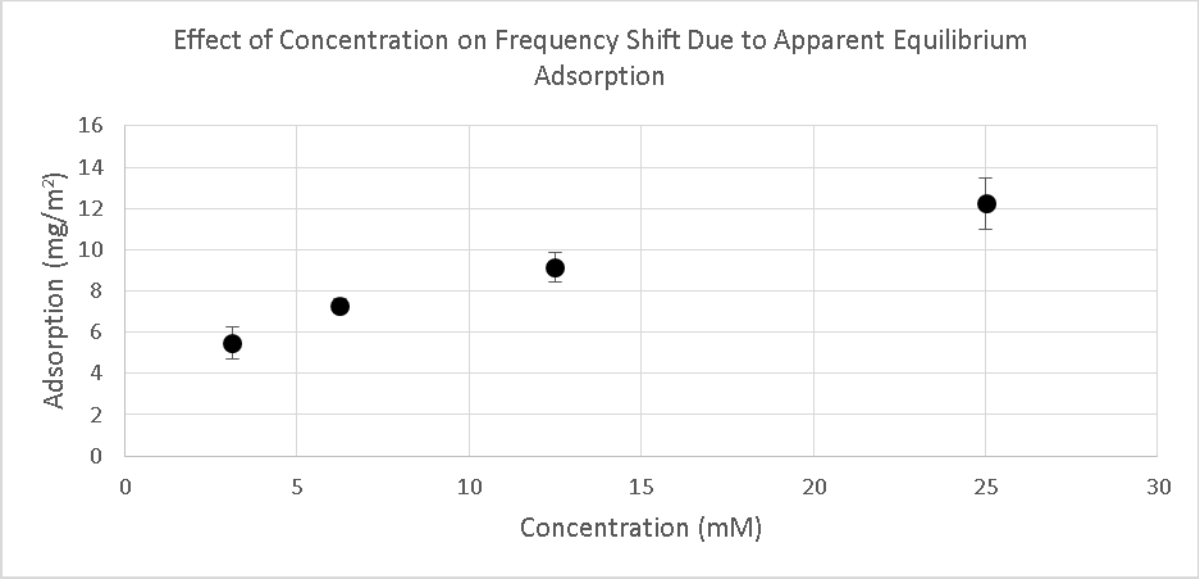

Figure 73: Apparent equilibrium adsorption at 18 °C of Ba(II) isopropoxide onto amorphous silica at four bulk solution concentrations (3.125 mM, 6.25 mM, 12.5 mM, 25 mM) as measured via QCM-D. Each data point consisted of the average of a minimum of six adsorption cycles and error bars represented the range of one standard deviation.

The data was analyzed and plotted according to the parameters of the various isotherm models (Figure 74 through Figure 76). The summary of the isotherm models and their linear forms are provided in Table 6. Each of the models were plotted with the data and the linear regression of the data was produced. The model that most accurately fit the data was deemed to be the model with the R^2 value closest to unity.

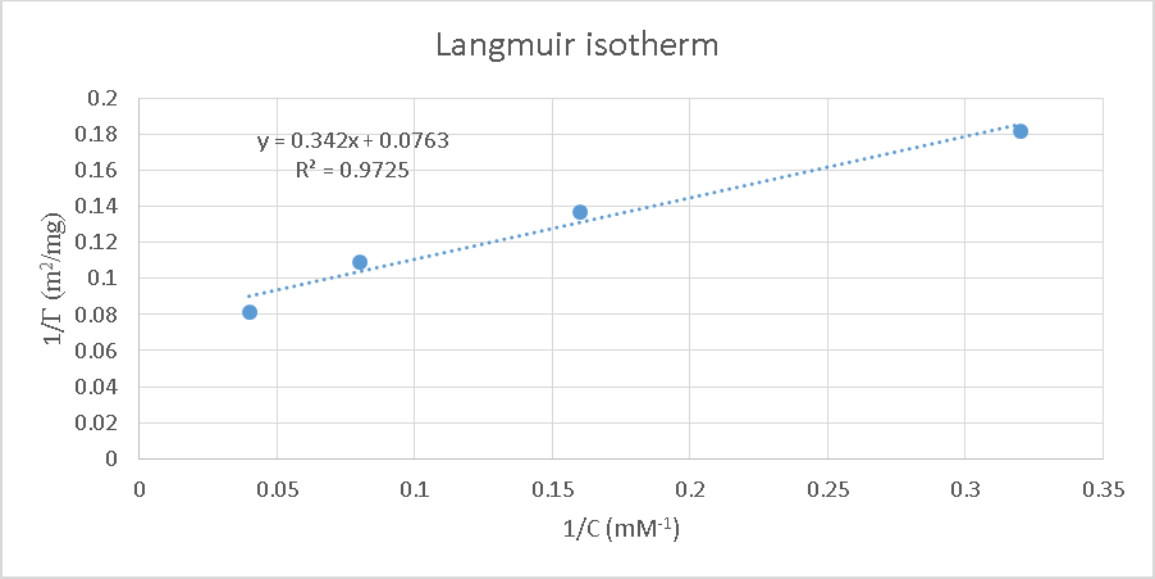

Figure 74: Fit of the apparent equilibrium adsorption of Ba(II) isopropoxide onto amorphous silica at 18 °C to the Langmuir isotherm model.

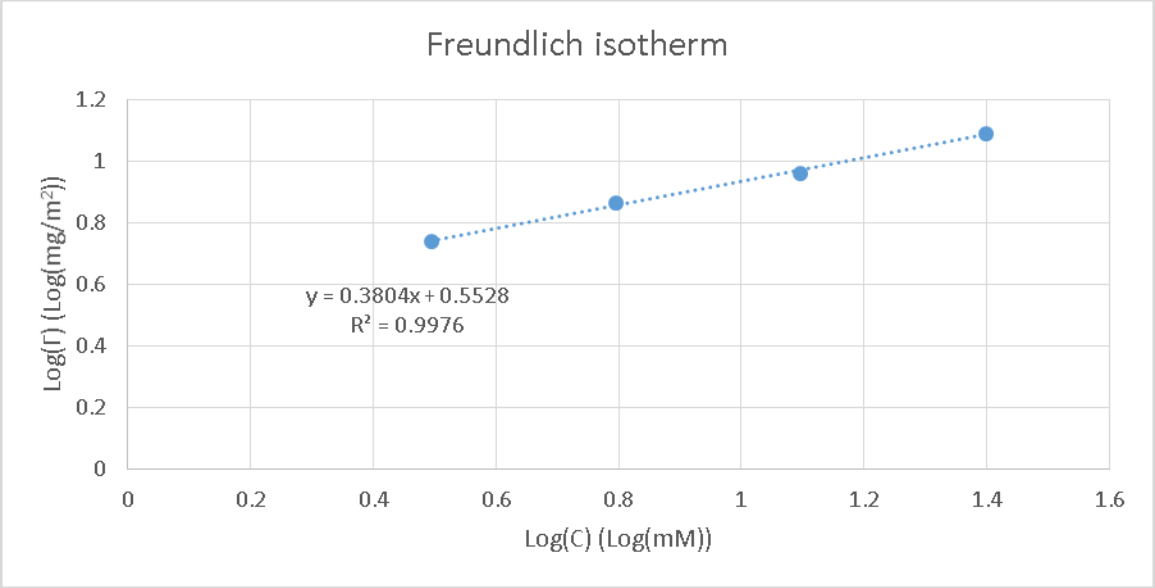

Figure 75: Fit of the apparent equilibrium adsorption of Ba(II) isopropoxide onto amorphous silica at 18 °C to the Freundlich isotherm model.

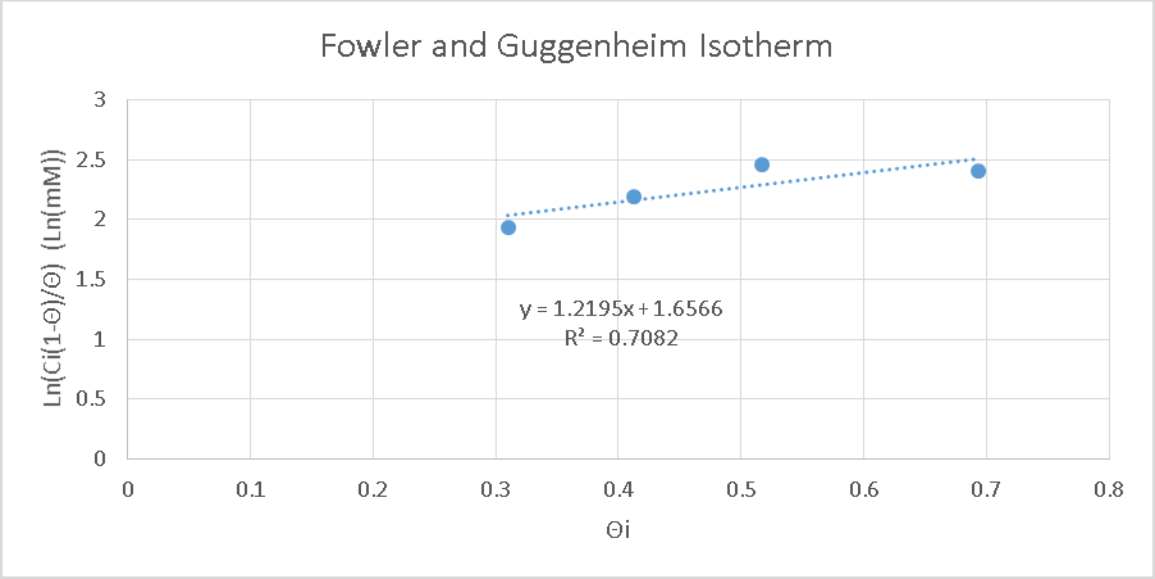

Figure 76: Fit of the apparent equilibrium adsorption of Ba(II) isopropoxide onto amorphous silica at 18 °C to the Fowler & Guggenheim isotherm model.

The equations from the regressions for each model and their respective R-squared values are tabulated below.

Table 6: Isotherm models, their linear forms, their linear regression, and the quality of fit represented by the R^2 value for adsorption of Ba(II) isopropoxide onto amorphous silica at 18 °C. The constants produced by the various models are also tabulated.

Variable	Langmuir	Freundlich	Fowler-Guggenheim
Linear Equation	$\frac{1}{\Gamma_i} = \frac{1}{\Gamma_i^{sat}} + \left(\frac{1}{K\Gamma_i^{sat}}\right)\left(\frac{1}{C_i}\right)$	$log\ \Gamma_i = log\ K_f + (1/n) log\ C_i$	$ln\frac{C_i(1-\theta_i)}{\theta_i} = -ln\ K - \frac{2\omega}{kT}\theta_i$
Regression	y = 0.342 x + 0.0763	y = 0.3804x - 0.5528	Y = 1.2195x + 1.6566
R^2	0.9725	0.9976	0.7082
Γ_i^{sat} (mg/m^2)	13.098	-	17.67
K (mM^{-1})	0.02684	-	-
K_{FG} (mM^{-1})	-	-	0.1908
K_f (mg/m^2)	-	3.571	-
n	-	2.629	-
ω (J)	-	-	-2.450E-21

This data shows that Ba(II) isopropoxide adsorbing onto an amorphous silica surface exhibited the best fit to the Freundlich model. The value determined for

the interaction constant, n, is similar to values presented in literature and suggests a moderately aggressive adsorption process.[13, 38] The best fit for each model was determined by linear regression and the equation of that model was then compared to the apparent equilibrium isothermal data to visually demonstrate the fit of the Freundlich model (Figure 77).

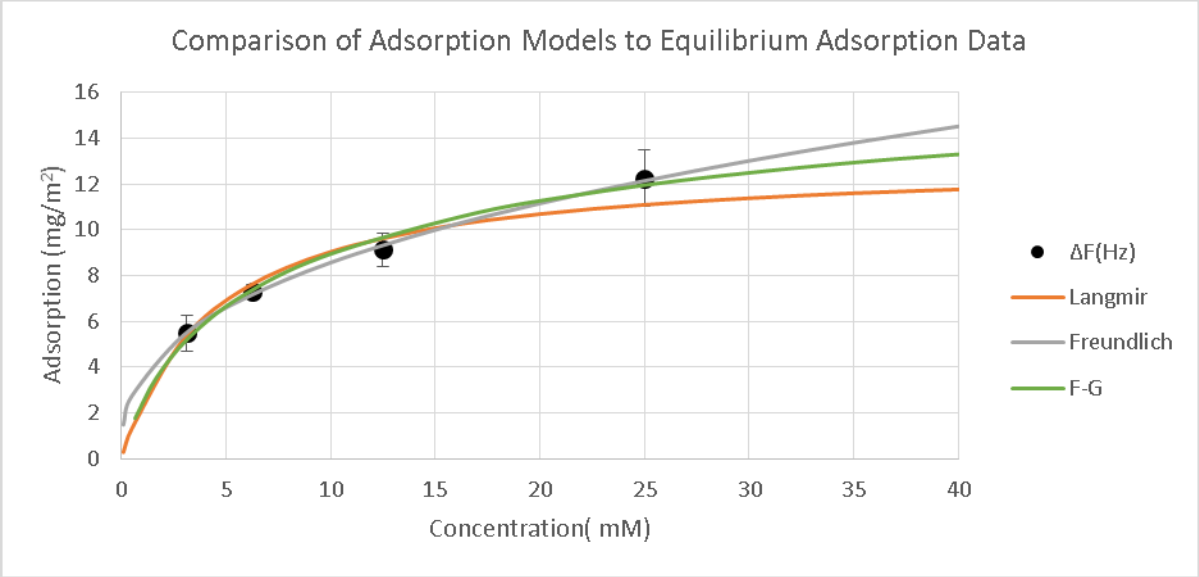

Figure 77: Comparison of Ba(II) isopropoxide adsorption onto amorphous silica at 18 °C with various isotherm models. The Freundlich model was the best fitting model. The error bars on the data represented a range of one standard deviation.

Interestingly, the Ba-O precursor isothermal adsorption followed the Freundlich model, whereas the Ti-O precursor isothermal adsorption followed the Fowler-Guggenhiem model. This suggested that while the Ba-O precursor was affected by the varied activities of the binding sites, the Ti-O precursor was more dominantly affected by adsorbate-adsorbate interactions. These behaviors may have been influenced by the number of ligands on the precursors. Because the Ti-O alkoxide precursor has four ligands as opposed to the two of the Ba-O

alkoxide precursor, the bound Ti-O precursor molecules could have undergone more interactions with neighboring bound Ti-O molecules.

5.5.2 Evaluation of the Kinetic Mechanism (Rate Limiting Step) of Deposition

The rate limiting step for the deposition of Ti(IV) isopropoxide onto a silica substrate at 18 °C was evaluated using a QCM-D. For a given alkoxide concentration, the flow rate was varied and the real-time deposition rate was observed. The flow rate was varied from 12.5 to 400 µL/min and the adsorption rate was measured by the slope of the resonant frequency change vs time. Because of the time required for the initial mixing of the concentrated precursor solution with pure IPA, the initial adsorption rate is always not used for kinetic analyses. Instead, the adsorption rate was obtained by evaluating the change in adsorption with time over the central fifty percent of the adsorption time period as shown in Figure 78. Linear regression techniques were used to analyze the slope of the line for the central 50% of adsorption.

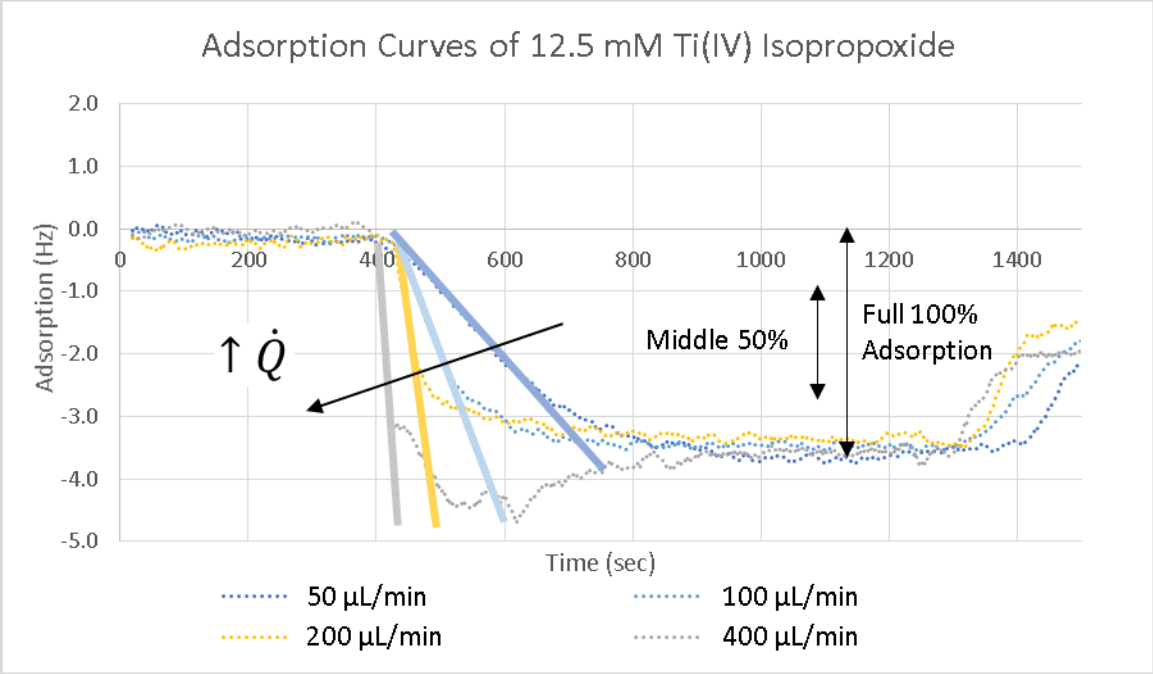

Figure 78: Real-time data of the adsorption kinetics of Ti(IV) isopropoxide from a 12.5 mM solution onto a SiO_2 coated QCM sensor for flow rates from 50 µL/min to 400 µl/min. The slopes of the curves demonstrate that the adsorption rate was affected by the flow rate up to a flow rate 200 µl/min, but the apparent equilibrium adsorption was not affected.

The flow rate was increased until the adsorption rate was no longer statistically dependent on the flow rate. At this point, the kinetic rate limiting step switched from being liquid phase diffusion controlled to being surface reaction limited. The transition can be seen to occur near the flow rate of 200 µL/min (Figure 79).

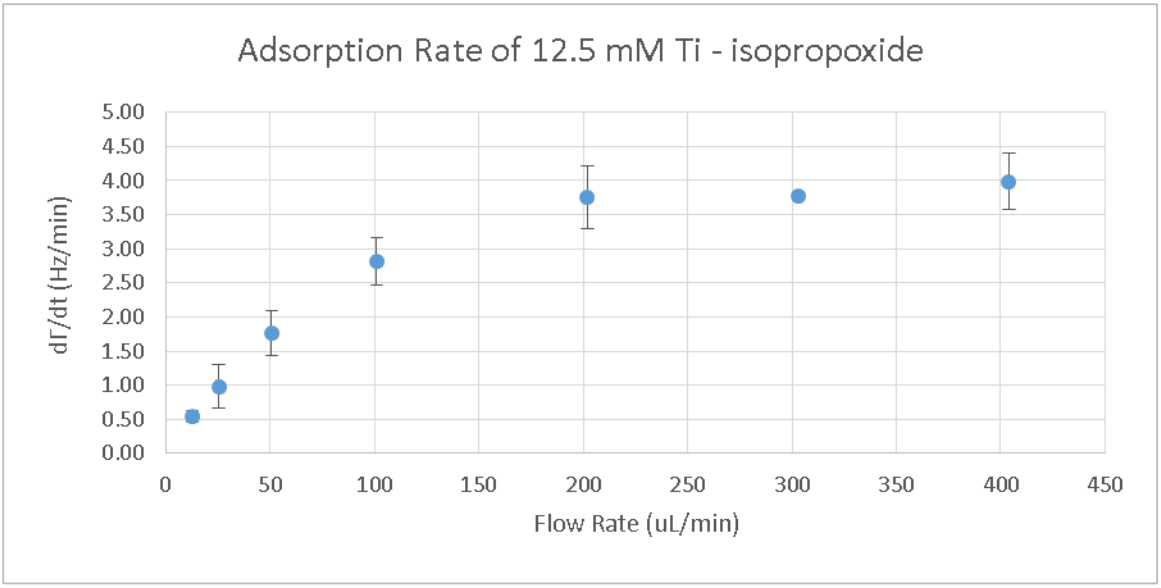

Figure 79: Adsorption rate of 12.5 mM Ti(IV) isopropoxide solution onto a SiO_2 coated QCM sensor for flow rate from 12.5 µL/min to 400 µl/min. Error bars represented the range of plus or minus one standard deviation.

In Figure 79, the adsorption rates for flow rates above 200 µL/min were not significantly different within the measured error range; that is, the adsorption rate was independent of flow rate for flow rates from 200 µL/min to 400 µL/min. For the region of flow rates below 200 µL/min, the adsorption rate dependence on flow rate was analyzed. The liquid phase diffusion control regime was analyzed via two types of flow analyses: the first as through a boundary layer caused by laminar flow over a flat plate (Figure 80), and the second as diffusion through a boundary layer defined by a Lévêque-Type equation (Figure 81).

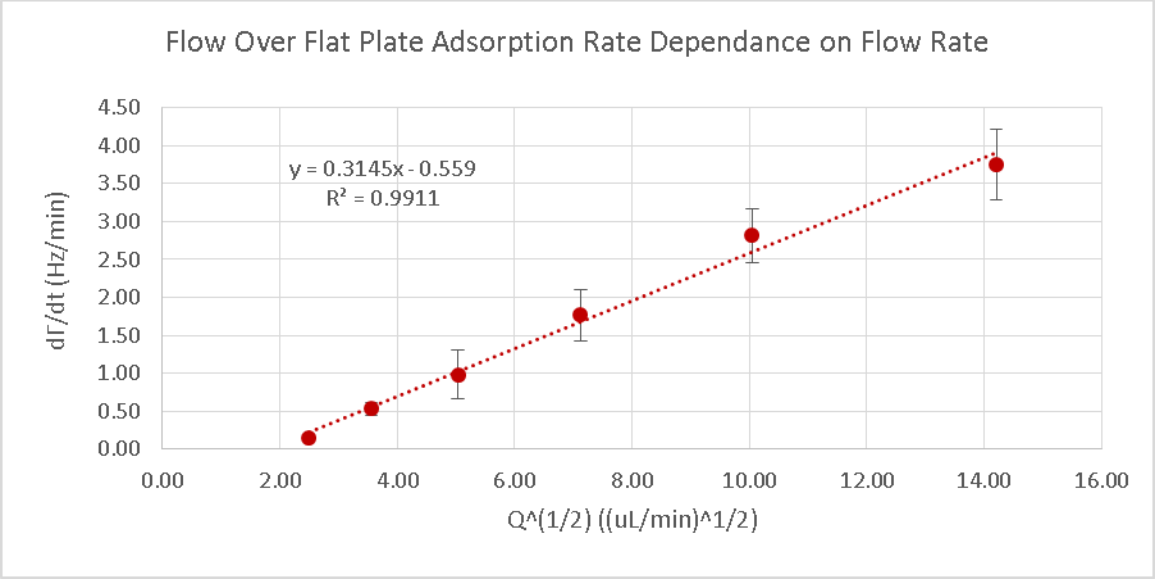

Figure 80: Linear regression analysis of the adsorption rate vs. the square root of the flow rate, for diffusion through a boundary layer defined by laminar flow over a flat plate.

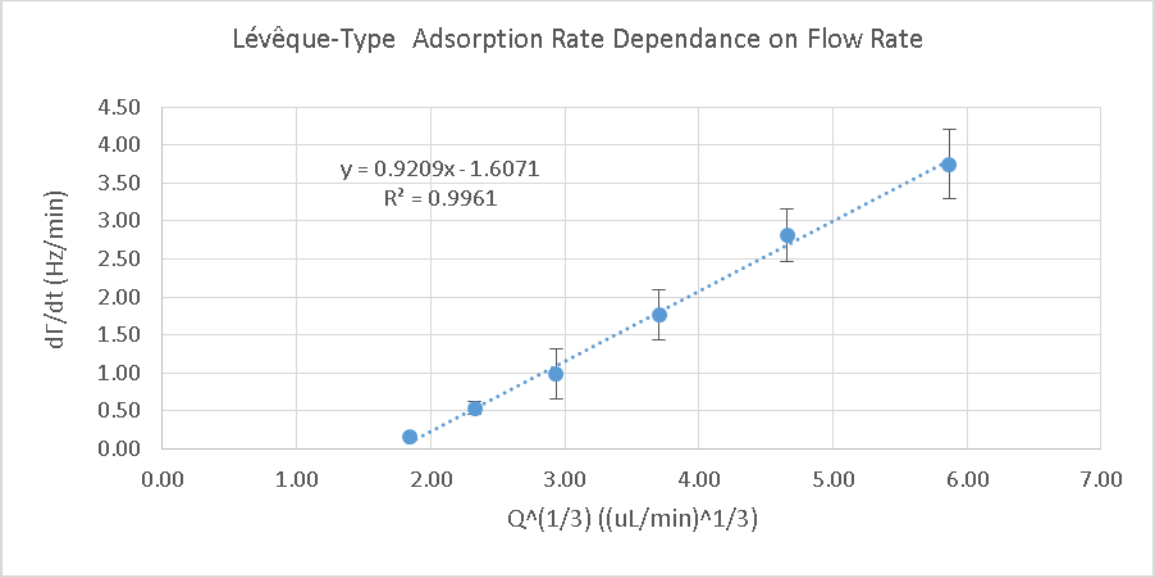

Figure 81: Linear regression analysis of the adsorption rate vs. the square root of the flow rate, for diffusion through a boundary layer defined by a Lévêque-type equation.

Both of the linear regressions show a good fit, with R-squared values of 0.9911 and 0.9961 for square root and cube root dependences, respectively. The result of the fit for the model of the flow over a flat plate, although good, was unrealistic due to the predicted boundary layer thickness. Figure 82 shows the calculated boundary layer thicknesses for the both laminar flow over a flat plate

and for a Lévêque-type calculation. The calculations of the boundary layer thicknesses can be found in APPENDIX A on page 219.

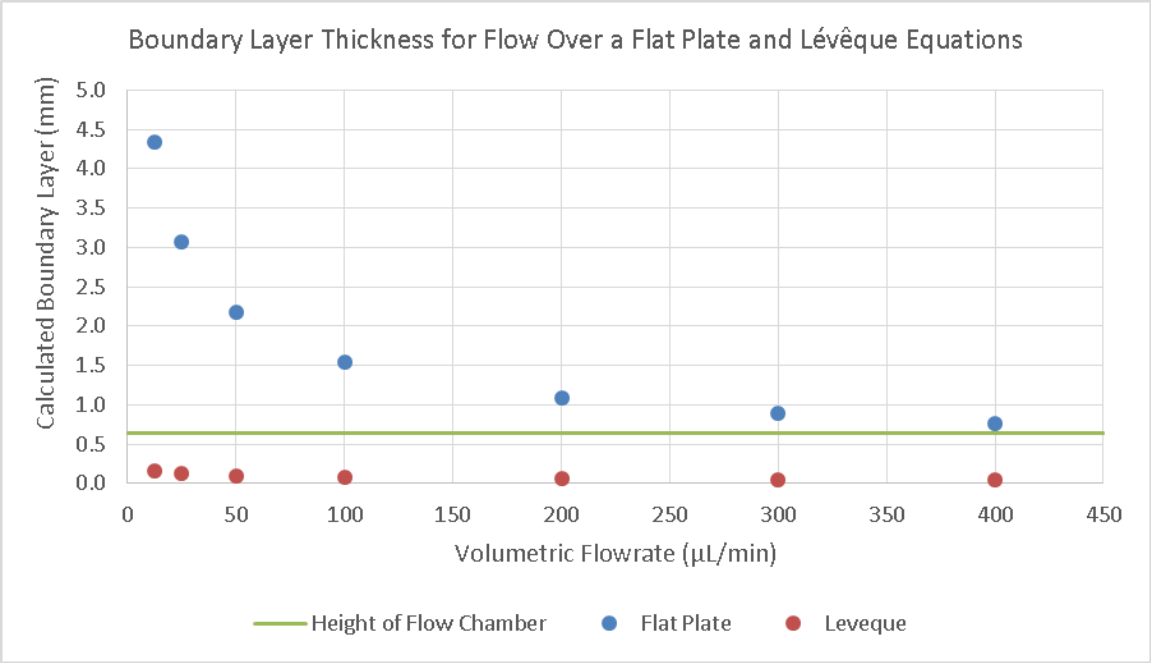

Figure 82: Graph showing the variation in the calculated boundary layer thickness for both flow over a flat plate and for a Lévêque flow scenarios with x=5.5 mm. The Flat Plate calculation is greater than the total height of the flow chamber and is thus not realistic.

Because the calculated boundary layer thickness for laminar flow over a flat plat was greater that the height of the QCM chamber, that model was not appropriate. The Lévêque calculated height was well below the thickness of the height of the QCM chamber and thus was applicable.

Under the condition that the flow rate was at or above 200 µL/min, the adsorption of Ti(IV) isopropoxide onto the silica surface was not liquid phase diffusion controlled. Thus, the order of the chemical reaction was analyzed in this high flow rate regime. Only a precursory analysis of the chemical reaction is presented here. Three models were compared to the adsorption kinetic data to evaluate the dependence of the adsorption rate on the adsorption

concentration. This analysis was performed on multiple adsorption cycles of 12.5 mM Ti(IV) isopropoxide onto amorphous silica at a flow rate of 200 µL/min in a PTFE QCM-D flow module. Figure 83 shows a characteristic adsorption curve used in the following analysis.

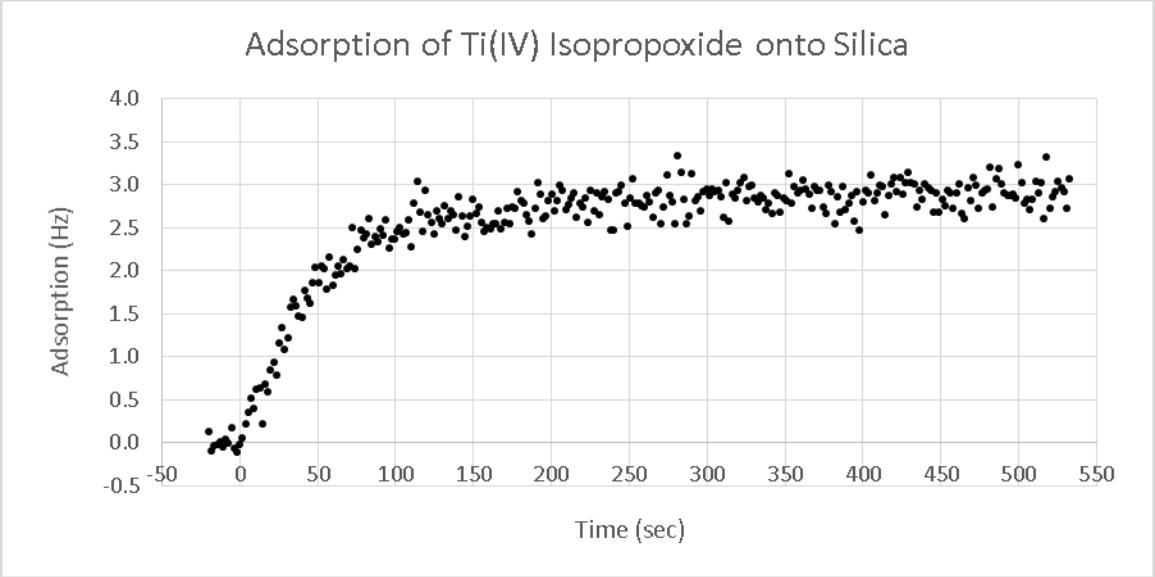

Figure 83: Graph of the raw QCM data from a characteristic adsorption cycle of 12.5 mM Ti(IV) isopropoxide onto amorphous silica at a flow rate of 200 µL/min in a PTFE QCM-D flow module.

Due to the noise inherent in the QCM data, a 5 point running average was used in the analysis of the above data. The analysis below is of the first minute of adsorption after excluding the first 10 seconds which are potentially affected by the initial mixing with the pure IPA. The comparison of the adsorption data to the zeroth-, first-, and second-order chemical reaction models can be seen in Figure 84, Figure 85, and Figure 86, respectively.

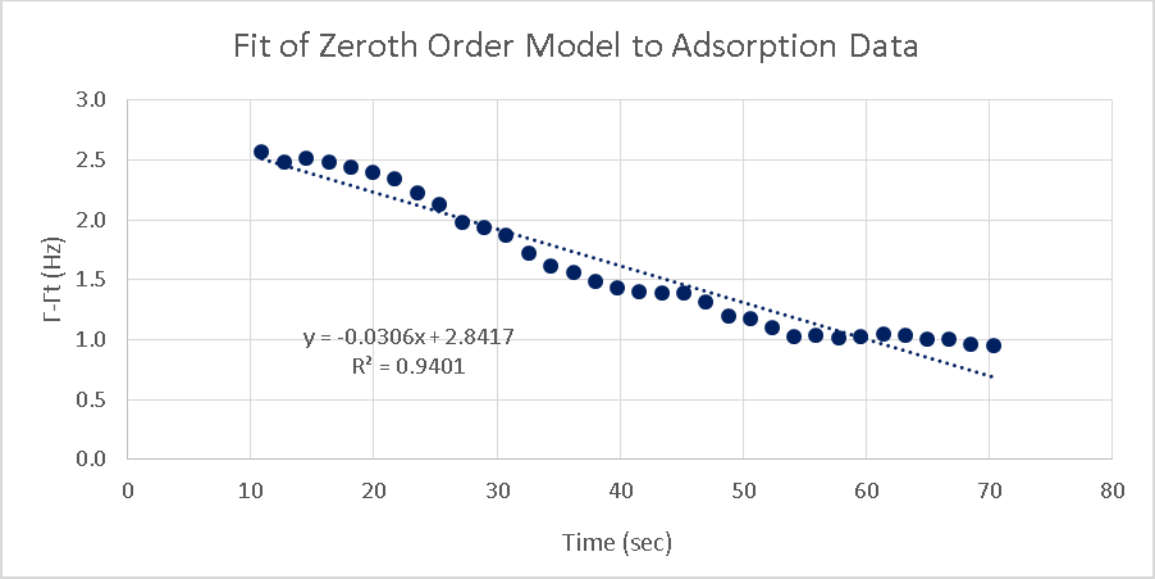

Figure 84: Graph of adsorption data of 12.5 mM Ti(IV) isopropoxide onto silica at 200 µL/min at 18 °C fitted to the zeroth-order chemical reaction law.

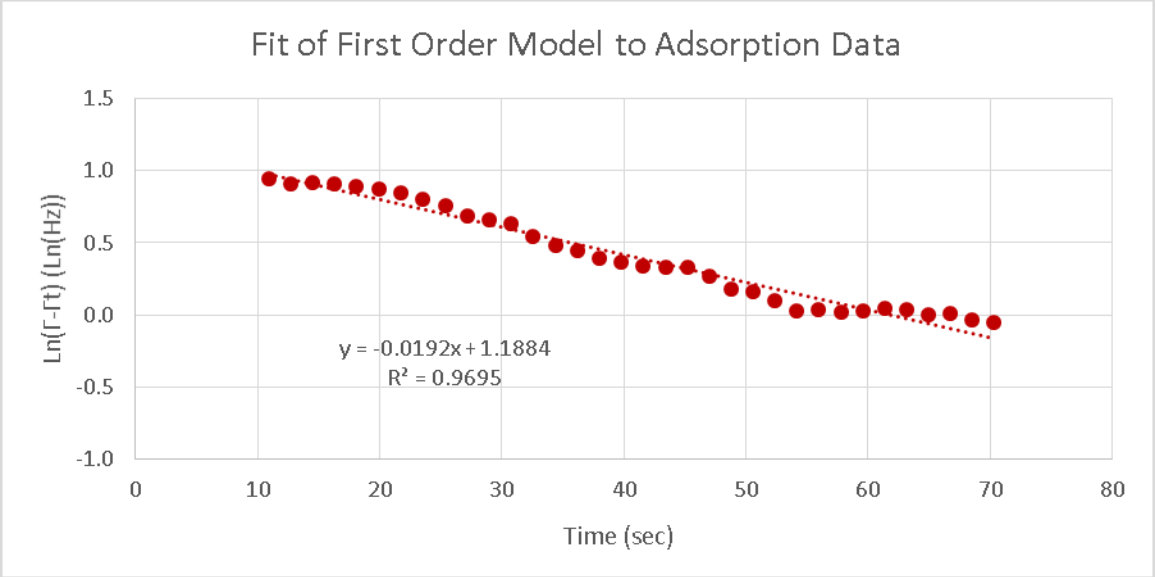

Figure 85: Graph of adsorption data of 12.5 mM Ti(IV) isopropoxide onto silica at 200 µL/min at 18 °C fitted to the first-order chemical reaction law.

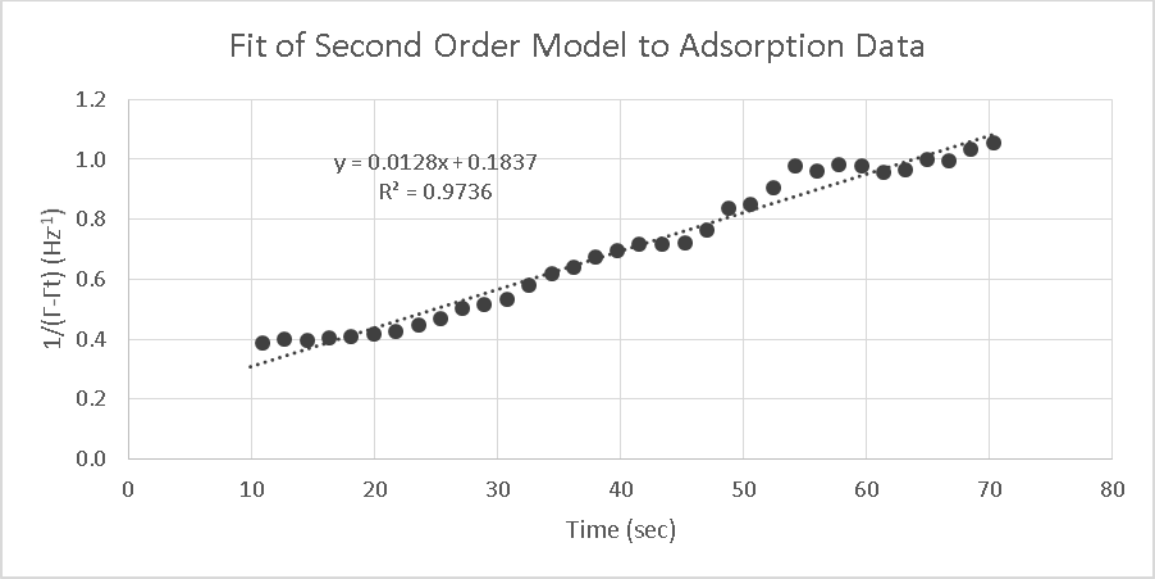

Figure 86: Graph of adsorption data of 12.5 mM Ti(IV) isopropoxide onto silica at 200 µL/min at 18 °C fitted to the second-order chemical reaction law.

Given that all of the fitted rate laws have high r-squared values, it is not particularly clear which model represents the adsorption of Ti(IV) isopropoxide onto the silica surface the most accurately. The data from the regressions and the calculated values for the three rate laws can be found in Table 7.

Table 7: Regression statistics and interpreted values (including equilibrium adsorption and rate of reaction) from the in-situ adsorption data of Ti(IV) isopropoxide onto silica.

	0th Order	1st Order	2nd Order
Slope	-0.031	-0.019	0.013
Y-Intercept	2.842	1.188	0.184
R^2	0.940	0.970	0.974
Γ_{equ} (µmol/m²)	2.564	2.961	4.912
k_0 (µmol/s)	2.76E-02	-	-
k_1 (1/s)	-	1.73E-02	-
k_2 (1/µmol*s)	-	-	1.16E-02

Another factor that was used to analyze the accuracy of the models was the predicted equilibrium adsorption. The actual equilibrium adsorption from the

deposition was 2.706 μmol/m^2. The 1st order and 2nd order reaction rate laws have larger r-squared values than the 0th order. Between the 1st and 2nd rate laws, the 1st rate law predicted a much more accurate equilibrium adsorption (Γ_{equ} = 2.961 μmol/m^2) than that of the 2nd order reaction rate law (Γ_{equ} = 4.12 μmol/m^2).

5.6 Concluding Remarks

In this chapter, the deposition behaviors of titanium and barium isopropoxide precursors onto amorphous silica substrates were investigated at 18 °C. The apparent equilibrium adsorption was measured for varied concentrations of these precursors and the apparent equilibrium adsorption data was compared to known isotherm models. The Ba-O precursor isothermal adsorption followed the Freundlich model, whereas the Ti-O precursor isothermal adsorption followed the Fowler-Guggenheim model. This suggested that while the Ba-O precursor was affected by the varied activities of the binding sites, the Ti-O precursor was more dominantly affected by adsorbate-adsorbate interactions. This behavior may have been a result of the differing number of ligands on the precursors. Because the Ti-O alkoxide precursor has four ligands, as opposed to the two of the Ba-O alkoxide precursor, the bound Ti-O molecule may have had more interactions with its neighboring bound molecules. The scientific knowledge gained in this study is directly relevant to the SSG coating method used in the previous chapters. Additionally, for Ti(IV) isopropoxide, the kinetic mechanism (rate limiting step) of reaction was evaluated. It was found that, for the commonly utilized 12.5 mM Ti(IV) isopropoxide precursor solution, the reaction

was liquid phase diffusion controlled until the flow rate reached approximately 200 μL/min. At higher flow rates, the adsorption of Ti(IV) isopropoxide onto a silica substrate at 18 °C was found to be most consistent with a first order chemical reaction with respect to the adsorbate.

5.7 References

[1] I. Ichinose, H. Senzu, and T. Kunitake, "Stepwise adsorption of metal alkoxides on hydrolyzed surfaces: A surface sol-gel process," *Chemistry Letters,* pp. 831-832, 1996 1996.

[2] I. Ichinose, H. Senzu, and T. Kunitake, "A surface sol-gel process of TiO2 and other metal oxide films with molecular precision," *Chemistry of Materials,* vol. 9, pp. 1296-&, Jun 1997.

[3] G. Sauerbrey, *The use of quartz crystal oscillators for weighing thin layers and for microweighing applications*, 1991.

[4] M. Rodahl, F. Höök, A. Krozer, P. Brzezinski, and B. Kasemo, "Quartz crystal microbalance setup for frequency and Q-factor measurements in gaseous and liquid environments," *Review of Scientific Instruments,* vol. 66, pp. 3924-3930, 1995.

[5] I. Langmuir, "the constitution and fundamental properties of solids and liquids. part i. solids," *Journal of the American Chemical Society,* vol. 38, pp. 2221-2295, 1916.

[6] H. Freundlich, "Over the adsorption in solution," *J. Phys. Chem,* vol. 57, p. e470, 1906.

[7] K. Foo and B. Hameed, "Insights into the modeling of adsorption isotherm systems," *Chemical Engineering Journal,* vol. 156, pp. 2-10, 2010.

[8] Y. Ho, J. Porter, and G. McKay, "Equilibrium isotherm studies for the sorption of divalent metal ions onto peat: copper, nickel and lead single component systems," *Water, Air, and Soil Pollution,* vol. 141, pp. 1-33, 2002.

[9] O. Redlich and D. L. Peterson, "A useful adsorption isotherm," *Journal of Physical Chemistry,* vol. 63, pp. 1024-1024, 1959.

[10] F. Haghseresht and G. Lu, "Adsorption characteristics of phenolic compounds onto coal-reject-derived adsorbents," *Energy & Fuels,* vol. 12, pp. 1100-1107, 1998.

[11] L. Jossens, J. Prausnitz, W. Fritz, E. Schlünder, and A. Myers, "Thermodynamics of multi-solute adsorption from dilute aqueous solutions," *Chemical Engineering Science,* vol. 33, pp. 1097-1106, 1978.

[12] S. R. H. FOWLER and E. A. Guggenheim, *Statistical Thermodynamics, Etc.(Second Impression with Corrections.)*: University Press, 1949.

[13] O. Hamdaoui and E. Naffrechoux, "Modeling of adsorption isotherms of phenol and chlorophenols onto granular activated carbon: Part I. Two-parameter models and equations allowing determination of

thermodynamic parameters," *Journal of Hazardous Materials,* vol. 147, pp. 381-394, 2007.

[14] M. Temkin and V. Pyzhev, "Kinetics of ammonia synthesis on promoted iron catalysts," *Acta physiochim. URSS,* vol. 12, pp. 217-222, 1940.

[15] J. Toth, "State equations of the solid-gas interface layers," *Acta Chim Acad Sci Hungar,* vol. 69, pp. 311-328, 1971.

[16] O. Hamdaoui and E. Naffrechoux, "Modeling of adsorption isotherms of phenol and chlorophenols onto granular activated carbon: Part II. Models with more than two parameters," *Journal of Hazardous Materials,* vol. 147, pp. 401-411, 8/17/ 2007.

[17] P. Nikitas, "Generalized Flory–Huggins isotherms for adsorption from solution," *Journal of the Chemical Society, Faraday Transactions 1: Physical Chemistry in Condensed Phases,* vol. 80, pp. 3315-3329, 1984.

[18] G. Halsey and H. S. Taylor, "The adsorption of hydrogen on tungsten powders," *The Journal of Chemical Physics,* vol. 15, pp. 624-630, 1947.

[19] A. A. Noyes and W. R. Whitney, "The rate of solution of solid substances in their own solutions," *Journal of the American Chemical Society,* vol. 19, pp. 930-934, 1897.

[20] W. Nernst, "Theory of reaction velocity in heterogenous systems," *Zeit. physikal. Chem,* vol. 47, pp. 52-55, 1904.

[21] E. L. Cussler, *Diffusion: mass transfer in fluid systems*: Cambridge university press, 2009.

[22] B. K. Lok, Y.-L. Cheng, and C. R. Robertson, "Protein adsorption on crosslinked polydimethylsiloxane using total internal reflection fluorescence," *Journal of Colloid and Interface Science,* vol. 91, pp. 104-116, 1983.

[23] T. Gervais and K. F. Jensen, "Mass transport and surface reactions in microfluidic systems," *Chemical engineering science,* vol. 61, pp. 1102-1121, 2006.

[24] R. B. Bird, W. E. Stewart, and E. N. Lightfoot, *Transport phenomena*: John Wiley & Sons, 2007.

[25] S. Lagergren, "About the theory of so-called adsorption of soluble substances," *Kungliga Svenska Vetenskapsakademiens Handlingar,* vol. 24, pp. 1-39, 1898.

[26] P. Ganesan, R. Kamaraj, and S. Vasudevan, "Application of isotherm, kinetic and thermodynamic models for the adsorption of nitrate ions on

graphene from aqueous solution," *Journal of the Taiwan Institute of Chemical Engineers,* vol. 44, pp. 808-814, 2013.

[27] Y.-S. Ho and G. McKay, "Pseudo-second order model for sorption processes," *Process Biochemistry,* vol. 34, pp. 451-465, 1999.

[28] S. A. Maurer, C. N. Bedbrook, and C. J. Radke, "Competitive Sorption Kinetics of Inhibited Endo- and Exoglucanases on a Model Cellulose Substrate," *Langmuir,* vol. 28, pp. 14598-14608, 2012/10/16 2012.

[29] J. Vernon, "Morphology-preserving chemical conversion of bioorganic and inorganic templates," Ph.D. Dissertation, Materials Science and Engineering, Gerorgia Institute of Technology, Gerorgia Institute of Technology, 2012.

[30] Q-Sense, "Q-Sense Basic Training," Q-Sense, Ed., ed, 2006, p. 27.

[31] C. Cameron, "NATURAL AND ARTIFICIAL FLUORESCENCE ON 3-DIMENSIONAL BIOORGANIC NANOSTRUCTURES," Ph.D. Dissertation, Materials Science and Engineering, Georgia Institute of Technology, Georgia Institute of Technology, 2014.

[32] M. Edvarsson, "Q-Sense E4 Operator Manual," Q-Sense, Ed., ed. Sweden, 2010.

[33] J. Tokunaga, "Solubilities of oxygen, nitrogen, and carbon dioxide in aqueous alcohol solutions," *Journal of Chemical & Engineering Data,* vol. 20, pp. 41-46, 1975/01/01 1975.

[34] J. Lawrence and R. Parsons, "Adsorption isotherms in mixed solvent systems," *The Journal of Physical Chemistry,* vol. 73, pp. 3577-3581, 1969.

[35] H. Dhar, B. Conway, and K. Joshi, "On the form of adsorption isotherms for substitutional adsorption of molecules of different sizes," *Electrochimica Acta,* vol. 18, pp. 789-798, 1973.

[36] K. G. Bhattacharyya and S. S. Gupta, "Adsorption of Fe (III) from water by natural and acid activated clays: studies on equilibrium isotherm, kinetics and thermodynamics of interactions," *Adsorption,* vol. 12, pp. 185-204, 2006.

[37] Y. Aoki, M. Hashizume, S. Onoue, and T. Kunitake, "Determination of Surface Area and Porosity of Small, Nanometer-Thick Films by Quartz Crystal Microbalance Measurement of Gas Adsorption," *Journal of Physical Chemistry B,* vol. 112, pp. 14578-14582, Nov 2008.

[38] R. Treybal, "Molecular diffusion in fluids," *Mass-Transfer Operations. 3rd Edition, McGraw-Hill, Singapore,* pp. 21-44, 1981.

CHAPTER 6: Monolayer-by-Monolayer Deposition of High Index of Refraction Material for Tuning of Reflection Spectra of Inverse Opals

6.1 Summary

Low index silica Inverse opal samples were coated in an automated computer controlled coating machine using the surface sol-gel (SSG) method. This system allowed for quick repeatable LbL coating to be applied without the constant involvement and observation of a human operator. Inverse opal samples were coated with tin-doped titania in 50 cycle increments. Coated samples were analyzed via microscopic and spectral characterization in nine prescribed areas, XRD analysis of the phases present, and SEM and EDS of the coating to evaluate coating composition and conformality. This process was repeated after each increment of 50 cycles of tin-doped titania had been deposited, up to 300 total cycles of SSG and thereafter following firing at 500 ˚C.

The coating process resulted in a monotonic red shift from the initial colors of the uncoated inverse opal to an inverse opal coated with 300 layers of tin-doped titania. Upon firing to 500 ˚C, there was a dramatic blue shift due to the decrease in the fill-fraction of the inverse opal, but the extent of this blue shift was partially mitigated due to the increase in the index of refraction upon crystallization of the coating.

6.2 Introduction

The conception of manipulating light through the use of highly ordered, periodic materials with optical bandgaps was first proposed in the late 1980s. [1]. Inspired by electronic bandgaps in semiconductors, formed by the periodic

variation in electrical potential created by the crystal lattice, it was suggested that structures containing a periodicity on the order of the optical wavelength and periodic variation in the dielectric constant could be used to form materials with photonic bandgaps. Recently, the Aizenberg group at Harvard University developed a lithography-free process based on the sol-gel deposition of SiO_2 around a matrix of self-assembled polystyrene spheres.[2] This process allows for the relatively inexpensive fabrication of wide-area, low-defect density, 3D photonic structures of SiO_2.[2] Previous research into the chemical modification of inverse opals has focused on gas/solid chemical reaction-based transformation of the opal structure into high-index materials.[2, 3] This chapter focuses on methods involving surface chemical modification (coating) to modify the inverse opal reflection spectra.

6.3 Experimental Procedures

6.4 Inverse Opals

Highly-ordered, periodic structures known as photonic crystals have attracted significant attention due to their extraordinary ability to manipulate light.[2] Sol-gel deposition of SiO_2 around a matrix of self-assembled polystyrene spheres allows for the relatively inexpensive fabrication of wide-area, low-defect density, 3D photonic structures of SiO_2.[2] Due to the low index of refraction of silica and the size of polystyrene spheres used to fabricate these inverse opals, such SiO_2-based inverse opals exhibit appreciable light reflection only in the vicinity of 500 nm.

6.4.1 Cleaning of Inverse Opals and Pretreatments

The silica inverse opal segments were fired before coating to pre-shrink the inverse opal structure. The segments were fired to 500˚C for 4 hr. The silica inverse opal segments were then cleaned using an RCA cleaning protocol. Each inverse opal segment was immersed in concentrated HCl (12.1 N, 100 mL, Fisher Scientific) and methanol (100 mL, 99.9%, Fisher Scientific) for 1 h with stirring. The inverse opals were then rinsed with deionized water for 5 minutes. Each opal segment was then placed in a solution of DIW (140 ml) and NH_4OH (30%, 30 mL, Fisher Scientific), followed by addition of H_2O_2 (30%, 30 mL, Alfa Aesar). The resulting mixture was incubated with stirring in a 75 °C water bath for 1 h. After rinsing 3 times with DIW (600 mL) the inverse opal segments were left in DIW until needed. This procedure was conducted by Dr. Yunnan Fang.[4] Segments were rinsed with IPA 3 times immediately before coating, and dried with warm air for five minutes.

6.4.2 SSG Coating of Inverse Opals

Ti-Sn-O bearing coatings were deposited using the SSG method using a D1 robotic coating system explained in CHAPTER 2 on page 27. Coatings were deposited onto cleaned, dry inverse opal segments inside of a glass reaction chamber. Each SSG deposition cycle was conducted by: i) immersing the inverse opal segment in a 50 mM mixed alkoxide precursor of 80 %at Titanium isopropoxide and 20 %at Sn(IV) isopropoxide (Alfa Aesar, Ward Hill, MA, USA) in anhydrous isopropanol (99.8+% purity, Acros Organics, Geel, Belgium) for 5 min at allow for chemisorption of a Sn-Ti-O bearing layer, ii) rinsing three times with

isopropanol (99.5% purity, BDH, PA, USA) to remove any physisorbed precursor, iii) immersion in 60%v DI water in isopropanol for 5 min, to allow for hydrolysis of the alkoxide layer, iv) rinsing 3 times with isopropanol and v) and then drying with warm air from a heat gun for 5 minutes.

This process (alkoxide incubation, isopropanol rinse, DI incubation, isopropanol rinse, drying) was repeated for 100, 150, 200, 250, and 300 cycles to apply a Sn-Ti-O bearing coating at varied thickness. The process is represented in Figure 87.

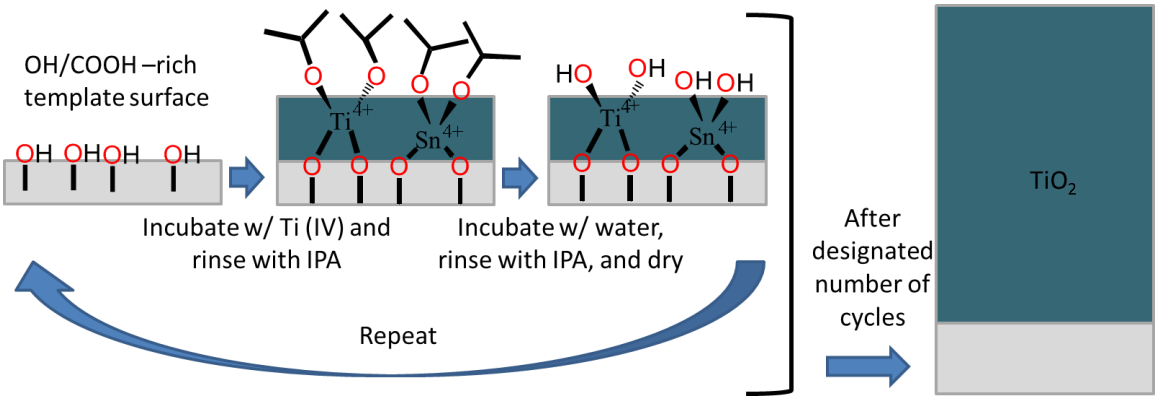

Figure 87: A schematic representation of the SSG process for deposition of a mixed precursor solution of titanium(IV) isopropoxide and tin (IV) isopropoxide.

6.4.3 Crystallization of the SSG Coating

Inverse opal segments were heated in an MgO crucible in a tube furnace (Lindberg Blue M, Thermo Fisher Scientific Inc., MA, USA) at 120 °C/hr to 500 °C and held at this temperature for 4 hr in air to allow for crystallization of the titania doped with tin oxide. The furnace was then cooled at 120 °C/hr to below 100 °C before the sample was removed from the furnace.

6.4.4 FIB Milling For Area Identification

The inverse opal segments that were used in this research were approximately 5 mm X 5 mm in area. To gather reliable, repeatable data on the change in reflected color, optical images and spectral data needed to be gathered from the same area after each new coating was applied. An SEM with a focused ion beam (FIB) (Nova Nanolab 200 FIB/SEM, FEI, Hillsboro, OR, USA) was used to make reference cuts in the inverse opal so that the area to be optically interrogated could be easily found with a 50X optical objective. Typical FIB-milled markings can be seen in Figure 88.

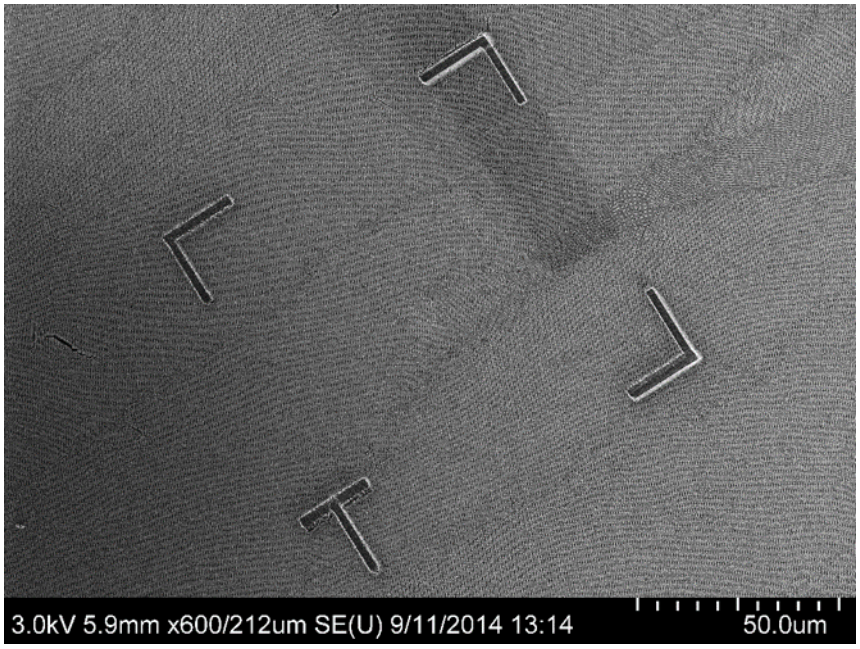

Figure 88: Secondary Electron (SE) micrograph of a FIB-milled "marked" area of an inverse opal. FIB milled marks are designed to repeatedly locate the same area for reflection spectra to be gathered. The "T" shaped mark was used to designate the bottom left corner.

The analytical spot size of the spectrometer was 6 μm X 6 μm. To gather a statistically significant data set an array of 3 X 3 areas were analyzed. The area from which the spectrometer gathered data could be identified using a CCD

camera that allowed the user to select exactly where to conduct spectral analysis. From the view of the camera, the area from which the spectra was gathered was represented by a black box (Figure 89). To be able to gather spectra from the exact same areas, images were gathered with the spectral black box in each location using the CCD camera, and those images were overlaid with an SEM micrograph, as shown in Figure 89.

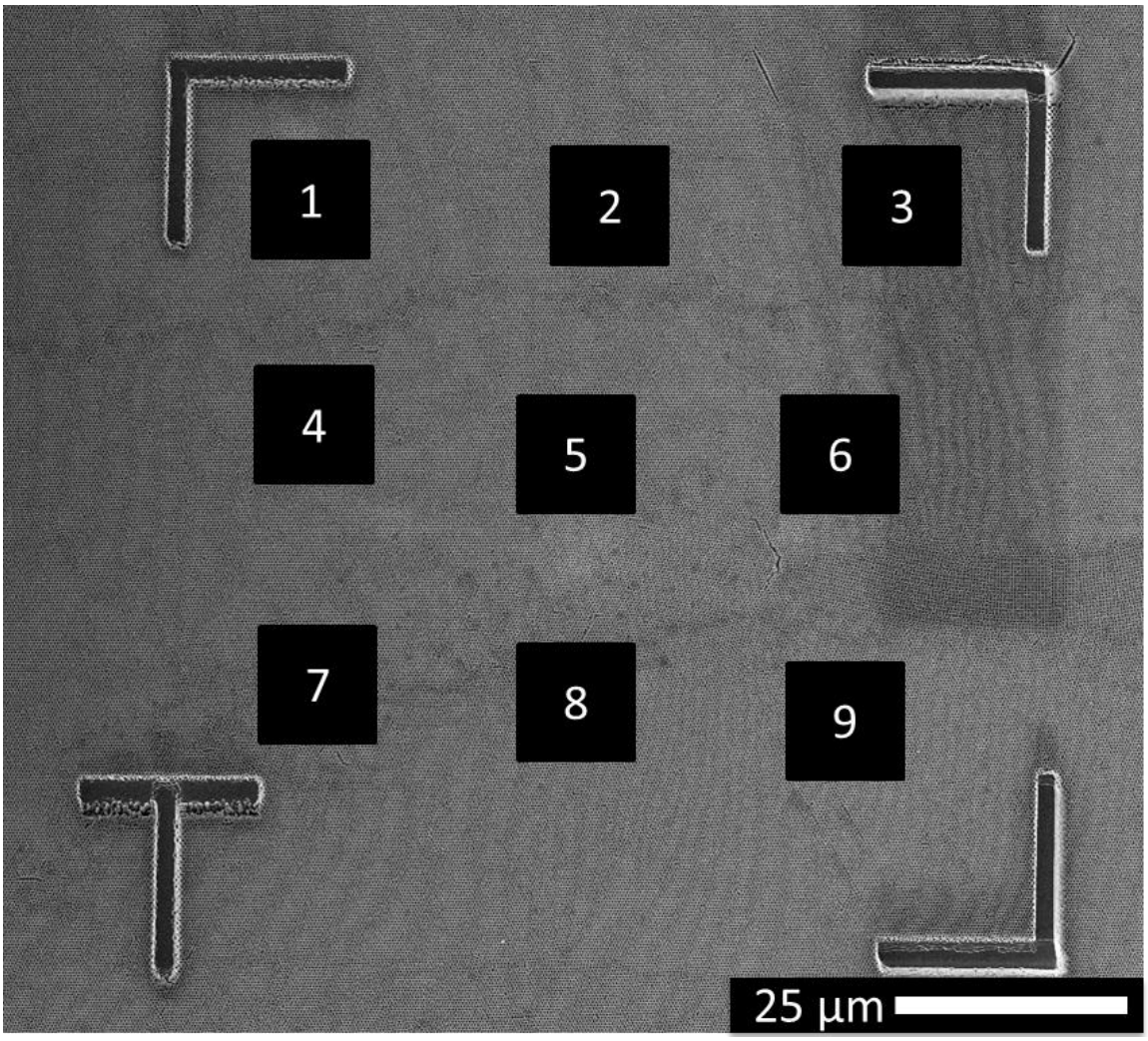

Figure 89: Nine optical images of an inverse opal segment each referencing the location in which a spectrum was gathered (represented by black box). For every change in the inverse opal, i.e. for each 50 cycle increment of SSG, all nine spectra were gathered from the exact same areas. For each inverse opal sample, these images were captured to be used as a reference for spectral gathering for that particular sample.

6.4.5 Optical Analyses

Optical measurements of inverse opals were acquired using an Olympus BX60 (Olympus America, Inc., PA, USA) upright microscope. Images were gathered with a Nikon D300 (Nikon USA, NY, USA) attached to the camera port. Spectral measurements were acquired with a SEE 1000 microscope spectrometer (SEE Science, MA, USA) attached to the microscope camera port with software from Craic Technologies (Version 4.3.1, Craic Technologies, CA, USA). Images and spectra were acquired with an Olympus MPlan FL N 50X objective (0.80 numerical aperture) using a 6 μm x 6 μm spot size. For bright field (BF) white light (WL) illumination, a halogen lamp (Olympus America, Inc., PA, USA) was used. A diffuse reflectance standard (WS-1-SL, Ocean Optics, FL, USA) was used as the WL standard.

6.4.6 Scratch Test with AFM for Thickness Measurement

The thicknesses of coatings on planar substrates were measured using a scratch test with subsequent surface height analysis using an AFM. To ensure that the scratch was made in a repeatable fashion, and that the silicon wafer substrate was not being indented, a wafer scratcher was created. The scratcher was made out of PVC sheet (Chemical-Resistant Type I PVC Sheet, McMaster-Carr, PA, USA), Aluminum T-slot lengths (Aluminum T-Slotted Framing Extrusion, McMaster-Carr, PA, USA), a T-slot hinge (Hinge For 1" T-slotted Framing Extrusion, McMaster-Carr, PA, USA) and a scalpel blade mounted vertically (#15 blade, McMaster-Carr, PA, USA).

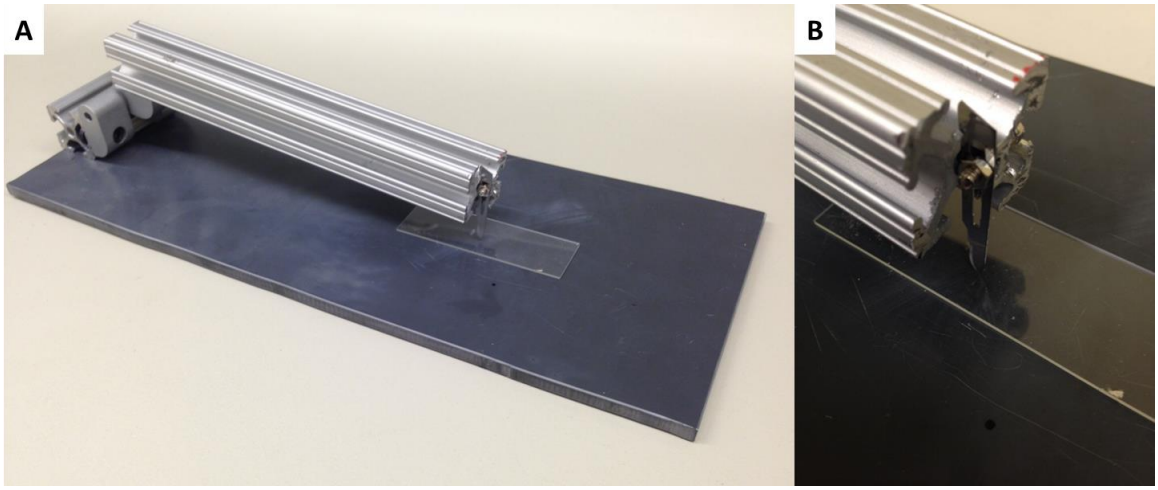

Figure 90: Optical Images of the sample scratcher. A) Full view of scratcher and base, B) close up view of the razor blade tip on a glass slide for demonstration purposes.

The force on the scalpel blade was measured using an analytical balance (AE240, Mettler-Toledo Inc., OH, USA). This setup produced a force of 0.751 N on the tip of the scalpel blade. This force was found to be sufficient to scratch the as-coated SSG coating, but light enough so as not scratch the silica layer on the silicon wafer. This was verified by scratching a clean silicon wafer, and a silicon wafer coated with 100 cycles of as-coated 20%at Sn(IV) isopropoxide and 80%at Ti(IV) isopropoxide. The scratched area on each wafer was analyzed using the AFM and the height profile of the scratch edge was measured. The two AFM scans can be seen below in Figure 91.

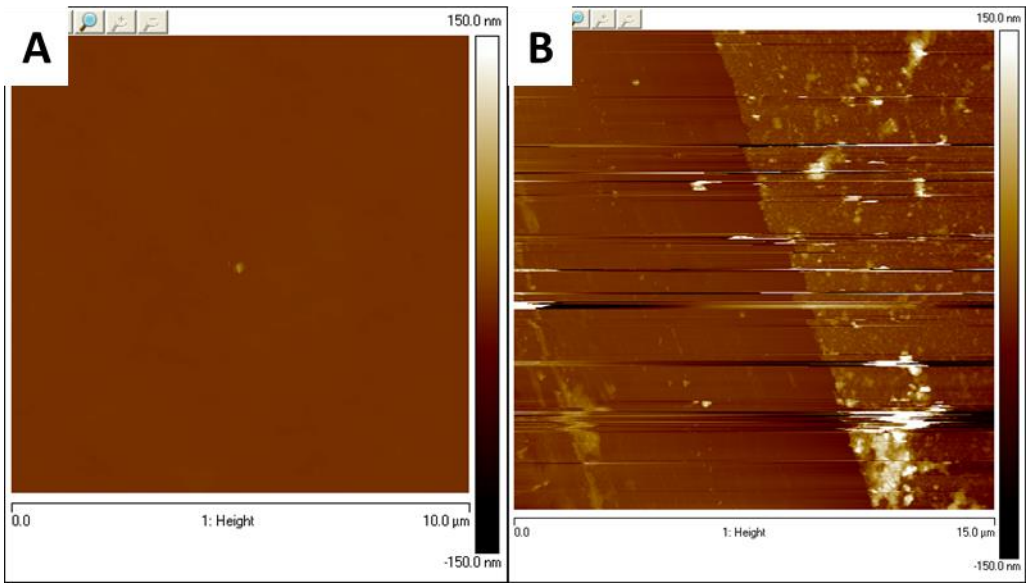

Figure 91: Micrographs of AFM scans of scratched areas on: A) a clean silicon wafer and B) a silicon wafer coated with 100 cycles of 20%at Sn(IV) isopropoxide and 80%at Ti(IV) isopropoxide. Courtesy of Ben deGlee.

The thickness of the coating was measured by preforming a line scan over the edge of the scratch. On the clean silicon wafer, no indentation was detected. On the coated sample, however, the increase in the height across the scratched region was approximately 23 nm for this particular measurement, see Figure 92.

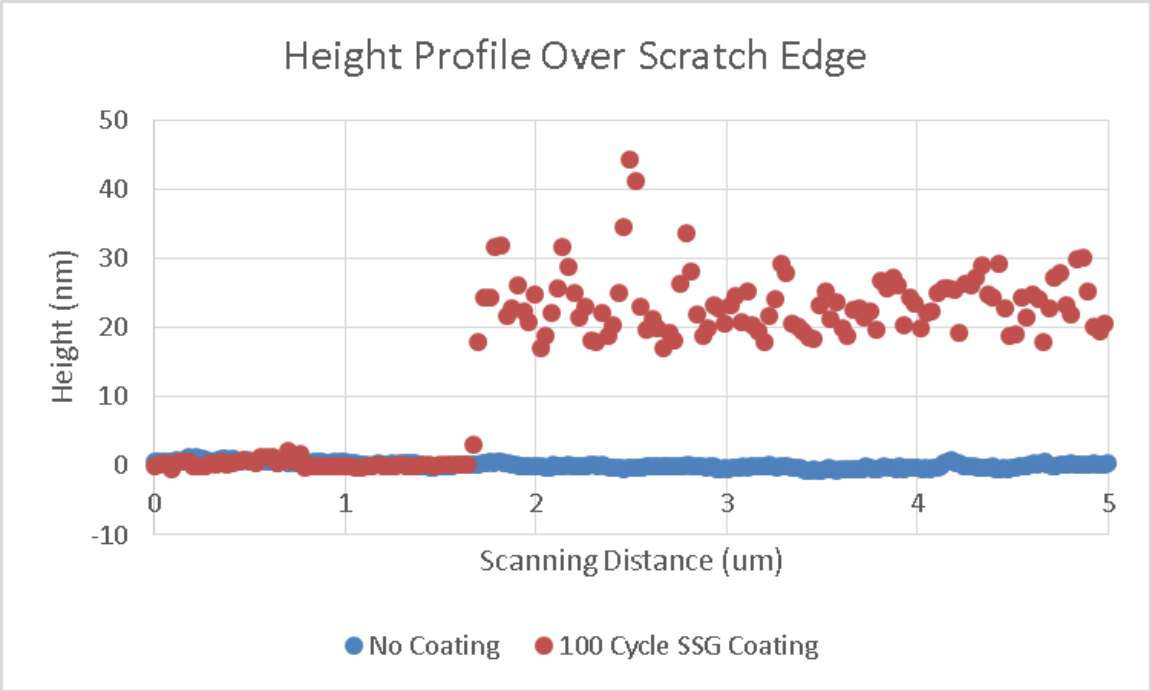

Figure 92: Plot of the differential height as measured by a line scan via the AFM of both a clean silicon wafer (Red) and a silicon wafer coated with 100 cycles of as-coated 20%at Sn(IV) isopropoxide and 80%at Ti(IV) isopropoxide. Courtesy of Ben deGlee.

The line scan data shows that within the scratched region of the coated silicon wafer (i.e. the exposed polished silicon surface) the height was uniform whereas the unscratched region (i.e. where the film remained) was rough. The measured RMS roughness of the scratched area (i.e. the exposed polished silicon surface) of the coated silicon wafer and of the clean silicon wafer were both below 1 nm, suggesting that the scratcher fully removed the SSG coating in the scratched region.

6.4.7 Phase and Morphology Analyses

The morphology of the inverse opal samples was characterized using an SEM (SU8010, Hitachi, Krefeld, Germany) and TEM (FEI Tecnai F30 microscope, FEI, OR, USA). All TEM analyses were performed by Dr. Ye Cai, Sandhage Group,

Georgia Institute of Technology. Top-down SEM analyses were conducted on individual inverse opal segments. Before the sample was coated and after every coating step, the inverse opal morphology was analyzed using top-down SEM micrographs. High resolution images were taken of the exact same area after each 50 layer increment to monitor the growth of the Sn-Ti-O bearing coating.

For samples sputtered with carbon, a Quorum Q150T ES (Energy Beam Sciences, INC., CT, USA) sputter coater was utilized. Cross-sections of samples and surface markings were created via focused ion beam (FIB) milling (Nova Nanolab 200 FIB/SEM, FEI, OR, USA).

XRD analyses were conducted on segments of inverse opal mounted with clay on a sample holder using an X'Pert Pro Alpha-1 diffractometer (PANalytical, Almelo, Netherlands) with monochromatic Cu Ka1 (1.540598 Å) radiation from a 1.8 kW (45 kV, 40 mA) X-ray tube filtered via a symmetrical Johannson monochromator and detected by an X'Celerator detector. The source was limited by a 1° fixed anti-scatter slit, a ½° programmable divergence slit, and a 15 mm mask. The diffracted X-rays were subject to a 0.04 radian soller slit and a 5.5 mm anti-scatter slit before the X'Celerator detector. Diffraction specimens were placed on B doped p-type Si zero background plate (MTI Corp, CA, USA). The sample support was rotated at 8 sec per revolution.

6.5 Results & Discussion

Many types of analyses were performed on the silica inverse opals before coating, after each coating session, and after firing of the sample. EDS, SEM and XRD were collected each step of the coating and firing process and TEM was

gathered only after firing. In-situ QCM experiments were performed to analyze the deposition process and for dynamic analysis of the thickness of the Sn-Ti-O coating.

6.5.1 Determination of Coating Composition

The SSG coating on the inverse opals was interrogated with EDS to verify that the coating contained both titanium and tin. EDS measurements were conducted using an energy dispersive X-ray spectrometer (EDS) (INCA 7426, Oxford Instruments, UK) which was used in combination with a field-emission scanning electron microscope (1530 FESEM, Carl Zeiss, NY USA). EDS analysis was also performed on a FIB cross section of the inverse opal sample in the area of the coating.

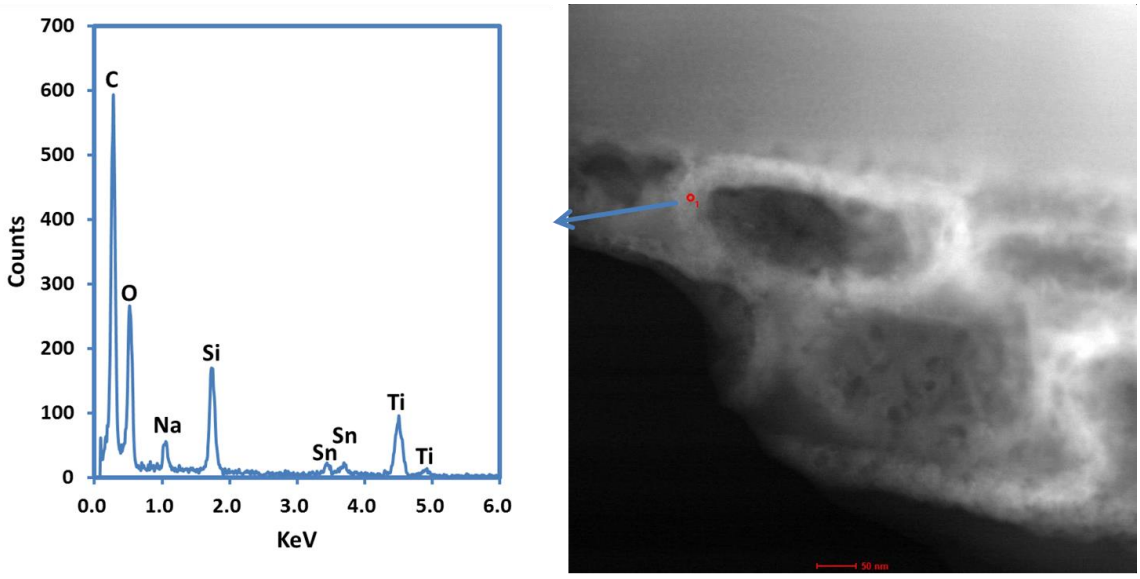

Figure 93: STEM/EDS analysis of silica inverse opal coated with $Sn_{0.2}Ti_{0.8}O_2$ fired at 500 °C for 4 hr. Courtesy of Dr. Cai.

EDS analyses show that the as-coated and fired inverse opal samples possessed elemental tin and titanium in the coating. The sodium present in the EDS analysis was native to the glass slide substrate. The carbon was due to carbon sputtering.

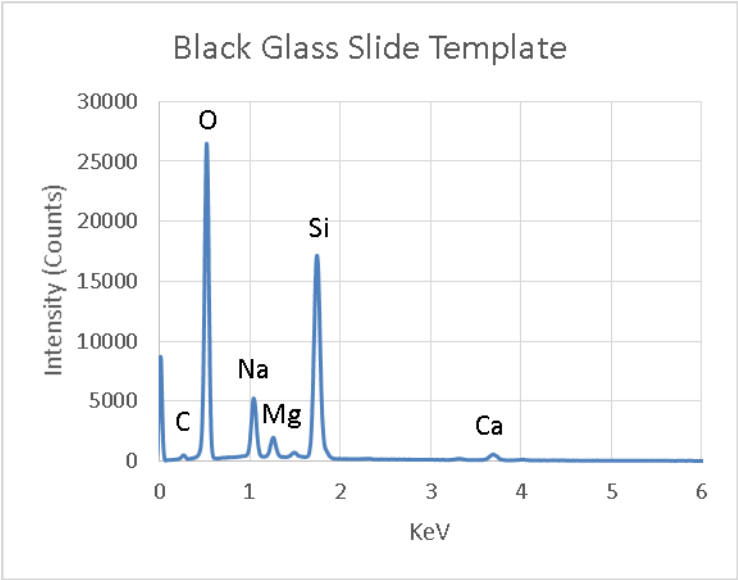

Figure 94: EDS of blank glass slide template showing the presents of sodium, magnesium, and calcium before the creation of the inverse opal structure. Courtesy of Dr. Feng.

Figure 94 shows the presence of sodium, magnesium and calcium in the glass slide substrate on which the inverse opal structure was fabricated (48382-179, Micro Slides, VWR, PA, US).

6.5.2 Determination of Coating Phase

After each step in the coating process each inverse opal sample was interrogated using XRD to determine the phase purity of the coating. After 300 SSG cycles of 20%at Sn(IV) isopropoxide and 80%at Ti(IV) isopropoxide the sample was fired at 500 °C for 4 hr to crystalize the coating into rutile titania.

Figure 95 shows the XRD data of an as-received inverse opal segment and that same segment after coating and firing which shows the presence of rutile titania.

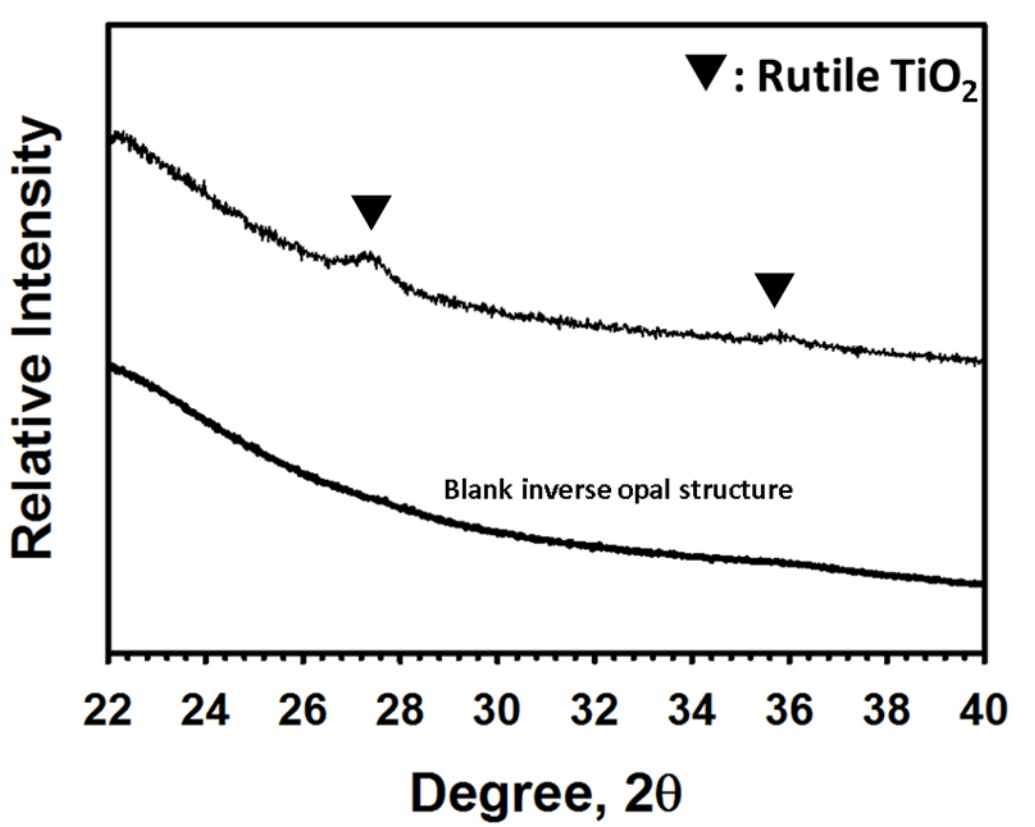

Figure 95: XRD of Bottom: uncoated silica inverse opal and Top: silica inverse opal with 300 SSG cycles of 20%at Sn(IV) isopropoxide and 80%at Ti(IV) isopropoxide and fired at 500 °C for 4 hr. Courtesy of Dr. Feng.

6.5.3 Determination of Thickness of SSG Coating

The peak reflection of the inverse opal should red shift as the fill fraction increases and as the index of refraction of the material increases. Each additional SSG layer increases the fill fraction of the inverse opal by an amount dependent on the current fill fraction and the thickness of the individual layer. The individual layer thickness is important in predicting the change in fill fraction for each layer. All layers were deposited onto the inverse opal segments using an automated coating system as described in CHAPTER 2. The deposition conditions

for each layer were held constant for all of the coatings. The precursor solution was a mixture of 20%at Sn(IV) isopropoxide and 80%at Ti(IV) isopropoxide in anhydrous isopropanol at a total isopropoxide concentration of 25 mM. The thickness of each coating layer was obtained by four independent methods, which were compared to each other and to a theoretical calculation. The four methods of determining the per-cycle thickness were: i) analysis of SEM micrographs taken throughout the coating process, ii) TEM of the final inverse opal segment, iii) AFM of an analog coated silicon wafer, and iiii) analysis of QCM data of the co-deposition of 20%at Sn(IV) isopropoxide and 80%at Ti(IV) isopropoxide.

The deposition of SSG coating layers was carried out in segments of 50 or 100 layers at a time to limit the amount of transportation of the sample. After each time the inverse opal segment was coated, the segment was removed from the coating chamber and characterized via SEM, EDS, XRD, and optical reflectance spectroscopy.

SEM micrographs were collected after each group of coatings. Micrographs were collected from a number of areas at varying magnifications. One area in particular was imaged at 100,000 X magnification for analysis of the shrinkage of the inverse opal pore diameter. Figure 96 shows the change in the size of the pores as the coating thickness was increased.

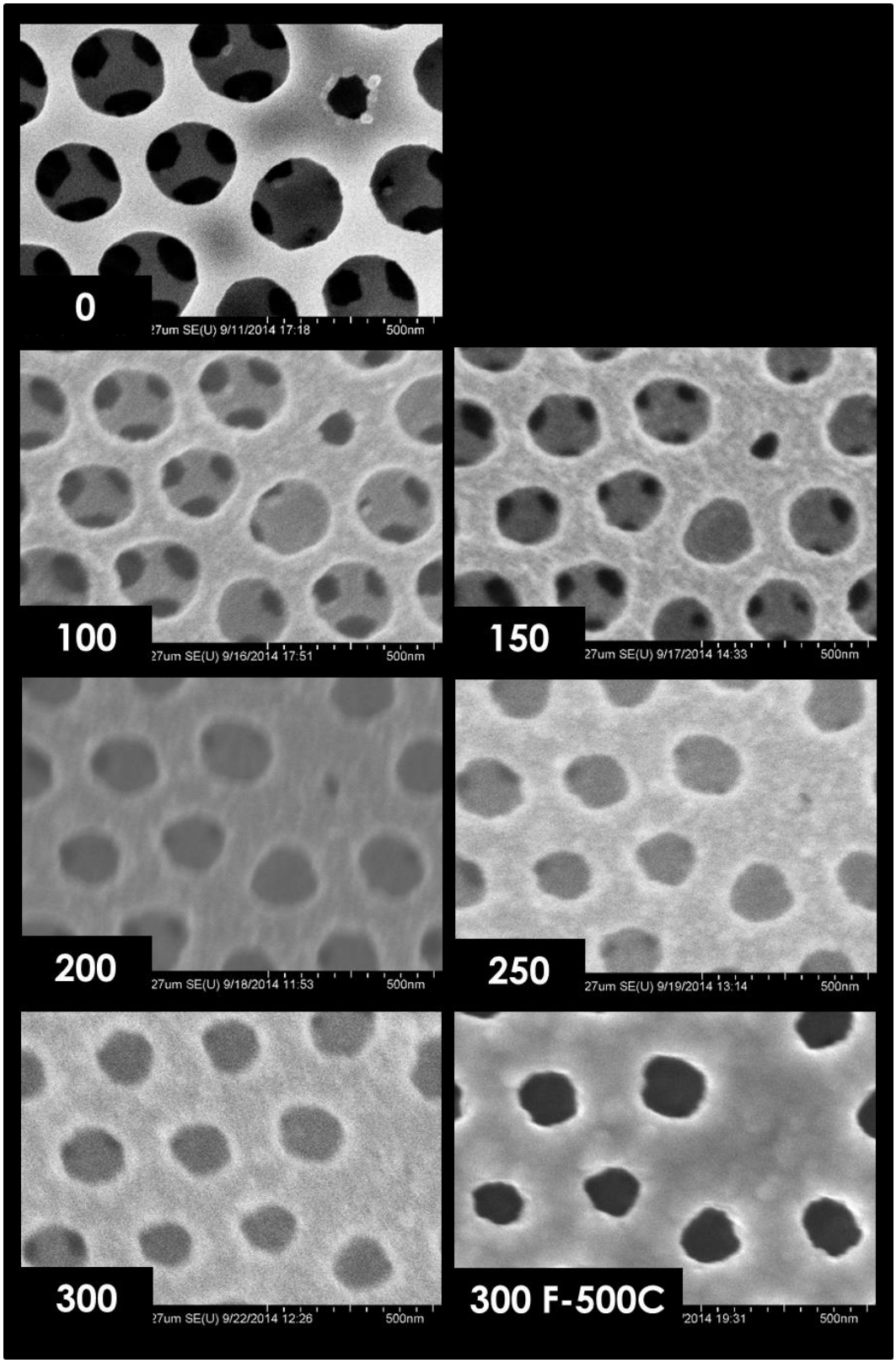

Figure 96: SEM micrographs of a particular section of inverse opal at 100,000X magnification showing the shrinking of the pores with increasing number of SSG deposition cycles. All micrographs are of the same pores on the same sample at the same magnification.

The diameters of four pores were tracked during the coating process. Each pore was measured using the ImageJ software. The perimeter of each pore was carefully traced, and by setting the linear scale using the scale bar, the ImageJ software was used to calculate the circumscribed area. The pores of the inverse opal were approximately circular and so an effective radius was calculated for each pore using equation (41).

$$r_{effective} = \sqrt{\frac{A_{pore}}{\pi}} \quad \textbf{(41)}$$

The calculated effective radius was used to evaluate the linear growth of the SSG coating. The four pores used in the analysis are shown in Figure 97. The effective radius obtained for each pore on: i) the blank sample, ii) after 100, 150, 200, 250, 300 deposition cycles, and iii) after 300 cycles and firing.

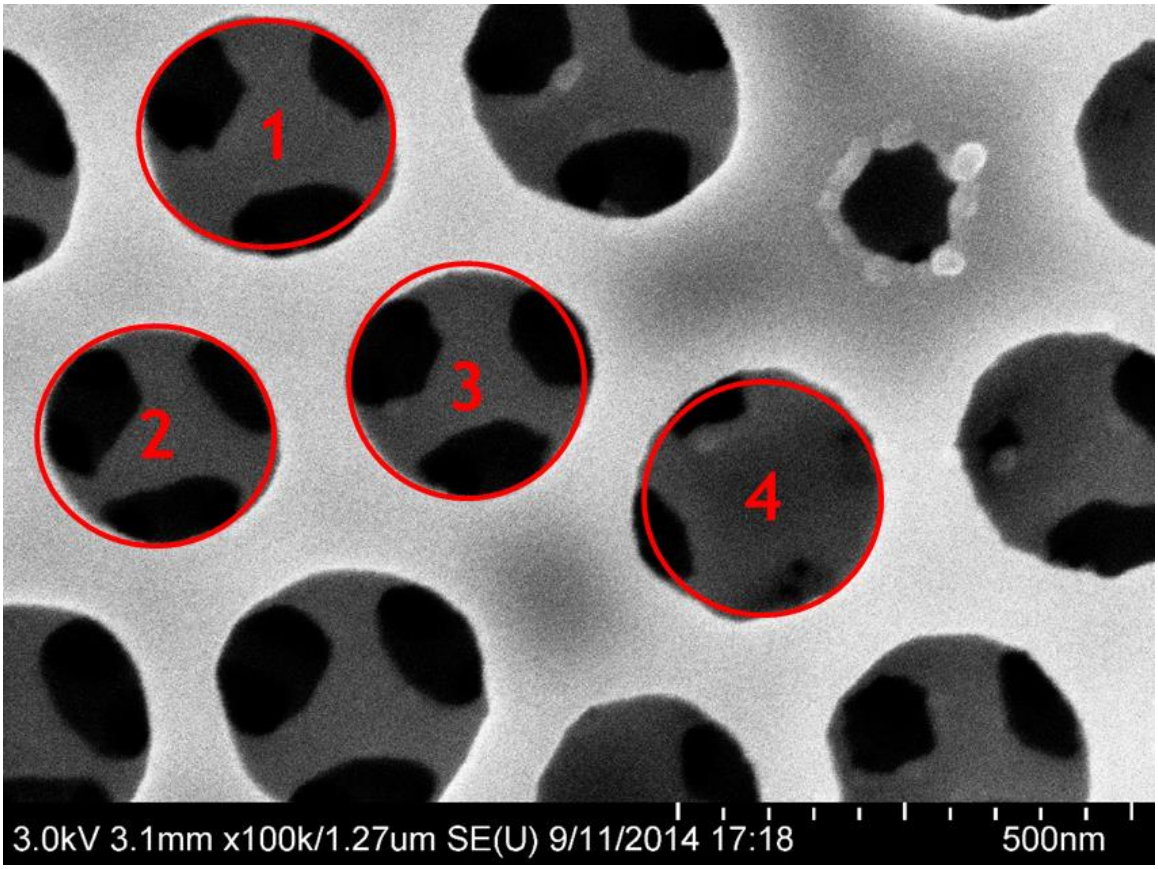

Figure 97: SEM micrograph of uncoated inverse opal segment with four red circles indicating pores that were analyzed. Areas were calculated by computer using the Image-j software.

From these measurements, both the as-coated per-cycle thickness and the fired per-cycle thickness were determined. The data show (Figure 98) that the coatings increase in thickness at a linear rate with respect to the number of deposition cycles and then shrank upon firing.

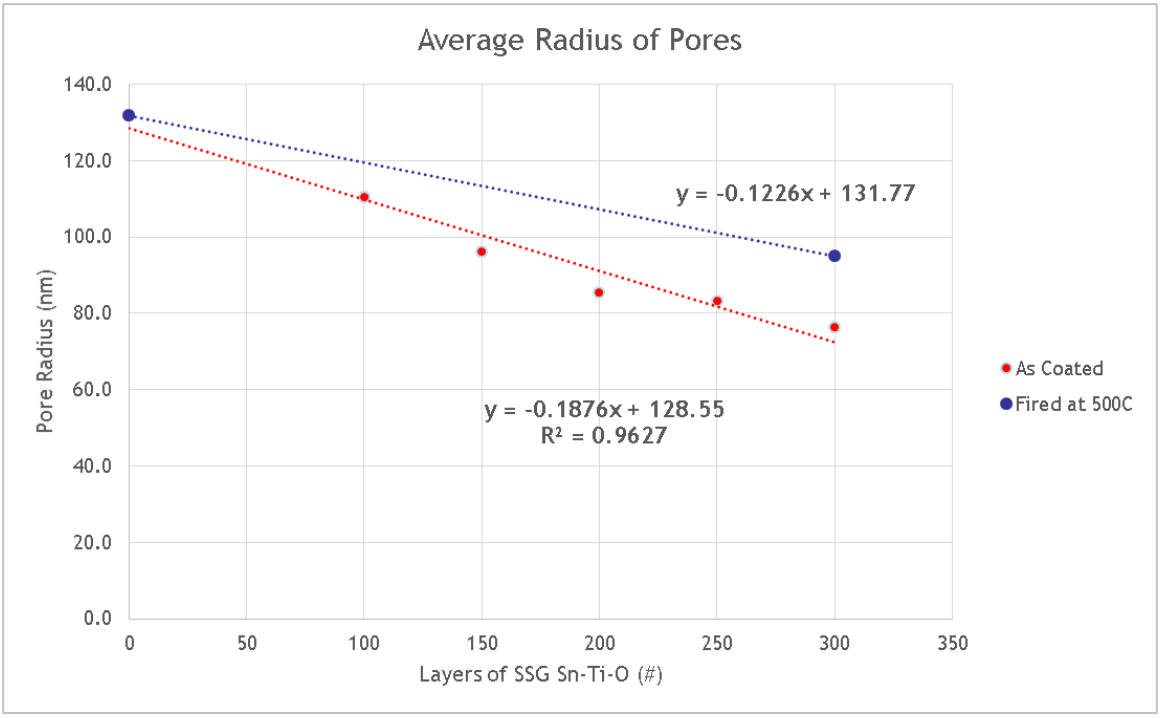

Figure 98: Graph representing the number of coating cycles of 20%at Sn(IV) isopropoxide and 80%at Ti(IV) isopropoxide on a silica inverse opal structure and its effect on the change in effective pore radius. Also shown is the effective pore radius of the inverse opal structure after firing in air at 500C for 4 hr.

This method provided data on both the as coated thickness and the fired thickness. The fired thickness was validated using HRTEM (Figure 99). The HRTEM, performed by Ye Cai, was analyzed by the local TEM software and by ImageJ to determine the thickness of the fired tin-titanium oxide coating. The coating was measure at 10 locations. From the resulting data an average thickness and a standard deviation were calculated.

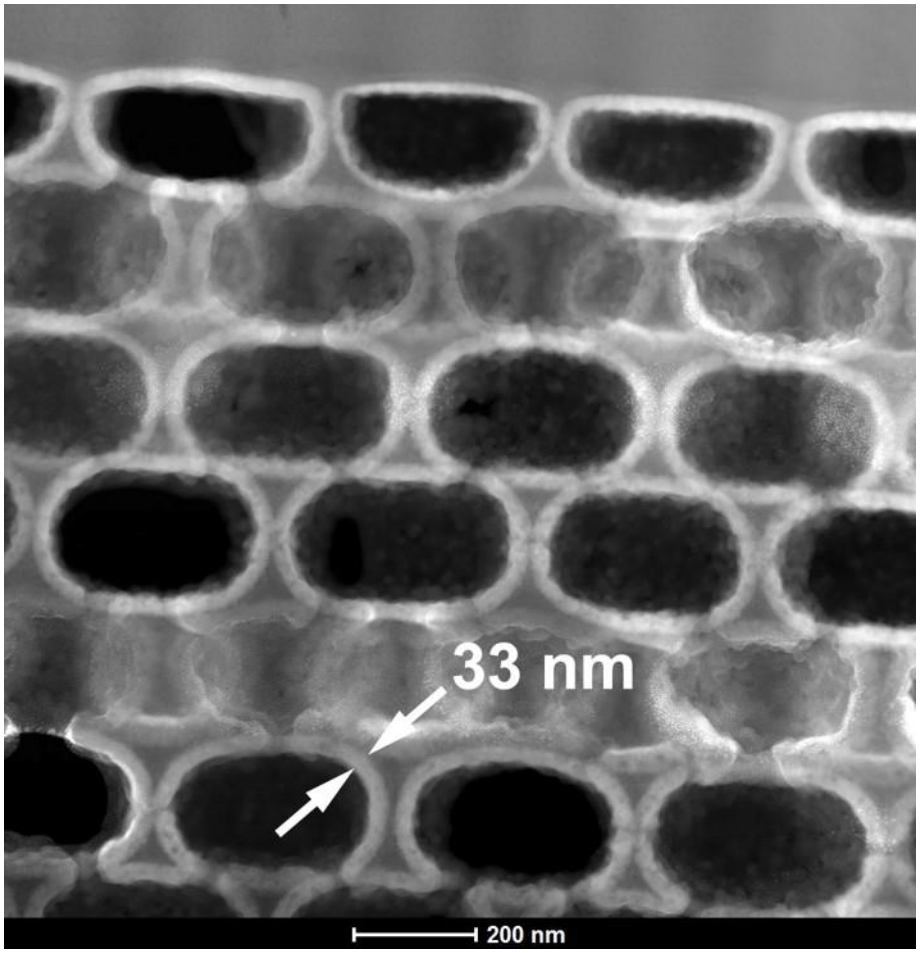

Figure 99: HRTEM of a cross section of an inverse opal coated with 300 cycles of exposure to 20%at Sn(IV) isopropoxide and 80%at Ti(IV) isopropoxide solution and after firing at 500 °C for 4 hr in air.

The as-coated thickness of the SSG coating on a cleaned silicon wafer was also determined by the scratch test. The silicon wafer was cleaned using IPA rinsing followed by DI rinsing, drying under dry N_2 gas and 30 minutes of exposure to UV/O_3. 100 SSG cycles were applied using a precursor solution of 20%at Sn(IV) isopropoxide and 80%at Ti(IV) isopropoxide in anhydrous isopropanol at a concentration of 25 mM. The AFM measurements were conducted after removal of a segment of the coating via use of the silicon wafer scratcher. AFM analyses were conducted by Ben deGlee.

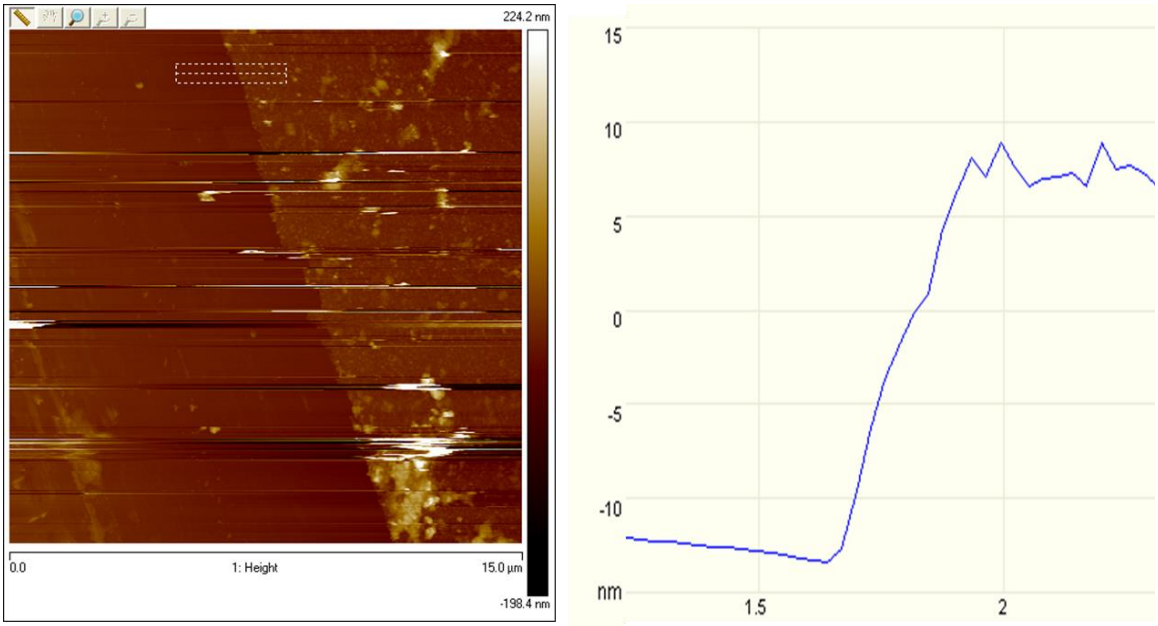

Figure 100: AFM Scratch test for thickness of As-Coated 100 cycle 20%at Sn(IV) isopropoxide and 80%at Ti(IV) isopropoxide on a (100) Si wafer (after 30 min of O_3 + UV) shows ~20nm thickness. (~2Å/cycle).

In-situ quartz crystal microbalance (QCM) analysis was used to measure the deposition rate on an amorphous SiO_2-coated substrate. The QCM, described in detail in CHAPTER 5, measured the change in frequency and damping of a resonating quartz crystal to determine the mass of the material deposited.

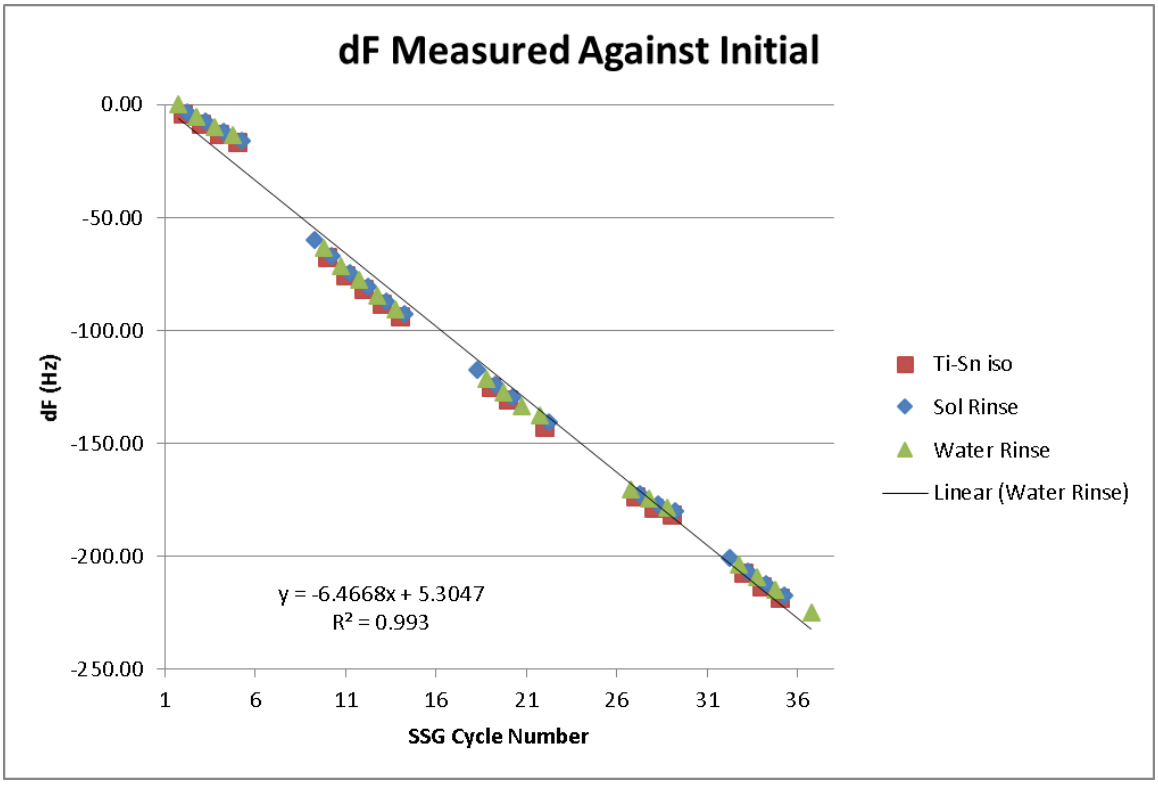

Figure 101: Graph of the change in frequency of a 5 Mhz quartz crystal with increasing number of coating cycles using a precursor solution with 20%at Sn(IV) isopropoxide mixed with 80%at Ti(IV) isopropoxide.

The independent measurements of the per cycle thickness of the 20%at Sn(IV) isopropoxide mixed with 80%at Ti(IV) isopropoxide were compared to theoretical values. Because the coordination number of the cations and anions, in the precursor molecules, are 4 and 2, respectively, it is assumed that this is also the coordination upon deposition. Additionally, because 20% of the cations are tin and 80% are titanium, the effective Ti/Sn-O bond length was calculated by weighting the two bond lengths with their relative concentrations to produce a composite bond length.[5] The Ti(IV) isopropoxide and Sn(IV) isopropoxide molecules each have four ligands positioned in a tetragonal shape the effective growth of a single bond could be as little as $\cos 109.5/2 = 0.5771$ times the actual bond length. The theoretical values were thus calculated using the effective

ionic radii of tin, titanium, and oxygen in two geometric orientations (linear and at a 54.75° angle based on the geometry of the tetrahedral) with coordination numbers of 4 and 2 for the cations and anions, respectively.

Table 8: Effective ionic bond radii for tin and titanium with coordination number 4 and for oxygen with coordination number 2. Linear single bond lengths of 80/20 mixture of Ti/Sn-O are calculated as well as an effective growth rate given at a 54.75 degree angle.[5]

	Sn	Ti	O	Linear	54.75° Growth
CN = 4/2	0.055	0.042	0.135	0.1796	0.1036

For one cycle of the SSG method, the surface hydroxyls are reacted with isopropoxide group(s) to deposit the alkoxide, followed by rinsing and hydration where the other pendant isopropoxide group(s) are reacted with water to produce new hydroxyl(s). Thus, the maximum growth per-cycle for a monolayer is 2 times the bond length between one Sn/Ti and one O. This number could be less due to incomplete coverage of the surface or non-normal direction of growth from the surface.

Upon crystallization, the effective per-cycle growth rate from the surface may be less due to crystallization of the amorphous material into rutile/cassiterite. Upon firing and crystallization, the coordination numbers for the cations and the anions become 6 and 3, respectively. Both rutile and cassiterite form body centered tetragonal structures, the lattice parameters of each material and a rule of mixtures approximation of their composite lattice based on Vegard's law are listed in Table 9.[6, 7]

Table 9: Lattice parameters for rutile, cassiterite, and a calculated 80/20 mixture of rutile and cassiterite. [8]

	Rutile	Cassiterite	80/20 Mixture
a (nm)	4.5937	4.7382	4.6226
c (nm)	2.9532	3.1871	2.9998

Because the $Sn_{0.2}Ti_{0.8}O_2$ structure could be oriented in any direction, the effective layer thickness per cycle was calculated by first averaging the a and c lattice parameters of rutile and cassiterite to calculate the unit cell parameters of the mixture. Then the dimensions of the cation polyhedral were calculated (Figure 102).

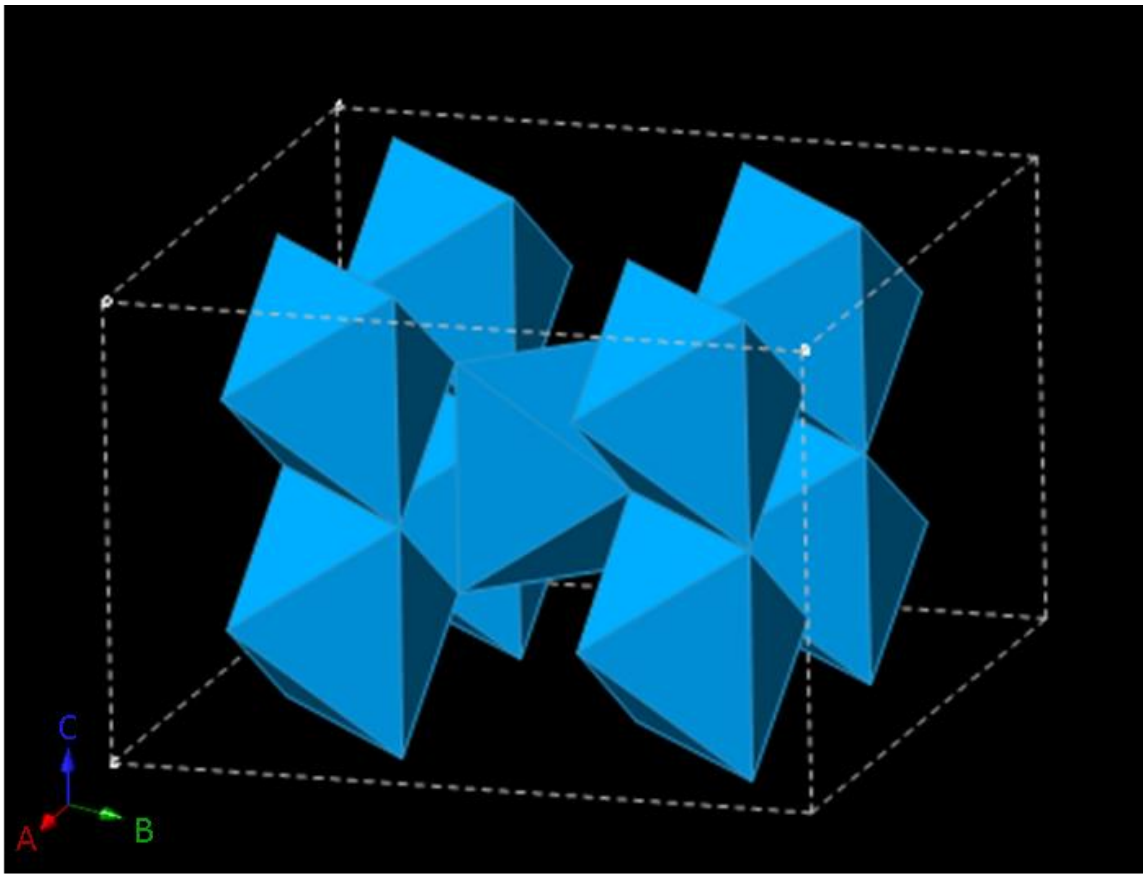

Figure 102: Figure of eight unit cells of rutile (2X2X2) showing the octahedral polyhera of eight oxygen atoms around each titanium.

Two growth geometries were identified as the shortest and the longest. The shortest was identified as the edge of the polyhedral in the c direction, and the longest was identified as the vertex to vertex distance. Figure 103 shows these two directions from the (110) direction.

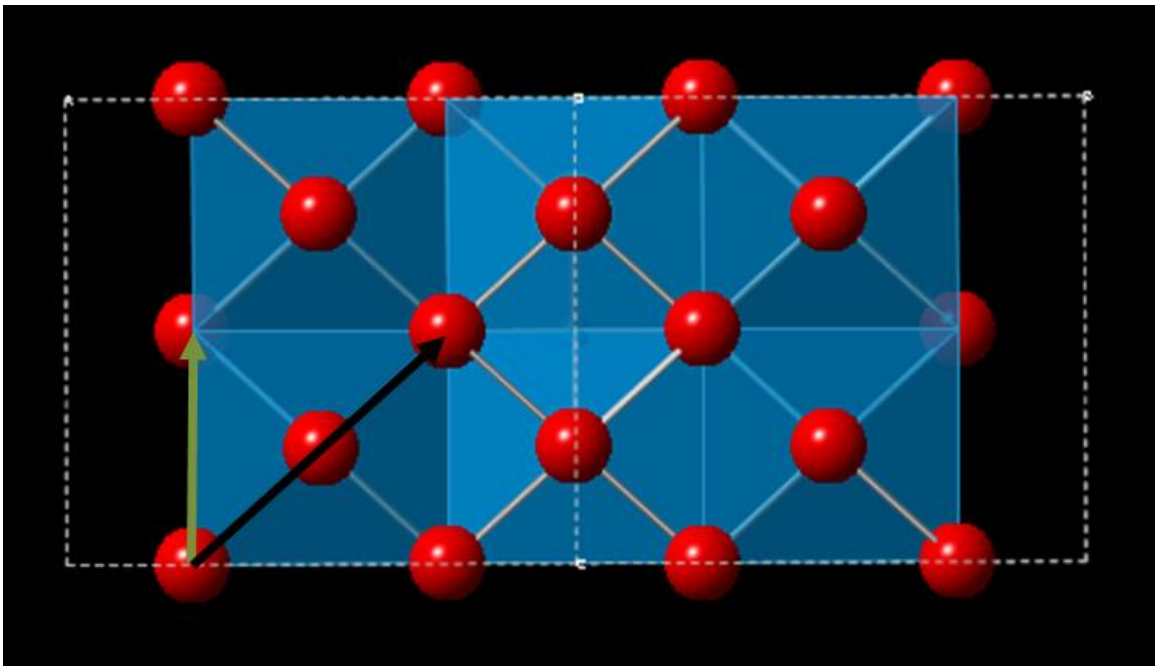

Figure 103: Figure of eight unit cells of rutile viewed from the (110) direction. The green arrow represents shortest direction of grown and the black arrow represents the longest direction of growth.

The magnitudes of these two lengths were calculated by simulating the $Sn_{0.2}Ti_{0.8}O_2$ structure in CrystalMaker and was also verified through the literature.[9] Each of the directions shown in Figure 103 was twice the magnitude of the theoretical per-cycle length so as to guide the eye. The shortest and longest two calculated lengths were 0.150 nm and 0.232 nm, respectively. The measured values of thickness on a per-cycle coating thickness for SEM, QCM, AFM, and TEM were compared to the theoretical thicknesses for an as-coated full monolayer and a fired monolayer, see Table 10.

Table 10: The determined thicknesses per cycle for Sn-Ti-O films both in the as-coated state and in the after firing. All values were in nanometers. Errors were represented as one standard deviation based on the measurements performed. Theoretical values assume a full monolayer is deposited each cycle.

	SEM	AFM/TEM	QCM	Theory
As-Coated (nm)	0.188±0.021	0.206±0.012	0.239±0.037	0.207-0.359
Fired (nm)	0.123±0.021	0.11±0.01	NA	0.150-.232

The data above shows that the thickness of the coating can be reliable measured with a variety of methods as being sub-monolayer deposition. The above data is also represented in graphical form below in Figure 104.

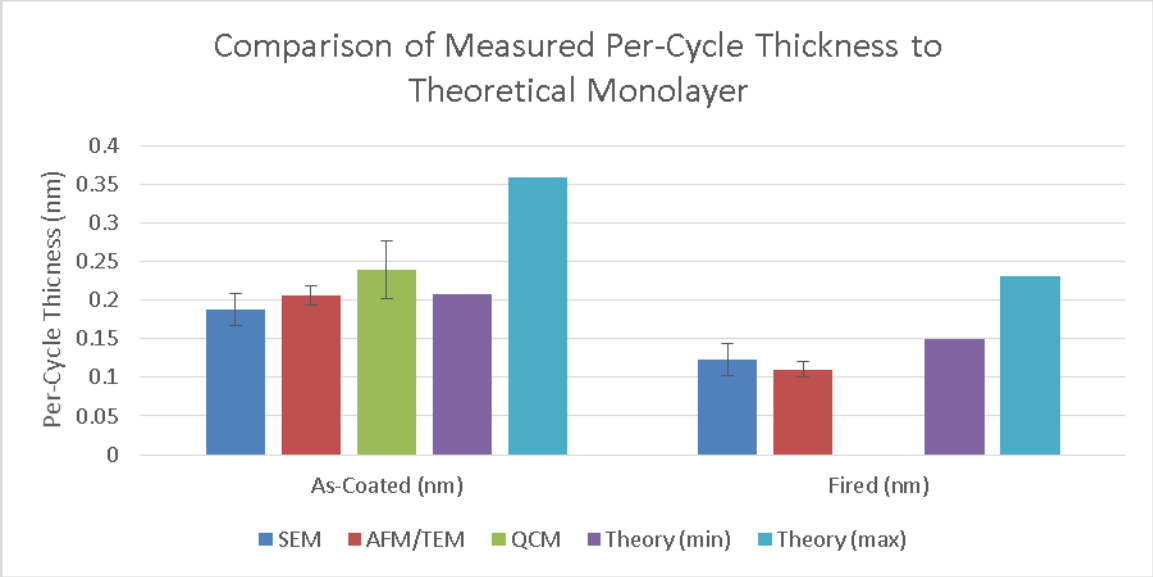

Figure 104: Graphical representation of the per-cycle coating thickness data that was measured via SEM, TEM, AFM, and QCM, as well as the theoretical maximum and minimums for a single monolayer of $Sn_{0.2}Ti_{0.8}O_2$ both for as-deposited and fired coatings. All error bars were one standard deviation.

6.5.4 SSG Cycles Effect on Inverse Opal Optical Reflection

Inverse opal segments were coated with 50 to 300 cycles of Sn-Ti-O via a LbL SSG method using a mixed precursor solution of 20%at Sn(IV) isopropoxide

and 80%at Ti(IV) isopropoxide in anhydrous isopropanol at a concentration of 25 mM. After each round of coating, the sample was optically characterized under white light illumination. Both optical images and spectra were gathered under the same lighting conditions. As the fill fraction of the inverse opal increased, the reflected light shifted from the blue into the green, to yellow and into reddish. This can be seen in Figure 105.

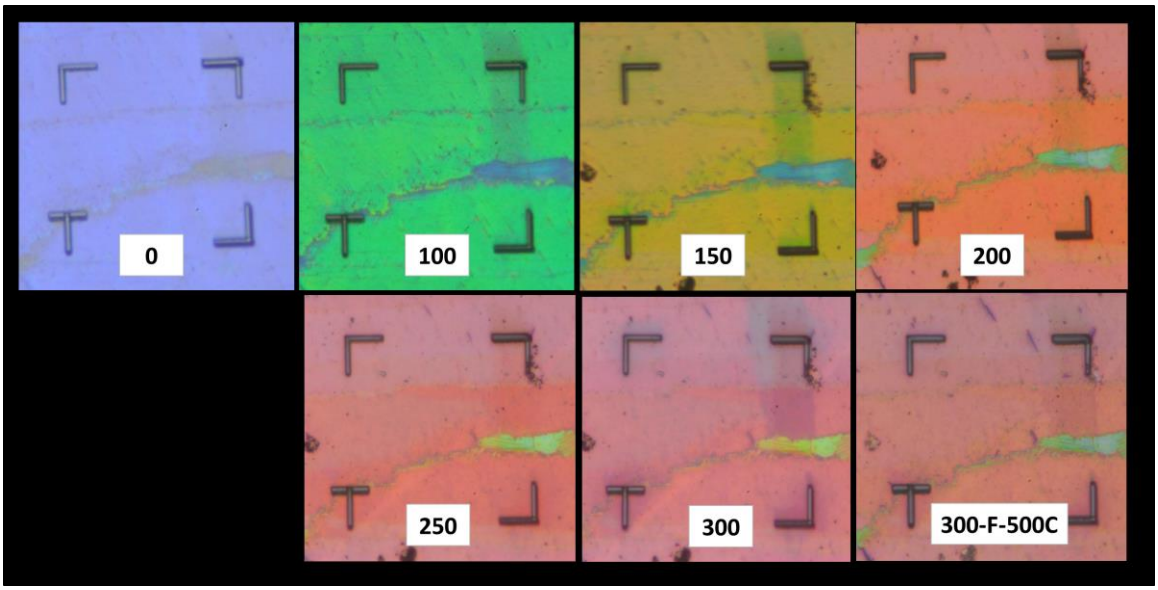

Figure 105: Optical refection images of an inverse opal segment. Number in white box indicates number of SSG coatings and firing conditions where included. The increase in number of coatings yielded a distinct red shift from blue to green to yellow to pink, although after 200 SSG layers, the apparent color shift was less noticeable.

In the optical images, it was difficult to see the optical effect of additional coatings after ~200 cycles, but by using a spectrometer, the change was evident.

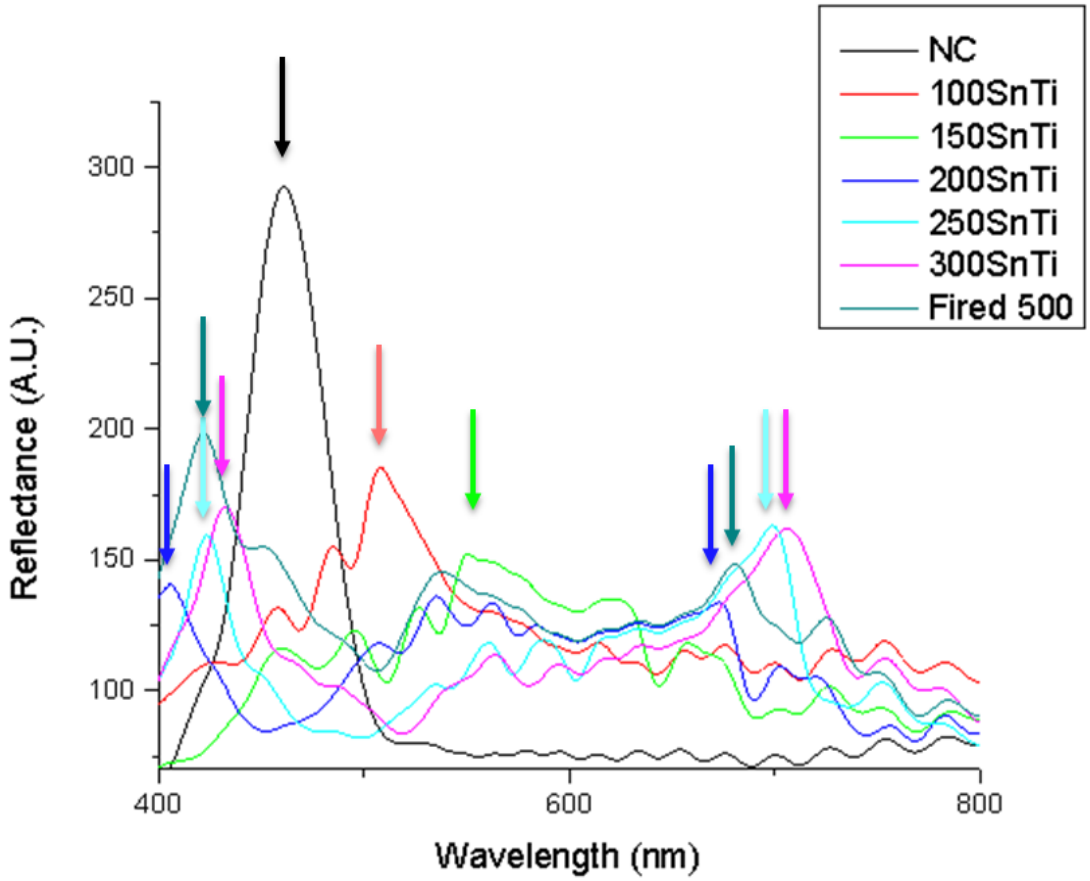

Figure 106: Spectral reflectance from incident WL normalized against a white reflection standard. Arrows indicate approximate locations of primary and secondary peaks when present.

The spectra data represented in Figure 106 demonstrates the shifting of the reflected light with increasing thickness of Sn-Ti-O coating. Upon firing and shrinking of the coating, the peak reflection shifts back towards the blue, but remains red-shifted due to the rutile coating on the surface.

6.6 Optical Approximation

The position of the maximum reflection, or minimum adsorption, can be approximated by modifying Bragg's law[10] with Snell's law to account for the

change in angle of the incident light upon entering medium with a different refractive index. [11-13] In Bragg's law, the angles are usually measured relative to the reflecting plane, and in Snell's law the angles are usually measured from the normal of the plane, that is, these angles are complementary angles.

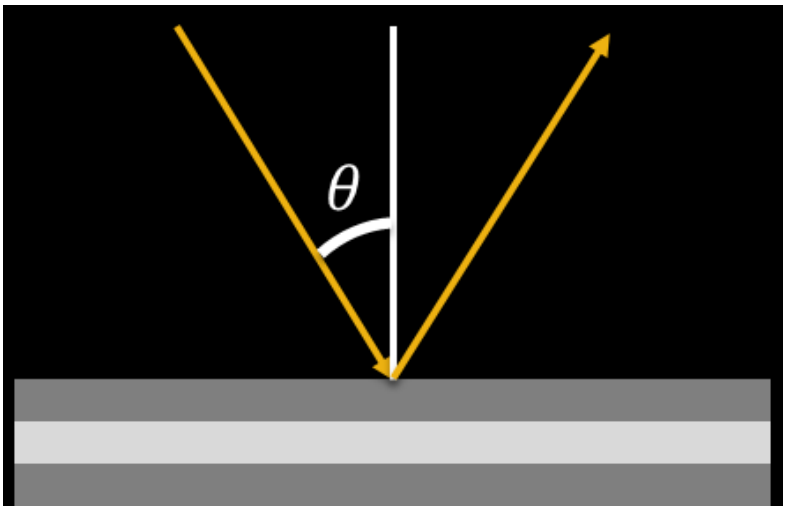

Figure 107: Diagram of an incident beam of light on a layered structure representing the definition of the angle used in Bragg's law and Snell's law in this work.

For consistency, all angles were defined in this work relative to the normal to the reflecting plane, represented in Figure 107, which causes Bragg's law and Snell's law to be represented by Equations (42) and (43), respectively.

$$\lambda = \frac{2d_{hkl}n_{avg}}{m} cos\,\theta \tag{42}$$

$$n_{out}\,sin\,\theta_{out} = n_{in}\,sin\,\theta_{in} \tag{43}$$

Because the angle in Bragg's law, θ, is inside the diffracting material, it is equivalent to the θ_{in} of Snell's law. Likewise, the $n_{avg}$is equivalent to n_{in}. By

squaring Snell's law and using the Pythagorean Theorem (Equation (44)) Equation (43) is transformed into Equation (45) .

$$sin^2\,\theta + cos^2\,\theta = 1 \quad \textbf{(44)}$$

$$n_{out}^2\,sin^2\,\theta_{out} = n_{avg}^2(1 - cos^2\,\theta_{in}) \quad \textbf{(45)}$$

By rearranging Equation (45) to solve for $n_{avg}\cos\theta_{in}$, Bragg's law can be modified to become Equation (46).

$$\lambda = \frac{2d_{hkl}}{m}\sqrt{n_{avg}^2 - n_{out}^2\,sin^2\,\theta_{out}} \quad \textbf{(46)}$$

Here, λ is the peak reflected wave length, d_{hkl} is the interlayer spacing, m is the order of Bragg diffraction, Θ_{out} is the angle between the normal to the packed planes and the incident light, n_{avg} and n_{out} are the indices of refraction of the average inverse opal structure and the air, respectively. Because the angle of the incident light is normal to the sample, Θ = 0, $\sin^2(\Theta) = 0$ and thus Equation (46) simplifies to Equation (47).

$$\lambda = \frac{2d_{hkl}}{m}n_{avg} \quad \textbf{(47)}$$

d_{hkl} is the distance between crystallographic planes in a crystal structure. The dhkl value is based on the crystal plane in question and the unit cell parameter, a, as shown in (48).

$$d_{hkl} = \frac{a}{\sqrt{h^2 + k^2 + l^2}} = \frac{D\sqrt{2}}{\sqrt{h^2 + k^2 + l^2}} \quad \textbf{(48)}$$

Here, h, k, and l are the lattice are the values of the respective Miller indices, and D is the pore spacing of the inverse opal. Figure 99 shows that the structure of the inverse opal is not an ideal inverse opal, but instead is contracted in the z direction. This contraction is significant and causes the pore size to be an inappropriate metric to define the opal. Because the (111) plane is parallel to the top surface, the d_{hkl} value for the (111) plane can be directly measured from Figure 99. By measuring the interplanar spacing associated with the (111), the effective D value was calculated to be 265.5 nm ± 0.3 nm.

To find n_{avg} it was necessary to average the weighted index of refraction values of the fluid in the pores (in this case air), the coating, and the silica substrate. The index of air is 1, the index of silica is varies significantly with wavelength; Figure 108 shows the dispersion of silica.[14, 15]

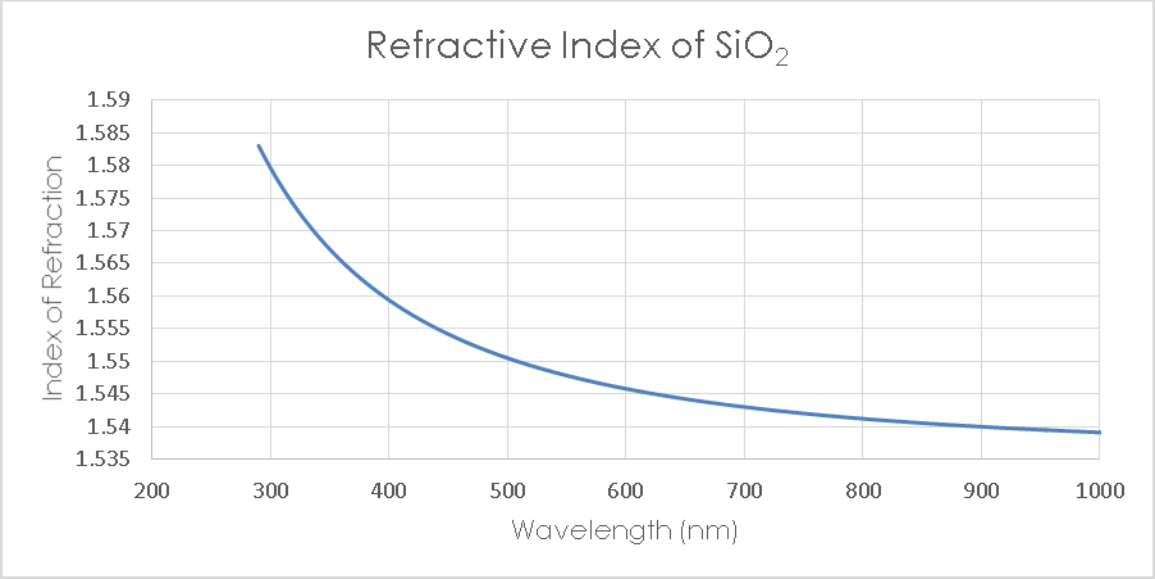

Figure 108: The refractive index of silica has significant dispersion so the index cannot be assumed to be constant over the full range of the spectrum modeled.[15]

The index of the coating was determined for the as coated state and for the fired state. The dispersion of the Ti-O gel, the Sn-O gel, and the 80/20 ratio of those two values can be seen in Figure 109. The dispersion of the mixture was found using a simple rule of mixtures.

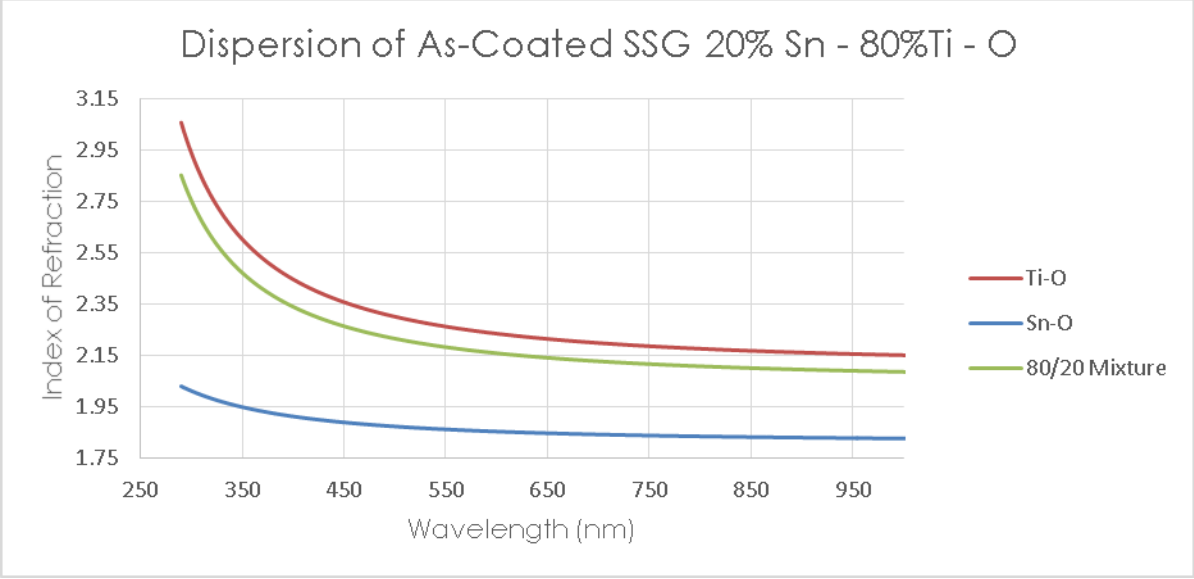

Figure 109: Graph of the dispersion of Ti-O gel, Sn-O gel, and a 80/20 mixture of the two materials. The calculated value for the 80/20 dispersion was found using the rule of mixtures.[16, 17]

After firing, the mixture of Sn-O and Ti-O was crystallized into rutile titania mixed with cassiterite. Although cassiterite does not have significant dispersion, rutile shows significant wavelength dependence. The dispersion of both materials and the 80/20 mixture of the two materials are shown in Figure 110.[18, 19]

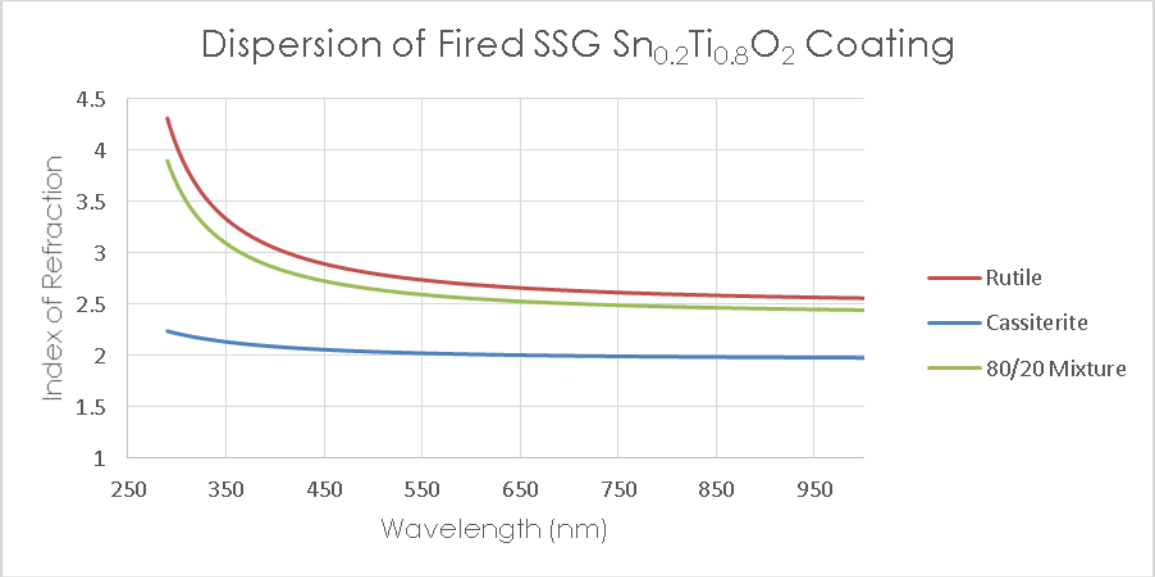

Figure 110: Graph of the dispersion of rutile titania, cassiterite, and a 80/20 mixture of the two materials. The calculated value for the 80/20 dispersion was found using the rule of mixtures. [18, 19]

With the above values, n_{avg} was calculated using Equation (49).

$$n_{avg} = n_{silica}\phi_{silica} + n_{coating}\phi_{coating} + n_{air}\phi_{air} \quad \textbf{(49)}$$

Here, the ϕs are the fill reactions and the ns are the index of refraction values of the constituents. To further refine the model, Dynamical Diffraction Theory (DDT) has been applied to account for coupling of incident and diffracted light.[13]

$$\lambda_D = \lambda_B \left(1 + \frac{\psi}{2}\right) \quad \textbf{(50)}$$

$$\psi = 3\left(\phi_{silica} + \phi_{coating}\right)\frac{r^2 - 1}{r^2 + 2} \quad \textbf{(51)}$$

$$r = \frac{n_{silica}\phi_{silica} + n_{coating}\phi_{coating}}{(1 - \phi_{air})n_{air}} \quad \textbf{(52)}$$

Here in Equations (50)-(52), λ_D and $\lambda_B$are the predicted wavelengths, and r is the ratio of the index of refraction values of the solid material and the air.

By using the above equations and values and by assuming that the conformal SSG coating grows evenly at the rate evaluated above, the following models have been developed.

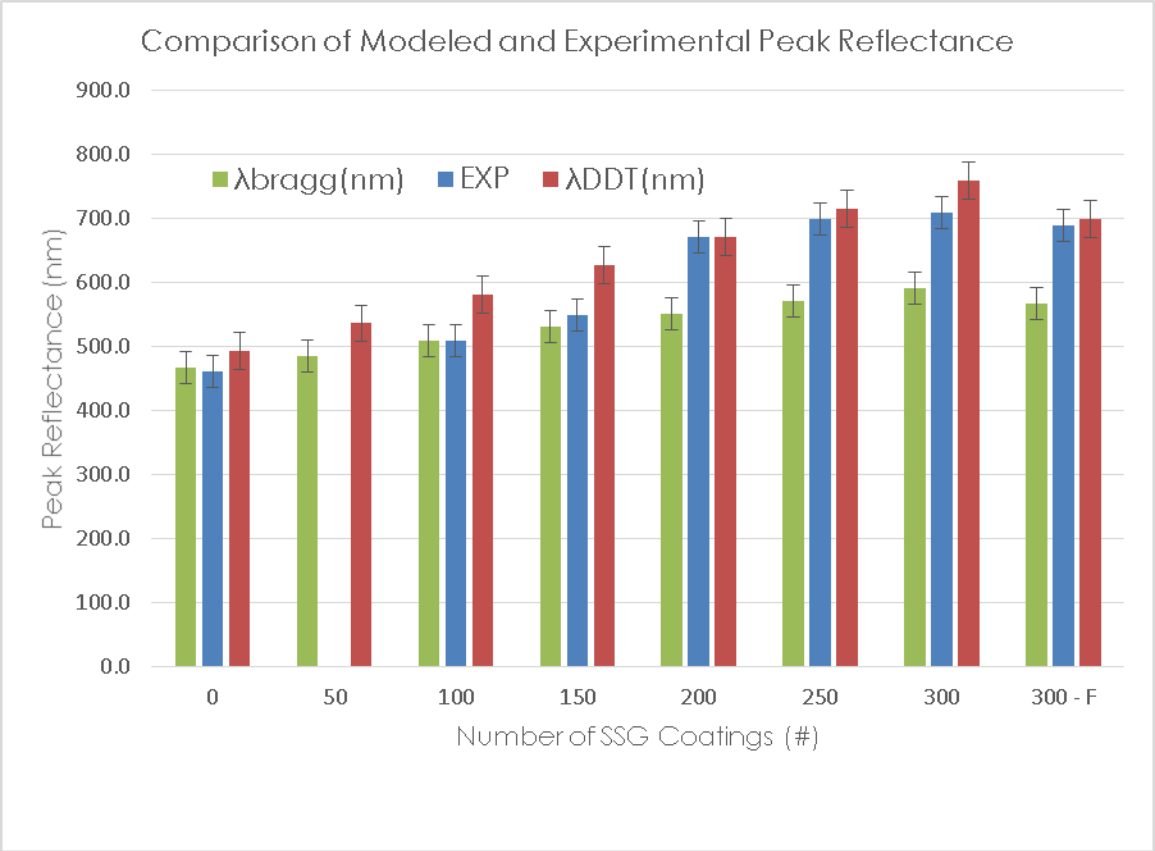

Figure 111: Graph of the comparison of the Bragg, DDT, and experimental peak reflection with various thicknesses of Sn-Ti-O SSG coating and after thermal treatment. Error bars on the experimental are the accuracy of the spectrometer and the accuracy of the accuracy of measurement of the produced spectrum, the error bars on the model include the standard deviation of the measured pore spacing and the assumed index of refractions.

Figure 111 shows the modeled (111) plane reflection of the measured pore spacing. The experimental data fits the Dynamical Diffraction Theory model better than the Bragg diffraction model at higher numbers of coatings. However, at lower number of coatings, the Bragg model matches the experiment data closer. The closer match of the Bragg model at lower coating number, and DDT at higher number, may be due to strong scattering as the coating thickness increases. The inverse opal can be observed to be oriented in with the <111> direction parallel to the incident light, but other crystallographic orientations could be present. Because the crystal is an FCC structure, a plane with an hkl

combination of even and odd numbers is disallowed. But other orientations with only even or only odd values are allowed (e.i. (111), (200), (220), (311) etc.). With the uncoated inverse opal, these reflections are modeled to be present at around 481 nm (111), 417 nm (200), 295 nm (220), and 251 nm (311). All of these values are near the lower limit of the spectrometer and do not necessarily exist in the region being interrogated.

The values of the model were kept constant, but the hkl values were varied for the four scenarios of the experimental data (200 cycles, 250 cycles, 300 cycles, and 300 cycles and firing) where a secondary peak appears in the data. If the secondary peak was from a secondary grain it may be identifiable as one of the other four identified planes.

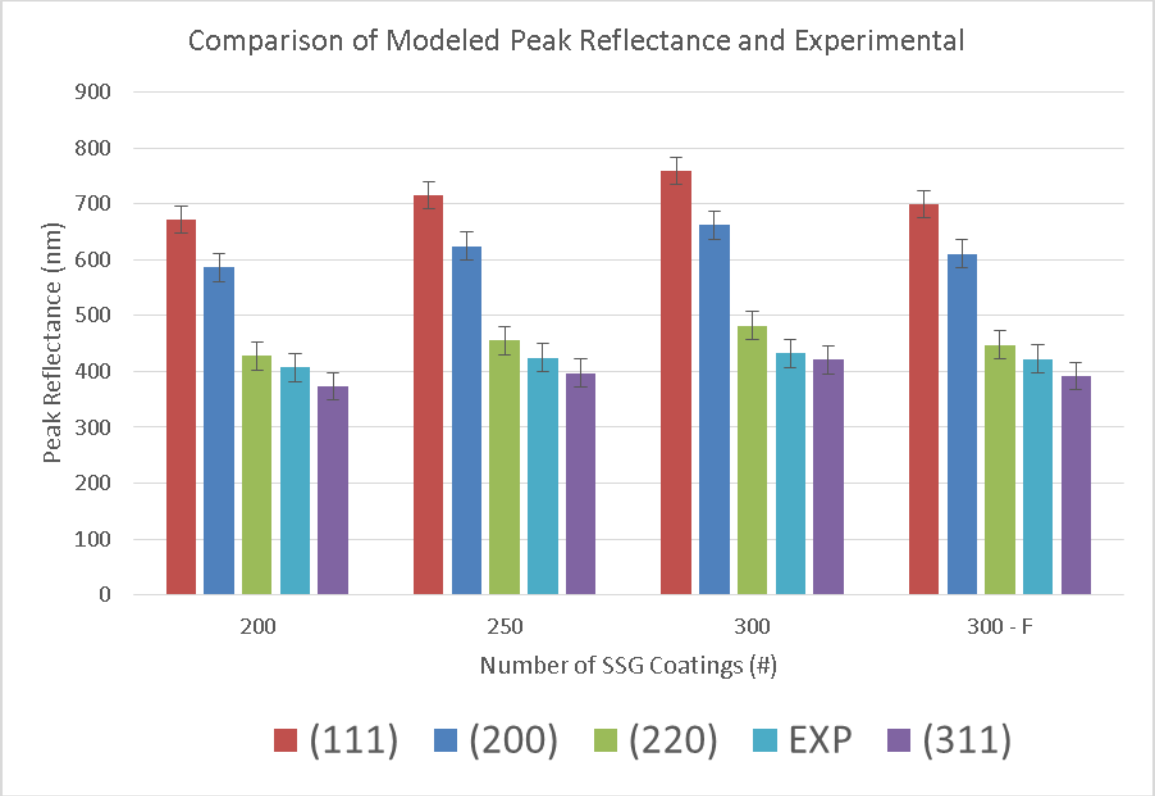

Figure 112: Graph of the comparison of the experimental and modeled secondary reflection peak with various thicknesses of Sn-Ti-O SSG coating and after thermal treatment for various possible secondary crystallographic planes. Error bars on the experimental are the accuracy of the spectrometer and the accuracy of the accuracy of measurement of the produced spectrum, the error bars on the model include the standard deviation of the measured pore spacing and the assumed index of refractions.

Figure 112 shows that the secondary peaks that appear in the blue region of the crystal are likely due to a grain oriented with either the (220) or (311) plane reflecting as opposed to the (111) which provides the main peak reflection.

6.7 Concluding Remarks

The effect of a submonolayer-by-submonolayer deposition of a mixed alkoxide precursor onto a silica inverse opal structure on the reflection spectra has been examined. The Sn-Ti-O coating was deposited via a mixed precursor SSG coating method. SEM, TEM, AFM, and QCM all agree with theoretical calculations for the thickness of the as-coated and as-fired coating thickness. All

of these methods confirm that the coating process resulted in submonolayer deposition per cycle. The reflected color of the inverse opal was tuned from a bluish color to a reddish color solely by coating with the amorphous material. Further, this research also demonstrated the effect of densifying that coating and increasing its index of refraction on blue shifting the reflected color.

6.8 References

[1] E. Yablonovitch, "Inhibited spontaneous emission in solid-state physics and electronics," *Physical review letters,* vol. 58, p. 2059, 1987.

[2] B. Hatton, L. Mishchenko, S. Davis, K. H. Sandhage, and J. Aizenberg, "Assembly of large-area, highly ordered, crack-free inverse opal films," *Proceedings of the National Academy of Sciences,* vol. 107, pp. 10354-10359, 2010.

[3] A. S. Gordin, "Shape-Preserving Physical and Chemical Transformations of Si and SiO2 Nano- and Microstructures," Ph.D. Dissertation, Materials Science & Engineering, Georgia Institute of Technology, Georgia Institute of Technology, 2014.

[4] G. Wang, Y. Fang, P. Kim, A. Hayek, M. R. Weatherspoon, J. W. Perry*, et al.*, "Layer-By-Layer Dendritic Growth of Hyperbranched Thin Films for Surface Sol-Gel Syntheses of Conformal, Functional, Nanocrystalline Oxide Coatings on Complex 3D (Bio)silica Templates," *Advanced Functional Materials,* vol. 19, pp. 2768-2776, Sep 9 2009.

[5] R. t. Shannon, "Revised effective ionic radii and systematic studies of interatomic distances in halides and chalcogenides," *Acta Crystallographica Section A: Crystal Physics, Diffraction, Theoretical and General Crystallography,* vol. 32, pp. 751-767, 1976.

[6] L. Vegard, "Die Konstitution der Mischkristalle und die Raumfüllung der Atome," *Zeitschrift für Physik,* vol. 5, pp. 17-26, 1921/01/01 1921.

[7] A. R. Denton and N. W. Ashcroft, "Vegard's law," *Physical Review A,* vol. 43, pp. 3161-3164, 03/01/ 1991.

[8] J. W. Anthony, R. A. Bideaux, K. W. Bladh, and M. C. Nichols, "Handbook of Mineralogy, Mineralogical Society of America, Chantilly, VA 20151-1110, USA," ed, 2011.

[9] F. Grant, "Properties of rutile (titanium dioxide)," *Reviews of Modern Physics,* vol. 31, p. 646, 1959.

[10] W. H. Bragg and W. L. Bragg, "The reflection of X-rays by crystals," *Proceedings of the Royal Society of London Series a-Containing Papers of a Mathematical and Physical Character,* vol. 88, pp. 428-428, Jun 1913.

[11] C. F. Blanford, R. C. Schroden, M. Al-Daous, and A. Stein, "Tuning Solvent-Dependent Color Changes of Three-Dimensionally Ordered Macroporous (3DOM) Materials Through Compositional and Geometric Modifications," *Advanced Materials,* vol. 13, pp. 26-29, 2001.

[12] R. C. Schroden, M. Al-Daous, and A. Stein, "Self-modification of spontaneous emission by inverse opal silica photonic crystals," *Chemistry of materials,* vol. 13, pp. 2945-2950, 2001.

[13] R. C. Schroden, M. Al-Daous, C. F. Blanford, and A. Stein, "Optical properties of inverse opal photonic crystals," *Chemistry of Materials,* vol. 14, pp. 3305-3315, Aug 2002.

[14] E. D. Palik, *Handbook of optical constants of solids* vol. 3: Academic press, 1998.

[15] I. Malitson, "Interspecimen comparison of the refractive index of fused silica," *JOSA,* vol. 55, pp. 1205-1208, 1965.

[16] S. Kermadi, N. Agoudjil, S. Sali, L. Zougar, M. Boumaour, L. Broch*, et al.*, "Microstructure and optical dispersion characterization of nanocomposite sol–gel TiO2–SiO2 thin films with different compositions," *Spectrochimica Acta Part A: Molecular and Biomolecular Spectroscopy,* vol. 145, pp. 145-154, 6/15/ 2015.

[17] F. E. Ghodsi and J. Mazloom, "Optical, electrical and morphological properties of p-type Mn-doped SnO2 nanostructured thin films prepared by sol–gel process," *Applied Physics A,* vol. 108, pp. 693-700, 2012/09/01 2012.

[18] J. R. DeVore, "Refractive indices of rutile and sphalerite," *JOSA,* vol. 41, pp. 416-417, 1951.

[19] R. D. Shannon, R. C. Shannon, O. Medenbach, and R. X. Fischer, "Refractive Index and Dispersion of Fluorides and Oxides," *Journal of Physical and Chemical Reference Data,* vol. 31, pp. 931-970, 2002.

APPENDIX A: QCM Flow Module Boundary Layer Calculations

To confirm the validity of the kinetic rate limiting step of adsorption of Ti(IV) isopropoxide o nto amorphous silica, the boundary layer thickness was calculated for the full range of flow rates used in this research based on two models. The first model calculated the boundary layer based on the assumption that the flow was similar to that of flow over a flat plate. The second model that was used was based on a Lévêque-type equation which depends on the wall shear rate and is more commonly used in microfluidic conditions. The equations to calculate the boundary layer for flow over a flat plate and the Lévêque-type equation are shown in Equations (53) and (54). [1]

$$\delta_{FOFP} = \frac{4.64(X)^{1/2}(D_i)^{1/3}(v)^{1/6}}{(V)^{1/2}} \quad \textbf{(53)}$$

Here, X is the distance from the leading edge of the plate, D_i is the diffusivity of the dissolved species, v is the kinematic viscosity of the liquid, and V is the velocity of the bulk fluid.[2]

$$\delta_{Lévêque} = \left(\frac{D_i X}{\gamma}\right)^{\frac{1}{3}} \quad \textbf{(54)}$$

Here, X is the distance from the leading edge of the plate, D_i is the diffusivity of the dissolved species, and γ is the wall shear rate which is given in Equation (55).

$$\gamma = \frac{6Q}{b^2 W} \quad (55)$$

Here, Q is the volumetric flow rate, b is the height of the chamber, and W is the width of the chamber.

For both calculations of the boundary layer thickness, the diffusivity of the solute and the fluid properties of the solvent need to be known at the working temperature of 18 °C. The viscosity of isopropanol at 18 °C was found by plotting published data, fitting a line to that data, and calculating the appropriate value.[3-5]

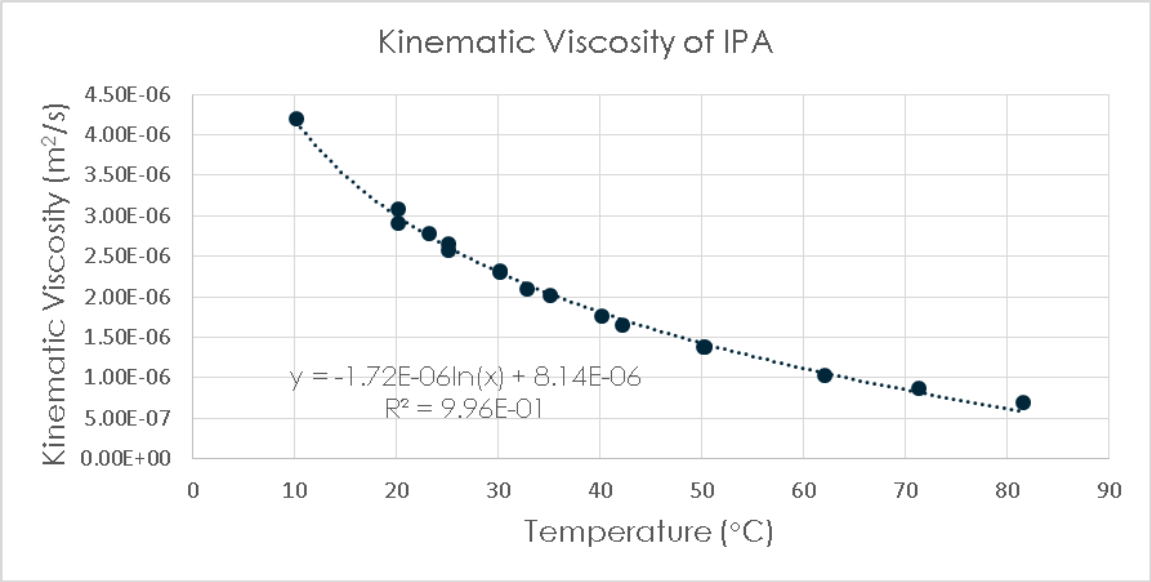

Figure 113: Graph of the kinematic viscosity of isopropanol with respect to temperature and a logarithmic regression fit to the data. [3-5]

The equation from the logarithmic regression in Figure 113 was used to estimate the kinematic viscosity of isopropanol at 18 °C. The approximate value of the density of isopropanol was found using the same method, the respective data and linear regression can be seen in Figure 114.[6, 7]

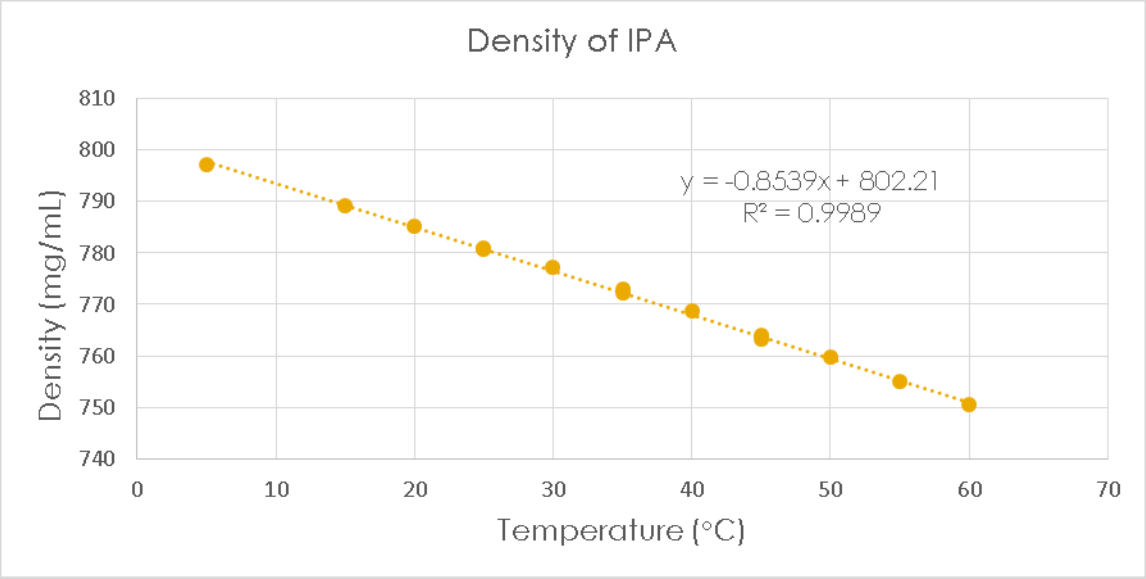

Figure 114: Graph of the density of isopropanol with respect to temperature and a linear regression fit to the data. [6, 7]

With the density and kinematic viscosity of isopropanol known, the dynamic viscosity was calculated using Equation (56).

$$\mu = \rho v \tag{56}$$

Here, μ is the dynamic viscosity, ρ is the density, and v is the kinematic viscosity. The dynamic viscosity was used to calculate the diffusion coefficient of Ti(IV) isopropoxide in isopropanol using the Stokes-Einstein-Sutherland equation; see Equation (57).

$$D_i = \frac{k_B T}{6\pi\mu r} \tag{57}$$

Here, D_i is the diffusion constant, k_B is Boltzmann's constant, T is the absolute temperature, μ is the dynamic viscosity, and r is the estimated radius of the

solute. Because the Ti(IV) isopropoxide molecule is coordinated in the shape of a tetrahedral with isopropoxide groups at each vertex, the molecule can be considered approximately spherical. The radius of the solute can be estimated using the van der Waals volume equation; see Equation (58).

$$r = \left(\frac{3MM}{4\pi N_A \rho}\right) \quad \textbf{(58)}$$

Here, MM is the molar mass of the solute (for Ti(IV) isopropoxide MM = 284.23 g/mol), N_A is Avogadro's number, and ρ is the density of the solute (for Ti(IV) isopropoxide ρ = 0.971 g/ml). Using Equation (58), the effective radius of Ti(IV) isopropoxide was found to be 4.878 Å. With the effective radius and the temperature dependence of the physical properties of isopropanol known, the diffusion coefficient for Ti(IV) isopropoxide was calculated for a range of temperatures and was plotted in .

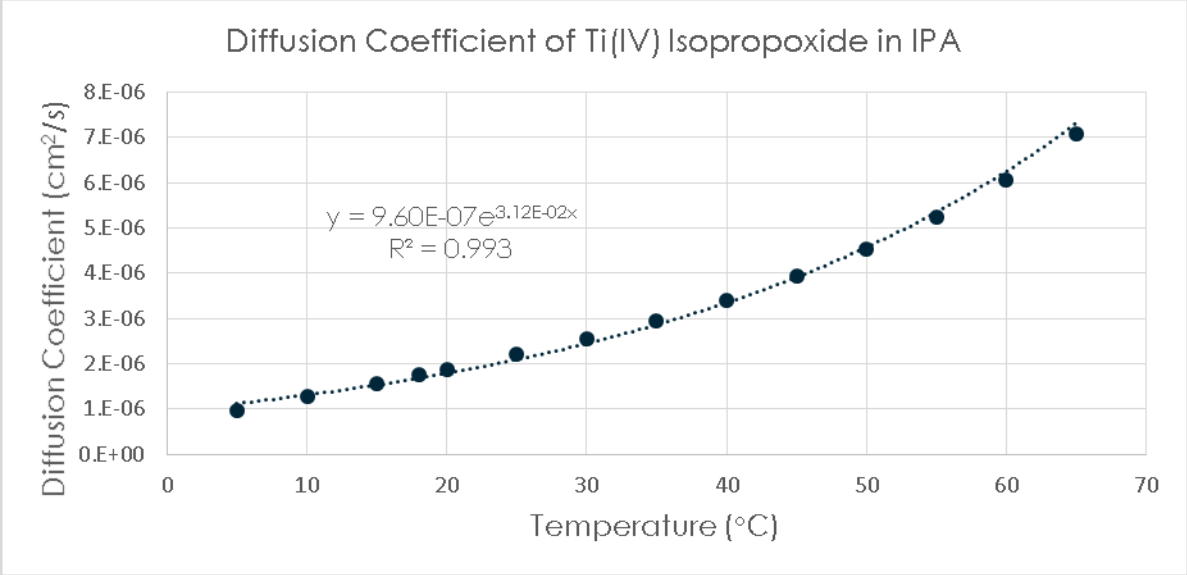

Figure 115: Graph of the diffusion coefficient of Ti(IV) isopropoxide in isopropanol with respect to temperature.

The diffusion coefficient for Ti(IV) isopropoxide in isopropanol at 18 °C was calculated to be approximately 1.75E-6 cm^2/s. This value was used along with the physical properties of isopropanol to calculate the boundary layer thicknesses used in CHAPTER 5.

A.1 References

[1] E. L. Cussler, *Diffusion: mass transfer in fluid systems*: Cambridge university press, 2009.

[2] H. Martin, "The generalized Lévêque equation and its practical use for the prediction of heat and mass transfer rates from pressure drop," *Chemical Engineering Science,* vol. 57, pp. 3217-3223, 2002.

[3] S. V.P, "Study of Viscosity and Critical Temperatures of Deuterium Compounds and Their Mixtures," *Ukrainskii Khimicheskii Zhurnal,* vol. 24, pp. 7-12, 1958.

[4] K. Soliman and E. Marschall, "Viscosity of selected binary, ternary, and quaternary liquid mixtures," *Journal of Chemical & Engineering Data,* vol. 35, pp. 375-381, 1990/10/01 1990.

[5] M. N. Sovilj, "Kinematic viscosities of binary and ternary liquid mixtures involving chloroform, 2-propanol, and 2-butanol at several temperatures," *Journal Name: Journal of Chemical and Engineering Data; Journal Volume: 40; Journal Issue: 5; Other Information: PBD: Sep-Oct 1995,* pp. Medium: X; Size: pp. 1058-1061, 1995.

[6] M. Sakurai, "Partial molar volumes in aqueous mixtures of nonelectrolytes. II. Isopropyl alcohol," *Journal of Solution Chemistry,* vol. 17, pp. 267-275, 1988/03/01 1988.

[7] F.-M. Pang, C.-E. Seng, T.-T. Teng, and M. H. Ibrahim, "Densities and viscosities of aqueous solutions of 1-propanol and 2-propanol at temperatures from 293.15 K to 333.15 K," *Journal of Molecular Liquids,* vol. 136, pp. 71-78, 11/15/ 2007.

Vita

Philip Davis Brooke was born to Allan and Katherine Brooke in 1988 in Dallas Texas. He grew up with his older brother Alban and younger siblings Priscilla, Sarah, and Thomas in Jacksonville Florida. He was educated by his parents and local community through the Elijah Homeschool Group through high school. In December of 2010, he graduated from the University of North Florida where he earned his Bachelor of Science degree in Mechanical Engineering. In the fall of 2011, he joined Dr. Kenneth H. Sandhage's research laboratory in the School of Materials Science and Engineering at the Georgia Institute of Technology.